Breakup of a laminar liquid jet by coaxial non-swirling and swirling air streams

Yifan Liang

Doctor of Philosophy

THE UNIVERSITY OF EDINBURGH

2023

To my dear Martina

Abstract

This thesis describes an experimental study on shear-based spray formation. A laminar liquid jet was ejected inside co-annular non-swirling and swirling air streams. The aerodynamic Weber numbers (We_A) and swirl numbers (S) of the flow cases ranged from 4 to 1426 and from 0 to 3.9, respectively. High-speed shadowgraphy was utilised to obtain data on the first droplet locations, breakup lengths of the liquid jets, and two-dimensional wave spatiotemporal spectra for the jets. In order to detect the large-scale instabilities of the central liquid jet, proper orthogonal decomposition (POD) was performed on the high-speed shadowgraphic images. Stereo particle image velocimetry (SPIV) was utilised to investigate the annular air flow fields with S in the range of $0-2.5$. Phase Doppler interferometry (PDI) was utilised to measure the droplet size and velocity distributions. It was found that air swirl promotes the morphological development of the jets with S in the range of $1.2-2.5$. Both the breakup length and axial distance between the first droplet separation and the nozzle exit reduce as We_A and S increase. In terms of the air flow fields, radial expansion of the annular swirling air jets was observed, and the annular swirling jets expand radially further as S goes up. Central reversal air flows appear near the nozzle exit when $S \geq 1.2$, and some small droplets are blown upwards to the nozzle exit by these central reversal air flows. In terms of large-scale instabilities, flapping is the dominant instability across most of the flow cases (as revealed by the first POD mode). Wavy and explosive breakup appear as the secondary breakup modes when We_A is low (≤ 110). In the absence of the central reversal air flows, the temporal frequencies of the instabilities of the air-water interfaces increase as S goes up. It was found that the central reversal air flows tend to stabilize the air-water interfaces. The spatial frequencies of the instabilities of the air-water interfaces remain low (≤ 0.06 mm^{-1}) across all the flow cases which produce long wave structures.

As S increases, atomization is improved in a way that the droplets are blown outward from the central axis of the nozzle. However, for some specific flow cases, the median droplet diameter (D) does not appear to be related to S. Those specific flow cases are discussed in this work. For $S \geq 0.3$, upward motion of droplets located at the central axis of the nozzle was observed, which was caused by recirculating air flows. In addition, it was found that when S increases to 2.5, recirculating air flows start to penetrate to the water exit, which momentarily stops portions of the central laminar water jets from exiting. This pattern will be called turn-off behaviour in this thesis. In order to study the underlying mechanisms behind the turn-off behaviour, proper orthogonal decomposition (POD) was performed on the shadowgrams. It was found that the timing of turn-off initiation is random.

In general, there are three breakup mechanisms including turbulence in the liquid, aerodynamic forces acting on the gas-liquid interface, and cavitation inside the nozzle. In this project, shear forces are isolated from the other breakup mechanisms. How shear forces and air swirl influence the breakup of a co-annular air-water jet was investigated.

Lay Summary

Spray systems are widely used in many areas of life such as the injector of internal combustion (IC) engine, for coating surfaces, and drug delivery to human air passages, for example. A spray is produced by an atomizer. There are many types of atomizers such as pressure, rotary, air-assist, air blast atomizers, etc. The liquid jet will experience a pressure drop and then break into drops and ligaments after it leaves the nozzle. That process is called atomization. The size and velocity distributions of the droplets play a key role in spray system performance.

The shear-based sprays are widely used in industry. For example, jets in cross flow, as used in gas turbine combustors, break up mainly by shear. The combustion efficiency is related to the way that a spray is used in a combustor. It is therefore necessary to gain better understanding of how the droplets and ligaments are formed in the spray. Hence, to make the best use of a spray system, it is important to make the process of formation of droplets and ligaments controllable. Unfortunately, there is currently no fully predictive model for realistic spray formation owing to the lack of detailed spray formation statistics. The aim of this thesis is to develop a comprehensive database for shear-based spray formation which can be used for the validation on a predictive model.

Acknowledgements

In the past three and a half years, I came across many difficulties in my life and research. I would not be able to overcome all the difficulties without the help of my supervisor and my friends.

First and foremost, I would like to thank my PhD supervisor, Prof. Mark Linne. He is the best supervisor I have ever seen. During the lockdown of Edinburgh in 2020, he gave me many mental supports and taught me how to write a PhD thesis. He gave me a lot of advice when I was doing data processing and troubleshooting for my set-up, which helped me a lot. Thanks for teaching me how to align the optics and lasers. Thanks for the numerous beers that he invited me to. Thanks for teaching me how to write an academic paper.

Next, I would like to thank Dr. Lars Christian Johansen. He gave me a lot of advice on how to do image processing. I specially would like to thank him for teaching me how to do proper orthogonal decomposition and 2D FFT by developing some tutorial codes. Thanks for teaching me how to align the optics and how to use the lasers and PDI equipment. Thanks for all the advice that he gave me when I was working on this PhD project. I would like to thank Dr. Brian Peterson for sharing his experience with me when I was doing SPIV. Thanks Dr. Shangze Yang for helping me when I was working in the lab, and for teaching me how to find a job in China. Thanks Dr. David Escofet-Martín and Dr. Ojo Anthony for giving me advice when I was doing the troubleshooting for my set-up.

Finally, I would like to thank my friends, George Kasapis, Nicolas Alexander, Hibbah Akhtar, Donghui Xu, Tiejun Ding, Xuan Wang and many others. It's been a pleasure knowing them and hanging out with them. I had a great time with them in Edinburgh. Thanks Calum Melrose and Scott Cummings for helping me manufacture the mechanical parts for my project. Thanks Zhizhu Tan for manufacturing some air swirlers using a 3D printer. Thanks my girlfriend, Martina, for encouraging me when I was facing challenges. Thanks my parents, Guoxin Liang and Hongjie Xu, for supporting me financially and mentally.

Declaration

I declare that this thesis was composed by myself, that the work contained herein is my own except where explicitly stated otherwise in the text, and that this work has not been submitted for any other degree or professional qualification except as specified. Two journal papers have been published already as part of this research. Sections from those two papers have been used in this thesis. The full citations and the sections extracted from those publications are listed below.

- Liang, Y., Johansen, L. C.,& Linne, M. (2022). Breakup of a laminar liquid jet by coaxial non-swirling and swirling air streams. Physics of Fluids, 34(9), 093606. https://doi.org/10.1063/5.0100456.

  Extracts included and/or adapted from this publication are: Chapter 3 except sections 3.5 and 3.7, Chapter 4 and Chapter 6.

- Liang, Y., Johansen, L. C.,& Linne, M. (2022). Characteristics of sprays produced by coaxial non-swirling and swirling air-water jets with high aerodynamic Weber numbers. Physics of Fluids, 34(10), 103604. https://doi.org/10.1063/5.0107480.

  Extracts included and/or adapted from this publication are: Chapter 3 except subsection 3.6.2 and sections 3.4 and 3.7, Chapter 5 and Chapter 6.

Yifan Liang

Contents

Appendices

Figures and Tables

Figures

Tables

Nomenclature

Acronyms

B	bag breakup regime
BF	boundary of fiber-type atomization
CB	conical breakdown
CTRZ	central toroidal recirculation zone
DMD	dynamics mode decomposition
F	fiber-type atomization
FFT	fast Fourier transform
FWI	first-wind induced breakup regime
IC	internal combustion
MFC	mass flow controller
PDI	phase Doppler interferometry
POD	proper orthogonal decomposition
PTU	programmable timing unit
PVB	pre-vortex breakdown
SPIV	stereoscopic particle image velocimetry
SVD	singular value decomposition
SWI	second-wind induced breakup regime
VCC	vortex core centre

Symbols

α	angle that an image plane is rotated with respect to the lens plane by [rad]
ζ	two dimensional coordinate
$\boldsymbol{a}$	acceleration [m/s^2]
$\boldsymbol{D}$	electric displacement [c/m^2]
$\boldsymbol{E}$	electric field strength [V/m]

$\boldsymbol{H}$	magnetic field strength $[T]$
$\boldsymbol{I}$	identity matrix
$\boldsymbol{k}$	wavenumber vector $[m^{-1}]$
$\boldsymbol{P}$	Poynting vector $[W/m^2]$
$\boldsymbol{q}_{ij}$	velocity field $[m/s]$
$\boldsymbol{R}$	rotational matrix
$\boldsymbol{S}$	current density $[A/m^2]$
$\boldsymbol{T}$	translation vector
$\boldsymbol{U}$	flow's velocity vector $[m/s]$
$\boldsymbol{U}_p$	particle's velocity vector $[m/s]$
$\boldsymbol{U}_s$	velocity lag of the seed particles in a continuously accelerating flow $[m/s]$
$\boldsymbol{x}_c$	intermediate camera coordinate system
$\boldsymbol{X}_w$	object space
Δx	actual width of the fringe $[m]$
δ_x	thickness of the liquid vorticity layer $[m]$
δ_y	thickness of the gas vorticity layer $[m]$
$\dot{m}_g$	gas mass flow rate $[kg/h]$
ε	permittivity $[F/m]$
ε_0	permittivity in vacuum $[F/m]$
$\varepsilon_{\text{flap}}$	singular value distribution for flapping modes
ε_i	singular value distribution of a principal component
ε_r	relative permittivity
ε_x	bias error at x direction
ε_y	bias error at y direction
κ	electric conductivity $[S/m]$
κ_1	the first radial distortion factor to correct for lens distortion (barrel or cushion)
κ_2	the second radial distortion factor to correct for lens distortion (barrel or cushion)
λ	wavelength of the illumination laser [m]

λ_i	singular value for a principal component
μ	magnetic permeability of the medium $[N/A^2]$
μ_0	magnetic permeability in vacuum $[N/A^2]$
μ_f	dynamic viscosity of the flow $[kg/(m \cdot s)]$
μ_l	dynamic viscosity of liquid $[kg/(m \cdot s)]$
μ_r	relative magnetic permeability
ν_g	kinematic viscosity of gas $[m^2/s]$
ν_l	kinematic viscosity of liquid $[m^2/s]$
ω	frequency of the wave $[Hz]$
ω_z	magnitude of the vorticity at z direction $[s^{-1}]$
$\overline{\Delta x}$	width of the magnified fringe $[m]$
ϕ	spatial cross-correlation value for a pair of interrogation windows
ρ	distribution of space charge
ρ_f	fluid density $[kg/m^3]$
ρ_g	gas density $[kg/m^3]$
ρ_l	liquid density $[kg/m^3]$
ρ_p	particle density $[kg/m^3]$
σ	random error
σ	surface tension of the droplet $[N/m]$
σ_l	surface tension of liquid $[N/m]$
σ_x	measurement error
τ_f	characteristic time scale in the flow $[s]$
τ_p	relaxation time $[s]$
θ	swirl vane angle $[rad]$
$\underline{\varepsilon}$	complex dielectric constant
A	grey pixel value for the interrogation window in the first image
A'	grey pixel value for interrogation window in the second image
A_e	area of the liquid jet exposed to the gas $[m^2]$

A_g	cross sectional area of gas tube [m^2]
A_l	cross sectional area of liquid tube [m^2]
c	propagation speed of the wave [m/s]
C_D	drag coefficient of liquid jet $\left(C_D = \frac{2F}{\rho_g A_e (U_g - U_c)^2}\right)$
D	droplet diameter [m]
d	characteristic length [m]
D_0	external diameter of the liquid tube [m]
d_0	outer diameter at the entrance of the contraction air cone [m]
d_c	width of a symmetrical correlation peak [m]
D_G	diameter of the vane pack hub [m]
D_g	diameter of gas tube [m]
D_I	size of the interrogation window [m]
D_i	inner diameter of the gas tube [m]
d_i	inner diameter at the entrance of the contraction air cone [m]
D_l	diameter of liquid tube [m]
D_o	outer diameter of the gas tube [m]
D_{32}	Sauter mean diameter [m]
d_τ	particle image diameter [m]
DOF	depth of field [m]
F	aerodynamic force [N]
F	focal length of the lens of the receiver [m/s]
f	principal distance between the pinhole location and the image plane [m]
$f^\#$	f-number of the camera lens
f_{flap}	frequency of the flapping instability $[Hz]$
f_D	Doppler burst signal frequency [Hz]
f_t	temporal frequency of the shear instability $[Hz]$
f_x	spatial frequency of the shear instability $[mm^{-1}]$
I	interrogation window in the first image

I'	interrogation window in the second image
k	wavenumber [m^{-1}]
L	breakup length [m]
L_e	entrance length for a laminar water flow [m]
M	gas to liquid momentum flux ratio $\left(M = \frac{\rho_g U_g^2}{\rho_l U_l^2}\right)$
m	liquid to gas mass flux ratio $\left(m = \frac{\rho_l U_l A_l}{\rho_g U_g A_g}\right)$
M_c	critical momentum flux ratio
M_n	magnification of the camera
n_η	maximum of the column numbers
n_ξ	maximum of the row numbers
N_I	seeding concentration [$pairs/window$]
Oh	Ohnesorge number (ratio of internal viscous forces to interfacial surface tension forces) $\left(Oh = \frac{\mu_l}{\sqrt{\rho_l \sigma_l d}}\right)$
P_1	correlation value for the first correlation peak
P_2	correlation value for the second correlation peak
P_σ	surface tension pressure [Pa]
P_A	aerodynamic pressure [Pa]
P_I	internal pressure at a certain point on a droplet surface [Pa]
P_{min}	lowest correlation value of the correlation plane
Q	peak ratio
R_O	outer radius of the co-flow tube [m]
Re_g	gas Reynolds number (ratio of gas inertial forces to gas viscous forces) $\left(Re_g = \frac{U_g(D_g - D_l)}{\nu_g}\right)$
Re_l	liquid Reynolds number (ratio of liquid inertial forces to liquid viscous forces) $\left(Re_l = \frac{U_l D_l}{\nu_l}\right)$
Re_{D_l}	Reynolds number based on liquid tube diameter (D_l)
S	swirl number (ratio of axial flux of swirl momentum to axial flux of axial momentum) $\left(S = \frac{\int_0^\infty U_y U_\theta r^2 dr}{R_O \int_0^\infty U_y^2 r dr}\right)$
s	sizing slope factor
S_{meas}	measured swirl number

S_x	pixel aspect ratio correction
S_{cr}	critical swirl number
S_{pixel}	known pixel size [m]
Stk	Stokes number $(Stk = \tau_p/\tau_f)$
U	magnitude of the velocity at x direction [m/s]
U_θ	tangential velocity [m/s]
U_a	bulk velocity of the annular fluid jet [m/s]
U_c	bulk velocity of the central fluid jet [m/s]
U_c	convection velocity of the waves on the liquid-gas interface [m/s]
U_g	gas velocity [m/s]
U_l	liquid velocity [m/s]
U_t	bulk velocity of the tangential fluid jet [m/s]
U_y	axial velocity [m/s]
V	magnitude of the velocity at y direction [m/s]
V_D	droplet velocity [m/s]
W	magnitude of the velocity at z direction [m/s]
w	energy density [J/m^3]
We_A	aerodynamic Weber number (ratio of aerodynamic forces to liquid surface tension forces) $\left(We_A = \frac{\rho_g (U_g - U_l)^2 D_l}{\sigma_l}\right)$
We_l	liquid Weber number (ratio of fluid's inertial forces to liquid surface tension forces) $\left(We_l = \frac{\rho_l (U_g - U_l)^2 D_l}{\sigma_l}\right)$
X_{measure}	value that is measured from an experiment
X_{ture}	true value
Y	first droplet location [m]

Chapter 1

Introduction

Spray systems are widely used in many industrial applications. Sprays are produced by an atomizer, among which there are many types (pressure, rotary, air-assist, air blast atomizers, etc.) (Lefebvre & McDonell, 2017). A liquid jet will undergo a pressure drop as it leaves a nozzle, and then break into drops and ligaments during the atomization process (Heywood, 2018). The size and velocity distributions of the droplets play a key role in spray system performance.

Unfortunately, there is currently no fully predictive model for realistic spray formation owing to the lack of detailed spray formation statistics. In general, there are three major breakup mechanisms including turbulence in the liquid, aerodynamic forces acting on the gas-liquid interface (which are also called "shear forces"), and cavitation inside the nozzle (Lefebvre & McDonell, 2017). Hence, in order to develop a database for research groups in CFD, each of these breakup mechanisms should be isolated from the others and a complete validation dataset obtained. After that, researchers can validate their simulation approach by comparing them with that database. Otherwise, atomization might be simultaneously caused by interaction of these three breakup mechanisms, which will make CFD validation more difficult and uncertain. For example, in this project, in order to separate the shear forces from the other breakup mechanisms, the liquid flow is laminar, and the liquid delivery tube is long and straight to ensure that there is no cavitation inside the nozzle. CFD research groups can compare their results with the data obtained from this project to check whether their codes can correctly predict the spray formation caused by shear forces alone.

This thesis discusses experiments on a co-annular (air and water) jet, and the development of a CFD validation database for shear breakup. Hence, the basic theories of coaxial jets and droplet formation are introduced here. The definition of a co-annular jet is that a central fluid jet and its annular fluid jet are ejected simultaneously, and these two fluid jets subsequently interact with each other. There are many types of co-annular jets depending on the types of the fluids that are used for the central and annular fluid flows, such as an air-water jet and an air-air jet. A complete introduction on all types of co-annular jets is beyond the scope of this thesis. Instead, an air-water jet that is investigated in this project is discussed in this subsection. Fig. 1.1 shows the general structure of an air-water jet. As shown in the figure, D_g is the diameter of the gas tube, D_l is the diameter of the liquid tube, t is the thickness of the liquid tube, U_l

and U_g are the velocity of liquid and gas respectively, and L is the liquid core length where the intact liquid breaks. Liquid and gas are ejected from the middle liquid tube and surrounding gas tube, respectively. As mentioned in this chapter, shear instabilities occur at the liquid-gas interface, and the breakup of a liquid jet is related to shear instabilities. The amplitudes of the shear instabilities increase as in the downstream direction. At a certain downstream position, the amplitudes increase to a certain value beyond which the liquid jet breaks up completely into droplets. This process is called primary breakup. Primary breakup also includes the droplets, lumps or ligaments that are peeled off from the liquid core due to the aerodynamic forces acting on the liquid-gas interface. The internal pressure at any point on a droplet surface remains a constant if a droplet is stable (Lefebvre & McDonell, 2017). According to Lefebvre and McDonell (2017), for a stable droplet, the relationship among the internal pressure, aerodynamic pressure and surface tension pressure is given by:

$$P_I = P_A + P_\sigma = \text{constant}, \tag{1.1}$$

where, P_I is the internal pressure at a certain point on a droplet surface, P_A is the aerodynamic pressure, and P_σ is the surface tension pressure. According to Lefebvre and McDonell (2017), the surface tension pressure for a spherical droplet can be expressed by:

$$P_\sigma = \frac{4\sigma}{D}, \tag{1.2}$$

where, σ is the surface tension of the droplet, and D is the diameter of the droplet. If the increase of the aerodynamic pressure acting on the droplet surface cannot be compensated by the change of the surface tension pressure to keep the internal pressure as a constant, droplet breakup will happen (Lefebvre & McDonell, 2017). This process is called secondary breakup. Secondary breakup generates small drops which have high surface tension pressure. The small drops will become stable if the change of their surface tension pressure can compensate the change of the aerodynamic pressure. Otherwise, drop breakup will happen again until the equilibrium shown in equation (1.1) is achieved.

The rest of this chapter is divided into three sections: Sec. 1.1 (Co-annular Non-swirling Jet), Sec. 1.2 (Co-annular Swirling Jet) and Sec. 1.4 (Research Project). In terms of co-annular non-swirling jet, the breakup length of the liquid jet, breakup regimes, shear instability and droplet Sauter mean diameter (D_{32}) are four characteristics that are of main interest. In Sec. 1.1, therefore, terms normally associated with co-annular non-swirling jet are defined, and then the investigations that have been undertaken on these four characteristics are discussed. In Sec. 1.2, terms normally associated with co-annular swirling jet are defined, and then the investigations that have been done on the critical swirl number, D_{32} and modes of vortex breakdown are discussed. Sec. 1.4 shows the goal of this project and the questions that this project answers.

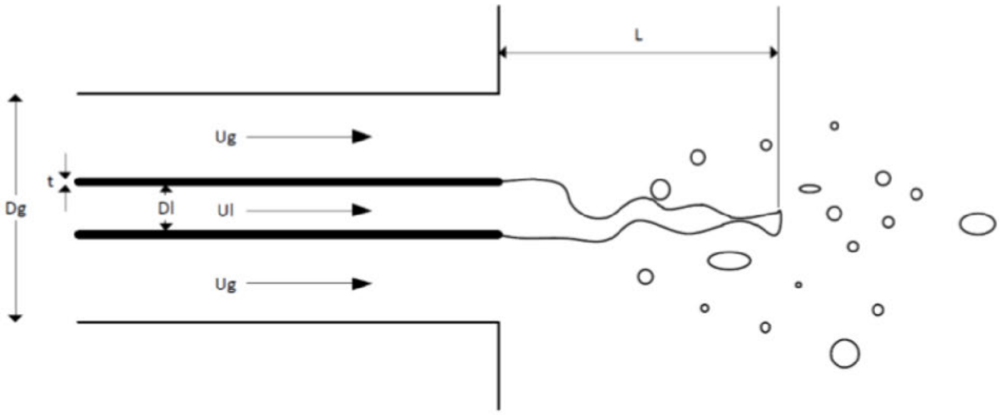

Figure 1.1: General structure of an air-water jet (Langeslag & Linne, 2016).

1.1 Co-annular Non-swirling Jets

Seven parameters (usually non-dimensional numbers) are generally used to describe the operating conditions of any spray, with their physical meanings summarized in Table 1.1. They include the Ohnesorge number,

$$Oh = \frac{\mu_l}{\sqrt{\rho_l \sigma_l d}}, \tag{1.3}$$

liquid Weber number,

$$We_l = \frac{\rho_l \left(U_g - U_l\right)^2 D_l}{\sigma_l}, \tag{1.4}$$

aerodynamic Weber number,

$$We_A = \frac{\rho_g \left(U_g - U_l\right)^2 D_l}{\sigma_l}, \tag{1.5}$$

liquid Reynolds number,

$$Re_l = \frac{U_l D_l}{\nu_l}, \tag{1.6}$$

gas Reynolds number,

$$Re_g = \frac{U_g \left(D_g - D_l\right)}{\nu_g}, \tag{1.7}$$

gas to liquid momentum flux ratio,

$$M = \frac{\rho_g U_g^2}{\rho_l U_l^2}, \tag{1.8}$$

Table 1.1: Physical meanings of the parameters used to describe the operating conditions of the co-annular non-swirling jet.

Parameter	Physical meaning
We_l (Weber number)	ratio of fluid's inertial forces to liquid surface tension forces
We_A (aerodynamic Weber number)	ratio of aerodynamic forces to liquid surface tension forces
Re_l (liquid Reynolds number)	ratio of liquid inertial forces to liquid viscous forces
Re_g (gas Reynolds number)	ratio of gas inertial forces to gas viscous forces
Oh (Ohnesorge number)	ratio of internal viscous forces to interfacial surface tension forces

and liquid to gas mass flux ratio,

$$m = \frac{\rho_l U_l A_l}{\rho_g U_g A_g}. \tag{1.9}$$

Here, d is a characteristic length, ρ_l is the density of the liquid, ρ_g is the density of the gas , U_g is the gas velocity, U_l is the liquid velocity, D_l is the diameter of the liquid tube, D_g is the diameter of the gas tube, σ_l is the surface tension of the liquid, ν_l is the kinematic viscosity of the liquid, ν_g is the kinematic viscosity of the gas, A_g is the cross sectional area of the gas tube, and A_l is the cross sectional area of the liquid tube. The physical meanings of these parameters are listed at Table 1.1. The aerodynamic Weber number includes the aerodynamic forces in the numerator, while the liquid Weber number does not. Hence, in order to include the influence of the aerodynamic forces from the coflowing gas on liquid jet breakup, the breakup regimes of a co-annular non-swirling jet (as studied here) are characterised by the aerodynamic Weber number and the liquid Reynolds number. Following atomization, the droplet size distribution can vary as a function of location and time. As a convenient way to present data, the Sauter mean diameter (D_{32}), given by:

$$D_{32} = \frac{\sum_{i=1}^{N} n_i d_i^3}{\sum_{i=1}^{N} n_i d_i^2}, \tag{1.10}$$

is generally used to describe the average size of droplets (Engelbert, Hardalupas, & Whitelaw, 1995). Here N is the number of ranges, and n_i is the number of the droplets with diameters equal to d_i within each range.

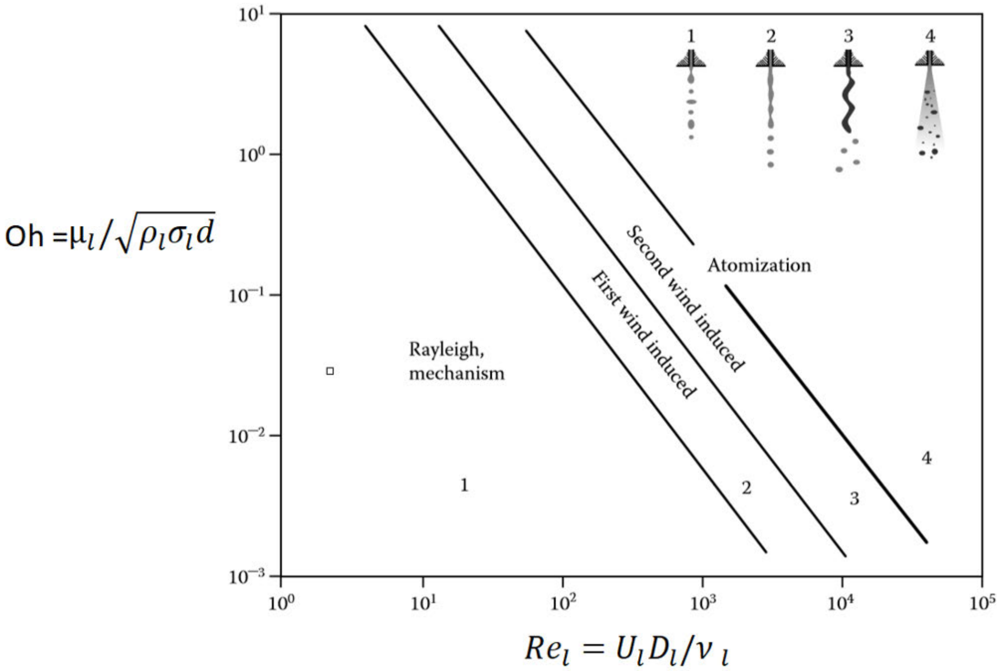

Figure 1.2: Four breakup regimes characterised by Oh and Re_l (Reitz, 1978). Region 1: Rayleigh break-up. Region 2: first wind-induced break-up. Region 3: second wind-induced break-up. Region 4: atomization.

When a liquid jet is ejected into a gas, inertial forces, surface tension of the liquid, and aerodynamic forces will simultaneously act on the liquid jet. According to Varga et al. (2003), the aerodynamic forces imposed by the ambient gas can be expressed by:

$$F = C_D \frac{1}{2} \rho_g \left(U_g - U_c\right)^2 A_e, \tag{1.11}$$

where C_D is the drag coefficient of liquid jet, U_c is the convection velocity of the waves on the liquid-gas interface, and A_e is the area of the liquid jet exposed to the gas.

Four breakup regimes have been identified by Reitz and Bracco (1986) under various operating conditions. They are Rayleigh breakup, first wind-induced or non-axisymmetric, wind stress or second-wind-induced, and atomization regimes (see Fig. 1.2). Reitz and Bracco (1986) ejected a liquid jet into a stagnant gas. They found that when the jet velocity is low (entering Rayleigh breakup regime), long-wavelength, small-amplitude disturbances caused by surface tension can be observed on the liquid-gas interface, and breakup happens many liquid tube diameters downstream. The droplet diameters are on the order of the liquid jet diameter and surface tension forces are dominant in the Rayleigh breakup regime.

When the jet velocity increases (entering the first-wind induced breakup regime), liquid jet breakup also occurs many liquid jet diameters downstream. The liquid jet enters the first-wind induced regime when the gas inertial forces exceed 10% of the surface tension forces (Ranz, 1956). Reitz (1978) ejected water and glycerol mixtures to a gas chamber. The gases that he used included air, nitrogen, helium and xenon. Reitz (1978) found that in the first-wind induced breakup regime, dilatational waves can be observed on the liquid-gas interface. In the first-wind induced breakup regime, the droplet diameter is nearly the same as the liquid tube diameter and the surface tension forces remain dominant (Reitz & Bracco, 1986). Aerodynamic forces begin to enhance the effect of surface tension forces because of the increase in the relative velocities between liquid and gas.

When the jet velocity increases further (entering the second-wind induced breakup regime), liquid jet breakup occurs several liquid jet diameters downstream. The liquid jet enters the second-wind induced breakup regime when the gas inertial forces have the same order of magnitude as surface tension forces (Ranz, 1956). Reitz (1978) found that a sinuous wave can be observed on the liquid-gas interface. The average droplet size is much smaller than the liquid tube diameter (Reitz, 1978). In the second-wind induced breakup regime, the liquid surface tension forces begin to oppose the wave growth.

The liquid jet enters the atomization regime when the jet velocity increases to a point where liquid jet breakup occurs near the nozzle exit. The breakup mechanics of this regime have not been fully explored (Lefebvre & McDonell, 2017; Reitz, 1978). Note that the discussions above on these four breakup regimes are for a liquid jet ejected into a stagnant gas, while this PhD thesis studies a co-annular non-swirling jet and a co-annular swirling jet. The physical behaviours of these four breakup regimes for a liquid jet ejected into a stagnant gas are similar to the ones for a co-annular non-swirling jet.

Lasheras and Hopfinger (2000) investigated a co-annular non-swirling air-water jet. Their liquid Reynolds numbers and aerodynamic Weber numbers ranged from 10 to 1.4×10^5 and from 10^{-3} to 10^5, respectively. They established a complete flow breakup regime map which includes those four breakup regimes for a co-annular non-swirling jet (see Fig. 1.3 on the following page).

Breakup length is one of the most important characteristics of a co-annular non-swirling jet. The breakup length of the liquid jet is related with the momentum flux ratio (M). When $M \ll 1$, the breakup length is determined by the liquid jet (Reitz & Bracco, 1986). On the other hand, when $M \gg 1$, the breakup length depends more on the gas jet (Hopfinger & Lasheras, 1996; Lasheras et al., 1998). If M exceeds the critical momentum flux ratio M_c (of about 50), a gas cavity is formed by the recirculating gas motion downstream of the liquid core. This gas cavity breaks the liquid core, and the breakup length becomes very short (Lasheras & Hopfinger, 2000).

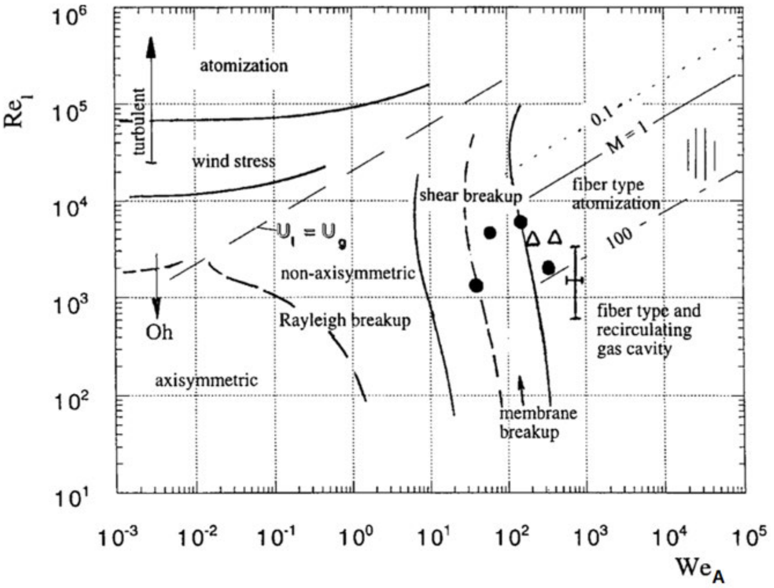

Figure 1.3: Flow regime map characterised by We_A and Re_l (Hopfinger, 1998; Lasheras & Hopfinger, 2000). • the operating conditions of the coaxial jets in Lasheras and Hopfinger (2000) Δ the operating conditions of the coaxial jets in Lasheras et al. (1998); ✠: the operating conditions of the coaxial jets in Lasheras and Hopfinger (2000); | | | the operating conditions of rocket engines.

Fig. 1.4 qualitatively illustrates five flow regimes that are characterised by jet velocity. They are dripping flow, laminar flow, transition, turbulent flow, and the fully developed spray regions. Note that Fig. 1.4 is for a liquid jet ejected into a stagnant gas. However, Lasheras and Hopfinger (2000) found that when the liquid jet velocity varies, the change of the breakup length of a co-annular non-swirling jet is qualitatively similar to the one of a liquid jet ejected into a stagnant gas. Based on the data for their co-annular non-swirling jet, Lasheras and Hopfinger (2000) quantitatively explain Fig. 1.4. They found that in the Rayleigh breakup regime (from points A to B), the breakup length (L) grows with the jet velocity until it reaches a maximum ($L = 100D_l$). As the jet velocity increases further, the liquid jet enters first-wind induced regime (from points B to C), and the breakup length decreases until it reaches a minimum ($L = 10D_l$). After that, the liquid jet enters second-wind induced regime where the breakup length experiences an increase with the jet velocity. This regime ends when the breakup length reaches its second maximum. Finally, the breakup length decrease to an asymptotic value. This asymptotic value is determined by the nozzle flow conditions, and especially on the liquid boundary layer thickness and turbulence level (Lin, 1996; Reitz & Bracco, 1986).

Lasheras et al. (1998) ejected a water jet inside a co-annular air jet, and established an entrainment model to describe qualitatively the liquid core length. The measurement techniques they used were high-speed shadowgrpahy and phase Doppler interferometry. The liquid Reynolds numbers ranged from 569 to 5689, and the aerodynamic Weber numbers ranged from 16 to

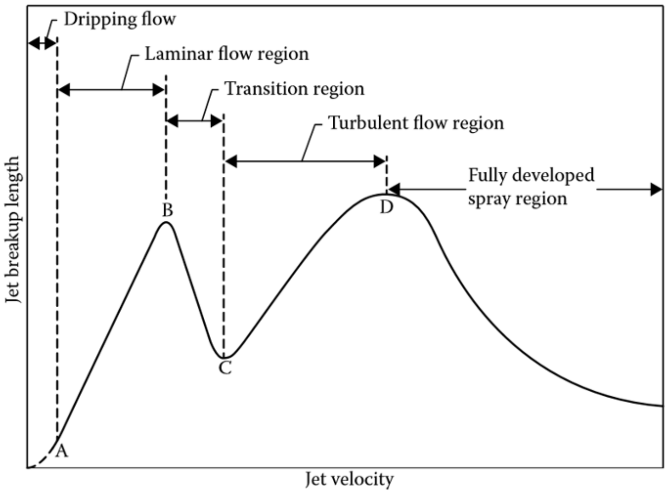

Figure 1.4: Flow regimes characterised by jet velocity (Lefebvre & McDonell, 2017).

800. To analyse theoretically the breakup length of a co-annular non-swirling jet, Lasheras and Hopfinger (2000) started with the dynamic pressure balance at the liquid-gas interface, producing a correlation for the liquid jet breakup length. Farago and Chigier (1992) utilized high-speed spark photography to investigate the breakup of a round liquid jet with a non-swirling coaxial air stream. Their aerodynamic Weber numbers and liquid Reynolds numbers ranged from 0.001 to 600 and from 200 to 20000, respectively. They obtained a correlation for breakup length as well. The empirical correlations for the liquid core length in the co-annular non-swirling jets obtained by Lasheras and Hopfinger (2000), and Farago and Chigier (1992) are shown in Table 1.2. The liquid core length data obtained from this project will be compared with these correlations.

Engelbert et al. (1995) used high-speed shadowgraphy and phase Doppler velocimetry to investigate a co-annular non-swirling jet over a wide range of aerodynamic Weber numbers, $We_A(70-3400)$, momenturm ratios, $M(3-175)$, liquid Reynolds numbers, $Re_l(4000-50000)$, and gas Reynolds numbers, $Re_g(50000-19000)$. The liquid and annular gas they used were water and air, respectively. They measured the breakup lengths of the liquid core, the temporal frequencies and amplitudes of the surface waves at the interface. Moreover, they also measured the velocities and Sauter mean diameters of the droplets at the downstream positions of 26, 52, and 91 liquid jet diameters. Engelbert et al. (1995) found that the breakup length of the liquid core is related with the momentum ratio and aerodynamic Weber number. When the momentum ratio or aerodynamic Weber number increases, the breakup length reduces. They also found that the amplitude of the surface waves reduces when the slip velocity between the central liquid jet and the annular air stream increases.The temporal frequencies of the surface waves reduce when the aerodynamic Weber number or momentum ratio increase. In terms of the measurement of velocities and size distributions of the droplets, it has been found that most of the droplets appear near the central axis of the nozzle where the Sauter mean diameters

Table 1.2: Correlations for the liquid core lengths.

Author	Correlation
Lasheras and Hopfinger (2000)	$\frac{L}{D_l} \approx \frac{6}{\sqrt{M}} \frac{1}{\sqrt{1-B_1\sigma_l/\mu_g U_g}}$, where $B_1 \approx 10^{-3}$, which is measured by Raynal (1997)
Farago and Chigier (1992)	$L = 0.66 D_l We^{-0.4} Re_l^{0.6}$, where We is based on the relative velocity between liquid and gas.

are larger than 100 $\mu\mathrm{m}$. As mentioned earlier, there are three breakup mechanisms including turbulence in the liquid, the aerodynamic forces acting on the gas-liquid interface (which are also called “shear forces”), and cavitation inside the nozzle (Lefebvre & McDonell, 2017). In order to establish a database for research groups in CFD, each of these three mechanisms should be isolated from the others. The drawback of the research undertaken by Engelbert et al. (1995) is that it involved two breakup mechanisms, including turbulence of the central liquid jet and the shear forces acting on the gas-liquid interface.

Coaxial non-swirling spray behaviours change with operating conditions. The spray behaviours are governed by the liquid Reynolds and aerodynamic Weber numbers. Hopfinger (1998) established a diagram of break-up regimes based on the various aerodynamic Weber numbers and liquid Reynolds numbers (see Fig. 1.3). Lasheras and Hopfinger (2000) performed an experiment with coaxial jets ejected from a convergent nozzle, and provided visualizations of membrane breakup and fibre-type atomization regimes using a high-speed camera (see Fig. 1.5). The convergent ratio of their nozzle was 7:1, and the diameters of the gas (D_g) and liquid tubes (D_l) were 11.3 mm and 7.6, respectively. At the onset of the “shear breakup regime”, the surface tension forces are dominant, and they oppose growth of the instability and formation of drops (see Fig. 1.5a). When the aerodynamic Weber number increases (entering the “membrane breakup regime”), ligaments are formed, and the aerodynamic forces acting on the liquid jet become large enough to blow up the liquid sheets behind the ligaments into bags (see Fig. 1.5b). The “membrane breakup regime” is also called “bag breakup regime”. When the aerodynamic Weber number increases further (entering the “fibre-type atomization regime”), the formation of fibres can be observed, and they subsequently break into smaller droplets (see Fig. 1.5c).

Apart from breakup regimes, shear instability and D_{32} are the characteristics that are of principal interest. Shear instability can be observed on the gas-liquid interface because the aerodynamic forces from the gas act on the liquid jet. The initial breakup mechanisms for the co-annular non-swirling jet have been studied qualitatively by Varga et al. (2003). When the coaxial annular air stream has low velocities, the air will introduce shear on the surface of the liquid jet once outside of the orifice, and the formation of ligaments can be observed on the gas-liquid interface. The lumps or ligaments stripping from the liquid jet appear after a

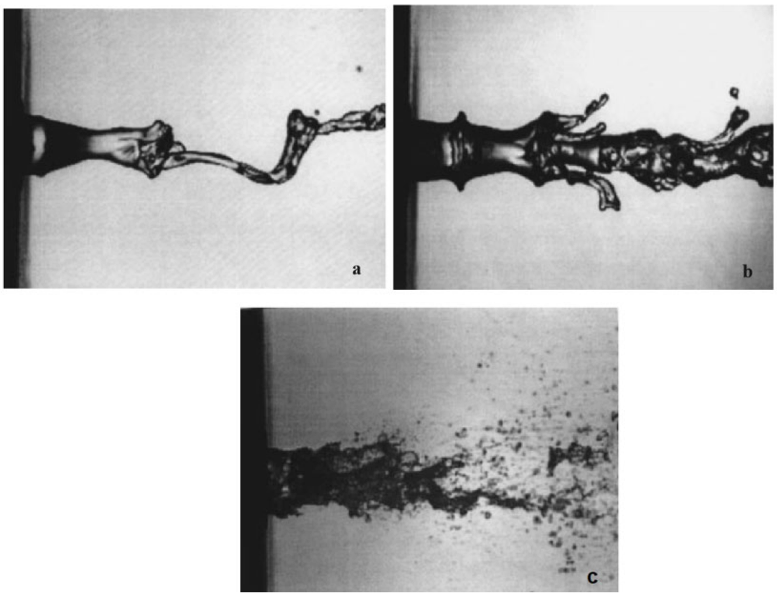

Figure 1.5: Visualizations of membrane breakup and fibre-type atomization. (a) Onset of shear breakup ($We_A = 38, U_l = 0.16$ m/s and $U_g = 19$ m/s). (b) Membrane breakup ($We_A = 58, U_l = 0.55$ m/s and $U_g = 21$ m/s). (c) Fibre-type atomization ($We_A = 316, U_l = 0.26$ m/s and $U_g = 50$ m/s) (Lasheras & Hopfinger, 2000).

few jet diameters, and subsequently they break into drops, which is called “primary breakup” or “spray formation”. Further downstream, when gas flow stresses acting on the droplets are large enough to destroy the stabilization maintained by the surface tension and viscosity, the droplets will break into smaller drops, which is called “secondary breakup” (Lasheras et al., 1998). In terms of destabilization of the interface, a Kelvin-Helmholtz instability driven by the shear force at the liquid-air interface can be observed near the nozzle exit. A velocity difference across the interface between two types of fluids can cause unstable vortex sheets, which subsequently roll up to spirals on the interface (Kelvin-Helmholtz instability). The Kelvin-Helmholtz instability propagates downstream and causes the breakup of the liquid jet. Further downstream, when the aerodynamic Weber number increases (entering the so-called “membrane regime”), Rayleigh-Taylor instabilities can be observed on the interface normal to the direction of the liquid jet (Varga et al., 2003). When there are two immiscible fluids with different densities, the lighter fluid pushes the heavier fluid and then an instability can be observed on the interface of these two fluids (Rayleigh-Taylor instability). Varga et al. (2003) ejected a water or ethanol jet into coflowing air, and developed a model to predict the R-T wavelengths which provided good agreement with their experimental data. The measurement techniques that they used were high-speed shadowgraphy and phase Doppler interferometry. The Reynolds numbers for the water jet ranged from 543 to 16567, and the aerodynamic Weber numbers ranged from 6 to 437. Varga et al. (2003) also utilised phase Doppler interferometry (PDI) to obtain the droplet size distributions and proposed scaling of drop-sizes. They found that the ratio of D_{32}

to the wavelength of Kelvin-Helmholtz instabilibity (λ_1), is related to the Weber number (We_{λ_1}). Their correlation for the droplet Sauter mean diameter collapsed well with the experimental data (see Fig. 1.6). Yang, Gao., Li, and Fu (2020) started from a stability analysis on the coaxial non-swirling air-liquid jet, and proposed a theoretical correlation to predict D_{32}. The working fluid that they used for the central liquid jet was water or ethanol, and their Reynolds numbers for the water jet ranged from 1597 to 5301. Their prediction on D_{32} collapsed well onto the experimental data given by Varga et al. (2003). The work of Lasheras et al. (1998), which has been introduced previously, also investigated near-field primary liquid break-up and secondary liquid break-up using a high-speed camera, together with drop size using a phase Doppler particle sizer (PDPA). The coaxial spray introduced by Lasheras et al. (1998) reached Weber numbers ranging from 10 to 800. For near-field breakup and atomization, they proposed an entrainment model to describe qualitatively the dependence of the measured liquid shedding frequency on the gas to liquid momentum flux ratio, M. For far-field breakup and atomization, they proposed two atomization models to explain the dependence of the breakup and coalesence of the droplets on the local turbulent dissipation rate in the gas stream, respectively. They found that the secondary breakup and coalescence of the droplets in the far field of the spray jet are mainly influenced by the total kinetic energy flux (mainly contained in the air jet) per unit total mass of air and water. They measured D_{32} at different locations on the far-field region over the wide range of liquid and gas conditions. It was found that at the downstream distances larger than 10 jet diameters, D_{32} reaches its minimum on the centreline of the liquid jet axis, and increases as one moves to the outer edge of the spray. Eroglu and Chigier (1991) ejected a water jet into coflowing air without swirl, and measured the initial drop size and velocity distributions using PDI. Their liquid Reynolds numbers ranged from 1097 to 4379. Eroglu and Chigier (1991) found that D_{32} grows when the velocity of liquid jet increases or the velocity of air jet decreases. They also found that the droplet mean velocities reach their minimum at the central axis of the nozzle, and the maximum droplet mean velocities appear on the periphery of the spray.

Aliseda et al. (2008) did a co-annular non-swirling jet experiment. The measurement techniques that they used were high-speed shadowgraphy and phase Doppler interferometry. The liquids they used were water and glycerol mixtures, and non-Newtonian liquids. More details about the non-Newtonian liquids can be found in Aliseda et al. (2008). Their nozzle is different from the traditional nozzle in the co-annular non-swirling jet experiment. In terms of experimental set-up, there is a central liquid jet, a coflowing annular gas jet and also two side air jets, which are located at the periphery of the annular gap and inclined at an angle of $45°$ to the central liquid jet. They started with the dispersion for non-Newtonian fluids given by Joseph, Beavers, and Funada (2002) and extended the modelling on droplet sizes developed by Varga et al. (2003)

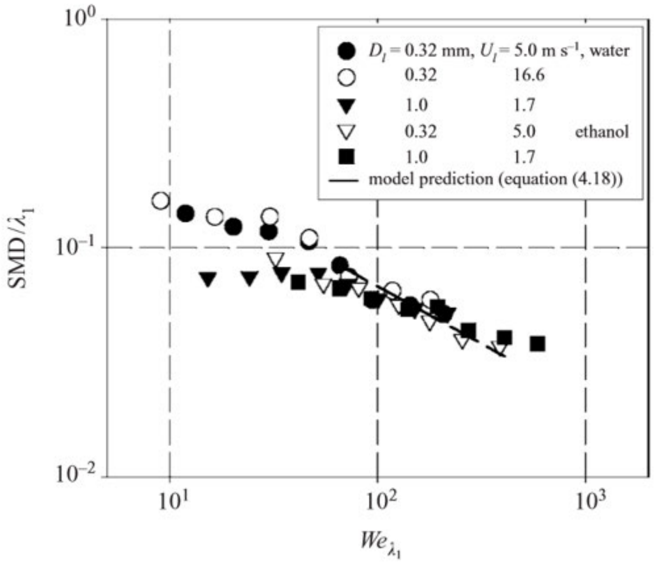

Figure 1.6: Ratio of D_{32} to wavelength (λ_1) of primary instability as a function of Weber numbers characterised by λ_1. $D_{32} = \frac{\sum_{i=1}^{N} n_i d_i^3}{\sum_{i=1}^{N} n_i d_i^2}$. Here N is the number of ranges, and n_i is the number of the droplets with diameters equal to d_i within each range. Data were measured at $x/D_g = 15$ (Varga et al., 2003).

to viscous and non-Newtonian liquid. Their predictions of D_{32} demonstrated good agreement with the data obtained from PDI. However, Varga et al. (2003) and Aliseda et al. (2008) did not provide a probability density function (PDF) for the drop-size and did not include the error bar at each data point.

Matas et al. (2018) also investigated shear instabilities in coaxial non-swirling jets using a high-speed camera. The central liquid jet they used was water, and the annular coflowing gas they used was air. Their liquid Reynolds numbers and aerodynamic Weber numbers ranged from 1400 to 7000, and from 30 to 72, respectively. In order to measure the shear instability frequency, Matas et al. (2018) performed fast Fourier transform (FFT) on the temporal signal measuring height of the air-water interface and obtained the frequency spectra of the shear instabilities (see Fig. 1.7). In Fig. 1.7, their power spectral density (PSD) plots indicate the magnitude of the wave amplitude. They found that based on the destabilization mechanisms, the shear instability can be categorized by three types; a convective instability, an absolute instability governed by surface tension, and an absolute instability governed by confinement (Matas et al., 2018). The convective instability permits the disturbance of the flow to move only in the downstream direction while absolute instability allows the disturbance of the flow to move in both downstream and upstream directions. Physically, when the interfacial velocity is so small that it allows the capillary waves to move upstream, the absolute instability governed by surface tension appears (Matas et al., 2018). When the spatial growth rate of the instability becomes large enough to cause cross-stream resonance, the absolute instability governed by

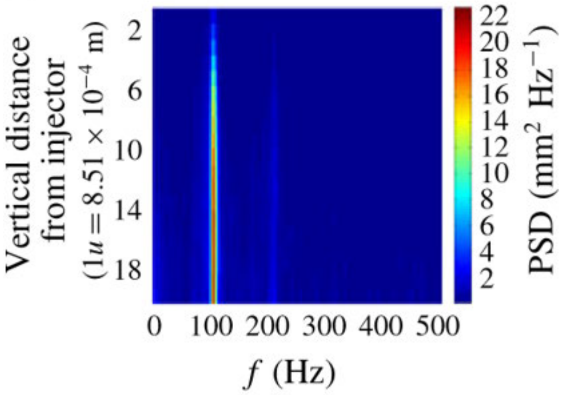

Figure 1.7: Frequency spectra of shear instabilities (Matas et al., 2018).

confinement appears (Matas et al., 2018). They also demonstrated that the frequencies of the convective instability, the absolute instability governed by surface tension, and the absolute instability governed by confinement vary as a function of the coflowing gas velocity, and they plotted the frequencies versus gas velocity. They also proposed scaling of the frequencies of these three shear instabilities, which collapsed well onto these graphs. A regime map of shear instability, which is governed by the Weber number (We_{U_i}) and momentum flux ratio (M), is shown in Fig. 1.8. Here $We_{U_i} = \rho_L U_i^2 / \sigma_l k_{imax}$, where U_i is the interfacial velocity, and k_{imax} is the growth rate of the most unstable wavelength. Although Matas et al. (2018) obtained the temporal frequency spectra of the shear instabilities, the spatial shear instability spectra remain unknown and are investigated in this project.

Absolute and convective instabilities have also been studied by Vihinen, Honohan, and Lin (1997) and Lin, Hudman, and Chen (1999). Vihinen et al. (1997) ejected a liquid jet into stagnant air. The liquid Reynolds numbers ranged from 0.04 to 0.4. The liquid Weber numbers ranged from 0.3 to 18. The liquids they used were silicon oil, glycerin and water mixtures, and SAE 10 oil. They captured the images of the convective and absolute instabilities, and plotted the transition region between absolute instability and convective instability on a We versus Re_l map. Lin et al. (1999) developed a similar experiment using the same apparatus as Vihinen et al. (1997). Lin et al. (1999) used an energy budget to calculate the time rate change of the disturbance kinetic energy, and found that surface tension is the main factor causing growth of the disturbance when the liquid jet experiences Rayleigh breakup. Umemura (2014) ejected a laminar liquid jet into stagnant air, and developed a model to predict formation of ligaments, which subsequently break into droplets. He obtained a diagram of the locations for the first ligament formation over the wide range of Reynolds numbers. However, A comprehensive database for spray formation should include the first droplet location data which has not been investigated in prior work. Hence, the relationships between the first droplet locations and aerodynamic Weber numbers and swirl numbers are investigated in this project.

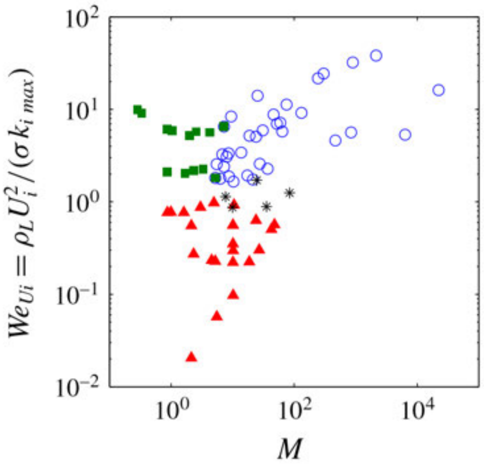

Figure 1.8: Instability regime map characterised by the Weber number (We_{U_i}) and momentum flux ratio (M) (Matas et al., 2018). Here $We_{U_i} = \rho_L U_i^2/\sigma_l k_{imax}$, where U_i is the interfacial velocity, and k_{imax} is the growth rate of the most unstable wavelength. Based on their destabilization mechanisms, each flow case is presented in this map. The blue circular symbols represent the flow cases showing the absolute instabilities governed by confinement. The red triangular symbols represent the flow cases showing the absolute instabilities governed by surface tension. The green square symbols represent the flow cases showing the convective instabilities. The black symbols with star shapes represent the situations where the growth rates of the confinement and surface tension instabilities are similar.

1.2 Co-annular Swirling Jets

Two parameters are generally used to describe the operating conditions of a co-annular swirling jet. They are swirl (S) and Rossby (Ro) numbers. According to Giannadakis, Perrakis, and Panidis (2008) and Ivanic, Foucault, and Pecheux (2003), the swirl number (S), ratio of axial flux of swirl momentum to axial flux of axial momentum, is given by:

$$S = \frac{\int_0^\infty U_y U_\theta \, r^2 dr}{R_O \int_0^\infty U_y^2 r \, dr}, \tag{1.12}$$

where U_y is the axial velocity, U_θ is the tangential velocity and R_O is the outer radius of the co-flow tube. The correlations for geometric swirl numbers depend on the type of the air swirler. Details about the correlations for geometric swirl numbers can be found in Giannadakis et al. (2008). According to Hardalupas and Whitelaw (1998), based on the type of the air swirler used in this project, the geometric swirl number is given by:

$$S = \frac{2}{3} \tan\theta \frac{1 - \left(\frac{D_O}{D_G}\right)^3}{1 - \left(\frac{D_O}{D_G}\right)^2}, \tag{1.13}$$

where θ is the swirl vane angle, D_0 is the external diameter of the liquid tube, and D_G is the diameter of the vane pack hub. The Rossby number (Ro),

$$Ro = \frac{U}{fL}, \tag{1.14}$$

where U is the velocity scale, f is the Coriolis parameter, and L is the horizontal length scale, is the ratio of inertial to Coriolis forces. However, according to Rajamanickam and Saptarshi (2018), Ro can be defined in terms of the geometry of the atomizer:

$$Ro \sim \frac{|\Delta U_y|}{U_t}, \tag{1.15}$$

where $\Delta U_y \sim U_c - U_a$. Here U_c is the bulk velocity of the central fluid jet, U_a is the bulk velocity of the annular fluid jet and U_t is the bulk velocity of the tangential fluid jet. Ro is commonly used to describe the features of the recirculating flow field. It has been found that vortex breakdown happens when the centrifugal momentum is larger than axial momentum (i.e. $\rho U_\theta^2 > \rho U_y^2$, where U_θ is the radial velocity of the air) (Rajamanickam & Saptarshi, 2018). Hence, the magnitude of Ro indicates the dominant momentum in the flow. If Ro is larger than 1, the axial momentum is dominant over centrifugal momentum. If Ro is less than 1, centrifugal momentum is dominant over axial centrifugal momentum. Both Rossby and swirl numbers of the flow influence jet breakup by the swirling flow. A flow regime map which is characterised by Rossby and swirl numbers will be discussed later (see Fig. 1.14 on page 22).

In order to investigate how air swirl influences spray performance, Hopfinger and Lasheras (1996) used high-speed shadowgraphy to investigate the breakup of a water jet by a coaxial swirling air jet over a wide range of liquid Reynolds numbers, $Re_l(740-11400)$, swirl numbers, $S(0.4-0.6)$, and gas to liquid momentum flux ratios, $M(1-1000)$. They found that the addition of a swirling annular gas stream has a significant effect on the liquid jet breakup if the swirl number goes beyond the critical swirl number. The effect of co-annular swirling gas on liquid jet breakup can be observed by comparing Fig. 1.9a with Fig. 1.9b. When the swirl number (S) is above the critical swirl number (S_{cr}), a central recirculating flow and a stagnation point on the centreline of the liquid jet axis can be observed (see Fig. 1.9b). It is obvious that the liquid jet expands significantly, which is called explosive breakup, and a hollow-cone type spray can be observed (see Fig. 1.9b). They found a relationship between the critical swirl number and the gas-to-liquid momentum flux ratio. When the gas-to-liquid momentum flux ratio (M) is less than 1, the critical swirl number shows asymptotic $M^{-1/2}$ dependence (see Fig. 1.10). On the other hand, if M is much larger than 1, S_{cr} remains a constant. That constant depends on the ratio of axial gas to liquid velocity at the nozzle, and the ratio of gas to liquid jet diameter (Hopfinger & Lasheras, 1996). However, the motion of the annular swirling gas remains unknown. Hardalupas and Whitelaw (1998) investigated the breakup of a turbulent water jet by a co-annular air stream with S in the range of $\sim 0-7.9$. They used PDI to measure

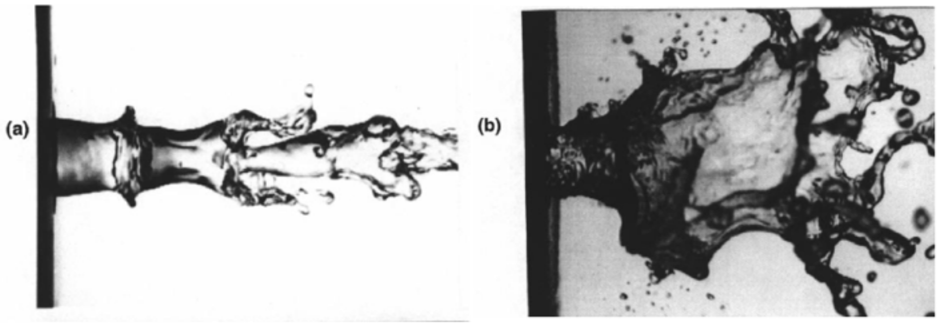

Figure 1.9: Water jet breakup by coflowing non-swirling and swirling air streams for $U_l = 0.55\ \mathrm{m/s}$ and $U_g = 22\ \mathrm{m/s}$, $M = 2.2$. (a) $S = 0$. (b) $S = 1.27$. $D_l = 7.6\ \mathrm{mm}$, $D_g = 11.3\ \mathrm{mm}$ (Lasheras & Hopfinger, 2000).

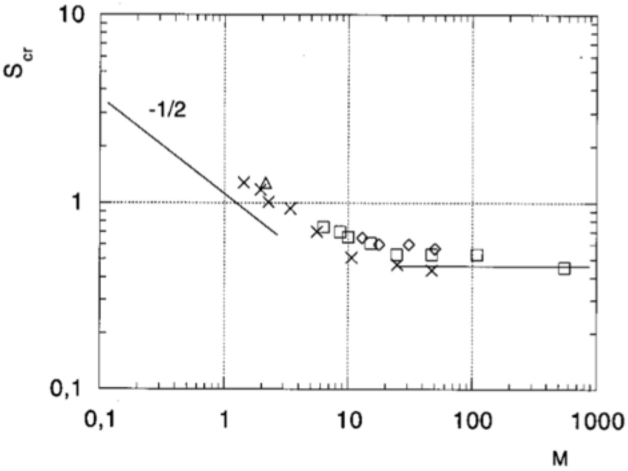

Figure 1.10: Relationships between S_{cr} and M (Hopfinger & Lasheras, 1996). The plotted symbols represent their experimental data.

the diameters, velocities and liquid fluxes of the droplets over a wide range of aerodynamic Weber numbers, $We_A(230-630)$. Hardalupas and Whitelaw (1998) observed the hollow cone-spray structures caused by the central recirculation of the swirling air flows with high S, which was consistent with what Hopfinger and Lasheras (1996) found. Hardalupas and Whitelaw (1998) found that the droplet size is related with the local Weber number (We_D) based on the droplet diameter and the relative velocity between the gas and liquid phases, rather than We_A, and that when $S > 0.3$, atomization is improved because droplets are blown outward away from the central axis of the nozzle. The hollow-cone spray structures were also observed by Machicoane et al. (2019) when they used high-speed X-ray radiography to investigate a central water jet surrounded by a coaxial air jet with and without swirl over a wide range of $Re_l(1100-6500)$, $M(6-202)$ and $S(0-1)$.

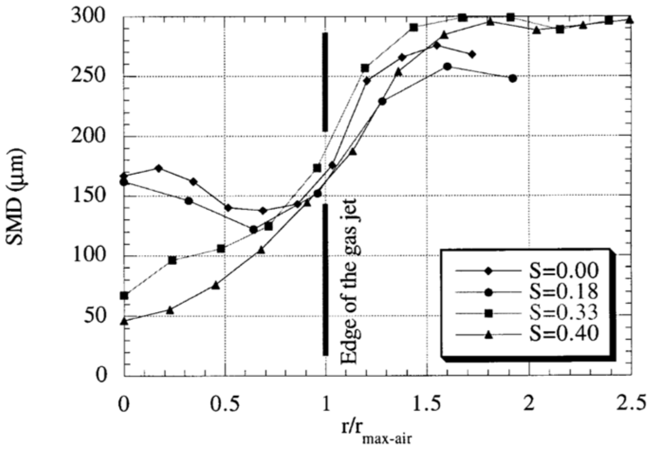

Figure 1.11: Radial droplet size distributions at $x/D = 20$ for various swirl numbers (Lasheras & Hopfinger, 2000).

Lasheras and Hopfinger (2000) measured the droplet size distributions for the breakup of a central liquid jet surrounded by a coaxial swirling air stream with S in the range of $0-0.4$, and pointed out that when S goes beyond S_{cr}, the spray can be divided into three regions in terms of D_{32}: an external region where D_{32} reaches its maximum; an internal region where the central recirculating air flow happens and D_{32} reaches its minimum; and a middle hollow conical region where the D_{32} distribution is bimodal (see Figs. 1.9b and 1.11). They also found that this middle hollow conical region is pushed outward with the increase of S, and that the sizes of the droplets located in that region are independent of S, while the sizes of the droplets located in the inner region depend on S. Lasheras and Hopfinger (2000) pointed out that the mechanism for atomization of the droplets in the outer region is primary breakup. Dunand, Carreau, and Roger (2005) used PDI, tomography and an optical fiber probe to investigate the breakup of a turbulent water jet by a coaxial air jet with S and M in the ranges of $\sim 0-0.6$ and $\sim 3-13.3$, respectively. They found that the hollow-cone spray appears when the gas swirl number goes beyond the critical swirl number of their nozzle. Furthermore, the transition to “explosive breakup” of the liquid jet (caused by a gas-phase recirculation zone) significantly reduces the breakup length (Dunand et al., 2005). They also found that the addition of the annular swirling gas stream reduces the breakup length of the liquid jet more significantly as the momentum ratio grows. Dunand et al. (2005) found that when S goes beyond S_{cr}, large droplets with ballistic trajectories appear on the jet periphery, while small droplets are located in the hollow-cone region caused by the recirculating air flows. They also found that when $S < S_{\text{cr}}$, big droplets are located near the central axis of the nozzle, while small droplets appear on the outer edge of the jet.

Although research on the breakup lengths of the co-annular non-swirling jets has been reported (Eroglu, Chigier, & Farago, 1991; Kumar & Sahu, 2018a; Leroux, Delabroy, & Lacas, 2007; Zhao et al., 2014), only a handful of studies on the breakup lengths of the co-annular swirling jets have been reported. Kumar and Sahu (2018b) used the optical connectivity technique to investigate a central turbulent water jet surrounded by a co-annular air flow with and without swirl over a wide range of aerodynamic Weber numbers, $We_A(80-300)$, gas to liquid momentum flux ratios, $M(1-8)$, and swirl numbers, $S(0-0.8)$. They obtained an empirical correlation for the turbulent liquid breakup length in a co-annular swirling jet. They found that the turbulent liquid breakup length decreases as M or S increases. Machicoane, Ricard, Osuna-Orozco, Huck, and Aliseda (2020) ultilized high-speed shadowgraphy to measure the breakup length of a laminar water jet in a co-annular air jet with S in the range of $\sim 0-1$. They found that the liquid core length average and standard deviation decrease as M and S increase.

In order to understand how the strength of the air swirl makes a difference to the large-scale instabilities of the co-annular swirling and non-swirling jets, Kumar and Sahu (2019) used high-speed shadowgraphy and POD (proper orthogonal decomposition) to investigate a central turbulent water jet surrounded by a co-annular air flow with and without swirl over a wide range of aerodynamic Weber numbers, $We_A(80-958)$, momentum ratios, $M(1-26)$, and swirl numbers, $S(0-1.6)$. It should be noted that the correlation that they used to calculate the swirl number is different to the ones given by Giannadakis et al. (2008). The reason is that Kumar and Sahu (2019) used contraction nozzles, which required them to use a modified correlation to calculate the swirl number. According to Marklund and Engstrom (2010) and Kumar and Sahu (2019), the modified correlation for the swirl number (S) is shown as follows:

$$S = tan\theta \frac{\left(D_o^2 - D_i^2\right)^2 \left(d_o^3 - d_i^3\right)}{\left(d_o^2 - d_i^2\right)^2 \left(D_o^3 - d_i^3\right)}, \tag{1.16}$$

Where, D_i and D_o are the inner and outer diameters of the gas tube, respectively, d_0 and d_i are the outer and inner diameters at the entrance of the contraction air cone, respectively, and θ is the swirler vane angle.

POD was applied to the images obtained from high-speed shadowgrpahy to detect the dominant modes, which represents the dominant instabilities in all the flow cases. More details about the principle of POD can be found in Sec. 2.5. Based on the extracted POD modes, they found three types of large-scale instabilities, including jet flapping, wavy or sinuous breakup and explosive breakup, for a wide range of liquid and gas conditions. The jet flapping instability is defined as the lateral oscillation of the tail end of the liquid core. The wavy or sinous breakup instability is characterized by the bending/twisting of the liquid jet before it experiences breakup. The explosive breakup instability is defined as a radical expansion of the liquid jet (Kumar & Sahu, 2019). As discussed above, Lasheras and Hopfinger (2000) also observed the explosive breakup of the liquid jet when the swirl number went beyond the critical swirl number of their nozzle. In terms of POD, it has been found that the temporal dynamic features described by a POD mode can be obtained by performing a Fourier analysis on the temporal coefficients of that POD mode (Arienti & Soteriou, 2009; Charalampous & Hardalupas, 2014; Kumar & Sahu, 2019; Rajamanickam & Saptarshi, 2018). Hence, Kumar and Sahu (2019) performed Fourier analysis on the temporal coefficients of the POD modes to obtain the temporal frequencies of the instabilities for each flow case from the Fourier spectra . In addition, in order to understand how the strength of the air swirl influences on the Kelvin-Helmholtz instability near the nozzle exit, Kumar and Sahu (2019) measured the height of the air-water interface at a downstream position of one fourth of the liquid tube diameter at various swirl numbers, performed FFT on that temporal signal, and obtained the temporal frequency of the Kelvin-Helmholtz instability driven by the shear force at the air-water interface. Kumar and Sahu (2019) found that although the strength of the air swirl increases the atomization rate of the jet, it makes a small difference in the breakup regime of the co-annular swirling jet (see Fig. 1.12). However, when the swirl number increases and the axial air velocity is kept constant, the temporal frequency of the Kelvin-Helmholtz instability becomes larger. This happens because higher tangential air velocity causes larger reduction of the shear layer thickness, which results in the increase of the shear stress acting on the water-air interface, and subsequently the growth of the shear stress reduces the amplitude but increases the frequency of the Kelvin-Helmholtz instability (Kumar & Sahu, 2019; Maddahian, Farhanieh, & Firoozabadi, 2011; Maddahian, Kebriaee, Farhanieh, & Firoozabadi, 2011). On the other hand, when the axial gas velocity increases and the swirl number remains constant, which causes the growth of the tangential air velocity, the temporal frequency of the Kelvin-Helmholtz instability grows due to the increase of the shear force at the liquid-air interface caused by the growth of the tangential air velocity. Kumar and Sahu (2019) developed regime maps characterized by swirl number and momentum ratio for a co-annular swirling jet (see Fig. 1.13). It should be noted that the large-scale instability is represented by the second and third modes so the regime maps were established based on the second and third POD modes. It is obvious in Fig. 1.13a that the jet flapping instability which is also called as the flapping mode, is dominant when the momentum ratio is low, and the explosive breakup instability which is also called as the explosive mode, becomes dominant when the momentum ratio is large. Moreover, the wavy breakup instability, which is also called as wavy mode, plays a role as subservient mode when the momentum ratio is low (see Fig. 1.13). On the other hand, wavy breakup becomes negligible when the momentum ratio is not low. The strength of the air swirl makes a small difference in the development of the wavy breakup instability (see Fig. 1.13). However, air swirl enhances the explosive breakup instability in a way that the increase of the strength of the air swirl aids air recirculation.

Generally, vortex breakdown can be observed if the swirl number is larger than 0.6 (Benjamin, 1967). Rajamanickam and Saptarshi (2018) investigated a co-annular swirling air jet around a central air jet using two-dimensional particle image velocimetry (PIV). Their swirl numbers range from 0 to 3. They found that under different swirl numbers, different modes

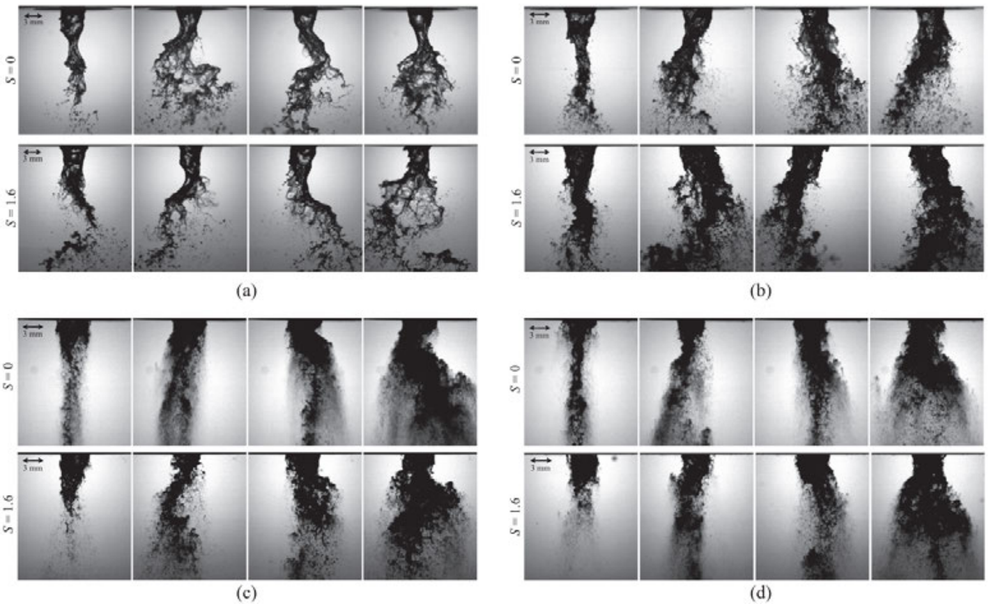

Figure 1.12: Visualizations of membrane-fiber transition breakup and fibre-type breakup (Kumar & Sahu, 2019). (a) Membrane-fiber transition breakup ($We_A = 83.5,\ M = 2.4$). (b) Fibre-type breakup ($We_A = 295.4,\ M = 5.3$). (c) Fibre-type breakup ($We_A = 611,\ M = 16.8$). (d) Fibre-type breakup ($We_A = 958,\ M = 26.3$).

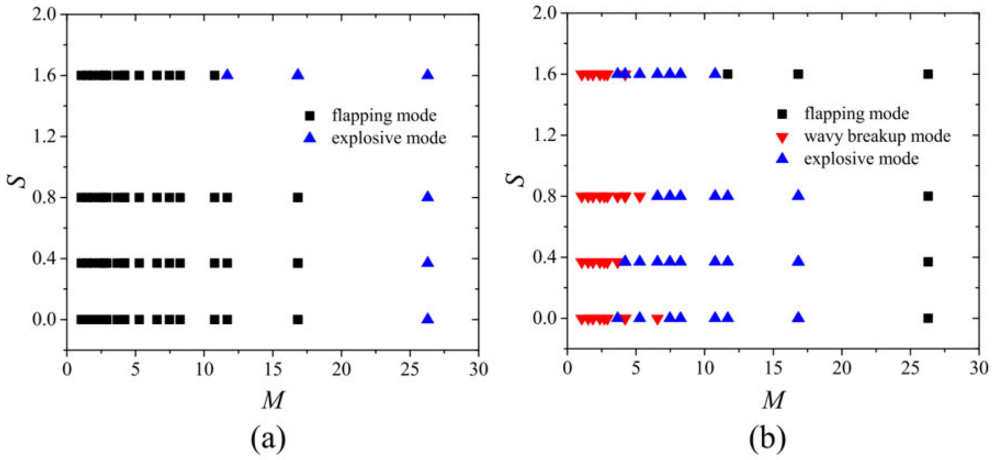

Figure 1.13: Flow Regime maps showing the breakup modes characterized by S and M (Kumar & Sahu, 2019). (a) The second POD mode. (b) The third POD mode.

of vortex breakdown such as pre-vortex breakdown (PVB), central toroidal recirculation zone (CTRZ) and conical breakdown (CB), can be observed (see Fig. 1.14). Fig. 1.14 also shows the corresponding streamline for each mode of vortex breakdown on the vertical plane near the nozzle exit. Conical sheet breakdown was also observed by Billant, Chomaz, and Huerre (1998) and Santhosh, Miglant, and Basu (2014) in their co-annular swirling jet experiments. It is obvious that CB occurs when the centrifugal momentum is larger than axial momentum (i.e. $\rho U_\theta^2 > \rho U_y^2, Ro < 1$) (see Fig. 1.14). Although the centrifugal momentum remains dominant in the range of Rossby numbers $0 < Ro < 1$, the CB exists across a small range of swirl numbers $2.4 < S < 2.6$. In order to understand the underlying dynamics of CB, Rajamanickam and Saptarshi (2018) investigated the most energetic fluid structure and characteristic frequencies of the dominate modes using proper orthogonal decomposition (POD) on the vertical and horizontal planes near the nozzle exit, respectively. Furthermore, they obtained the frequency contributions in each mode using DMD (dynamics mode decomposition). After they extracted the most energetic fluid structure in CB, they found that the shedding vortices are dominant in the CB, and that the higher-order frequencies of the shedding vortices (revealed by the first four POD modes) act as the energy sources for CB. They also found that when the swirl numbers increase (entering the CB from CTRZ), the higher-order frequencies with large amplitudes appear in the frequency spectra for the first four POD modes, which accounts for the occurrence of CB. The drawback to their research is that they use two-dimensional PIV to investigate the coaxial swirling flow. In swirling flow, out-of-plane motion can dominate. Hence, to get more accurate data, stereoscopic PIV (SPIV) should be used to investigate the coaxial swirling flow. In order to understand why the CB exists across a short range of swirl number $2.4 < S < 2.6$, the three-dimensional motion of the vortices should be obtained. Furthermore, the behaviours of the co-annular swirling air jet surrounding the central liquid jet break-up have not received adequate study.

As discussed above, in terms of the co-annular swirling gas-liquid jet, Lasheras and Hopfinger (2000) found that when S is above S_{cr}, the liquid jet will experience explosive breakup and the central recirculating air flow can be observed. Hence, It is expected that CTRZ occurs on the centreline of the liquid jet when S is above S_{cr}. However, whether other modes of vortex breakdown such as PVB and CB exist over the wide range of swirl numbers of the co-annular swirling gas-liquid jet remains unknown. The behaviours of the co-annular swirling air jet surrounding the central liquid jet break-up need further study.

Rajamanickam and Saptarshi (2017a) ultilised PIV, PDI and high-speed shadowgraphy to investigate the breakup of a hollow-cone water sheet by a coaxial swirling air jet over a wide range of gas Reynolds numbers, $Re_g(0-33888)$, and momentum ratio, $M(0-6100)$. Their liquid Reynolds number and swirl number were 750 and 0.81, respectively. Their experimental setup is illustrated in Fig. 1.15. Note that their PIV measurements were performed only on the annular air fields. The hollow-cone water sheet was produced by a Simplex nozzle. In a typical

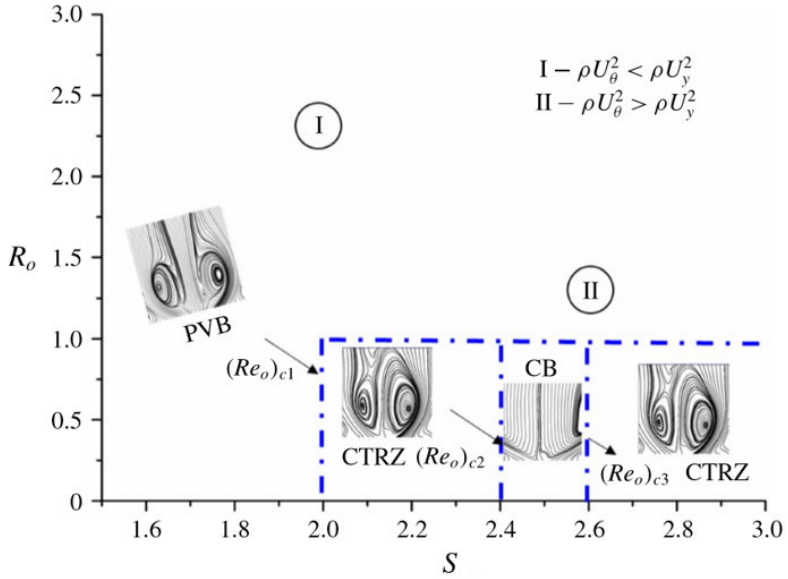

Figure 1.14: Flow regimes map characterised by the Rossby (Ro) and swirl (S) numbers. U_θ is the radial velocity of the air (Rajamanickam & Saptarshi, 2018). Region I: axial momentum is dominant. Region II: tangential momentum is dominant.

Simplex nozzle, working liquids flow through tangential ports and then enter a swirl chamber. Hollow-cone liquid sheets appear after the working liquids leave the orifice. Rajamanickam and Saptarshi (2017a) found that the near-field breakup of the liquid sheet is mainly governed by the Kelvin-Helmholtz instability. They also observed strong vortices causing flapping induced breakup for swirling flow cases. Rajamanickam and Saptarshi (2017b) utilised high-speed shadowgraphy and PIV to investigate the breakup of droplets in an annular swirling air flow with $S = 0.8$. Their momentum ratios (M) and air Reynolds numbers (Re_g) ranged from 0 to 8164, and from 0 to 33888, respectively. The liquid Reynolds number was 675. Water droplets were injected as monodispersed streams into several preselected locations in the annular swirling air flow fields, and they utilised PIV to measure the air flow fields with and without the presence of droplets. They observed that in the absence of droplets, there are two counter-rotating eddies, one at each side of the central axis (see Fig. 1.16(a)). Base on that, Rajamanickam and Saptarshi (2017b) injected droplets at the intermediate, upstream and downstream positions of the vortex core centre (VCC) (see Fig. 1.16(a) and (b)). Rajamanickam and Saptarshi (2017b) found that for the flow cases with $M = 185$ and $Re_g = 5089$, the injected droplets enter the vortex core region and there is a momentum transfer from the droplets to air flows. This leads to a slight variation in droplet trajectories and a huge change of the air flow fields (Rajamanickam & Saptarshi, 2017b). The injected Droplets does not break up in that operating condition (Rajamanickam & Saptarshi, 2017b). However, Rajamanickam and Saptarshi (2017b) found that for the flow cases with $14000 < Re_g \leq 33888$ and $1920 < M \leq 8164$, a momentum transfer from the air flows to droplets occur, which accounts for various forms of droplet breakup and dispersion. For these operating conditions, the topologies of the air flow fields are the same

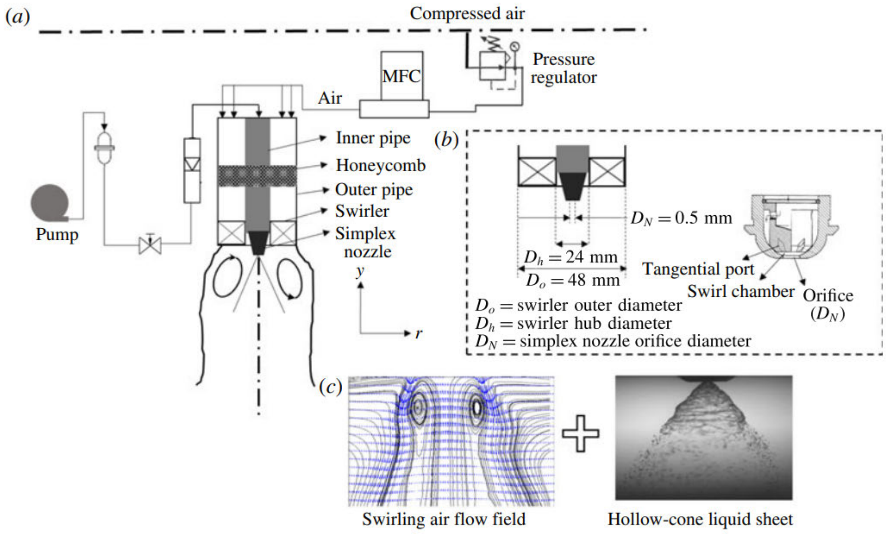

Figure 1.15: Simplex nozzle with a coaxial swirling air jet (Rajamanickam & Saptarshi, 2017a). (a) Experimental set-up. (b) Geometry of simplex nozzle and air swirler. (c) Swirling air flow field (obtained from the PIV measurements) and high-speed shadowgram of hollow-cone liquid sheet.

as the ones measured in the absence of droplets (see Fig. 1.16). The transition between those two conditions appear at $Re_g \sim 7965$ and $M \sim 450$ where the injected droplets start to stop affecting the air flow fields (Rajamanickam & Saptarshi, 2017b). Although Rajamanickam and Saptarshi (2017a) and Rajamanickam and Saptarshi (2017b) investigated the coaxial swirling jet with $S = 0.8$, the structures of their atomizer and air swirler are different enough to the ones used in this project, which makes comparions between our data impossible. For example, the central orifice of their simplex nozzle is located downstream of the air swirler (see Fig. 1.15). The behaviours of the co-annular swirling air jet over a wide range of swirl numbers need further study.

In order to understand how the strength of the air swirl affects the instability of the central water jet, some stability analyses have been performed on the coaxial liquid jet surrounded by a swirling gas stream (A. A. Ibrahim & Jog, 2006; Lian & Lin, 1990; Liao, Jeng, Jog, & Benjamin, 2000). However, for the breakup of a coaxial liquid jet in a swirling gas stream, a drop size model has not been developed, and a droplet size database that can be used to provide validation on a drop size model needs to be established. Although Hardalupas and Whitelaw (1998) measured the droplet size and velocity distributions for the breakup of a turbulent water jet by a co-annular air stream with S in the range of $\sim 0 - 7.9$, and Lasheras and Hopfinger (2000) investigated the droplet size distributions for a coaxial swirling air-liquid jet with S in the range of $\sim 0 - 0.4$, the droplet size and velocity distributions for the breakup of a central laminar water jet by a swirling air stream with S in the range of $\sim 0.4 - 3.9$ remain unknown and are explored in this project.

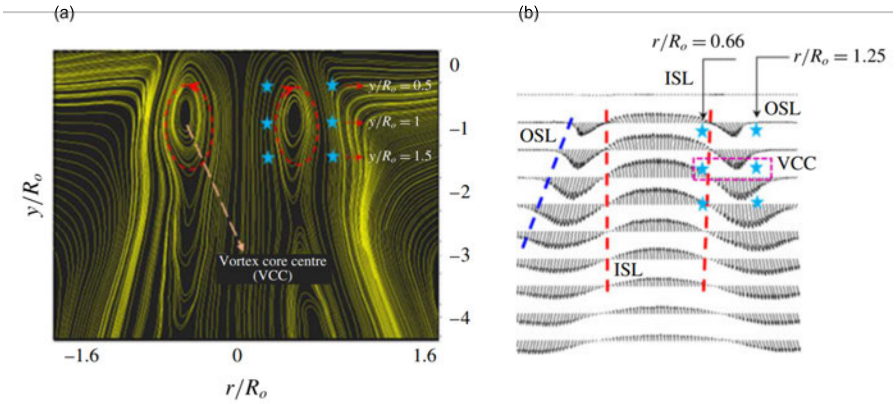

Figure 1.16: Time-average air flow fields with $S = 0.8$ in the absence of droplets (Rajamanickam & Saptarshi, 2017a, 2017b). The blue star symbols represent droplet injection locations. (a) streamline plot. (b) vector field. OSL: outer shear layer; ISL: inner shear layer; VCC: vortex core centre.

Although Lasheras and Hopfinger (2000) established the regime map characterised by the liquid Reynolds number and aerodynamic Weber number, there is a dearth information on how the strength of the air swirl influences the morphological development of the breakup regimes, which is explored in this project. Although the research discussed above has been done on the breakup of a central turbulent liquid jet surrounded by a co-annular air flow with and without swirl, the breakup of a central laminar liquid jet surrounded by a co-annular air flow with and without swirl remains unknown and is investigated in this present study. It is our view that the use of a laminar liquid jet simplifies model validation. How the strength of the air swirl and the aerodynamic forces influence the first droplet locations and 2D shear instability spectra remains an unresolved question, which is explored in this project. Although Machicoane et al. (2020) measured the breakup length of the laminar water jet in a co-annular air jet with S in the range of $\sim 0-1$, the relationships between the laminar liquid breakup lengths and the aerodynamic Weber numbers when $1 < S \leq 3.9$ remain unknown and are investigated in this present study. Although Kumar and Sahu (2019) investigated large-scale instabilities of a central turbulent water jet surrounded by a co-annular air flow with S in the range of $\sim 0-1.6$, large-scale instabilities of a central laminar water jet surrounded by a co-annular air flow with S in the range of $\sim 0-3.9$ were investigated in this project. A detailed analysis on the motion of the co-annular air flows near the nozzle exit remains absent in the literature, which is investigated using SPIV in this present study.

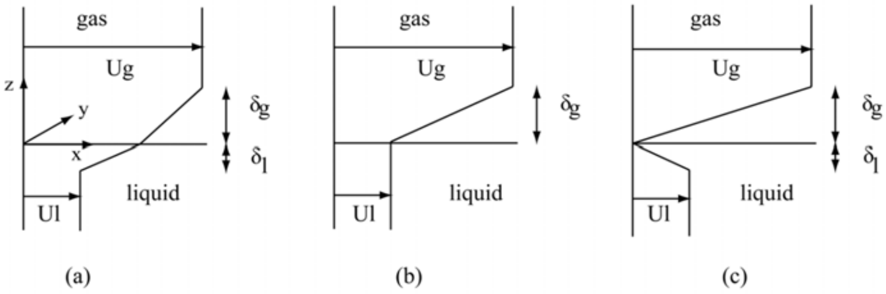

Figure 1.17: Velocity profiles of the air and water streams with vorticity layers. δ_g: gas vorticity thickness (Matas et al., 2011); δ_l: liquid vorticity thickness; U_g: gas velocity; U_l: liquid velocity. (a) Velocity profile with liquid and gas vorticity layers. (b) Velocity profile with a gas vorticity layer only. (c) Velocity profile showing a velocity deficit at the liquid-gas interface.

1.3 Review of the CFD Studies on Shear Breakup

As mentioned earlier, this thesis aims to provide a comprehensive database for shear-based spray formation. This database can be used for CFD validation. Hence, in this section, a brief review of the CFD studies modelling shear breakup is presented, and how the comprehensive database in this thesis could help the future CFD studies is discussed.

Matas et al. (2011) did an inviscid spatial linear stability analysis on a planar air-water mixing layer. They stated that a velocity deficit occurs at the nozzle exit (see Fig. 1.17(c)). This is due to the presence of the separator plate between the air and water flows. Matas et al. (2011) pointed put that the velocity profiles of air and water streams change from Fig. 1.17(c) to Fig. 1.17(a) further downstream. Both the interfacial velocity and finite gas thickness influence the shear instability of a planar air-water mixing layer. Otto, Rossi, and Boeck (2013) did a viscous spatial-temporal stability analysis on a sheared air-water interface. Their velocity ratios (R_v) ranged from 0.853 to 0.984. Here $R_v = \frac{U_g - U_l}{U_g + U_l}$, where U_g and U_l are the velocities of air and water, respectively. Otto et al. (2013) found that a velocity deficit caused by the wake behind a separator plate (see Fig. 1.17(c)), and the boundary layer thicknesses of the air and water flows, affect the instability of a sheared liquid-gas mixing layer.

As mentioned in Sec. 1.1, Matas et al. (2018) established an instability regime map for a coaxial non-swirling air-water jet (see Fig. 1.8). As discussed above, a velocity deficit at the liquid-gas interface cannot be neglected when simulating the shear instability of a liquid-gas interface. When defining the base flow conditions, Matas et al. (2018) included the error functions accounting for the wake behind a separator plate. Their linear instability analysis was based on those base flow conditions. Bozonnet, Matas, Balarac, and Desjardins (2022) also included the error functions when investigating the absolute instability of a planar air-water mixing layer induced by confinement (i.e. finite thicknesses of gas and liquid streams). They found that the frequency of the shear instability increases as the smallest injector size (liquid or gas) decreases.

A few studies simulate the breakup of a central liquid jet in a swirling gas stream. E. A. Ibrahim and Marshall (2000) simulated the nonlinear breakup of a coaxial water jet in a swirling air. They found that air swirl destabilizes the water jet. Liao et al. (2000) did a temporal linear stability analysis on a viscous liquid jet surrounded by a swirling air stream. The air swirl profiles that they defined were the free vortex and solid-body rotation. They found that air swirl tends to stabilize the liquid jet. However, those studies neglect the wake behind a separator plate, which is one of the important factors affecting the instability of the liquid jet. A detailed analysis on the shear instability in a coaxial swirling gas-liquid jet (taking a velocity deficit into account) remains absent in the literature. A drop size model for the breakup of a central liquid jet by a coaxial swirling gas stream has not been developed in the literature. Since the swirling flows is highly three-dimensional, 3D mesh convergence would be needed to investigate the shear instability of a coaxial swirling gas-liquid jet. The comprehensive database established in this thesis can provide a validation on a shear breakup model (with swirling air streams) proposed by future CFD studies.

1.4 Research Project

In general, there are three breakup mechanisms including turbulence in the liquid, aerodynamic forces acting on the gas-liquid interface, and cavitation inside the nozzle (Lefebvre & McDonell, 2017). In this project, shear forces are isolated from the other breakup mechanisms. How shear forces and air swirl influence the breakup of a co-annular air-water jet is investigated. The goal of the present work is to develop a comprehensive database for spray formation caused by shear forces, in part by removing turbulence from the liquid jet. In addition to turbulence, cavitation, and shear forces, capillary forces will also contribute (e.g., during liquid column pinch-off) just as they do during Rayleigh breakup. The database is meant for use as a CFD validation tool. This project uses SPIV to investigate the motion of the annular air flow. It also relies upon high-speed shadowgraphy to obtain data on the first droplet locations, breakup lengths of the liquid jets, and wave spatial spectra for the shear jet. PDI is utilised to obtain velocity distributions, and the size distributions for the droplets in the coaxial swirling and non-swirling jets respectively. Two databases containing these results have been prepared and they are available to interested parties (Liang, Johansen, & Linne, 2022a, 2022b). In summary, this PhD project answers the following questions:

1. How does air swirl influence spray morphology? (High-speed Shadowgraphy)

2. What are the relationships between the swirl numbers and three-dimensional gas flow fields? (SPIV)

3. How do the first droplet locations and breakup lengths of coaxial shear jets change with the aerodynamic Weber and swirl numbers? (High-speed Shadowgraphy)

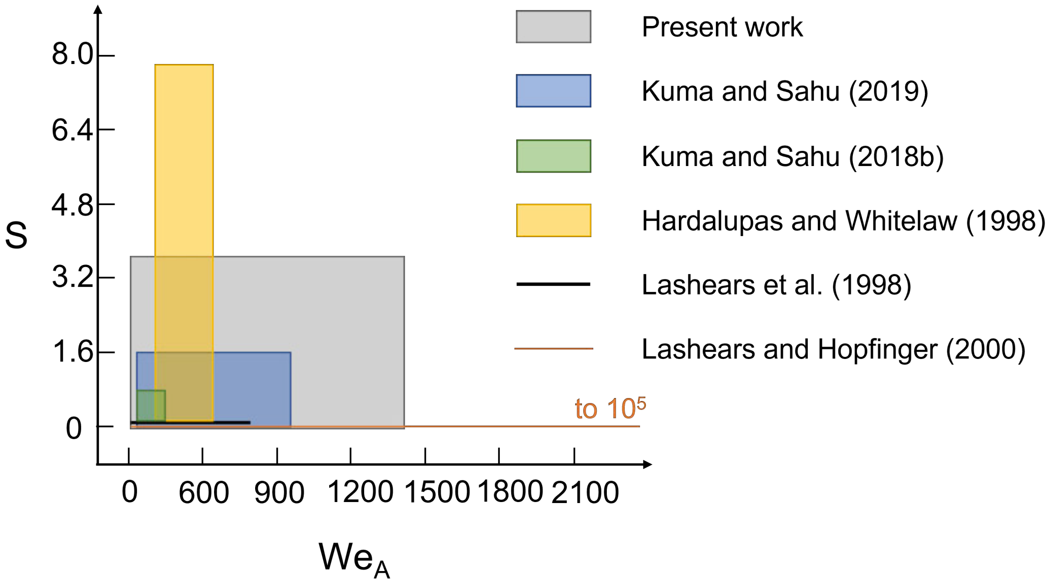

Figure 1.18: Regime map characterised by the swirl number (S) and aerodynamic Weber number (We_A). The operating conditions investigated in this thesis are compared with other literature. Note that only the previous research over a wide range of operating conditions is plotted.

4. What are the effects of air swirl and aerodynamic forces on the 2D shear instability spectra of coaxial shear jets? (High-speed Shadowgraphy)

5. What are the effects of air swirl and aerodynamic forces on the velocity and size distributions of the droplets for coaxial swirling and non-swirling jets respectively? (PDI)

6. What are the effects of air swirl and aerodynamic forces on the large-scale instabilities of coaxial shear jets? (POD)

Fig. 1.18 shows the regime map characterised by the swirl number (S) and aerodynamic Weber number (We_A). It can be found that this project extends the previous research. Note that Kumar and Sahu (2018b) and Kumar and Sahu (2019) investigated the breakup of a central turbulent water jet by a coaxial air jet, while this project investigated the breakup of a central laminar water jet by a coaxial air jet. A summary of the present and previous work on co-annular liquid-gas jets is shown in Table 1.3. Note that research works of others listed in Table 1.3 did not report on the type of breakup regime investigated.

The structures of this thesis is as follows: chapter 1 gives an introduction to the investigations that have been undertaken on co-annular non-swirling and swirling jets. Chapter 2 talks about the theoretical background of SPIV, PDI, POD and FFT. Chapter 3 contains the experimental methods that were used in this project. Chapters 4 and 5 analyse data obtained from PDI, SPIV and high-speed shadowgraphy. For example, it provides the 3D views on how vortices evolve in a co-annular swirling jet. Chapter 6 presents conclusions of this project.

Table 1.3: Summary of the present and previous works on co-annular liquid-gas jets.

Researchers	Liquid	Gas	Re_l	S
Lasheras and Hopfinger (2000)	Water	Air	$10-1.4\times10^5$	0
Lasheras et al. (1998)	Water	Air	$569-5689$	0
Farago and Chigier (1992)	Water	Air	$200-2\times10^4$	0
Engelbert et al. (1995)	Water	Air	$4000-5\times10^4$	0
Varga et al. (2003)	Water/ethanol	Air	$543-16567$ (for water jet)	0
Eroglu and Chigier (1991)	Water	Air	$1097-4379$	0
Matas et al. (2018)	Water	Air	$1400-7000$	0
Hopfinger and Lasheras (1996)	Water	Air	$740-1.14\times10^4$	$0.4-0.6$
Hardalupas and Whitelaw (1998)	Water	Air	Turbulent	$0-7.9$
Machicoane et al. (2019)	Water	Air	1100-6500	$0-1$
Dunand et al. (2005)	Water	Air	Turbulent	$0-0.6$
Kumar and Sahu (2018b)	Water	Air	Turbulent	$0-0.8$
Machicoane et al. (2020)	Water	Air	Laminar	$0-1$
Kumar and Sahu (2019)	Water	Air	Turbulent	$0-1.6$
Present work	Water	Air	Laminar	$0-3.9$

As mentioned in the Declaration, two journal papers and a conference paper have been published already as part of this research. Those papers are shown below.

- Liang, Y., Johansen, L. C.,& Linne, M. (2022). Breakup of a laminar liquid jet by coaxial non-swirling and swirling air streams. Physics of Fluids, 34(9), 093606. https://doi.org/10.1063/5.0100456.
- Liang, Y., Johansen, L. C.,& Linne, M. (2022). Characteristics of sprays produced by coaxial non-swirling and swirling air-water jets with high aerodynamic Weber numbers. Physics of Fluids, 34(10), 103604. https://doi.org/10.1063/5.0107480.
- Liang, Y., Johansen, L. C.,& Linne, M. (2021). The breakup of a laminar liquid jet with coaxial non-swirling and swirling air streams. ICLASS, 15^{th} Triennial International Conference on Liquid Atomization and Spray Systems, Edinburgh.

Chapter 2

Data Acquisition and Analysis

In this chapter, the theories of particle image velocimetry (PIV), phase Doppler interferometry (PDI), proper orthogonal decomposition (POD) and fast Fourier transform (FFT) are discussed.

2.1 Particle Image Velocimetry (PIV)

In this subsection, the principle of PIV, recording modes of PIV, interrogation windows, correlation techniques and the types of stereoscopic PIV (SPIV) are introduced. Calibration models are presented and the uncertainty of SPIV is discussed.

2.1.1 Two-dimensional PIV

PIV is a method to image fluid velocities. The general process of PIV is illustrated in Fig. 2.1, and they are shown as follows: tracer particles are introduced continuously into the flow. Two laser pulses formed into sheets of light then illuminate the flow. The tracer particles move with local flow velocity during the period between these two illuminations (Raffel et al., 2018). The camera records the light scattered by the illuminated particles as two images of the two pulses. The images are then evaluated using correlation techniques to provide an image of velocity. There are two types of correlation techniques such as auto-correlation and spatial cross-correlation. The algorithms for these correlation techniques will be discussed later.

Based on the PIV recording modes, PIV is divided into two types: double-exposure/single-frame (or multi-exposure/single-frame) PIV (Fig. 2.2) and single-exposure/double-frame (or single-exposure/multi-frame) PIV (Fig. 2.3). The former records the particle images at multiple times onto a single frame while the latter produces an image of the distribution of the illuminated particles for each illumination (Raffel et al., 2018). The double-exposure/single-frame PIV uses auto-correlation to determine the velocity field of the flow while single-exposure/double-frame uses spatial cross-correlation to calculate the velocity field of the flow (Atkins, 2016). Double-exposure/single-frame PIV can cause $180°$ directional ambiguity of the displacement vector, which means that additional techniques are required to determine the sign of the displacement vector. However, single-exposure/double-frame PIV can avoid this problem because the particles are captured in the successive frames. Hence, the single-exposure/double-frame PIV has been chosen in in this project.

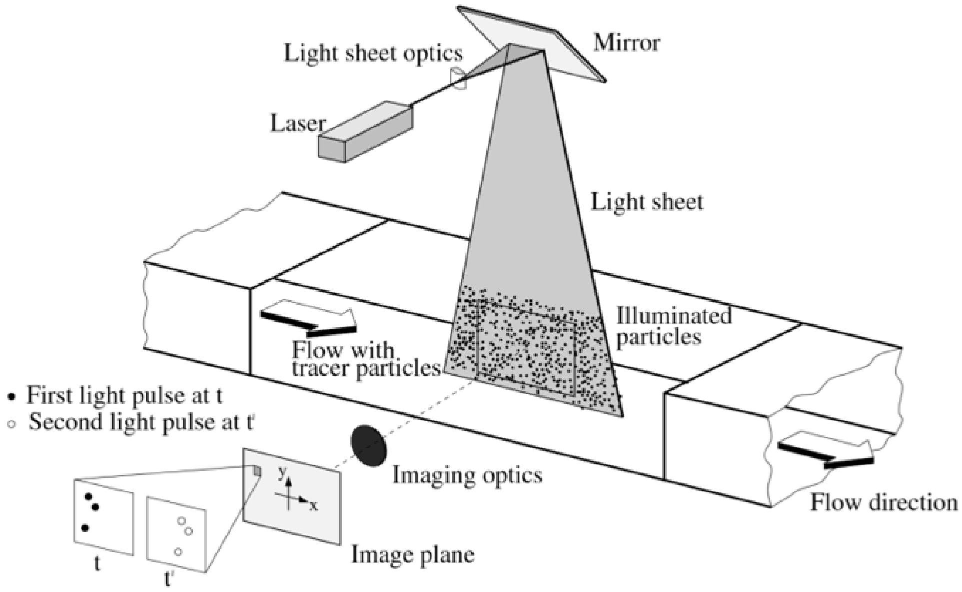

Figure 2.1: PIV experimental set-up in a wind tunnel (Raffel et al., 2018).

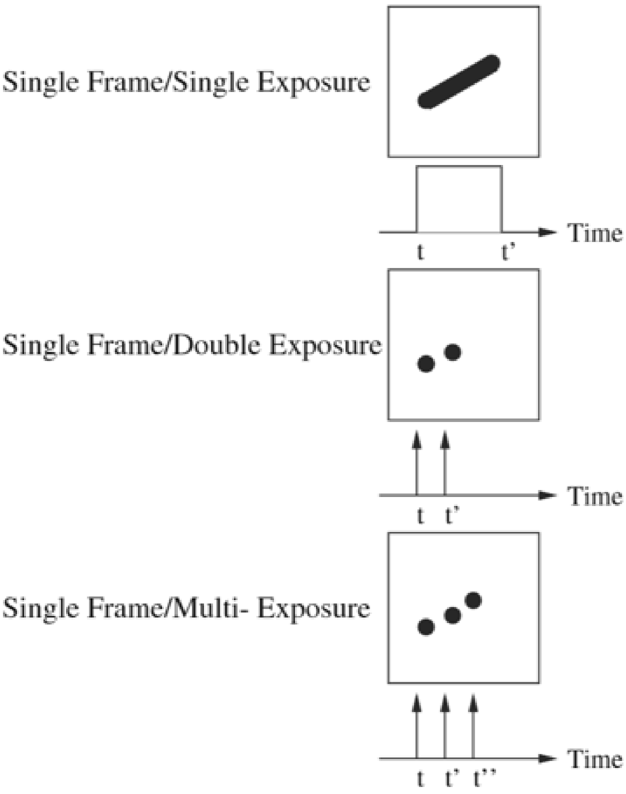

Figure 2.2: single-frame recording modes (Raffel et al., 2018).

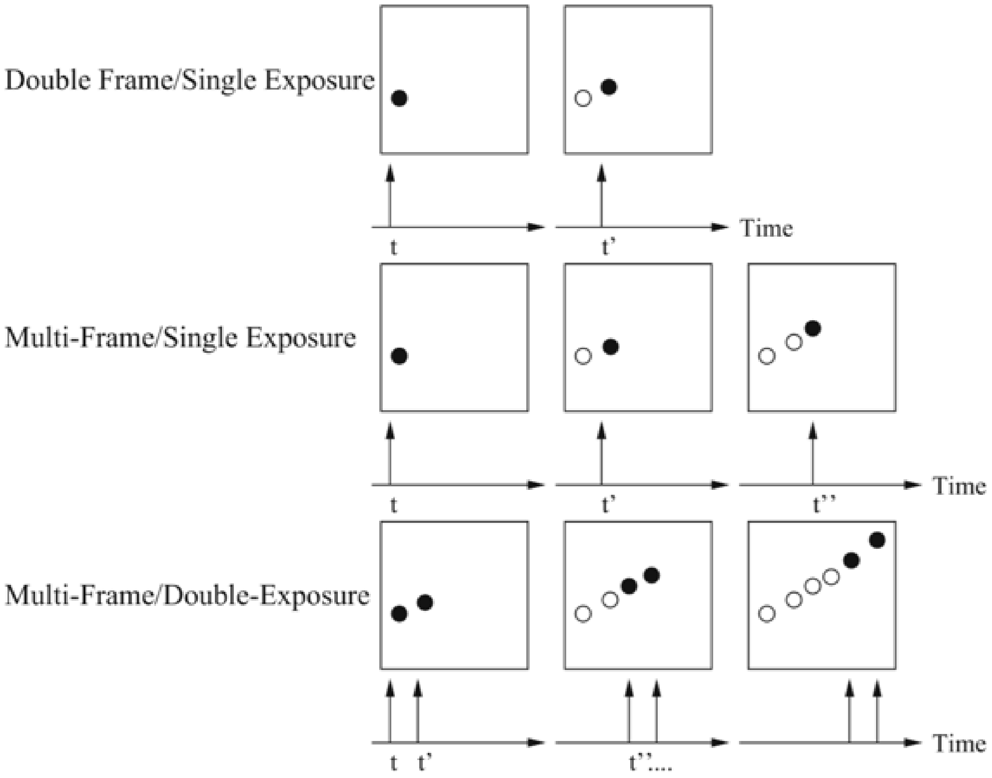

Figure 2.3: Multi-frame recording modes (Raffel et al., 2018). Open circles indicates the illuminated particles' positions on last frame.

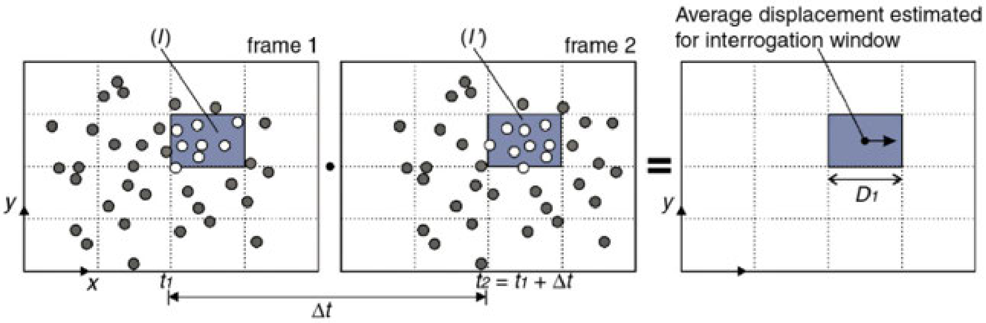

Figure 2.4: Schematic illustrating the calculation of the velocity vector for the interrogation window (I, I') (Atkins, 2016). The open circles indicate the particles' positions in the interrogation windows (I and I'). Δt is the laser pulse time. D_1 is the length of the interrogation window. It is measured in units of pixels.

As mentioned earlier, single-exposure/double-frame PIV uses spatial cross-correlation to calculate the velocity field of the flow, the algorithm for which will be discussed here. In general, how single-exposure/double-frame PIV determines the velocity of the flow are illustrated in 2.4. Initially, the pairs of frames are divided into many subregions which are called interrogation windows. Then the camera records two images for two illuminations. I is an interrogation window at frame 1 and I' is the corresponding interrogation window at frame 2 (see Fig. 2.4). Groups of seed particles move inside each interrogation window during the time interval of two illuminations. The time interval should be short enough to allow the seed particles to stay inside the interrogation window while in motion. The motion of the groups of seed particles inside each interrogation window represents the motion of the flow (if they follow the flow). After that, the computer uses spatial cross-correlation to match the same groups of seeding particles between two frames for each interrogation window. Then the displacements of the particle images in the x and y directions are calculated to derive the velocity vectors for each interrogation window.

In order to measure the degree of 'match-up' between two interrogation windows (I and I'), the two-dimensional spatial cross-correlation for this pair of interrogation windows is given by:

$$\phi_{AA'}(x,y) = \sum_{i=-\infty}^{\infty} \sum_{j=-\infty}^{\infty} \left[A\left(i,j\right)\right] \left[A'\left(i+x,j+y\right)\right], \tag{2.1}$$

where i, j are the positions of the interrogation window, x, y are the shifted variables, A is the matrix of the pixel gray values for the interrogation window I on frame 1, and A' is the matrix of the pixel gray values for the interrogation window I' on frame 2 (Fig. 2.4). The general process is that I' is shifted on top of I until they overlay each other. This results in a peak value of $\phi_{AA'}$, which is called correlation peak (see Fig. 2.5 and Equation (2.1)). Then a curve fit is applied to the profile of the correlation peak to calculate the location of the peak on the correlation plane. This process is called subpixel interpolation, which can provide a more precise estimate

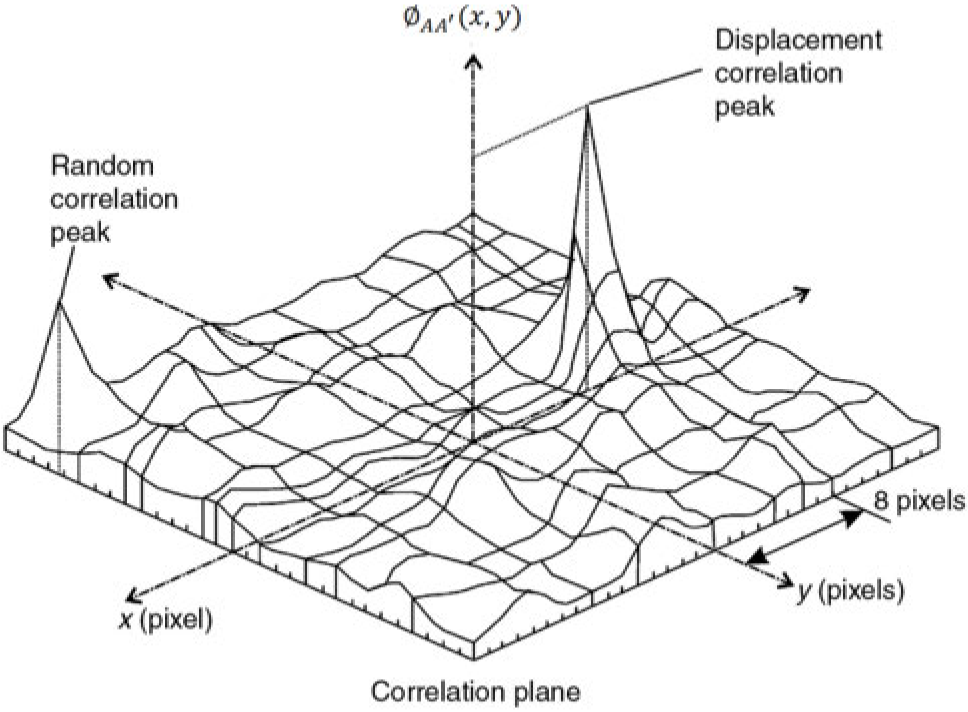

Figure 2.5: Schematic illustrating the correlation peak on the correlation plane (Atkins, 2016). x and y are the shifted variables.

of the location of the displacement peak with subpixel precision. Then the values of the shifted variables (x, y) are regarded as the instantaneous values of the displacement vector of the flow inside the interrogation window I. The spatial cross-correlation calculation is applied to each interrogation window, which finally results in a image of velocity vectors.

2.1.2 Interrogation Schemes

There are three main types of interrogation schemes that are commonly used in PIV. They are called single pass, muti pass with constant window size, and muti pass with decreasing window size. Single pass is that the correlation calculation is applied to each interrogation window at a single pass. Muti pass with constant size is that at the first pass the correlation calculation is applied to each interrogation window with constant size to get the velocity. At the second pass, each interrogation window at the first frame is shifted by $(-dx/2, -dy/2)$ while the one at the second frame is shifted by $(dx/2, dy/2)$ so that each interrogation window at the second frame is shifted by (dx, dy) with respect to its corresponding interrogation window at the first frame (Fig. 2.6). Note that dx and dy denote the local particle displacements at the directions of x and y axes of an interrogation window during the period between two illuminations from two laser pulses, respectively. Muti pass with decreasing window size is that at the first pass the correlation calculation is applied to each interrogation window with initial size to get the initial velocity field, which is the same as the first step of the second type of interrogation schemes

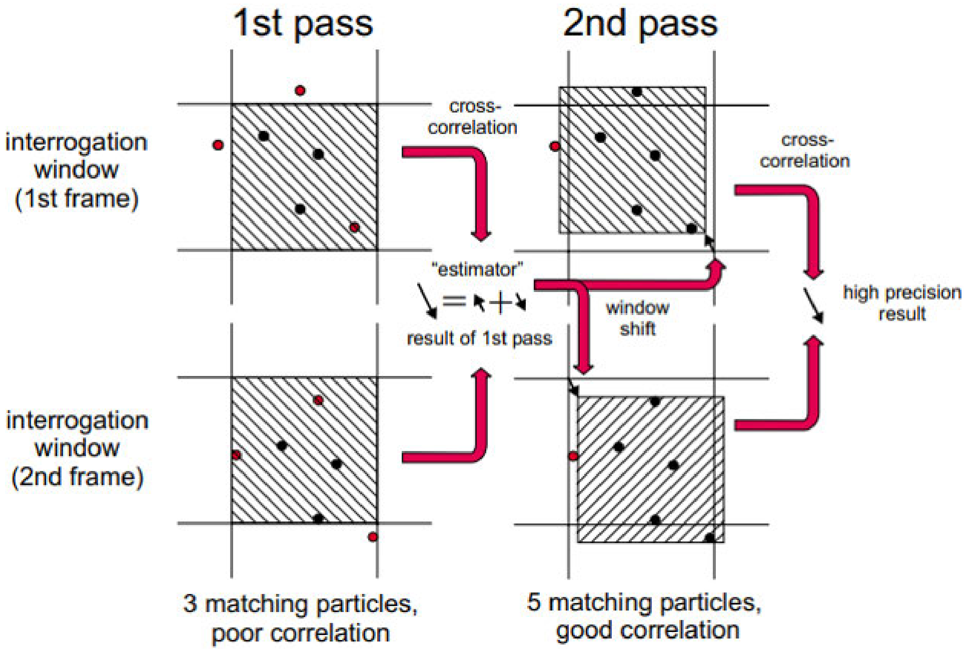

Figure 2.6: Principal of multi pass with constant window size ("FlowMaster", 2020).

("Muti pass with constant window size"). At the next pass, the size of each interrogation window decreases to the desired size, and each interrogation window is shifted based on its initial vector obtained from the first pass. Note that the way each interrogation window is shifted based on the initial vector field is the same as the one mentioned above. For the remaining passes, the size of each interrogation window does not change, but for each pass, each interrogation window is shifted based on the vector field obtained from the last pass. Compared with the other two interrogation schemes, "muti pass with decreasing window size" increases the spatial resolution of the velocity field while producing less spurious velocity vectors ("FlowMaster", 2020).

There is a second method, which is always used with the interrogation schemes, called overlapping. The interrogation windows can be arranged in a way that they overlap with each other. Overlapping can increase the spatial resolution of the velocity field. Fig. 2.7 illustrates the various layouts of the interrogation windows. Note that the coordinate of a point (x/y) is given in pixels. The cross symbols represent the centers of the interrogation windows. Fig. 2.7(1) shows two interrogation windows with the identical size of 32×32 pixels. The distance between these two displayed vectors shown in Fig. 2.7(1) is 32 pixels because the ratio of overlap is 0%. Fig. 2.7(2) shows that the window with the red edges at the first frame is shifted by $(-5/0)$, and the corresponding one at the second frame is shifted by $(5/0)$ since the local particle displacements dx and dy are equal to 10 pixels and 0 pixel, respectively. How the windows are shifted based on the local particle displacements has been mentioned above. Note that the window with the red edges at the first frame spans from $(-5/0)$ to $(26/31)$ while

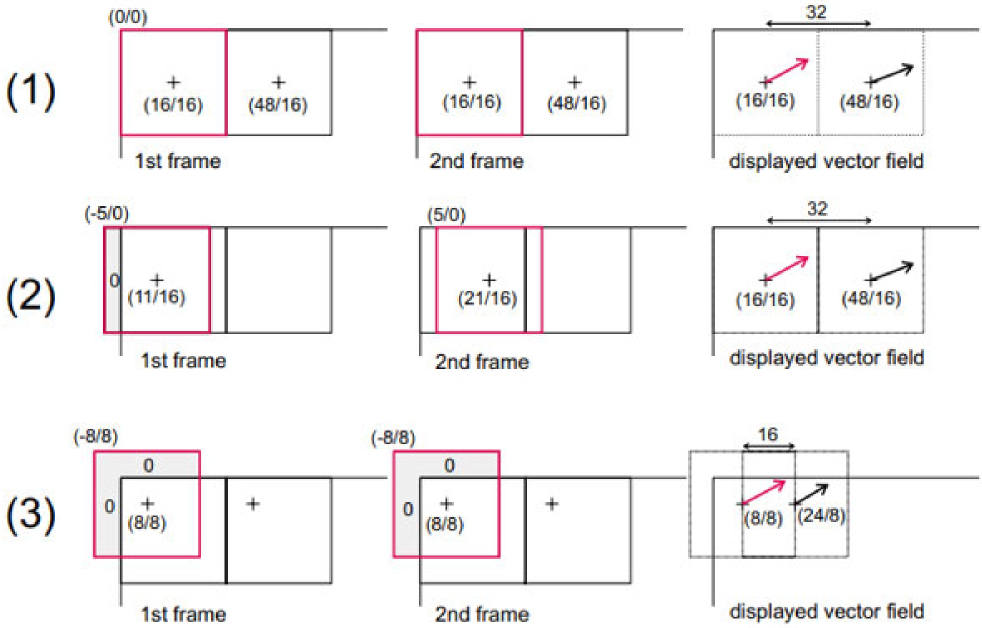

Figure 2.7: Three typical types of the layouts of the interrogation windows ("FlowMaster", 2020). (1) Window size: 32×32 pixels. Overlap: 0%. Window shift: $dx = 0$ pixel, $dy = 0$ pixel. (2) Window size: 32×32 pixels. Overlap: 0%. Window shift: $dx = 10$ pixels, $dy = 0$ pixel. (3) Window size: 32×32 pixels. Overlap:50%. Window shift: $dx = 0$ pixel, $dy = 0$ pixel

the one at the second frame spans from $(5/0)$ to $(36/31)$. The region outside the image is regarded as zero intensity. Fig. 2.7(3) shows that both of these two windows with the red edges at two frames spans from $(-8/8)$ to $(23/23)$, which makes the distance between these two displayed vectors equal to 16 pixels.

2.1.3 Vector Post-processing

After the vector field computation is done, vector post-processing should be performed on this vector field to detect and remove the outliers, which makes the vector field reliable. There are two types of filters that are commonly used for vector posting-processing. They are the median filter and filter based on the peak ratio.

Fig. 2.8 shows the definitions of the central vector and its neighbouring vectors. The central vector is located at the central grey grid, and it has eight neighbouring vectors. The principle of a local median filter is shown as follows: the median value (U_{median}) and deviation (U_{rms}) of all U components of a set of the neighboring vectors are calculated at first. The median value (V_{median}) and deviation (V_{rms}) of all V components of that set of the neighboring vectors are calculated as well. Then, whether the magnitudes of the U and V components of the corresponding central vector fall within the ranges of $U_{\text{median}} \pm U_{\text{rms}}$ and $V_{\text{median}} \pm V_{\text{rms}}$ is checked. If they are outside of their corresponding ranges, they will be rejected. If the U component of the central vector is rejected, the new U component of the central vector corresponding to the

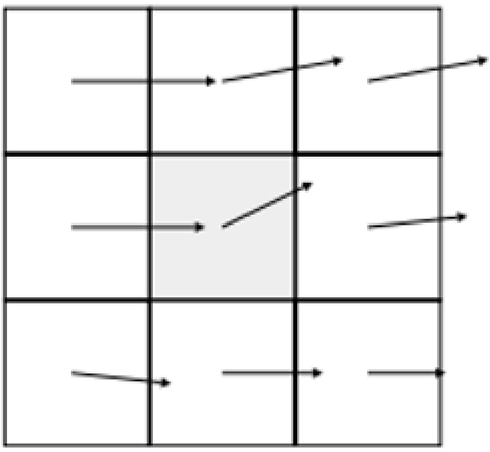

Figure 2.8: Central vectors and its eight neighbouring vectors (“FlowMaster”, 2020).

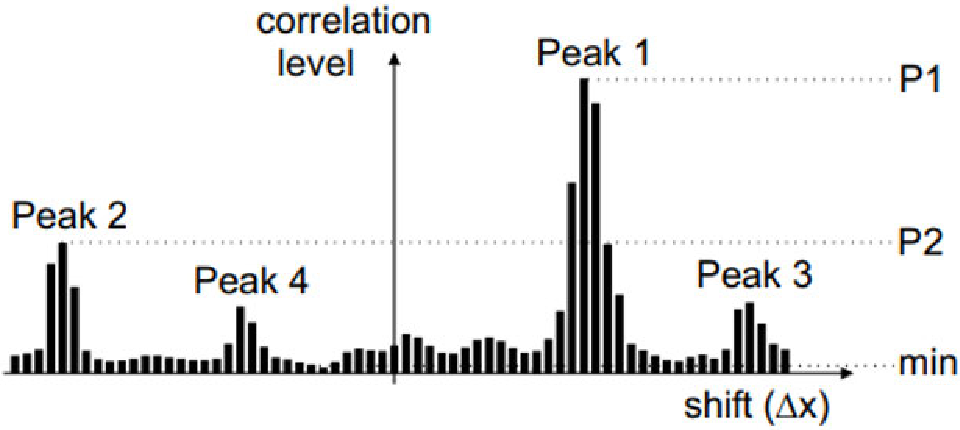

Figure 2.9: Side view of a correlation plane (“FlowMaster”, 2020).

second, third or fourth highest correlation peak will be interpolated if its magnitude falls within the range of $U_{\text{median}} \pm U_{\text{rms}}$. If the V component of the central vector is rejected, the new V component of the central vector corresponding to the second, third or fourth highest correlation peak will be interpolated if its magnitude falls within the range of $V_{\text{median}} \pm V_{\text{rms}}$.

For the second type of filter, the vector acceptance criterion is based on the peak ratio of the correlation plane. The peak ratio is given by:

$$Q = \frac{P_1 - P_{min}}{P_2 - P_{min}}, \tag{2.2}$$

where, P_{min} is the lowest correlation value of the correlation plane, and P_1 and P_2 are correlation values of the first and second correlation peaks respectively (see Fig. 2.9). A vector with high peak ratio is reliable since the correlation value of the first correlation peak is much larger than the correlation value of the second correlation peak.

2.1.4 Stereoscopic PIV

If the motion of the flow is three dimensional, stereoscopic PIV (SPIV) should be utilized to investigate this flow because SPIV can generate a 2-D image of the three-dimensional velocity vector field. Unlike two-dimensional PIV, SPIV requires two cameras which work synchronously. As mentioned earlier, two laser pulses formed into sheets of light illuminate the flow. These two cameras record the light scattered by the illuminated particles as two images of the two pulses, respectively. These two pairs of images are then evaluated respectively using correlation techniques to provide two images of velocity. After that, these two images of velocity are combined to obtain the three-dimensional velocity field. This process is called reconstruction.

Types of SPIV Systems

The SPIV systems can be divided into two types: (i) translation systems and (ii) rotational systems. In translation systems, the axes of the cameras are parallel to each other, and orthogonal to the object plane (laser sheet) (Fig. 2.10). In terms of rotational systems, in order to ensure that the image plane, object plane and lens plane are colinear, the image plane is rotated with respect to the lens plane by an angle α, which is called Scheimpflug condition (Fig. 2.11) (Prasad, 2000). The advantage of the translation systems is their simplicity. The image field has identical magnification in the translation systems. The relative error in the out-of-plane motion is related with the off-axis angle θ. The relative error will decrease if the off-axis angle θ increases (Prasad, 2000). In terms of translation systems, there is a upper limit for the off-axis angle θ because there is a upper bound to the distance between two lenses. For a given object distance (d_0), the distance between two lenses is limited by the specification of the lens; If the distance between two lenses is too large, the performance of these two lenses will degrade because they work at the outer limit of their specifications (Prasad, 2000). Hence, the drawback of translation method is that it has a limitation on reducing the relative error in the out-of-plane motion. The advantage of rotational method is that there is no upper limit for the off-axis angle θ. Hence, in this project, rotational method was chosen for SPIV. Note that the magnification is not uniform in this method because the image plane is rotated with respect to lens plane by α. Image calibration should be done before the SPIV measurements start (this is discussed in more detail in Sec. 2.1.5).

Reconstruction method

There are many types of reconstruction methods which are commonly used in SPIV. A complete summary is far beyond the scope of this subsection. Instead, the reconstruction method used in this project is presented here. However, Prasad (2000) provides an excellent overview of the reconstruction methods which are commonly used in SPIV. The strategy of Davis 10.1, which is the software used to perform SPIV in this project, is that it corrects the images first and then calculates the two-dimensional vector at the correct global gird position. Fig. 2.12 contains a flow chart of the three-dimensional vector field calculation. For the first pass of the vector field computation, two frames of each camera are dewarped first (based on a prior

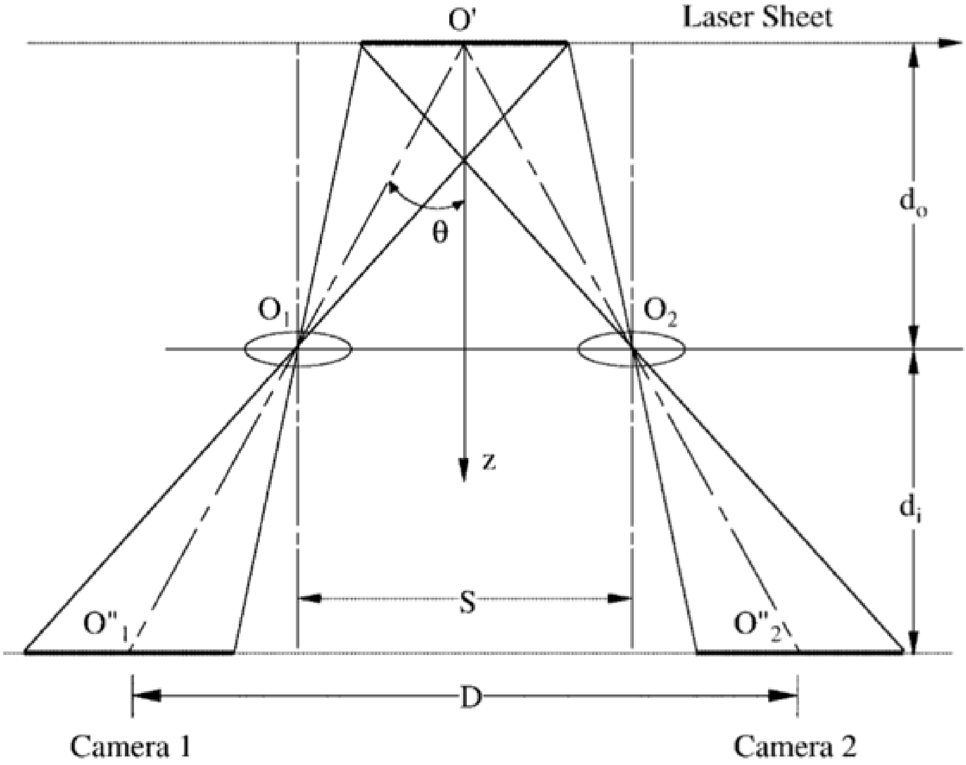

Figure 2.10: Configuration of a translation system (Prasad, 2000).

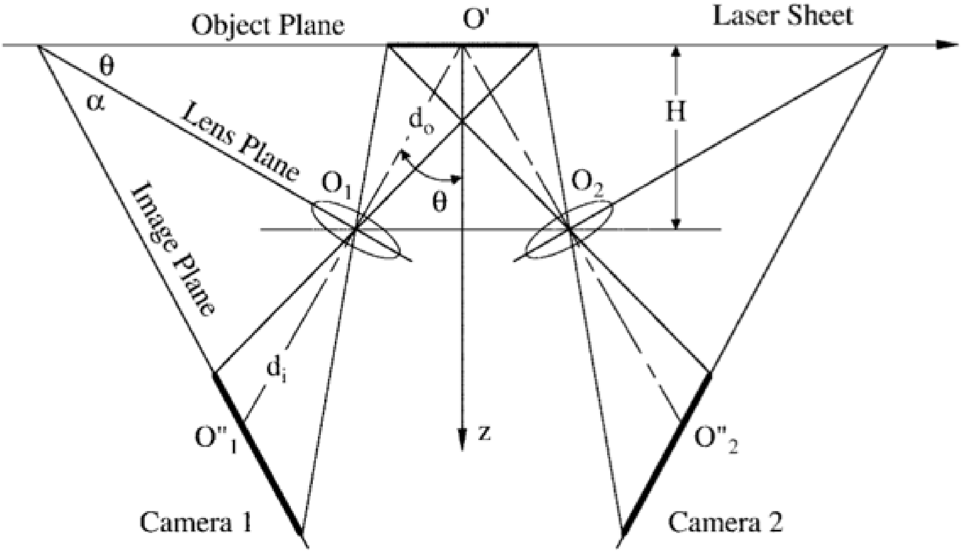

Figure 2.11: Configuration of a rotational system (Prasad, 2000).

image calibration), and then these two dewarped images of each camera are correlated to get a two-dimensional vector field. These two two-dimensional vectors fields from two cameras are combined to reconstruct a three-dimensional vector field by solving a system equation with three unknowns (u, v, w) (equation (2.15)). After that, the (u_1, v_1) and (u_2, v_2) components are computed from (u, v, w) again, and these two components are compared with their corresponding measured (u_1, v_1) and (u_2, v_2) components respectively. The deviations from the measured (u_1, v_1) and (u_2, v_2) components are called reconstruction errors . If the reconstruction error of a two-dimensional vector is larger than the threshold value, this two-dimensional vector will be eliminated from the two-dimensional vector field. After that, vector validation is performed on the two-dimensional vector field for each camera. The missing vectors are interpolated, and the vector fields are smoothed at the end of the first pass. The resulting vector fields are used as the reference vector fields for the next pass of the vector field computation. For the second pass of the vector field computation, the interrogation windows are shifted based on their corresponding vector in the reference vector field. For each camera, each interrogation window at the first frame is shifted by $(-dx/2, -dy/2)$ while the one at the second frame is shifted by $(dx/2, dy/2)$ so that each interrogation window at the second frame is shifted by (dx, dy) with respect to its corresponding interrogation window at the first frame. The two-dimensional vector fields start to converge suffciently after three or four passes ("FlowMaster", 2020). At the end of the final pass the three-dimensional vector field goes through the process of the vector validation. Note that the three-dimensional vector fields obtained before the final pass are used to calculate the reconstruction errors and eliminate the spurious vectors from the two-dimensional vector fields, and only the three-dimensional vector field obtained at the final pass is saved and goes through the process of the vector validation.

2.1.5 Calibration Models

The relationships between the true particle displacements and the particle displacements captured by cameras should be obtained before PIV measurements start. A calibration plate should be placed at the measurement volume, and a calibration model should be used to derive the relationships between the particle displacements on the object plane and on the image plane. This process is called calibration. There are two calibration models which are commonly used in PIV. They are pinhole camera model and polynomial model. The pinhole camera model is illustrated in Fig. 2.13. The main idea of pinhole camera model involves four transformation, where an object space $\boldsymbol{X}_w = (X_w, Y_w, Z_w)$ is transformed into an intermediate camera coordinate system $\boldsymbol{x}_c = (x_c, y_c, z_c)$, to an undistorted sensor coordinate (x_u, y_u), to a distorted sensor coordinate (x_d, y_d), and ultimately to an image coordinate (u, v) (Willert, 2006).

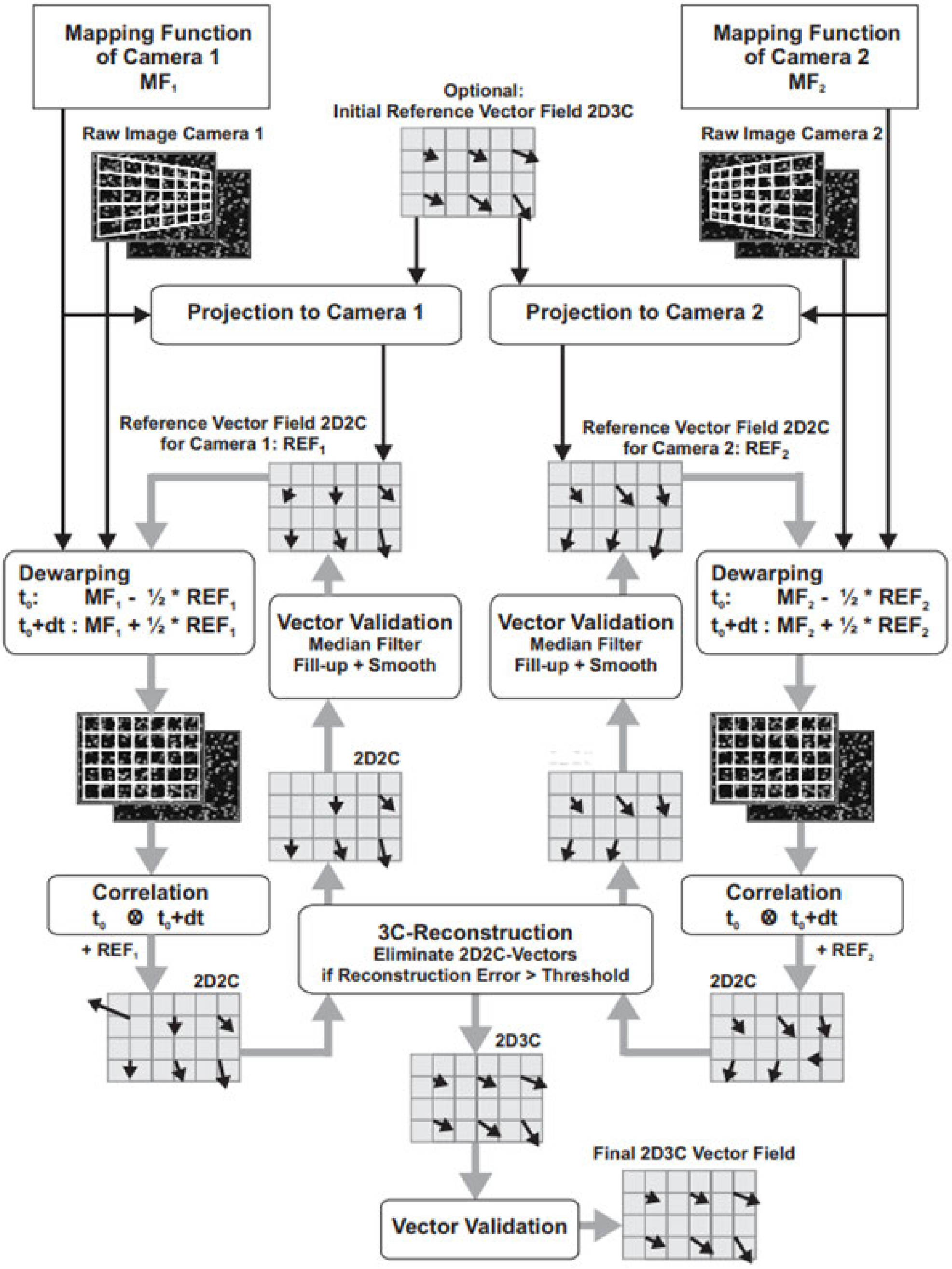

Figure 2.12: Process of computing the three-dimensional vector field (“FlowMaster”, 2020).

The relationship between the object space $\boldsymbol{X}_w = (X_w, Y_w, Z_w)$ and the intermediate camera coordinate system $\boldsymbol{x}_c = (x_c, y_c, z_c)$ is given by:

$$\begin{bmatrix} x_c \\ y_c \\ z_c \end{bmatrix} = \begin{bmatrix} r_1 & r_2 & r_3 \\ r_4 & r_5 & r_6 \\ r_7 & r_8 & r_9 \end{bmatrix} \cdot \begin{bmatrix} X_w \\ Y_w \\ Z_w \end{bmatrix} + \begin{bmatrix} t_X \\ t_Y \\ t_Z \end{bmatrix} \tag{2.3}$$

$$\boldsymbol{x}_c = \boldsymbol{R} \cdot \boldsymbol{X}_w + \boldsymbol{T}, \tag{2.4}$$

where, $\boldsymbol{R}$ is the rotational matrix. It can be rewritten as $[R_x, R_y, R_z]$, where R_x, R_y and R_z correspond to the rotations around the x, y and z axes, respectively. $\boldsymbol{T}$ is called the translation vector. Then the the intermediate camera coordinate system is transformed into the undistorted sensor coordinate system, which is given by:

$$\begin{bmatrix} x_u \\ y_u \end{bmatrix} = \frac{f}{z_c} \cdot \begin{bmatrix} x_c \\ y_c \end{bmatrix}, \tag{2.5}$$

where, f is the principal distance between the pinhole location and the image plane or effective focal length (Willert, 2006). After that, the undistorted sensor coordinate system is transformed into the distorted sensor coordinate system, which is given by:

$$\begin{bmatrix} x_d \\ y_d \end{bmatrix} = (1 + \kappa_1 r^2 + \kappa_2 r^4) \cdot \begin{bmatrix} x_u \\ y_u \end{bmatrix} \tag{2.6}$$

$$r^2 = x_d^2 + y_d^2. \tag{2.7}$$

Here, κ_1 and κ_2 represent the radial distortion factors to correct for lens distortion (barrel or cushion) (Willert, 2006). Finally, the distorted sensor coordinate system is transformed into the image coordinate, which is given by:

$$\begin{bmatrix} u \\ v \end{bmatrix} \frac{1}{S_{\text{pixel}}} \begin{bmatrix} s_x x_d \\ y_d \end{bmatrix} + \begin{bmatrix} u_0 \\ v_0 \end{bmatrix}, \tag{2.8}$$

where, S_{pixel} is the known pixel size, s_x represents the pixel aspect ratio correction, and (u_0, v_0) is the coordinate of the intersection point of the optical axis with the image plane (Willert, 2006).

The principle of the polynomial model is discussed in the rest of this subsection. According to Prasad (2000), the relationship between the particle positions on the object plane (x) and on the image plane $(\boldsymbol{X})$ is given by:

$$\boldsymbol{X} \;=\; \boldsymbol{F}(\boldsymbol{x}), \tag{2.9}$$

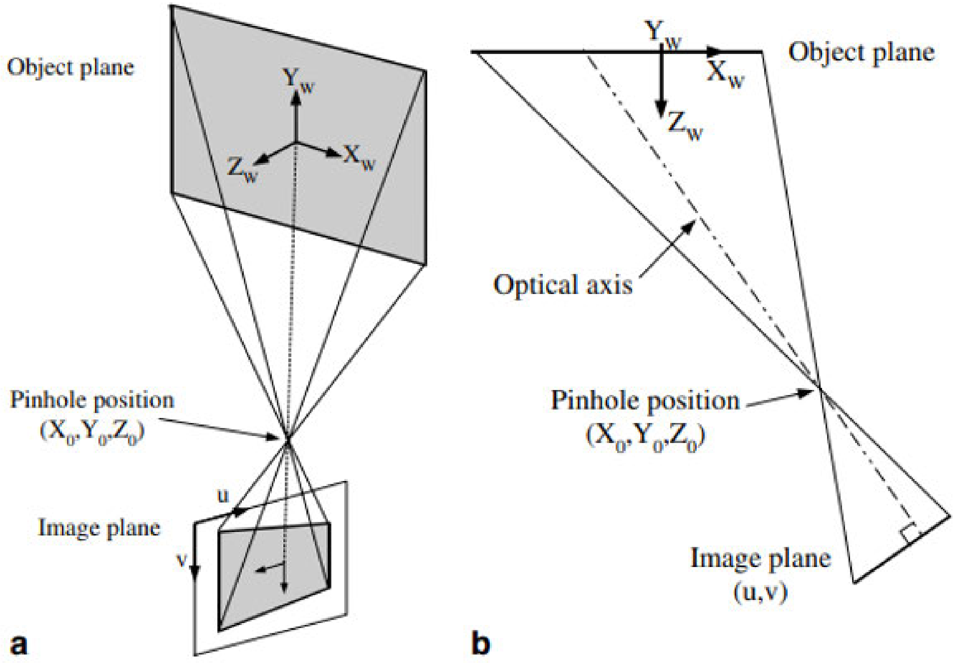

Figure 2.13: Schematic illustrating the Pinhole model (Willert, 2006). (a) Three-dimension view of the pinhole model. (b) XZ projection of the pinhole model onto the XZ plane.

where, according to Prasad (2000) and Soloff, Adrian, and Liu (1997), $\boldsymbol{F}$ can be approximated by:

$$\begin{aligned} \hat{\boldsymbol{F}}(x) = a_0 + a_1x_1 + a_2x_2 + a_3x_3 + a_4x_1^2 + a_5x_1x_2 + a_6x_2^2 \\ + a_7x_1x_3 + a_8x_2x_3 + a_9x_3^2 + a_{10}x_1^3 + a_{11}x_1^2x_2 + a_{12}x_1x_2^2 \\ + a_{13}x_2^3 + a_{14}x_1^2x_3 + a_{15}x_1x_2x_3 + a_{16}x_2^2x_3 + a_{17}x_1x_3^2 + a_{18}x_2x_3^2, \end{aligned} \tag{2.10}$$

where, a_i are vector-valued coefficients. Here, Four sets of a_i are required. One for each $X_1^{(1)}$, $X_2^{(1)}$, $X_1^{(2)}$ and $X_2^{(2)}$, where the superscripts denote cameras 1 and 2. According to Prasad (2000) and Soloff et al. (1997), the relationship between the particle displacements on the image plane ($\Delta\boldsymbol{X}$) and on the object plane ($\Delta\boldsymbol{x}$) is given by:

$$\Delta\boldsymbol{X} = \boldsymbol{F}(\boldsymbol{x} + \Delta\boldsymbol{x}) - \boldsymbol{F}(\boldsymbol{x}), \tag{2.11}$$

$$\Delta\boldsymbol{X} \approx \nabla\boldsymbol{F}(\boldsymbol{x})\Delta\boldsymbol{x}, \tag{2.12}$$

$$\text{where}, (\nabla\boldsymbol{F})_{ij} = (\partial F_i)/(\partial x_j) = F_{i,j}, \tag{2.13}$$

$$\text{where}, i = 1,\ 2 \text{ and } j = 1,\ 2,\ 3. \tag{2.14}$$

Hence, equation (2.12) can be rewritten as:

$$\begin{bmatrix} \Delta \boldsymbol{X}_1^{(1)} \\ \Delta \boldsymbol{X}_2^{(1)} \\ \Delta \boldsymbol{X}_1^{(2)} \\ \Delta \boldsymbol{X}_2^{(2)} \end{bmatrix} = \begin{bmatrix} F_{1,1}^{(1)} & F_{1,2}^{(1)} & F_{1,3}^{(1)} \\ F_{2,1}^{(1)} & F_{2,2}^{(1)} & F_{2,3}^{(1)} \\ F_{1,1}^{(2)} & F_{1,2}^{(2)} & F_{1,3}^{(2)} \\ F_{2,1}^{(2)} & F_{2,2}^{(2)} & F_{2,3}^{(2)} \end{bmatrix} \begin{bmatrix} \Delta x_1 \\ \Delta x_2 \\ \Delta x_3 \end{bmatrix}. \qquad (2.15)$$

Note that the superscripts denote cameras 1 and 2 (see equation (2.15)).

2.1.6 Uncertainty of PIV

According to Raffel et al. (2018), in general, a value that is measured from an experiment (X_{measure}) is given by:

$$X_{\text{measure}} = X_{\text{true}} \pm \delta_x, \qquad (2.16)$$

where X_{true} is the true value, and δ_x is the measurement error. The measurement errors include systematic errors and random errors. The systematic errors, which are also called bias errors, are caused by incorrect operation of the experimental equipment or incorrect calibration (Raffel et al., 2018). As mentioned in Sec. 2.1.5, calibration is the process of deriving the relationships between the displacements of particles on the image plane and on the object plane. The bias error is always a constant value, and can be compensated if detected correctly (Raffel et al., 2018).

Random error, which cannot be predicted, is characterised by its standard deviation (σ). According to Raffel et al. (2018), the standard deviation of the random error (σ) can be expressed by:

$$\sigma = \sqrt{\frac{1}{n-1}\sum_{i=1}^{n}(x_i - <x>)^2}, \qquad (2.17)$$

where x_i is the value of sample from the i^{th} individual measurement, $<x>$ is the mean value of these individual measurements, i is the control variable, and n is the number of samples. The random error influences the precision of the experiment. How the bias and random errors simultaneously influence data is illustrated in Fig. 2.14. The black dots are the data points obtained from a large number of individual measurements. Note that ε_x and ε_y (bias errors) are the mean offset to the true value. The data points are scattered because of the existence of the random errors.

There are some design rules for PIV experimental setup aiming at reducing the measurement errors. The loss of pairs of particles in the interrogation window can reduce the amplitude of the displacement correlation peak by the spatial cross-correlation algorithm. If the size of the interrogation window is too small or there are insufficient numbers of particle pairs in the interrogation window, a large amount of loss of in-plane particle pairs will happen, which results in the small amplitude of the displacement correlation peak. In order to ensure the displacement

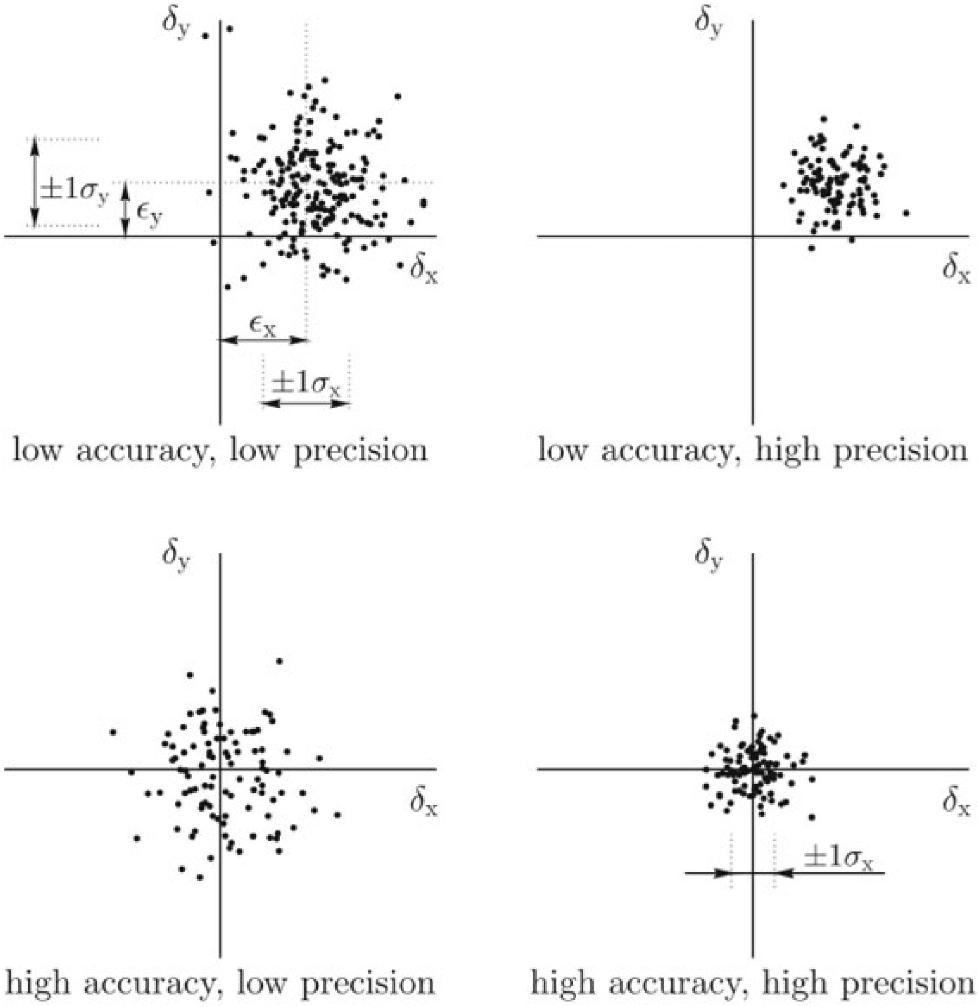

Figure 2.14: Schematic illustrating the precision and accuracy of two-dimensional data (Raffel et al., 2018). ε_x, ε_y are the bias errors in x and y directions respectively. σ_x, σ_y are the standard deviations of the random errors on x and y directions respectively.

correlation peak detectability, the amplitude of the displacement correlation peak should be 1.2 times larger than the nearest noise correlation peak (Adrian, 1991). This requires that the seeding concentration (N_I), which refers to the number of particle images in an interrogation window, is larger than 6 (i.e. $N_I > 6$) (Atkins, 2016; Keane & Adrian, 1992), and that the mean displacement of the particles (Δx) (unit: pixels) should be less than a quarter of the size of the interrogation window (D_I) (i.e. $\Delta x \leq D_I/4$) (Atkins, 2016). Although large interrogation windows avoid loss of in-plane particle pairs, it can result in low spatial resolution. Hence, a compromise should be made. In order to have a good curve fit for the profile of the displacement correlation peak (subpixel interpolation), the width of the displacement correlation peak should range from 2 to 7 pixels (Atkins, 2016). According to Atkins (2016), the relationship between the width of a symmetrical correlation peak (d_c) and the particle image diameter (d_τ) is given by:

$$d_c = \sqrt{2} \times d_\tau. \tag{2.18}$$

Particle images are the localized high pixel gray values (Atkins, 2016). The particle image diameter (d_τ) (unit: pixel) is the number of pixels that are illuminated across the isolated bright spots (Atkins, 2016). The minimum of measurement error happens when $d_\tau/d_r \approx 2$, where d_r is the pixel size (Atkins, 2016; Prasad, Adrain, Landreth, & Offutt, 1992; Raffel et al., 2018; Westerweel, 1997, 2000). The particle image diameter (d_τ) can be adjusted by changing the f-number ($f^\#$) of the camera lens, which is the ratio of the focal length of the lens to the aperture size. In addition, the magnitude of the laser pulse timing should be chosen carefully to ensure that the mean displacement of particles is less than a quarter of the size of the interrogation window during that time interval (i.e. $\Delta x \leq D_I/4$).

The laser sheet thickness should lie in the range of the depth of field of the camera so that the particles are in focus. According to Prasad (2000), the depth of field (DOF) is expressed by:

$$DOF = 4\left(1 + M_n^{-1}\right)^2 \left(f^\#\right)^2 \lambda, \tag{2.19}$$

where M_n is the magnification of the camera, $f^\#$ is the f-number of the camera lens, and λ is the wavelength of the illumination laser. Hence, in order to have a good depth of field and a small particle diameter, there is a compromise setting for the f-number ($f^\#$) of the camera lens. In addition, the laser sheet thickness should also fulfil the "one-quarter" rule, which means that the mean displacement of the particle at z direction (Δz) should be less than a quarter of the laser sheet thickness (T) (i.e. $\Delta z \leq T/4$) (Atkins, 2016).

As mentioned earlier, data obtained from PIV is based on particle motion. It is important to ensure that the seed particles follow the flow so that the motion of the particles can represent the flow motion. According to Raffel et al. (2018), the velocity lag ($\boldsymbol{U}_s$) of the seed particles in a continuously accelerating flow can be expressed by:

$$\boldsymbol{U}_s = \boldsymbol{U}_p - \boldsymbol{U} = d_p^2 \frac{\rho_p - \rho_f}{18\mu_f} \boldsymbol{a}, \tag{2.20}$$

where $\boldsymbol{U}_p$ is the particle's velocity vector, $\boldsymbol{U}$ is the flow's velocity vector, $\boldsymbol{a}$ is the acceleration, d_p is the particle diameter, ρ_p is the density of the particle, ρ_f is the density of the fluid, μ_f is the dynamic viscosity of the flow. According to Raffel et al. (2018), if the flow is suddenly decelerated and $\rho_p \gg \rho_f$, the step response of U_p can be given by:

$$\boldsymbol{U}_p(t) = \boldsymbol{U}\left[1 - \exp\left(\frac{-t}{\tau_p}\right)\right], \tag{2.21}$$

with the relaxation time (τ_p) expressed by:

$$\tau_p = d_p^2 \frac{\rho_p}{18\mu_f}. \tag{2.22}$$

According to Raffel et al. (2018), in order to detect whether the seed particles follow the flow's motion exactly, the Stokes number (Stk) is given by:

$$Stk = \tau_p / \tau_f, \tag{2.23}$$

where τ_f is the characteristic time scale in the flow. The magnitude of τ_f, which is the ratio of a length scale to a characteristic velocity of the flow, can be obtained from the dimensional analysis (Raffel et al., 2018). For example, in terms of turbulent boundary layer flow, τ_f is the ratio of boundary layer thickness to the free stream velocity. In terms of swirling flow, τ_f is the ratio of vortex diameter to swirling velocity (Raffel et al., 2018). In order to ensure that the seed particles follow the flow with good fidelity, the Stokes number should be much less than 0.1 (i.e. $\ll 0.1$) (Raffel et al., 2018; Samimy & Lele, 1991). Hence, the diameter of the seed particles should be chosen to be small enough to ensure that the Stokes number is less than 0.1. However, if the diameter of the seed particles is too small, the amount of the light scattered by the particles will reduce, which results in the reduction on the amplitude of the displacement correlation peak. Hence, a compromise should be made.

2.2 High-speed Shadowgraphy

High-speed shadowgraphy, which is an optical method (Settles, 2001), is commonly used to investigate spray formation. In terms of the raw images captured by the camera, the water droplets and jet are black while the backgrounds are grey because the difference between the refractive indexes of water and air. The water casts shadow, and the raw images captured by the camera are called shadowgrams. Performing post-processing on these raw images can identify and extract some features of the spray, such as the breakup lengths of the liquid jets, liquid-gas interface locations, first droplet locations and large-scale instabilities of the liquid jets. The associating algorithms are discussed in detail in Chapter 3.

2.3 Phase Doppler Interferometry (PDI)

In this section, the fundamentals of electromagnetic waves and interference of homogeneous plane waves are introduced. Then, the principles of PDI are discussed.

2.3.1 Fundamentals of Electromagnetic Waves

According to Born (1933), Born and Wolf (1999), Albrecht, Borys, Damaschke, and Tropea (2003), and Hecht (2018), a theory of electromagnetic fields can depict the light propagation, which is given by:

$$curl\,\boldsymbol{H} = \boldsymbol{S} + \frac{\partial D}{\partial t},\; curl\,\boldsymbol{E} = -\frac{\partial B}{\partial t}, \tag{2.24}$$

$$div\,\boldsymbol{D} = \rho,\; div\,\boldsymbol{B} = 0, \tag{2.25}$$

$$\boldsymbol{D} = \varepsilon\boldsymbol{E},\; \boldsymbol{S} = \kappa\boldsymbol{E},\; \boldsymbol{B} = \mu\boldsymbol{H}, \tag{2.26}$$

where, $\boldsymbol{H}$ is the magnetic field strength, $\boldsymbol{E}$ is the electric field strength, $\boldsymbol{D}$ is the electric displacement, $\boldsymbol{S}$ is the current density, $\boldsymbol{B}$ is the magnetic induction, ε is the permittivity, κ is the electric condutivity, μ is the magnetic permeability of the medium, and ρ denotes the distribution of space charge. Note that the above theory of electromagnetic fields are based on Maxwell's equations (Albrecht et al., 2003). According to Albrecht et al. (2003), the relative permittivity ε_r and magnetic permeability μ_r are commonly used, which are given by:

$$\varepsilon_r = \frac{\varepsilon}{\varepsilon_0}, \tag{2.27}$$

$$\mu_r = \frac{\mu}{\mu_0}, \tag{2.28}$$

Where,

$$\varepsilon_0 = 8.8543 \times 10^{-12} \qquad [AsV^{-1}m^{-1}] \tag{2.29}$$

$$\mu_0 = 1.2566 \times 10^{-6} \qquad [VsA^{-1}m^{-1}] \tag{2.30}$$

Here, ε_0 and μ_0 denote the permittivity and magnetic permeability in vacuum respectively. According to Albrecht et al. (2003), the energy density w stored in the electromagnetic field can be described as:

$$w = \frac{1}{2}\left(\boldsymbol{E}\cdot\boldsymbol{D} + \boldsymbol{H}\cdot\boldsymbol{B}\right). \tag{2.31}$$

According to Albrecht et al. (2003), the Poynting vector $\boldsymbol{P}$, which can be interpreted as the energy flux, can be described as:

$$\boldsymbol{P} = \boldsymbol{E}\times\boldsymbol{H} \tag{2.32}$$

The Poynting vector describes the energy per unit time passing through a unit surface (Albrecht et al., 2003).

According to Albrecht et al. (2003), in terms of a harmonic oscillator, the Maxwell's equations can be rewritten as:

$$curl\,\underline{\boldsymbol{H}} = \underline{\boldsymbol{S}} + j\omega\underline{\boldsymbol{D}},\; curl\,\underline{\boldsymbol{E}} = -j\omega\underline{\boldsymbol{B}}, \tag{2.33}$$

$$div\underline{\boldsymbol{D}} = \rho,\; div\underline{\boldsymbol{B}} = 0, \tag{2.34}$$

$$\underline{\boldsymbol{S}} = \kappa\underline{\boldsymbol{E}},\; \underline{\boldsymbol{D}} = \varepsilon\underline{\boldsymbol{E}},\; \underline{\boldsymbol{B}} = \mu\underline{\boldsymbol{H}}, \tag{2.35}$$

where the underline denote complex quantity, and ω is the angular frequency. Albrecht et al. (2003) prove that in terms of charge-free space ($\rho = 0$), solving equations (2.33), (2.34) and (2.35) yields the well-known wave equations of the electromagnetic field, which are given by:

$$\Delta\underline{\boldsymbol{E}} + \underline{k}^2\underline{\boldsymbol{E}} = 0, \tag{2.36}$$

$$\Delta\underline{\boldsymbol{H}} + \underline{k}^2\underline{\boldsymbol{H}} = 0, \tag{2.37}$$

where, k is the wavenumber of the wave. The wavenumber k is given by:

$$\underline{k} = \sqrt{\varepsilon\mu\omega^2 - j\omega\kappa\mu} = \omega\sqrt{\underline{\varepsilon}\mu}, \tag{2.38}$$

$$\underline{\varepsilon} = \varepsilon - j\frac{\kappa}{\omega}, \tag{2.39}$$

where $\underline{\varepsilon}$ is the complex dielectric constant (Albrecht et al., 2003). Equation (2.38) is called dispersion relation.

2.3.2 Homogeneous Plane Waves

The condition of a homogeneous plane wave is that all points located on an arbitrary plane normal to the propagation direction of the wave have the same phase for a given moment (Albrecht et al., 2003). Also, a solution value remains constant in each plane of a constant phase (Albrecht et al., 2003). For simplicity, a non-conducting medium (i.e. $\kappa = 0$) and a sinusoidal behaviour in time and space are assumed. According to Albrecht et al. (2003), the solutions of the wave equations (2.36) and (2.37) for the homogeneous plane wave are given by:

$$\underline{\boldsymbol{E}} = \underline{\boldsymbol{E}_0} \exp\left[j\left(\omega t - \boldsymbol{k}\cdot\boldsymbol{r}\right)\right],\ \underline{\boldsymbol{H}} = \underline{\boldsymbol{H}_0} \exp\left[j\left(\omega t - \boldsymbol{k}\cdot\boldsymbol{r}\right)\right] \tag{2.40}$$

$$\boldsymbol{k} = k\boldsymbol{e}_k = \frac{\omega}{c}\boldsymbol{e}_k = \frac{2\pi}{\lambda}\boldsymbol{e}_k, \tag{2.41}$$

where, $\boldsymbol{k}$ is the wavenumber vetor, $\boldsymbol{r}$ is the vector to an aribitray point in the field, c is the propagation speed of the wave, and λ is the wavelength of the wave. Note that based on the assumption of the non-conducting medium (i.e. $\kappa = 0$), k remains real (equation (2.38)) (Albrecht et al., 2003).

According to Albrecht et al. (2003), the energy density equation (2.31) of the homogeneous plane wave can be described as:

$$w = \frac{1}{2}\left(\varepsilon E^2 + \mu H^2\right),\ E = |\underline{\boldsymbol{E}}|,\ H = |\underline{\boldsymbol{H}}|. \tag{2.42}$$

Since the solutions for the homogeneous plane wave are given, the interference of two homogeneous plane waves propagating in different directions will be discussed below. Two homogeneous plane waves with wavenumber vectors $\boldsymbol{k}_1$ and $\boldsymbol{k}_2$. For simplicity, it is assumed that these two waves have the same frequencies ω and amplitude $\underline{E_0}$. The angle between their wavenumber vetors is 2α (see Fig. 2.15). Hence, the electric field strength of these two homogeneous plane waves can be described as:

$$\underline{\boldsymbol{E}_1} = \underline{\boldsymbol{E}_0} \exp\left[j\left(\omega t - \boldsymbol{k}_1\cdot\boldsymbol{r}_1\right)\right],\ \underline{\boldsymbol{E}_2} = \underline{\boldsymbol{E}_0} \exp\left[j\left(\omega t - \boldsymbol{k_2}\cdot\boldsymbol{r}_2\right)\right], \tag{2.43}$$

where, $\underline{\boldsymbol{E}_0} = \boldsymbol{E}_0 e^{j\varphi_0}$. Note that φ_0 is the initial phase, and $\boldsymbol{r}_1$ and $\boldsymbol{r}_2$ are two vectors pointing from the sources to the arbitrary points, respectively. The electric field strength of the resulting electromagnetic wave $\left(\underline{\boldsymbol{E}_3}\right)$, which is the superposition of those two homogeneous plane waves, is given by:

$$\underline{\boldsymbol{E}_3} = \underline{\boldsymbol{E}_1} + \underline{\boldsymbol{E}_2} = \underline{\boldsymbol{E}_0} e^{j\omega t}\left(e^{-j\boldsymbol{k}_1\cdot\boldsymbol{r}_1} + e^{-j\boldsymbol{k}_2\cdot\boldsymbol{r}_2}\right). \tag{2.44}$$

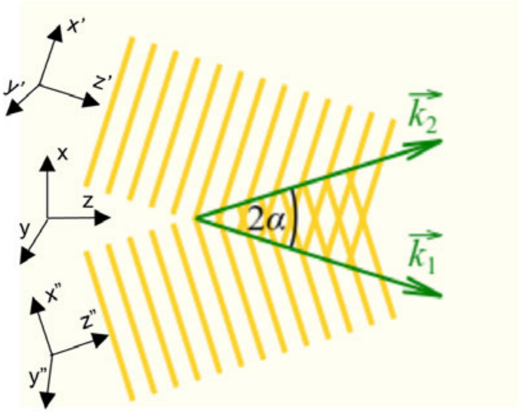

Figure 2.15: Two homogeneous plane waves (*Collection of Solved Problems in Physics*, 2018). xyz is the global coordinate system while $x'y'z'$ and $x''y''z''$ are local coordinate systems. Note that the the directions of z' axis and z'' axis are parallel to the wavevectors $\boldsymbol{k}_1$ and $\boldsymbol{k}_2$, respectively.

According to Albrecht et al. (2003), the energy intensity (I) of a homogeneous plane wave is given by:

$$I = \frac{1}{2} c\varepsilon \underline{\boldsymbol{E}} \cdot \underline{\boldsymbol{E}}^*, \tag{2.45}$$

Where, the superscript $*$ denotes the complex conjugate. Hence, the energy intensity of the resulting electromagnetic wave I_{total} is obtained by substituting equation (2.44) into equation (2.45), which can be expressed as:

$$\begin{aligned}
I_{\text{total}} &= \frac{1}{2} c\varepsilon \underline{\boldsymbol{E}_3} \cdot \underline{\boldsymbol{E}_3}^* \\
&= \frac{1}{2} c\varepsilon \underline{\boldsymbol{E}_0} e^{j\omega t} \left(e^{-j\boldsymbol{k}_1 \cdot \boldsymbol{r}_1} + e^{-j\boldsymbol{k}_2 \cdot \boldsymbol{r}_2} \right) \cdot \underline{\boldsymbol{E}_0} e^{-j\omega t} \left(e^{j\boldsymbol{k}_1 \cdot \boldsymbol{r}_1} + e^{j\boldsymbol{k}_2 \cdot \boldsymbol{r}_2} \right) \\
&= \frac{1}{2} c\varepsilon |\boldsymbol{E}_0|^2 \left(2 + e^{j(k_2 \cdot z'' - k_1 z')} + e^{-j(k_2 \cdot z'' - k_1 z')} \right) \\
&= \frac{1}{2} c\varepsilon E_0^2 \left(2 + e^{j(k_2 \cdot z'' - k_1 z')} + e^{-j(k_2 \cdot z'' - k_1 z')} \right) \\
&= \frac{1}{2} c\varepsilon E_0^2 \left(2 + 2cos \left(k_2 \cdot z'' - k_1 z' \right) \right) \\
&= \frac{1}{2} c\varepsilon E_0^2 \left[2 + 2cos \left(k_1 \left(z'' - z' \right) \right) \right].
\end{aligned} \tag{2.46}$$

The relationships between the global coordinate system and the local coordinate systems (i.e. $x'y'z'$ and $x''y''z''$) are given by:

$$z' = \frac{z}{cos\alpha} + xsin\alpha - \frac{z\,(sin\alpha)^2}{cos\alpha}, \tag{2.47}$$

$$z'' = (z - xtan\alpha)\,cos\alpha, \tag{2.48}$$

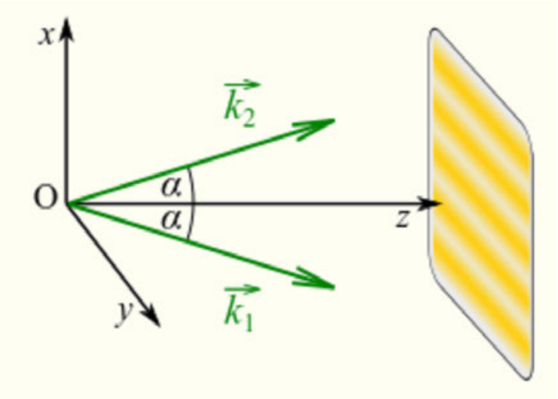

Figure 2.16: Fringe pattern (*Collection of Solved Problems in Physics*, 2018). Note that the plane at the right hand side is perpendicular to z axis.

Where, α is one half of the angle between the propagating directions of those two laser beams. Substituting equations (2.47) and (2.48) into (2.46) yields:

$$\begin{aligned} I_{total} &= \frac{1}{2}c\varepsilon E_0^2\left[2+2cos\left(k_1\cdot 2xsin\alpha\right)\right] \\ &= c\varepsilon E_0^2\left[1+cos\left(2k_1xsin\alpha\right)\right] \\ &= c\varepsilon E_0^2\times 2cos^2\left(k_1xsin\alpha\right). \end{aligned} \tag{2.49}$$

It is obvious that an interference fringe is directed along y axis because equation (2.49) does not include y (see Fig. 2.16). The width of the fringe Δx, which is on the order of the distance between two subsequent minima of I_{total} is given by:

$$\Delta x = x_2 - x_1, \tag{2.50}$$

$$k_1x_1sin\alpha = \frac{\pi}{2}+m\pi,\ m\in Z, \tag{2.51}$$

$$k_1x_2sin\alpha = \frac{\pi}{2}+(m+1)\pi,\ m\in Z, \tag{2.52}$$

where, x_1 and x_2 denote the positions of the m^{th} and $(m+1)^{th}$ minima, respectively. Substituting equations (2.51) and (2.52) into (2.50) yields the width of the fringe Δx, which is described as:

$$\Delta x = \frac{\pi}{ksin\alpha} = \frac{\lambda}{2sin\alpha}. \tag{2.53}$$

2.3.3 Principles of PDI

As mentioned in Sec. 2.3.2, when two coherent laser beams intersect, they will create a fringe pattern at the intersection. The width of the fringe is related with the wavelengths of those two laser beams, and the angle of the propagating directions of those two laser beams (see equation (2.53)). When a droplet passes through a fringe pattern, it will reflect or refract the local fringe pattern with respect to the optical axis of the laser transmitter by a certain angle. This angle is called the collection angle (θ) which is related to the material of the droplet (see Fig. 2.17). In order to analyze the local fringe pattern scattered by the droplet, a receiver is placed at a position where the angle between the optical axes of the receiver and laser transmitter is on the order of the collection angle. Then, the receiver directs the local fringe pattern to photomultiplier tubes, which provide a Doppler burst signal (see Fig. 2.18). When a droplet passes through a fringe, a burst signal can be observed. Hence, the velocity of the droplet is given by:

$$V_D = f_D \times \Delta x, \tag{2.54}$$

where, V_D is the drop velocity, f_D is the Doppler burst signal frequency, and Δx is the width of the fringe. A typical PDI system is shown in Fig. 2.19. A laser beam is split into two beams with the same intensity, and those two laser beams are focused by a transmitter lens. There are three photodectors on the receiver which are numbered 1, 2 and 3 (see Fig. 2.19). When a droplet passes through a fringe pattern, the fringe pattern will be projected onto the receiver, and will be magnified by a certain degree which is related to the droplet size (“2D PDI User Manual”, 2022). Hence, there are phase differences for the fringe patterns detected by the photodectors. A small droplet has large curvature and consequently leads to big divergence of the fringe pattern, causing a small phase difference for the fringe patterns detected by those three photodectors. On the other hand, a large droplet will have small curvature and consequently lead to small divergence of the fringe pattern, causing large phase differences for the fringe patterns detected by the photodectors. Hence, according to “2D PDI User Manual” (2022), the size of the droplet can be expressed as:

$$D = \frac{F\overline{\Delta x}}{s\Delta x}, \tag{2.55}$$

where, D is the diameter of the droplet, F is the focal length of the lens of the receiver, $\overline{\Delta x}$ is the width of the magnified fringe, s is the sizing slope factor, and Δx is the actual width of the fringe. According to “2D PDI User Manual” (2022), the width of the magnified fringe ($\overline{\Delta x}$) is determined using the phase differences for the fringe patterns detected by different photodectors, and the spatial spacing between the centers of different photodectors.

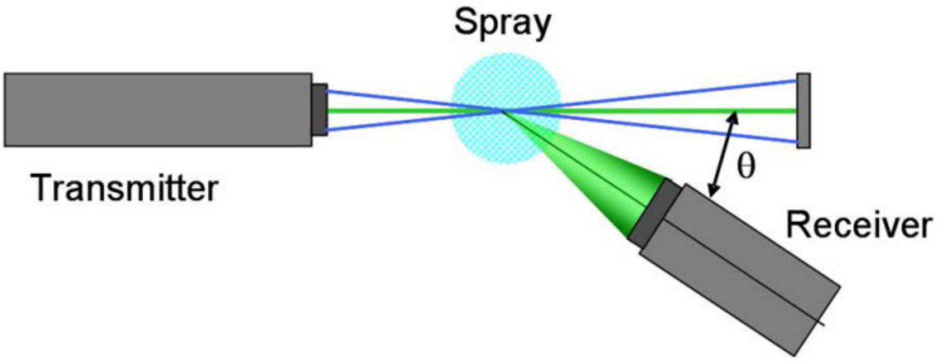

Figure 2.17: Collection angle (θ). Note that this is a 2D PDI system since two pairs of laser beam are shown in this figure.

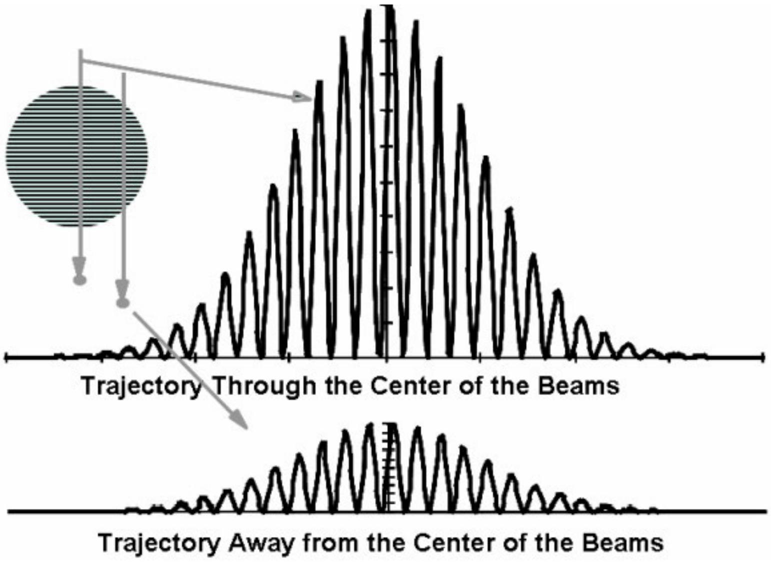

Figure 2.18: Doppler burst signals created by different trajectories of the particles though the fringe pattern (“2D PDI User Manual”, 2022).

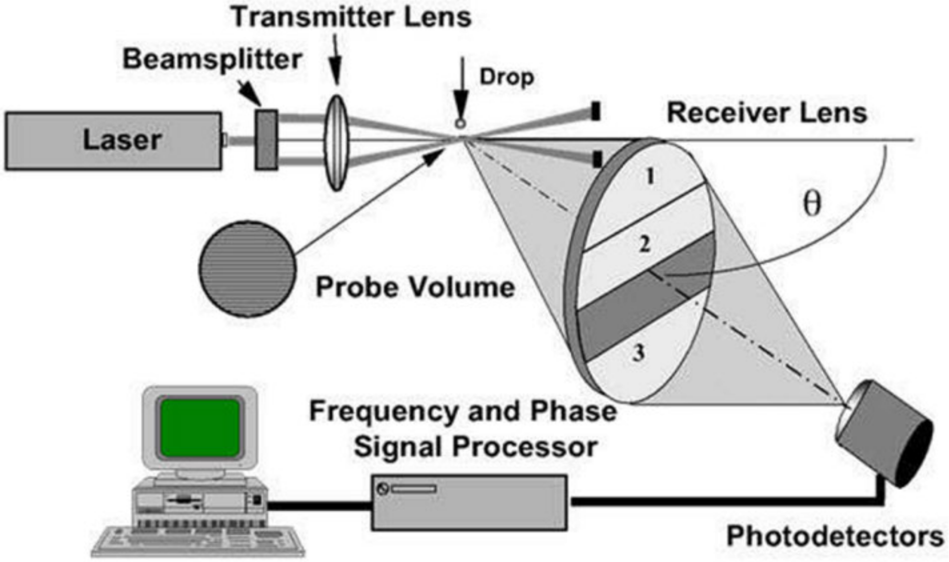

Figure 2.19: A typical 1D PDI system. θ: collection angle.

2.4 Proper Orthogonal Decomposition (POD)

Proper orthogonal decomposition (POD) is one of the most important matrix factorizations in data analysis. POD can decompose a high-dimensional rectangular data matrix, which is composed of scalar (e.g, temperature) field or vector field (e.g, velocity), into a group of POD modes in the order of the importance in terms of the relative amount of energy captured by each POD mode (Taira et al., 2017). The high-dimensional data matrix can be represented by this set of POD modes. The number of the POD modes is equal to the rank of the data matrix (Strang, 2019). Each POD mode has its corresponding singular value, and the relative magnitude of the singular value shows how important and dominant the mode corresponding to that singular value is. Generally, they are two ways to perform POD on fluid flow data; spatial (classical) POD and snapshot POD. Spatial POD can be determined using singular value decomposition (SVD) (Taira et al., 2017). More details about the spatial POD method and snapshot POD method can be found in Taira et al. (2017). In what follows, the algorithm of SVD will be introduced since SVD was chosen as the method to perform POD on the fluid flow data in this project.

A velocity field $\boldsymbol{q}_{ij}$ is chosen as fluid flow data to introduce the SVD algorithm. For simplicity, it is assumed that data are collected from a uniform two-dimensional gird. Fig. 2.20 shows the coordinate system of the velocity field. Hence, the velocity field $\boldsymbol{q}_{ij}$ can be mathematically described as,

$$\boldsymbol{q}_{ij} = (u_{ij}, v_{ij}) = (u(\xi_i, \eta_j), v(\xi_i, \eta_j)). \tag{2.56}$$

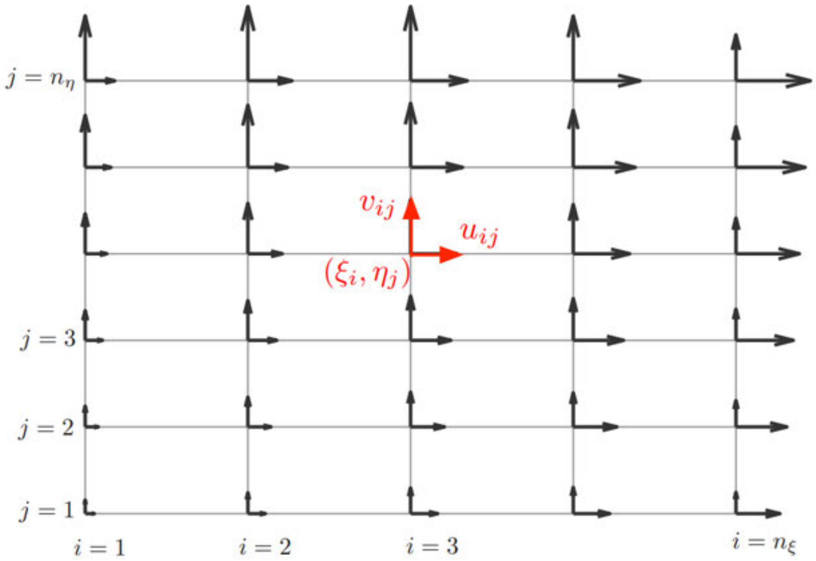

Figure 2.20: Coordinate system of the velocity field (Taira et al., 2017). (ξ_i, η_j) is the spatial coordinate. n_ξ and n_η are the maximums of the row and column numbers, respectively.

Firstly, the data matrix should be rearranged in the form of a group of data vectors $\boldsymbol{x}(t)$. Each data vector $\boldsymbol{x}(t)$ contains the data collected at different moments. In other words, the data which are collected at the same moment in time should be stacked into the same column (i.e. data vector). Fig. 2.21 shows how the data which are collected at $t = t_k$ are stacked into one column (i.e. data vector). Note that the data which are collected at $t = t_k$ is one of the sub-blocks of the data matrix $\boldsymbol{q}_{ij}$. According to Taira et al. (2017), after the rearrangement of the data matrix $\boldsymbol{q}_{ij}$, the matrix $\boldsymbol{X}$ is obtained, which is given by,

$$\boldsymbol{X} = [\boldsymbol{x}(t_1), \boldsymbol{x}(t_2), \boldsymbol{x}(t_3), \ldots, \boldsymbol{x}(t_m)] \in \mathbb{R}^{n \times m}, \tag{2.57}$$

where, n, which is equal to the grid points times the number of the variables to be considered in the flow field, is the number of the rows of matrix $\boldsymbol{X}$, m is the number of the measurement times, $\mathbb{R}$ is real numbers, and $\in$ represents "belongs to". Note that the data vectors should be placed in order of time when the data vectors are measured.

Then the mean values of $\boldsymbol{X}$ are subtracted from the matrix $\boldsymbol{X}$ to render the variance unitary before POD is performed (Brunton & Kutz, 2019). Hence, the fluctuating component of the vector field $\boldsymbol{X}(\zeta, t)$ is given by:

$$\boldsymbol{K}(\zeta, t) = \boldsymbol{X}(\zeta, t) - \overline{\boldsymbol{X}(\zeta)}, \tag{2.58}$$

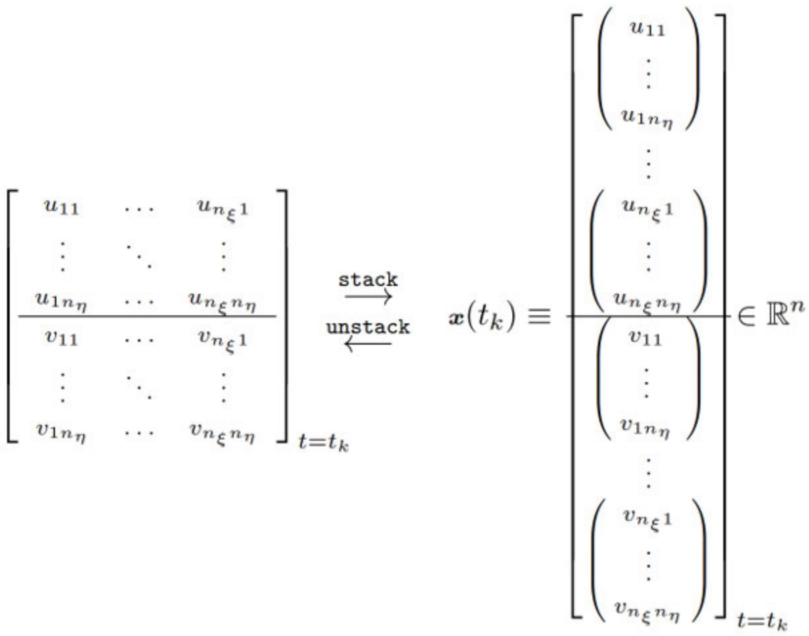

Figure 2.21: Illustration of how one of the sub-blocks of the data matrix is stacked into a data vector $\boldsymbol{x}(t)$ (Taira et al., 2017).

where, ζ denotes the two dimensional coordinate, t denotes different measurement times, $\boldsymbol{K}(\zeta, t)$ is the fluctuating component of the vector field $\boldsymbol{X}(\zeta, t)$, and $\overline{\boldsymbol{X}(\zeta)})$ is the matrix which contains the mean values for each row of the vector field $\boldsymbol{X}(\zeta, t)$. Note that the matrix $\boldsymbol{X}$ is written as $\boldsymbol{X}(\zeta, t)$ in equation (2.58) to emphasize that the data are collected from the two-dimensional grid at discrete moments t.

As mentioned earlier, a rectangular matrix can be decomposed with SVD. According to Strang (2019), after decomposed with SVD, the n by m martrix K is given by:

$$\begin{aligned}\boldsymbol{K} = \boldsymbol{U}\boldsymbol{\Sigma}\boldsymbol{V}^T = [\boldsymbol{u}_1, \boldsymbol{u}_2, \ldots, \boldsymbol{u}_r] &\begin{bmatrix} \sigma_1 & 0 & \ldots & 0 \\ 0 & \sigma_2 & \ldots & 0 \\ \vdots & \vdots & \ddots & \vdots \\ 0 & 0 & 0 & \sigma_r \end{bmatrix} \begin{bmatrix} \boldsymbol{v}_1^T \\ \boldsymbol{v}_2^T \\ \vdots \\ \boldsymbol{v}_r^T \end{bmatrix} \\ = \boldsymbol{u}_1\boldsymbol{\sigma}_1\boldsymbol{v}_1^T + \boldsymbol{u}_2\boldsymbol{\sigma}_2\boldsymbol{v}_2^T + \ldots + \boldsymbol{u}_r\boldsymbol{\sigma}_r\boldsymbol{v}_r^T, \qquad (2.59) \\ \boldsymbol{U} \in \mathbb{R}^{n \times r}, \boldsymbol{V} \in \mathbb{R}^{m \times r}, \boldsymbol{\Sigma} \in \mathbb{R}^{r \times r}, \sigma_1 \geq \sigma_2 \geq \ldots \geq \sigma_r > 0,\end{aligned}$$

where, r is the rank of the matrix $\boldsymbol{K}$, σ_i, $i = 1,2,...,r$, denote singular values, the superscript T denotes transpose, and $\boldsymbol{u}_i, \boldsymbol{v}_i$, $i = 1,2,...,r$ are called left singular vectors and right singular vectors, respectively (Strang, 2019). $\boldsymbol{u}_i$, $i = 1,2,...,r$, are also called the POD modes (Taira et al., 2017). It should be noted that the matrices $\boldsymbol{U}$ and $\boldsymbol{V}$ are orthonormal, which means that:

$$\boldsymbol{U}^T\boldsymbol{U} = \boldsymbol{V}^T\boldsymbol{V} = \boldsymbol{I}_{r\times r}, \tag{2.60}$$

where $\boldsymbol{I}$ denotes the identity matrix. Each POD mode $\boldsymbol{u}_i$ is therefore orthonormal to any other mode $\boldsymbol{u}_{j\neq i}$ and forms a linearly independent set. The same is true for $\boldsymbol{v}_i$.

The left singular vectors, or POD modes, $\boldsymbol{u}_i$ contain the spatial components of $\boldsymbol{K}$. The right singular vectors $\boldsymbol{v}_i$ contain the temporal components. Performing a Fourier transform on the matrix $\boldsymbol{V}$ obtained from SVD yields the frequency of each mode.

2.5 Fourier Series and Fourier Transforms

A piecewise smooth and periodic function $f(x)$ can be expressed by an infinite sum of cosine and sine functions (Brunton & Kutz, 2019). This infinite sum of cosine an sine functions is called the Fourier series. Hence, According to Brunton and Kutz (2019), a piecewise smooth and L-periodic function $f(x)$ on $[0,L)$ can be expressed as:

$$f(x) = \frac{a_0}{2} + \sum_{k=1}^{\infty}\left(a_k cos\left(\frac{2\pi kx}{L}\right) + b_k sin\left(\frac{2\pi kx}{L}\right)\right), \tag{2.61}$$

Where,

$$a_k = \frac{2}{L}\int_0^L f(x) cos\left(\frac{2\pi kx}{L}\right) dx, \tag{2.62}$$

$$b_k = \frac{2}{L}\int_0^L f(x) sin\left(\frac{2\pi kx}{L}\right) dx. \tag{2.63}$$

Note that equations (2.61), (2.62) and (2.63) cannot be applied to non-periodic functions. The Fourier transform integral is the limit of a Fourier series when L goes to infinity (Brunton & Kutz, 2019). This means that Fourier transform can be applied to non-periodic functions defined on $(-\infty,\infty)$ (Brunton & Kutz, 2019). According to (Brunton & Kutz, 2019), the inverse Fourier transform and Fourier transform of a function $f(x)$ are given by:

$$f(x) = \mathscr{F}^{-1}\left(\hat{f}(\omega)\right) = \frac{1}{2\pi}\int_{-\infty}^{\infty}\hat{f}(\omega)e^{i\omega x}d\omega, \tag{2.64}$$

$$\hat{f}(\omega) = \mathscr{F}(f(x)) = \int_{-\infty}^{\infty}\hat{f}(\omega)e^{-i\omega x}dx. \tag{2.65}$$

Equations (2.64) and (2.65) are called the Fourier transform pair. Both integrals in equations (2.64) and (2.65) converge when $f(x)$ satisfies the condition that $\int_{-\infty}^{\infty} |f(x)|\, dx < \infty$ and $\int_{-\infty}^{\infty} |\hat{f}(\omega)|\, d\omega < \infty$ (Brunton & Kutz, 2019).

2.5.1 Discrete Fourier Transform (DFT)

The Fourier series for a periodic function and the Fourier transform for a continuous function are discussed above. However, real-data is always discrete rather than continuous. This means that function $f(x)$ is always discretized into points at a regular spacing. In order to analyze this data, DFT, which is the discretized version of the Fourier transform, should be used at this case. According to Brunton and Kutz (2019), the discrete Fourier transform and inverse discrete Fourier transform are given by:

$$\hat{f}_k = \sum_{j=0}^{n-1} f_j e^{-i\cdot 2\pi jk/n}, \tag{2.66}$$

$$f_k = \frac{1}{n} \sum_{j=0}^{n-1} \hat{f}_j e^{i\cdot 2\pi jk/n}, \tag{2.67}$$

where, $(n+1)$ is the total number of the points that $f(x)$ is discretized into, the subscript k denotes the $(k+1)^{\text{th}}$ discrete point. According to Brunton and Kutz (2019), equation (2.66) can be rewritten in the form of matrices,

$$\hat{\boldsymbol{f}} = \boldsymbol{F}\boldsymbol{f}, \tag{2.68}$$

$$\begin{bmatrix} \hat{f}_0 \\ \hat{f}_1 \\ \vdots \\ \hat{f}_{n-1} \end{bmatrix} = \begin{bmatrix} 1 & 1 & 1 & \dots & 1 \\ 1 & \omega_n & \omega_n^2 & \dots & \omega_n^{n-1} \\ 1 & \omega_n^2 & \omega_n^4 & \dots & \omega_n^{2(n-1)} \\ \vdots & \vdots & \vdots & \ddots & \vdots \\ 1 & \omega_n^{n-1} & \omega_n^{2(n-1)} & \dots & \omega_n^{(n-1)^2} \end{bmatrix} \begin{bmatrix} f_0 \\ f_1 \\ \vdots \\ f_{n-1}, \end{bmatrix} \tag{2.69}$$

where,

$$\omega_n = e^{-2\pi i/n}. \tag{2.70}$$

Here $\hat{\boldsymbol{f}}$ is the output vector, $\boldsymbol{f}$ is the input vector, and $\boldsymbol{F}$ is called the DFT matrix. Note that the discrete real-data are arranged in the form of the vector $\boldsymbol{f} = [f_0 \; f_1 \; \dots \; f_{n-1}]^T$. Also, It is obvious that ω_n has three properties, which are expressed as:

$$\omega_n^{jk+n/2} = -\omega_n^{jk} \text{ (symmetric property)}, \tag{2.71}$$

$$\omega_n^{jk} = \omega_n^{jk+n} = \omega^{jk+2n} = \dots \text{ (periodic property)}, \tag{2.72}$$

$$\omega_{n/2}^{jk} = \omega_n^{2jk} \text{ (recursion property)}. \tag{2.73}$$

Computing equation (2.69) involves n^2 complex multiplications and $n(n-1)$ complex additions. Hence, the total number of complex operations is given by:

$$n^2+n(n-1)=2n^2-n\equiv O(n^2). \tag{2.74}$$

The drawback of DFT is that performing DFT is time-consuming since computing equation (2.69) requires $O(n^2)$ operations.

2.5.2 Fast Fourier Transform (FFT)

When the number of the data points n is a power of 2, the DFT can be implemented more efficiently with the properties of ω_n (equations (2.72) and (2.73)). This is the idea behind FFT (Brunton & Kutz, 2019). Compared with DFT, FFT requires $O(nlog_2n)$ operations, which is much less than the required operations in DFT (Brunton & Kutz, 2019). The algorithm of FFT and how FFT saves computational time when compared with DFT will be discussed in the following paragraphs.

The equation (2.66) can be rewritten as:

$$\begin{aligned}
\hat{f}_k &= \sum_{j=0}^{n-1} f_j e^{-i\cdot 2\pi jk/n} \\
&= \sum_{j=0}^{\frac{n}{2}-1} e^{-i2\pi\cdot 2jk/n} f_{2j} + \sum_{j=0}^{\frac{n}{2}-1} e^{-i2\pi\cdot(2j+1)k/n} f_{2j+1} \\
&= \sum_{j=0}^{\frac{n}{2}-1} e^{-i2\pi jk/(n/2)} f_{2j} + e^{-i2\pi k/n} \sum_{j=0}^{\frac{n}{2}-1} e^{-i2\pi jk/(n/2)} f_{2j+1} \\
&= \sum_{j=0}^{\frac{n}{2}-1} e^{-i2\pi jk/(n/2)} f_{2j} + \omega_n^k \sum_{j=0}^{\frac{n}{2}-1} e^{-i2\pi jk/(n/2)} f_{2j+1} \\
&= \sum_{j=0}^{\frac{n}{2}-1} \omega_{\frac{n}{2}}^{jk} f_{2j} + \omega_n^k \sum_{j=0}^{\frac{n}{2}-1} \omega_{\frac{n}{2}}^{jk} f_{2j+1} \\
&= A(k)+\omega_n^k B(k),\ k=0,1,\ldots,(n-1)
\end{aligned} \tag{2.75}$$

where,

$$A(k)=\sum_{j=0}^{\frac{n}{2}-1} \omega_{\frac{n}{2}}^{jk} f_{2j},\ B(k)=\sum_{j=0}^{\frac{n}{2}-1} \omega_{\frac{n}{2}}^{jk} f_{2j+1}. \tag{2.76}$$

Note that the magnitudes of f with even and odd subscripts are separated from each other, and $A(k)$ and $B(k)$ are two $(\frac{n}{2})-$point DFTs of f_{2j} and $f_{2j+1},\ j=0,1,\ldots,(n-1)$, respectively, when $k=0,1,\ldots,\frac{n}{2}-1$. Recalling the symmetrical and recursion properties of ω_n, we have,

$$A(k)=A(k+\frac{n}{2}),\ B(k)=B(k+\frac{n}{2}). \tag{2.77}$$

Hence, the whole DFT of $\hat{f}_k$ can be calculated as follows:

$$\hat{f}_k = A(k) + \omega_n^k B(K),\ k = 0, 1, ..., (\frac{n}{2} - 1) \tag{2.78}$$

$$\hat{f_{k+\frac{n}{2}}} = A(k + \frac{n}{2}) + \omega_n^{k+\frac{n}{2}} B(k + \frac{n}{2}) = A(k) - \omega_n^k B(k),\ k = 0, 1, ..., (\frac{n}{2} - 1). \tag{2.79}$$

A conclusion can be drawn from equations (2.78) and (2.79) that performing DFT directly on $f_j,\ j = 0, 1, ..., (n-1)$ can be decomposed into computing two $(\frac{n}{2})-$point DFTs of f_{2j} and $f_{2j+1},\ j = 0, 1, \ldots, (n-1)$. As the number of the data points n is a power of 2, separating the magnitudes of f with even and odd subscripts from each other can be done $\log_2 n$ times. Hence, the numbers of the resulting complex multiplications and complex additions, which are required to compute n-point DFT of $f_j,\ j = 0, 1, ..., (n-1)$, are reduced to $\frac{n}{2}\log_2 n$ and $n\log_2 n$, respectively (Arunachalam, Khairnar, & Desale, 2013). Therefore, the total number of the operations required to perform FFT on $f_j,\ j = 0, 1, ..., (n-1)$, is given by:

$$\frac{n}{2}\log_2 n + n\log_2 n = \frac{3}{2} n\log_2 n \equiv O(n\log_2 n). \tag{2.80}$$

The various data analysis techniques discussed in this chapter have been applied during and after the experiments described next.

Chapter 3

Experimental Setup and Procedure

In this chapter, the overall setup and operating conditions of the atomizer are introduced. Then, the experimental procedure is discussed. Finally, the PIV and PDI setups are introduced.

3.1 Overall Setup

The central liquid jet and annular gas stream in this study are water and air respectively (see Fig. 3.1). Two mass flow controllers (MFC) (Bronkhorst Inc, the Netherlands) are used to control and measure the air and water flow rates. The inner diameters of the liquid and co-flow tubes are 4 mm and 10 mm, respectively. The outer diameters of the liquid and co-flow tubes are 5 mm and 14 mm, respectively. Air enters the air sub-system through an inlet located at the bottom of the chamber. Then it flows through an air filter to render the nozzle in-flow azimuthally uniform, and it subsequently enters the co-flow tube (see Fig. 3.1a and Fig. 3.1b). In order to introduce swirl into the air, a swirler can be added to the inner surface of the co-flow tube (see Fig. 3.1c). The circular gap between the air swirler and the water tube is sealed with an O ring to avoid air leakage. There are seven types of air swirlers with different vane angles. A vane angle is defined as the angle between a tangent at the tip of the vane and a vertical line. The magnitudes of the vane angles for those air swirlers are shown in Table 3.1. All the air swirlers have a four-star shape. The cross-sectional areas of the air outlets with and without the air swirler are 28.09 mm^2 and 58.9 mm^2, respectively. The lengths of the water tubes and co-flow tubes are 140 mm and 43 mm, respectively. The drawings of the nozzle and air swirlers can be found in Appendix A.

The Reynolds number of the central water jet is kept at 480 for all the flow cases to ensure that the laminar pipe flow becomes fully developed before it leaves the nozzle exit. According to White (2016), Schlichting and Gersten (2017) and White (2005), the entrance length (L_e) for a laminar pipe flow is given by:

$$L_e = 0.06 \times Re_{D_l} \times D_l, \tag{3.1}$$

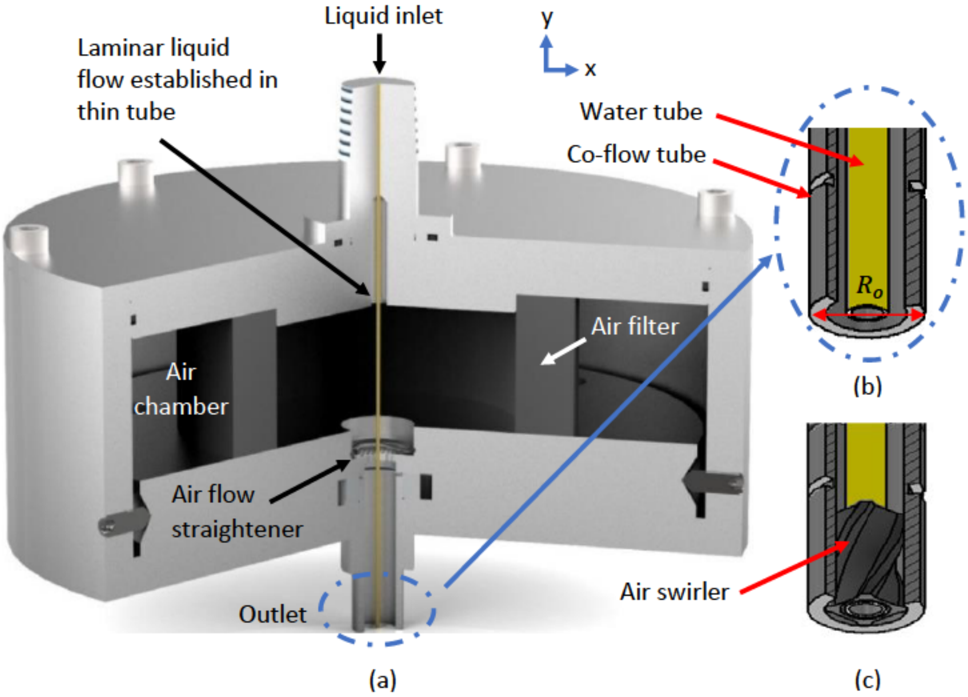

Figure 3.1: Images of the atomizer. (a) Broken-out view of the atomizer. (b) Broken-out view of the co-flow tube without air swirler attached on it. (c) Broken-out view of the co-flow tube with the air swirler.

Where, D_l is the inner diameter of the pipe, and Re_{D_l} is the Reynolds number based on D_l. The L_e for the laminar water flow in this work is given by:

$$L_e = 105.12 \text{ mm} < 140 \text{ mm (length of the water tube)},$$

which means that the central laminar water flow becomes fully developed before it leaves the nozzle exit. This conclusion was confirmed by the fact that in the absence of any air flow, the recognizable Rayleigh breakup was observed from the high-speed shadowgrams of the water jet, with no evidence for any fluid turbulence. In the absence of significant shear, a fully developed parabolic velocity profile evolves into a flat velocity profile after the liquid jet leaves the nozzle (Lefebvre & McDonell, 2017). The energy within the liquid jet redistributes simultaneously, which is thought by some to cause bursting breakup (Eisenklam & Hooper, 1958; Lefebvre & McDonell, 2017). E. A. Ibrahim and Marshall (2000) found that the effects of the parabolic velocity profile relaxation on jet instability are weaker than flat velocity profile relaxation. In this work, it was observed that in the absence of the co-annular air flows there is no contribution to the breakup of the central water jet from velocity profile relaxation.

Table 3.1: Vane angles for all the air swirlers.

S^1	θ^2
0.3	21.1°
0.8	45.8°
1.2	57.1°
1.5	62.6°
2.5	72.7°
3.1	75.9°
3.9	78.7°

[1] Swirl number
[2] Vane angle

In terms of the atomizer, the water tube, flow bench connector, perforated plate, gas tube and air swirlers were designed and manufactured in this project. Langeslag and Linne (2016) designed and manufactured gas drum lid and gas drum. All the components were assembled in this project, and their drawings can be found in Appendix A.

3.2 Operating Conditions for the Atomizer

As mentioned in Sec. 1.1, seven parameters (usually non-dimensional numbers) are generally used to describe the operating conditions of any spray. The characteristics of twin-fluid atomization, such as the first droplet location, jet instability and breakup length of the liquid jet, are related to the fluid material and the relative velocities between those two fluids. In this project, three non-dimensional parameters were used to describe the operating conditions of the twin-fluid atomizer. They are the aerodynamic Weber number (We_A, the ratio of the aerodynamic forces to the liquid surface tension forces), the liquid Reynolds number (Re_l, the ratio of the liquid inertial forces to viscous forces), and the gas to liquid momentum flux ratio (M). They are given by:

$$We_A = \frac{\rho_g (U_g - U_l)^2 D_l}{\sigma_l}, \tag{3.2}$$

$$Re_l = \frac{U_l D_l}{\nu_l}, \tag{3.3}$$

$$M = \frac{\rho_g U_g^2}{\rho_l U_l^2}. \tag{3.4}$$

Table 3.2: Comparisons between the geometric and actual swirl numbers.

S^3	${S_{\text{meas}}}^4$
0.3	0.1
0.8	0.3
1.2	0.5
1.5	0.7
2.5	1.3

[3] Geometric swirl number
[4] Measured swirl number

Here, ρ_l is the density of the liquid, ρ_g is the density of the gas, U_g is the gas velocity, U_l is the liquid velocity, D_l is the diameter of the liquid tube, σ_l is the surface tension of the liquid, and ν_l is the kinematic viscosity of the liquid. Additionally, as mentioned in Sec. 1.2, the swirl number (S), which is the ratio of the axial flux of swirl momentum to axial flux of axial momentum, is generally used to describe the operating conditions of a swirling flow. According to Giannadakis et al. (2008) and Ivanic et al. (2003), it is given by:

$$S = \frac{\int_0^\infty U_y U_\theta r^2 \, dr}{R_O \int_0^\infty U_y^2 r \, dr}, \tag{3.5}$$

where U_y is the axial velocity, U_θ is the tangential velocity and R_O is the outer radius of the co-flow tube (see Fig. 3.1b). The correlations for geometric swirl numbers depend on the type of the air swirler. Details can be found in Giannadakis et al. (2008). According to Hardalupas and Whitelaw (1998), based on the type of the air swirler used in this project, the geometric swirl number is given by,

$$S = \frac{2}{3} \tan\theta \frac{1 - \left(\frac{D_O}{D_G}\right)^3}{1 - \left(\frac{D_O}{D_G}\right)^2}, \tag{3.6}$$

where θ is the swirl vane angle, D_0 is the external diameter of the liquid tube, and D_G is the diameter of the vane pack hub. Table 3.2 shows a comparison between the geometric and measured swirl numbers. Note that the measured swirl numbers (S_{meas}) were calculated based on the SPIV data (the approach to calculate S_{meas}, and the differences between S_{meas} and S are discussed in detail in Sec. 4.3). In this work, the geometric swirl numbers (S) are used to describe the operating conditions of the atomizer. For simplicity, the term "swirl number" mentioned throughout the sections of this work refers to the "geometric swirl number".

The operating conditions of the atomizer are shown in Tables 3.3 and 3.4. Table 3.3 shows the flow cases within the first-wind induced (FWI), second-wind induced (SWI) and bag breakup regimes (B), while Table 3.4 shows the flow cases within the bag breakup and fiber-type atomization regimes (F). The magnitudes of We_A in the tables were chosen based on the rule that the operating conditions under each swirl number should include various types of breakup regimes. Note that we tried to ensure that all the flow cases shown in Table 3.4 should be within the fiber-type atomization regime. However, in this project, there is an experimental limit to the maximum of We_A that can be reached. Hence, for a few flow cases with $S \leq 1.2$, the operating conditions are within the bag breakup regime (see Table 3.4). Lasheras and Hopfinger (2000) pointed out that at large We_A (greater than 316), the breakup of a coaxial non-swirling air jet occurs in the forms of fibers, which produces finer droplets. This is called fiber-type atomizaion. In this work, three independent samplings of the data were collected for each operating condition shown in Table 3.3. For the flow cases shown in Table 3.3, breakup lengths, axial location of first droplet formation, large-scale, shear instabilities and air flow fields are reported and analyzed. A morphological study was performed on the operating conditions shown in Tables 3.3 and 3.4 (the morphological study is discussed in more detail in Sec. 4.1). It was found that both S and We_A determine the type of breakup regime for a laminar liquid jet in a coaxial swirling air flow (this is discussed in more detail in Sec. 4.1). Few droplets were observed when investigating the first three breakup regimes (FWI, SWI and B), and the drop sizes were large when compared with the flow cases within the fiber-type atomization regime. Many smaller droplets were produced when the liquid jet entered the fiber-type atomization regime, which implies that it was necessary to apply a different set of measurements and a different approach to analysis for the flow cases shown in Table 3.4. The drop size measurements for those flow cases shown in Table 3.4, determined using a phase Doppler particle size analyzer, will be presented in this work (this approach is discussed in more detail in Sec. 3.5). It should also be noted that U_l and U_g are the axial bulk velocities of the liquid jet and gas stream at the nozzle exit, respectively. The critical swirl number for our nozzle is equal to 0.8 (following Hopfinger and Lasheras (1996)).

3.3 Experimental Procedure

For high-speed shadowgraphy, a Phantom VEO 710L high-speed camera (Lavision Inc, Germany) acquired images of the swirling and non-swirling jets. The temperature for the fluids was $15^{\circ}C$. The air pressure was 8 bar. For the flow cases mentioned in Tables 3.3 and 3.4, the spatial resolutions were 140 $\mu\mathrm{m/pixel}$ and 119 $\mu\mathrm{m/pixel}$, respectively, and the exposure times were 10 $\mu\mathrm{s}$ and 30 $\mu\mathrm{s}$, respectively. Those spatial resolutions were based on the fact that locating the camera closer to the jet to achieve better resolution would have flooded it with water. The selected exposure times were much smaller than the time scales in the coaxial air flows, which ensures that each individual shaodowgram is an instantaneous image. As mentioned in Sec. 3.2, three independent samplings of the data were collected for each operating condition shown in Table 3.3. For all the flow cases shown in Table 3.3, the number of the images that were acquired per sampling ranged from 250 to 3800. The number of the images was chosen based on the rules that the sampling frequency should be much larger

Table 3.3: Operating conditions for the atomizer. FWI: first-wind induced; SWI: second-wind induced and B: bag breakup regime. Note that the accuracies of the gas and liquid mass flow controllers are $0.5\%RD + 0.1\%FS$ and $0.2\%RD$, respectively. Here, RD and FS represent "reading" and "full scale", respectively.

Case	$\dot{m}_g$ (kg/h)	We_A	M	S	Breakup regime	U_l (m/s)	Re_l
1	3	9	14	0	FWI	0.11	438
2	4	16	24		SWI		
3	5	25	38		B		
4	8	64	96		B		
5	10	100	150		B		
6	3	40	60	0.3	SWI		
7	6	158	237		B		
8	8	282	423		B		
9	10	440	660		B		
10	3	40	60	0.8	SWI		
11	6	158	237		B		
12	8	282	423		B		
13	10	440	660		B		
14	3	40	60	1.2	SWI		
15	5.5	133	200		B		
16	8	282	423		B		
17	10	440	660		B		
18	2	18	27	1.5	B		
19	3	40	60		B		
20	4	70	105		B		
21	5	110	165		B		
22	1.5	10	15	2.5	B		
23	1.8	14.3	21		B		
24	2	18	27		B		
25	3	40	60		B		
26	1	4	7	3.1	B		
27	1.3	7	11		B		
28	2	18	27		B		
29	3	40	60		B		
30	1	4	7	3.9	SWI		
31	2	18	27		B		
32	3	40	60		B		

Table 3.4: Operating conditions for the atomizer. B: bag breakup regime; F: fiber-type atomization and BF: boundary of fiber-type atomization. Note that the accuracies of the gas and liquid mass flow controllers are $0.5\%RD + 0.1\%FS$ and $0.2\%RD$, respectively. Here, RD and FS represent "reading" and "full scale", respectively.

Case	$\dot{m}_g$ (kg/h)	We_A	M	S	Breakup regime	U_l (m/s)	Re_l
33	16	256	384	0	B	0.11	438
34	18	324	486				
35	16	1126	1689	0.3			
36	18	1426	2139				
37	16	1126	1689	0.8	B		
38	18	1426	2139		BF		
39	16	1126	1689	1.2	B		
40	18	1426	2139		BF		
41	8	282	423	1.5	F		
42	10	440	660				
43	8	282	423	2.5			
44	10	440	660				
45	8	282	423	3.1			
46	10	440	660				
47	8	282	423	3.9			
48	10	440	660				

than the measured frequency, and that the recording time duration should be much longer than the measured period. Thresholding was applied to each image, and the first droplet locations and the breakup lengths of the liquid jets under various operation conditions were detected using image processing in Matlab. For each associated operating condition, the axial length of the largest continuous fluid structure extending from the nozzle exit was interpreted as a breakup length. Furthermore, based on the high-speed images, the interface positions were captured at many different moments in time using image processing in Matlab, and a two-dimensional FFT was performed on the data (the approach is described in more detail in Sec. 3.6.2). POD was also performed on these high-speed images, to find the dominant large-scale instability modes of the liquid jets (the approach is described in more detail in Sec. 3.6.1). The corresponding temporal frequencies of these modes were also obtained by performing FFT on the corresponding columns of the matrix $\boldsymbol{V}$ that contains the temporal patterns of the data (Brunton & Kutz, 2019).

The uncertainties of the breakup length and first droplet location data for each flow case, originating in the spatial resolution, thresholding level, and recording time duration, were evaluated. It was found that the uncertainties in the data caused by these factors are relatively small (of the order of 5%). The uncertainties in the POD data, caused by the spatial resolution and sampling frequency, were evaluated. It was found that the uncertainties of the data are relatively small (of the order of 3%). Furthermore, the periods and temporal frequencies of the large-scale instabilities are much smaller than the sampling time durations and frequencies, respectively. For the flow cases mentioned in Table 3.4, A turn-off behaviour was observed when S increases to 2.5 (this behaviour is described in more detail in Sec. 5.2). In order to study the underlying mechanisms behind the turn-off behaviours, POD was performed on the high-speed images (this approach is described in more detail in Sec. 3.6.1).

3.4 Stereoscopic Particle Image Velocimetry (SPIV)

The basic theories of SPIV are discussed in Sec. 2.1.4. Here, details of the SPIV setup are introduced. To perform SPIV, 3.5 $\mu\mathrm{m}$ graphite particles were used as the seeding material, with a Stokes number much less than 1. A seeder (Lavision Inc, Germany) was used to continuously introduce graphite particles into the air. A 10 Hz dual-pulse Nd: YAG laser (Quantel Inc.) at a wavelength of 532 nm was used to illuminate the seeding particles. Two Phantom VEO 710L cameras (Lavision Inc, Germany) with Scheimpflug mounts acquired images of the swirling and non-swirling air jets (see Fig. 3.2). The image resolution was 895 $\mathrm{pixel}\times$1283 pixel, with a spatial resolution of 12.15 $\mathrm{pixel/mm}$. The angle between the optical axes of these two cameras was 78°, as obtained via calibration in Davis 10.2 software (Lavision Inc, Germany). A negative cylinder lens was used to diverge the laser beam vertically. The laser sheet thickness at the jet center-line was 2.1 mm, as measured by a WinCamD (DataRay Inc, US). The laser sheet was aligned with the center of the nozzle exit (see Fig. 3.3). A programming timing unit (PTU, Lavision Inc, Germany) was used to synchronize the laser and the two cameras. The double-frame raw images were processed using Davis 10.2. Cross-correlation and multi-pass analysis, with reducing interrogation window size, were used to calculate 2D vector fields for each camera. For each pass, the corresponding 2D vectors from the two cameras were combined to reconstruct the 3D vectors. The corresponding 2D vector components were removed if their stereo errors were larger than 1 (the definition of the stereo error can be found in the manual of Lavision (“FlowMaster”, 2020)). After that, peak ratio ($Q > 1.5$) and median filters were applied to the 2D vector fields to remove spurious vectors. The 2D vector components (U, V) were removed by the median filter if their values did not satisfy the following rules: $U_{\mathrm{median}} - 3 \times U_{\mathrm{deviation}} < U < U_{\mathrm{median}} + 3 \times U_{\mathrm{deviation}}$ and $V_{\mathrm{median}} - 3 \times V_{\mathrm{deviation}} < V < V_{\mathrm{median}} + 3 \times V_{\mathrm{deviation}}$. The new candidates corresponding to the second, third or fourth correlation peak would be reinserted if they satisfied the rule that $U_{\mathrm{median}} - 2 \times U_{\mathrm{deviation}} < U < U_{\mathrm{median}} + 2 \times U_{\mathrm{deviation}}$ and $V_{\mathrm{median}} - 2 \times V_{\mathrm{deviation}} < V < V_{\mathrm{median}} + 2 \times V_{\mathrm{deviation}}$. For each camera, the final interrogation window size was 32 pixel × 32 pixel. The overlap ratio of the interrogation windows was 75%. Note that the basic theories of interrogation schemes are described in detail in Sec. 2.1.2. For each flow case, the time between pulses was determined by the rule that the maximum particle displacement should be less than one-fourth of the interrogation window size.

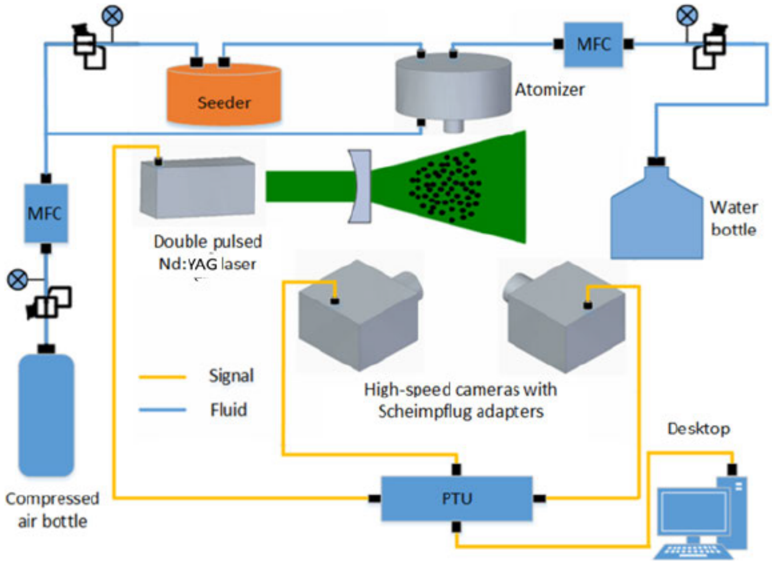

Figure 3.2: SPIV setup.

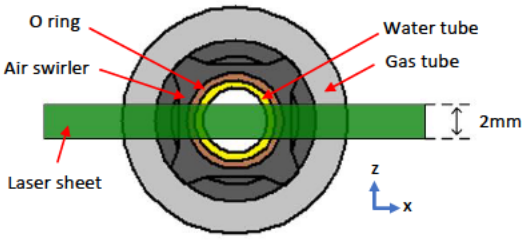

Figure 3.3: Bottom view of the nozzle exit with the laser sheet.

For the flow cases shown in Table 3.3, SPIV was used to measure the air flow fields without the presence of the central water jet. For SPIV, each camera took 100 images for each flow case. The average results were obtained using all 100 images. For most of the flow cases, after being removed by the median and peak ratio filters, the number of the source vectors at each grid to compute the average value was above 80. However, there were few high-swirl flow cases where the number of the source vectors at some grids near the nozzle exit was 55. This can be explained by the fact that the narrow air passages of the air swirlers combined with high exit velocity under high swirl numbers resulted in low particle density near the nozzle exit. The number of the source vectors at each grid for all the flow cases can be found in the database (Liang et al., 2022a).

In terms of the SPIV setup, the seeder, high-speed cameras, double pulsed Nd:YAG laser, PTU, Scheimpflug adapters, negative cylinder lens and mass flow controllers pre-existed in our lab. In this project, the equipment was set up and troubleshooting was done. The lasers were aligned with the lens. Calibration for those two cameras was done. PTU was ultilized to ensure that the laser and high-speed cameras work synchronously. Some graphite particles were purchased as the seeding material in this project.

3.5 Phase Doppler Interferometry (PDI)

For the flow cases shown in Table 3.4, a phase Doppler particle analyzer (Artium Inc, US) was used to measure the size and velocity distributions of the droplets produced by the atomizer. The basic theories of PDI are discussed in Sec. 2.3. Here, details of the PDI setup are introduced. The measurable droplet size and velocity ranges were from $1\ \mu\mathrm{m}$ to $195\ \mu\mathrm{m}$, and from $-133\ \mathrm{m/s}$ to $368\ \mathrm{m/s}$, respectively. The droplet size and velocity histograms were checked to ensure that the peaks of those histograms fell within those measurable droplet size and velocity ranges, respectively. It was found that there were few droplet size data (of the order of 2%) where the peaks of the histograms approached the lower end of the measurable range. The sprays were measured at two downstream positions; at $5D_l$ and $10D_l$, and at five radial positions of $-7.5D_l$, $-5D_l$, $-2.5D_l$, 0, $2.5D_l$, $5D_l$ and $7.5D_l$. Those measurement positions were chosen based on the rule that the PDI probes should be placed in a region between the dense zone and periphery of the spray. For each flow case, 5000 samples were collected at each measurement position. A 2-D translation stage was not available so the horizontal and vertical beams that the nozzle was mounted on were marked using a camera calibration, and the nozzle was moved by hand to change the positions of the measurement probes relative to the nozzle. The uncertainty introduced by manually moving the nozzle was evaluated and found to be between 0.5 mm and 1 mm ($\sim 5\% - 10\%$ of the radial interval between two measuring points).

The phase Doppler particle analyzer pre-existed in our lab. The laser emitter and signal receiver were set up in this project. Laser beams were aligned before the PDI measurements started.

3.6 Data Analysis Methods

As mentioned earlier, chapter 2 shows the basic theories of POD and FFT. Hence, in this subsection, how POD and 2D FFT are performed on the fluid flow data obtained from this project is discussed.

3.6.1 Proper Orthogonal Decomposition on Shadowgrams (POD)

In this work, proper orthogonal decomposition (POD) was applied to the jet shadowgrams. The corresponding MATLAB codes can be found in Appendix B. As mentioned in chapter 2, POD is a matrix factorization method and can decompose a rectangular data matrix, consisting of scalar or vector fields, into a set of rank 1 matrices, referred to as modes or principal components, ordered in terms of the data matrix covariance eigenvalues (Taira et al., 2017). When the data are a velocity field, the eigenvalues correspond to kinetic energy. POD is more generally known as principal component analysis (Strang, 2016; Taira et al., 2017). As mentioned in Sec. 2.4, the spatial POD can be determined using the singular value decomposition (SVD) (Taira et al., 2017). Spatial POD was used to analyse the shadowgram images of the jet in this work. Hence, spatial POD using the SVD is described in this section.

Each shadowgram image of the jet can be represented as a matrix $\boldsymbol{D} \in \mathbb{R}^{p \times q}$ with each entry d_{ij} corresponding to a spatial coordinate:

$$d_{ij} = k\left(\xi_i, \eta_j\right), \tag{3.7}$$

where k is a function over the spatial coordinates ξ_i and η_j. The shadowgram matrix $\boldsymbol{D}\left(t_k\right)$ for each image taken at time t_k is rearranged as a column vector $\boldsymbol{x}\left(t_k\right)$. There is no unique mapping between the image matrix $\boldsymbol{D}\left(t_k\right)$ and the image column vector $\boldsymbol{x}\left(t_k\right)$. The mapping used in the present work is given here as an example:

$$\boldsymbol{x}\left(t_k\right) = \begin{bmatrix} d_{1,1}\left(t_k\right) \\ d_{2,1}\left(t_k\right) \\ \vdots \\ d_{1,2}\left(t_k\right) \\ \vdots \\ d_{p,q}\left(t_k\right) \end{bmatrix}. \tag{3.8}$$

The set of column vectors $\boldsymbol{x}\left(t_k\right)$ forms a matrix $\boldsymbol{X}$ given by:

$$\boldsymbol{X} = \left[\boldsymbol{x}\left(t_1\right), \boldsymbol{x}\left(t_2\right), \boldsymbol{x}\left(t_3\right), \ldots, \boldsymbol{x}\left(t_m\right)\right] \in \mathbb{R}^{n \times m}, \tag{3.9}$$

where $n = p \times q$ is the number of spatial coordinates, and m is the number of the measurement times. Note that the data vectors should be placed in order of time at which each image was taken. Each row of $\boldsymbol{X}$ corresponds to a two-dimensional spatial coordinate and each column corresponds to a time. The mean value of each row of the matrix $\boldsymbol{X}$ is subtracted from $\boldsymbol{X}$ which provides the data matrix $\boldsymbol{K}(\zeta,t)$ containing the components of $\boldsymbol{X}(\zeta,t)$ which vary with time:

$$\boldsymbol{K}(\zeta,t) = \boldsymbol{X}(\zeta,t) - \overline{\boldsymbol{X}(\zeta)}, \tag{3.10}$$

where, ζ denotes the spatial coordinate and $\overline{\boldsymbol{X}(\zeta)}$ is the matrix that contains the mean value of each row of the scalar field $\boldsymbol{X}(\zeta,t)$, in each column. Note that the matrix $\boldsymbol{X}$ is written as $\boldsymbol{X}(\zeta,t)$ in equation (3.10) to emphasize that the data are collected from the two-dimensional grid at discrete moments t.

According to Strang (2019), the reduced SVD decomposition of the n by m matrix $\boldsymbol{K}$ is given by:

$$\begin{aligned}\boldsymbol{K} = \boldsymbol{U}\boldsymbol{\Sigma}\boldsymbol{V}^T = [\boldsymbol{u}_1, \boldsymbol{u}_2, \ldots, \boldsymbol{u}_r] &\begin{bmatrix} \sigma_1 & 0 & \ldots & 0 \\ 0 & \sigma_2 & \ldots & 0 \\ \vdots & \vdots & \ddots & \vdots \\ 0 & 0 & 0 & \sigma_r \end{bmatrix} \begin{bmatrix} \boldsymbol{v}_1^T \\ \boldsymbol{v}_2^T \\ \vdots \\ \boldsymbol{v}_r^T \end{bmatrix} \\ = \boldsymbol{u}_1\sigma_1\boldsymbol{v}_1^T + \boldsymbol{u}_2\sigma_2\boldsymbol{v}_2^T + \ldots + \boldsymbol{u}_r\sigma_r\boldsymbol{v}_r^T, \\ \boldsymbol{U} \in \mathbb{R}^{n \times r}, \boldsymbol{V} \in \mathbb{R}^{m \times r}, \boldsymbol{\Sigma} \in \mathbb{R}^{r \times r}, \sigma_1 \geq \sigma_2 \geq \ldots \geq \sigma_r > 0,\end{aligned} \tag{3.11}$$

where, r is the rank of the matrix $\boldsymbol{K}$, σ_i, $i = 1,2,...,r$, denote singular values, the superscript T denotes transpose, and $\boldsymbol{u}_i, \boldsymbol{v}_i$, $i = 1,2,...,r$ are called left singular vectors and right singular vectors, respectively (Strang, 2019). $\boldsymbol{u}_i$, $i = 1,2,...,r$, are also called the POD modes (Taira et al., 2017). It should be noted that the matrices $\boldsymbol{U}$ and $\boldsymbol{V}$ are orthonormal, which means that:

$$\boldsymbol{U}^T\boldsymbol{U} = \boldsymbol{V}^T\boldsymbol{V} = \boldsymbol{I}_{r \times r}, \tag{3.12}$$

where $\boldsymbol{I}$ denotes the identity matrix. Each POD mode $\boldsymbol{u}_i$ is therefore orthonormal to any other mode $\boldsymbol{u}_{j \neq i}$ and forms a linearly independent set. The same is true for $\boldsymbol{v}_i$.

The left singular vectors, or POD modes, $\boldsymbol{u}_i$ contain the spatial components of $\boldsymbol{K}$. The right singular vectors $\boldsymbol{v}_i$ contain the temporal components. Performing a Fourier transform on the matrix $\boldsymbol{V}$ obtained from SVD yields the frequency of each mode. The left singular vector $\boldsymbol{u}_i$ for each mode can be rearranged into a matrix with dimension $q \times p$, the same dimensions as the shadowgram image matrices $\boldsymbol{D}$, for visualization of the POD modes.

3.6.2 Two-dimensional Fast Fourier Transform (2D FFT)

The basic theories of FFT are introduced in Sec. 2.5.2. In this work, 2D FFT was performed on the liquid-gas interfaces to obtain the two-dimensional wave spatiotemporal spectra for the jets. The associating algorithms are described in detail in this subsection. The corresponding MATLAB codes can be found in Appendix B.

In this work, the left-hand-side air-water interface locations were captured at many different moments in time, and a two-dimensional FFT was performed on the data to obtain the temporal and spatial frequencies of the shear instabilities. The algorithm is explained as follows. For each operating condition, a group of shadowgrams was captured by the high-speed camera, and the minimum breakup length and interface locations were detected using Matlab. All the interface location data were truncated to the same length, which was equivalent to the minimum breakup length, before they were imported into a data matrix. The data matrix was organized so that each column represented the interface locations at different axial positions and a specific moment in time, while each row represented the interface locations at a fixed axial position and different moments. After that, the mean value of the data matrix was subtracted from the matrix. A 2D FFT was then performed on this data matrix to obtain the spatial and temporal frequencies of the shear instabilities on the left-hand-side air-water interfaces. The periods and temporal frequencies of the shear instabilities were much smaller than the sampling time durations and frequencies, respectively. The uncertainties of the wave spectra caused by the sampling time duration were evaluated and found to be of the order of 15%. The 2D FFT was performed only on data in which the long wave structures were sized so as to ensure that the sampling lengths were much larger than the wavelengths of the spatial signals. The spatial resolution of the images was much better than the spatial frequencies of the shear instabilities.

3.7 Issues Raised and Solved during this Project

There were some challenges associated with the SPIV measurements. First, the laser sheet thickness should lie in the range of the depth of field of cameras so that particles are in focus. Furthermore, the laser sheet thickness was related to how fast the measured flow fields were. Based on my calculation and the results of the preliminary SPIV measurements, my laser sheet thickness was on the order of 2.1 mm. Second, there was a time delay between the trigger signal and laser emission. A photodiode and an oscilloscope were utilized to measure that time delay. I set that time delay in PTU to ensure that the laser and high-speed cameras worked synchronously. I checked the timing graph both on the software (Davis 10.2) and an oscilloscope. Third, the laser intensity within the sheet should be as uniform as possible. I used a WinCamD (DataRay Inc, US) to check laser sheet profile. Fourth, an appropriate seeding density is very important for getting good PIV data. I varied the seeding density by adjusting the pressure regulator of the seeder. Fifth, I used as much of the camera chip as possible. I magnified the images as more as possible. Sixth, if the particles started to clog the nozzle, I was able to see few particles coming out from the nozzle exit. In this case, I needed to reduce the particle density.

When I changed measurement techniques, some associating Swagelok fittings should be changed. For SPIV, in order to introduce graphite particles into air flows, a hole was drilled on the gas lid. Preliminary measurements should be done so that I know the ranges of periods and frequencies of the measured characteristics. I needed to make sure that the sampling frequency and period should be much larger than the measured ones.

Chapter 4

Spray Morphology, Breakup Length, Axial location of first droplet formation, large-scale, shear instabilities and air flow field

In this chapter, spray morphology, breakup lengths, axial location of first droplet formation, large-scale, shear instabilities and air flow fields are reported and analyzed.

4.1 Morphological Study

Four breakup regimes were observed over a wide range of operating conditions. They are first-wind induced, second-wind induced, bag breakup and fiber-type atomization regimes. As mentioned in Sec. 1.1, when a liquid jet enters the first-wind induced breakup regimes, dilatational waves can be observed on the liquid-gas interface Reitz (1978). When a liquid jet falls within the second-wind induced breakup regime, a sinuous wave can be observed on the liquid-gas interface and ligaments appear. When a liquid jet enters the bag breakup regime, liquid structures with bag shapes can be observed within the liquid core or on the liquid-gas interface Lasheras and Hopfinger (2000). Lasheras and Hopfinger (2000) pointed out that at large We_A (greater than 316), the breakup of a coaxial non-swirling air jet occurs in the forms of fibers, which produces finer droplets. This is called fiber-type atomizaion. Fig. 4.1 shows example images of the flow cases and they illustrate these four typical breakup regimes. Note that these images were produced by applying background subtraction to the high-speed shadowgrams.

As mentioned in chapter 1, Hopfinger and Lasheras (1996) and Dunand et al. (2005) observed hollow-cone sprays, which are formed by strong reversal air flows, when S goes beyond S_{cr}. Kumar and Sahu (2019) observed hollow-cone sprays with high momentum ratios as well. However, in the present study, the hollow-cone spray structure does not appear in the flow cases where S goes beyond S_{cr} or where high M is achieved. This can be explained on the basis of the low kinetic energy that the central laminar liquid jet contains. The kinetic energy of the central laminar liquid jet in this present study is much smaller than the kinetic energy of the central turbulent liquid jets that Hopfinger and Lasheras (1996), Dunand et al. (2005), and Kumar and Sahu (2019) investigated. The hollow-cone spray structure indicates the interaction between the upward air flow motion towards the nozzle exit and the downward water jet motion. An equilibrium among the static pressure, the kinetic energy of the liquid jet and gas flow, and the ambient pressure should be achieved to sustain the hollow-cone spray structure (Hopfinger & Lasheras, 1996). However, in this present study, the kinetic energy inside the water jet is not high enough to fulfil the requirement, and as a result the upward air flows break the liquid jet directly into fibres instead (see Fig. 4.1d).

Fig. 4.2 contains a regime map for the flow conditions listed in both Tables 3.3 and 3.4, characterised by S and We_A. For high swirling flow cases with S ranging from 1.5 to 3.9, as the aerodynamic Weber number increases, the laminar liquid jet passes through the first-wind induced breakup regime, second-wind induced breakup regime, bag breakup regime and finally it falls within the fiber-type breakup regime. These four breakup regimes observed in this present study are consistent with what Lasheras and Hopfinger (2000) found when they investigated a coaxial non-swirling jet. Note that for S in the range of $0.3-0.8$, the liquid jet falls within the boundary of the fiber type atomization when We_A increases to 1426. This indicates that with a further increase in We_A the fiber-type regime might control breakup of the liquid jet. As the swirl number increases from 1.2 to 2.5, the aerodynamic Weber numbers corresponding to the start of the bag and fiber-type breakup regimes reduce significantly (see Fig. 4.2). With a further increase in swirl number the boundaries do not change significantly. This indicates that air swirl promotes the morphological development of the jets, especially for the high swirling flow cases with S in the range of $1.2-2.5$. Note that for the non-swirling flow cases, the highest We_A that the atomizer can reach is 324, where bag breakup was observed. Lasheras and Hopfinger (2000) found that further increases in We_A make the coaxial non-swirling jet enter the fiber-type breakup regime. A Bayesian analysis can provide the rigorous boundaries for the different breakup regimes and transitions illustrated in Fig. 4.2, which is suggested as future work.

4.2 Breakup Length and First Droplet Location

The influence of aerodynamic forces, including the effect of air swirl on the breakup lengths and first droplet locations, is investigated here. Figs. 4.3 and 4.4 show the relationships between the normalized breakup length (L/D_l) and the aerodynamic Weber numbers and swirl numbers. Fig. 4.5 illustrates the relationships between the normalized first droplet location (Y/D_l) and the aerodynamic Weber numbers and swirl numbers. The first droplet location (Y) refers to the axial distance between the first droplet separation and the nozzle exit. Note that the central line of each box indicates the median. The top and bottom edges of each box represent 25th and

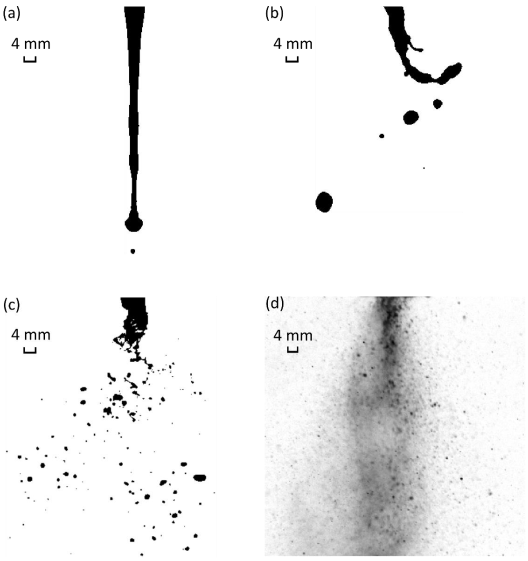

Figure 4.1: (a) First-wind induced breakup regime ($S = 0$, $We_A = 9$). (b) Second-wind induced breakup regime ($S = 1.2$, $We_A = 40$). (c) Bag breakup regime ($S = 0.8$, $We_A = 158$). (d) Fiber-type atomization ($S = 2.5$, $We_A = 440$).

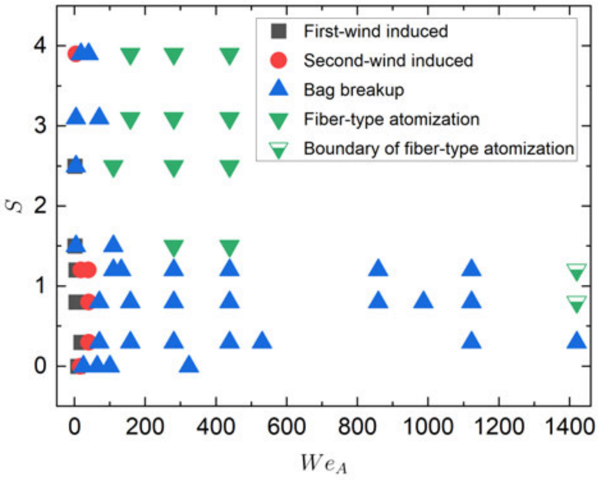

Figure 4.2: Regime map characterised by S and We_A.

75^{th} percentiles, respectively. Whiskers in the plot extend to the most extreme points. If sample values are more than 1.5 times the interquartile range away from the bottom or top edges of the boxes, they will be considered as “outliers” and will be plotted using plus symbols. For each box plot shown in Figs. 4.3, 4.4 and 4.5, the ratio of the number of "outliers" to the overall number of samples falls within the range of $\sim 0.4\% - 6.7\%$. When the aerodynamic Weber number increases, the medians of breakup lengths and the axial distances for the first droplet separation reduce. This can be explained on the basis of the increase in shear stress acting on the water-air interface, which leads to a more significant destabilization of the liquid jet. The addition of the swirling annular gas stream has a significant effect on reducing the breakup length of the liquid jet and axial distance for the first droplet separation, which indicates that the swirling annular air stream destabilizes the liquid jet more significantly compared with non-swirling annular air stream. During image processing, the largest continuous fluid structure extending from the nozzle exit is considered as a breakup length. The statistical distributions of breakup lengths obtained from the numerical calculation can be compared with the results shown in Figs. 4.3 and 4.4.

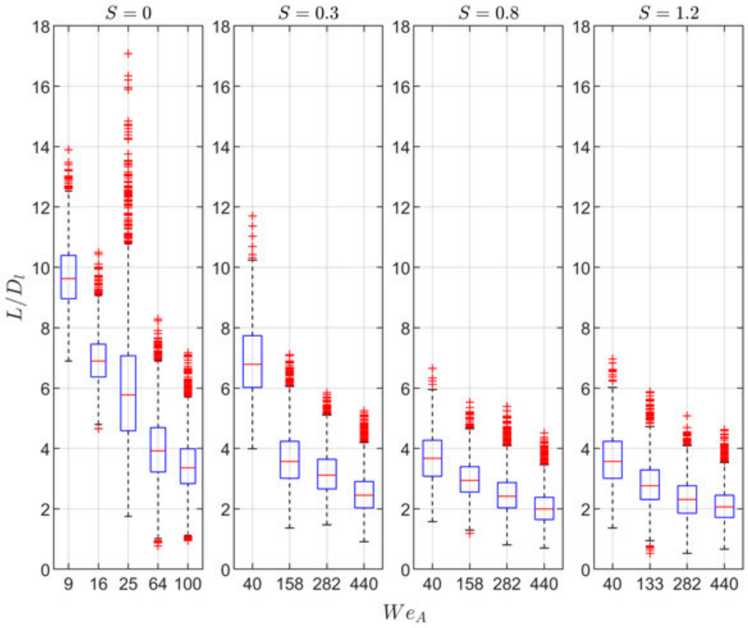

Figure 4.3: L/D_l vs We_A for S in the range of $0 - 1.2$. Note that the central line of each box indicates the median. The top and bottom edges of each box represent 25^{th} and 75^{th} percentiles, respectively. Whiskers in the plot extend to the most extreme points. If sample values are more than 1.5 times the interquartile range away from the bottom or top edges of the boxes, they will be considered as “outliers” and will be plotted using plus symbols. For each box plot shown in Figs. 4.3, 4.4 and 4.5, the ratio of the number of "outliers" to the overall number of samples falls within the range of $\sim 0.4\% - 6.7\%$.

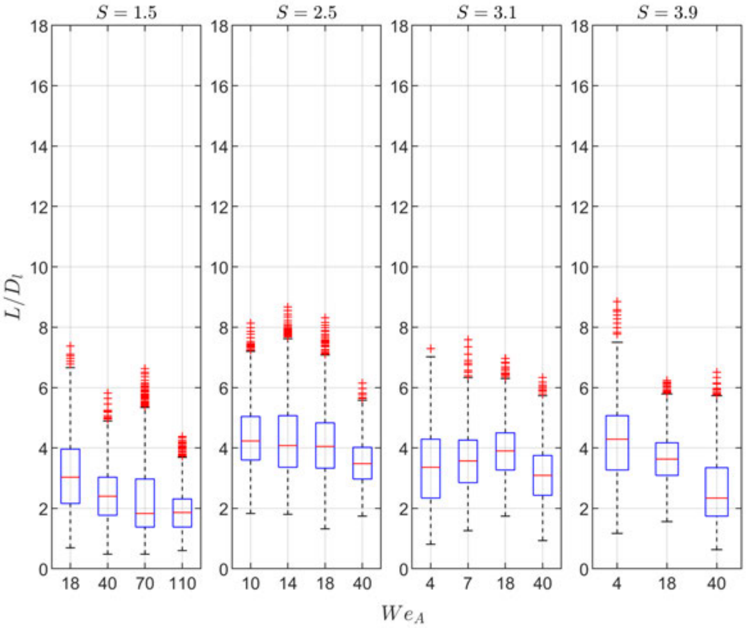

Figure 4.4: L/D_l vs We_A for S in the range of $1.5-3.9$.

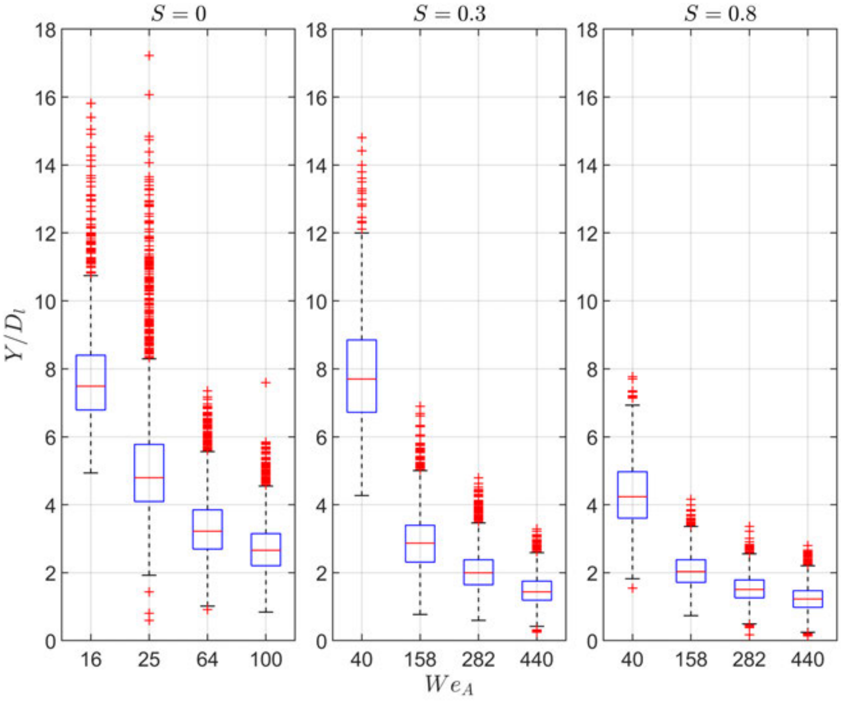

Figure 4.5: Y/D_l vs We_A for various swirl numbers.

For the high swirling flow cases with S ranging from 1.2 to 3.9, one can observe from the high-speed shadowgraphy that after the droplets are generated, they are blown upwards to the positions near the nozzle exit and then are blown sideways by the annular swirling air jet. The upwards motion of the droplets is caused by the central reversal air flows, which is demonstrated by SPIV and is discussed in Sec. 4.3. For the high swirling flow cases with $S = 3.9$ and $We_A \leq 17$, the upwards motion of the droplets does not happen. This might be because less interaction between the water jet and the annular swirling air jet happens as S goes up, and the low We_A for these flow cases might result in the weak air flows. The central reversal air flows do not happen for the low swirling flow cases with S ranging from 0.3 to 0.8. The first droplet measurements are only performed for the flow cases with S ranging from 0 to 0.8 because the first droplet location becomes ambiguous if drops are moving upwards.

Note that the optimum recording time duration and thresholding level were evaluated for each operating condition. The uncertainties of the non-dimensional breakup lengths and first droplet locations caused by the recording time duration and thresholding level were evaluated for each flow case and found to be small ($\sim$5%) (see Fig. 4.6 and Fig. 4.7). According to the Nyquist–Shannon sampling theorem, the minimum droplet size is specified as three pixels, which means that the droplets with sizes larger than 2 pixels are detected. The uncertainty of the first droplet locations caused by the smallest droplet size specified in the Matlab code is evaluated for each flow case and found to be small ($\sim$6%) (see Fig. 4.8).

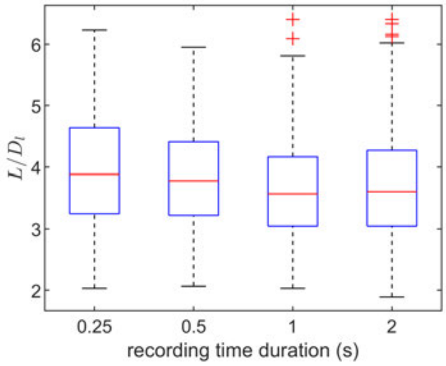

Figure 4.6: L/D_l vs recording time duration for case 10 ($S = 0.8$, $We_A = 40$).

Eroglu et al. (1991) ejected a central water jet inside a non-swirling coaxial air jet with the liquid Reynolds numbers ranging from 1097 to 9328. With the same aerodynamic Weber number, the mean values of the breakup lengths for the water jet that they studied are longer than the ones detected in the present study. This is because their liquid Reynolds numbers are higher than in this work. The breakup length of a liquid jet in a coaxial gas jet is proportional to the axial velocity of the liquid jet at the nozzle exit (Villermaux, 1998). Kumar and Sahu (2018a) investigated the breakup length of a turbulent liquid jet in a co-annular non-swirling air jet with the momentum flux ratios ranging from 1 to 8. With the same momentum flux ratio the

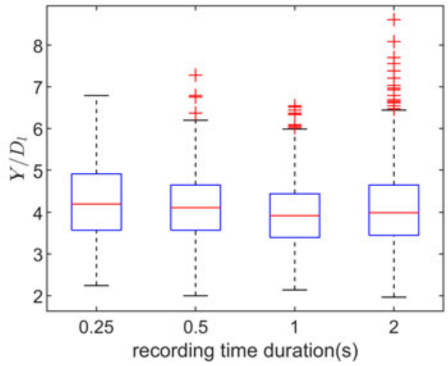

Figure 4.7: Y/D_l vs recording time duration for case 10 ($S = 0.8,\ We_A = 40$).

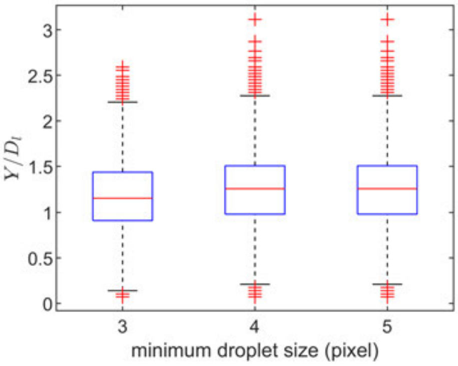

Figure 4.8: Y/D_l vs minimum droplet size for case 13.

mean breakup lengths that Kumar and Sahu (2018a) detected are much smaller than the ones measured in this project. With the same momentum flux ratio, the aerodynamic Weber numbers in the literature are much larger than the ones used in the present work, which indicates that different breakup regimes might control breakup of the liquid jet with the same momentum flux ratio for Kumar and Sahu (2018a) and this study. Dumouchel (2008) and Lasheras and Hopfinger (2000) found that a complete regime map of a coaxial liquid-gas jet should be based at least on the momentum flux ratio, liquid Reynolds number and aerodynamic Weber number. Kumar and Sahu (2018b) measured the breakup length of a central turbulent water jet surrounded by a co-annular air flow with and without swirl over a wide range of aerodynamic Weber numbers $We_A(80-300)$, momentum ratios, $M(1-8)$, and swirl numbers, $S(0-0.8)$. They found that the breakup length decreases as We_A and S goes up, which is consistent with the results shown in this project.

4.3 Non-swirling and Swirling Air Flow Fields

The influence of air swirl on the air flow field is investigated here. During this SPIV campaign, the liquid jet was not flowing so that the air structures very near the outlet could be probed. The liquid injector was left in place. This section thus describes exclusively the air flow field introduced by the air passages. SPIV was performed on all the swirling cases except $S = 3.1$ and 3.9, where the seeding particles clogged the small passages of the air swirlers. The topologies of the air flow fields for S ranging from 0 to 2.5 are discussed first in this section. Note that we discuss flows with specific We_A in the following section, despite the fact that the liquid was not flowing. By this we mean to designate the air flows used to create a specific We_A. Since, when flowing, the liquid jet flow rate was not changed, it is the air flow rate that sets We_A.

Fig. 4.9 shows selected projections of the 3D vector fields onto the 2D planes for different swirl numbers. The data in the images represent averages. Additional flow cases, together with the corresponding fluctuating components, are provided by Liang et al. (2022a). Different colorbars are used in the subplots to emphasize the topology of the air flow field. The origin of the coordinate system is located at the center of the nozzle exit. For the non-swirling flow case, the annular air flows in the axial direction after leaving the nozzle, which leaves a central dark region with nearly zero velocity right below the water tube. The annular air flows for $We_A = 9$ start to converge at the downstream position of $1.5D_l$. As We_A goes up, the convergence of the annular air flow occurs slightly closer to the nozzle exit. The annular air flows start to converge $1.4D_l$ downstream when We_A increases to 100. For the swirling flow cases, the air flows start to expand radially after they leave the nozzle, as expected. The extent of the expansion becomes larger as S goes up, which would be expected to affect the evolution of the shear layers in the coaxial swirling air-water jets. When S remains constant, the extent of the radial expansion of the annular swirling air flows does not change when We_A varies, which indicates that S determines the extent of the expansion. As mentioned in Sec. 1.2, Rajamanickam and Saptarshi (2017b) utilised PIV to measure the coaxial swirling air flow fields with $S = 0.8$. They found that in the absence of droplets, the topologies of the air flow fields are the same for $S = 0.8$, irrespective of air flow rates, which is consistent with what the present work found. Note that the velocity maxima in the subplots for the swirling flow cases are different and lower than the non-swirling flow case. This occurs because the flow cross sectional area expands right at the exit, and the expansion increases with S.

The velocity data collected at the downstream positions of $0.27D_l$ and $0.43D_l$ were substituted into Eq. 3.5, respectively, to calculate the measured swirl number. It was found that the swirl numbers calculated from those two data sets were consistent with each other. The differences between the measured and geometrical swirl numbers range from 48% to 66% (see Table 3.2 in Sec. 3.2). The air swirl strength dissipated somewhat after very little displacement downstream, i.e. where the measurement was taken. The ideal case would be to collect the velocity data at the nozzle exit to calculate the measured swirl number. However, since the flow was highly three-dimensional and the air passages of the air swirlers were narrow compared with the cross-sectional area of the co-flow tube, low graphite particle density was observed at the nozzle exit, which made it difficult to measure the air flow fields at the nozzle exit. It is also true that Eq. 3.6 is a fairly simplified design guideline. For simplicity, the term "swirl number" mentioned throughout the sections of this work refers to the "geometrical swirl number" and is used to describe the operating conditions of the atomizer.

Fig. 4.10 shows the relationship between the magnitude of the 3-D velocity and the radial position (X). Note that the data are collected at the axial position of 0.6D_l downstream. For each velocity profile, there are two peaks, one at each side of the central axis of the nozzle, and these peaks start to move outward significantly when S goes above 0.8. When S increases from 0.8 to 2.5, the locations of the peaks move from $X = 4.6$ mm (or -3.3 mm) to $X = 8.6$ mm (or -8.6 mm). This can be explained by the fact that the annular air flows expand further in the radial direction when S increases. The velocity profiles reach a local minimum (< 4 m/s) on the central axis of the nozzle ($X = 0$ mm). The magnitude of the velocity decreases to zero on the boundary between the annular air flow and the ambient, stagnant air.

Fig. 4.11 shows the relationship between the axial velocity and the radial position. The reversal flows start to appear near the central axis when S increases to 1.2. This can explain why the droplets that are located near the nozzle exit move upwards in the high-speed shadowgrams of the high swirling flow cases ($S \geq 1.2$). A further increase in S results in significant expansion of the central reversal air flow region.

Fig. 4.12 contains the radial profiles of the velocities in the out-of-plane direction (W) at the axial position of 0.6D_l downstream. For each velocity profile, W reaches its maximum and minimum at the right and left sides of the central axis of the nozzle, respectively. The radial locations that W reaches its maximum and minimum move outward when S goes up. They grow from $X = 4$ mm (or $X = -3.3$ mm) to $X = 8.6$ mm (or $X = -8.6$ mm) when S increases from 0.3 to 2.5. This means that the region where the significant out-of-plane motion of the swirling air can be observed expands further when S goes up. This is consistent with the development of the two-dimensional topologies of the air flow fields as S varies, which is mentioned above.

Fig. 4.13 shows the evolution of the inner and outer shear layers for various swirl numbers, based on vorticity maps. Note that a shear layer is defined as the layer where the velocity gradient starts. One can see that there are two inner shear layers (ISL) and two outer shear layers (OSL) in each subplot. For simplicity, one ISL and one OSL are marked in each subplot because the vorticity maps are symmetric. An increase in S results in a shift of the marked shear layers towards the upper-left corner of the image. That is caused by the fact that an

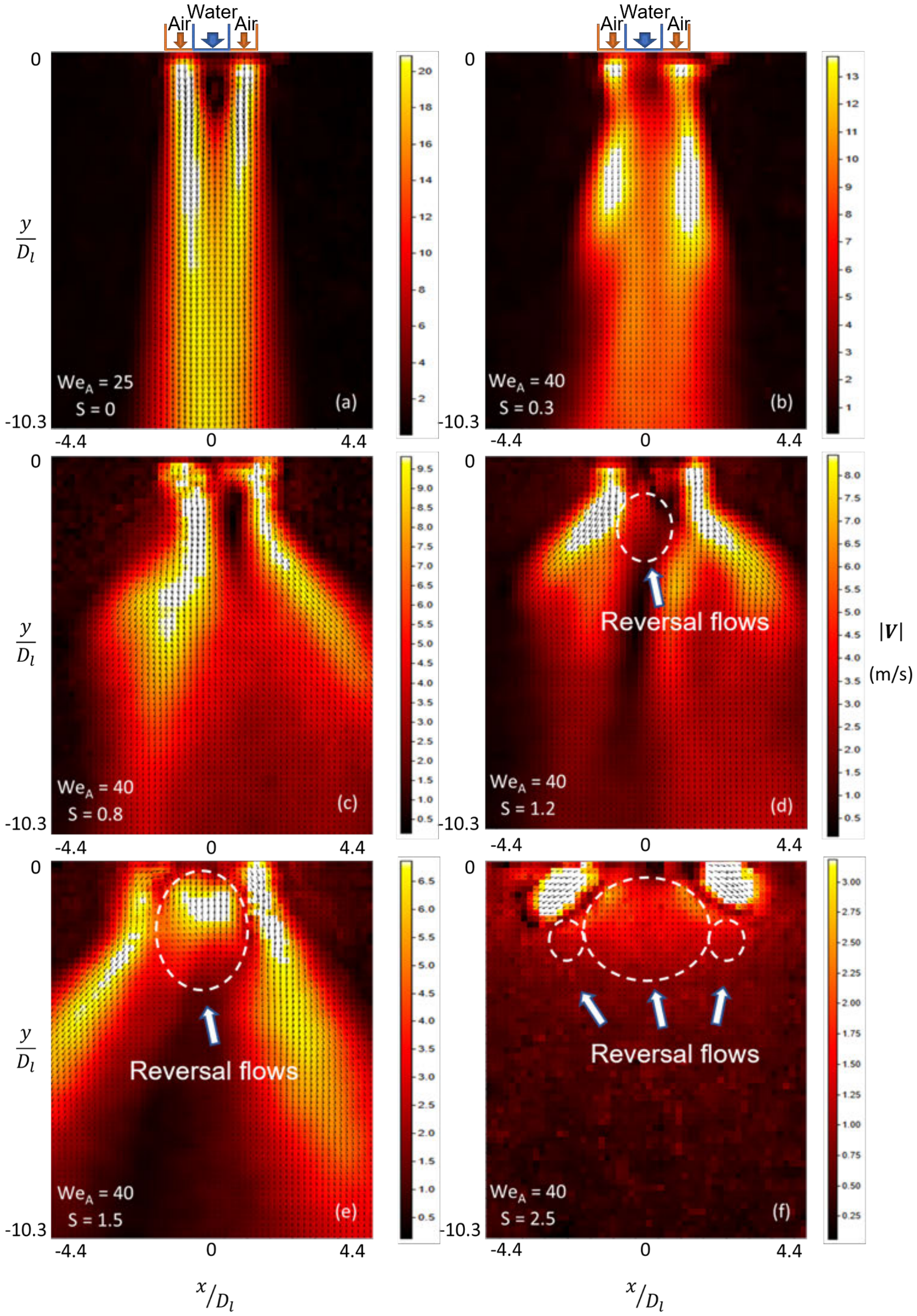

Figure 4.9: 3D vector fields projected onto the 2D planes for various swirl numbers. Note that the nozzle exits are shown on top of Figs. 4.9a and 4.9b. All the subplots have the same field of view. Reversal flow regions are highlighted in the associated subplots.

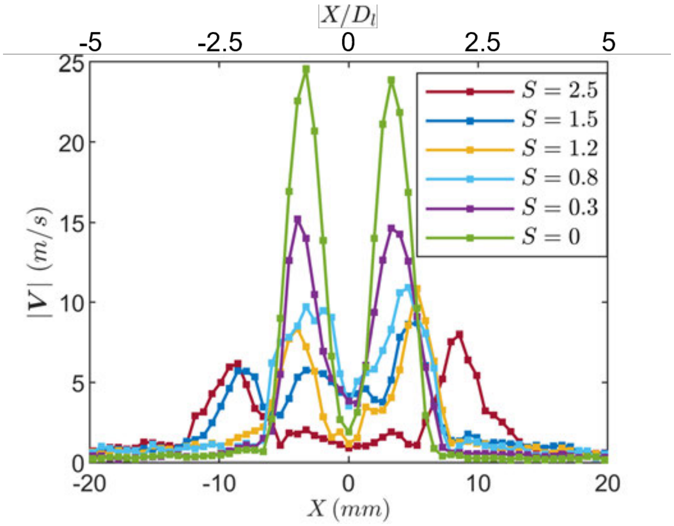

Figure 4.10: $|\boldsymbol{V}|$ vs X for various swirl numbers at $y = 0.6D_l$. $We_A = 40$ for $S \neq 0$; $We_A = 25$ for $S = 0$.

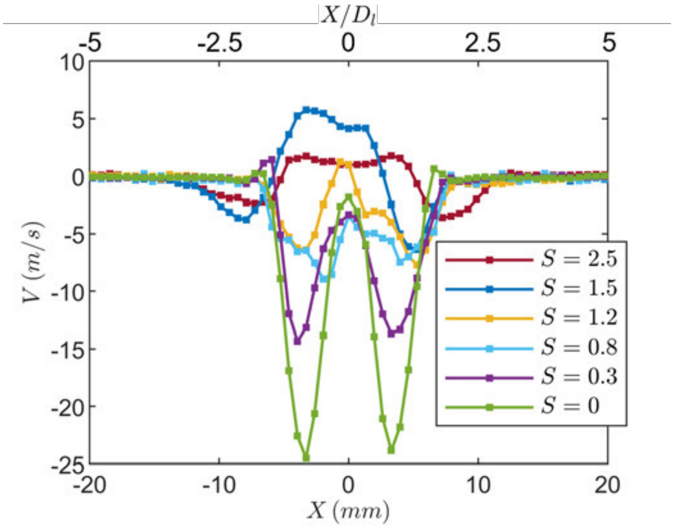

Figure 4.11: V vs X for various swirl numbers at $y = 0.6D_l$. $We_A = 40$ for $S \neq 0$; $We_A = 25$ for $S = 0$.

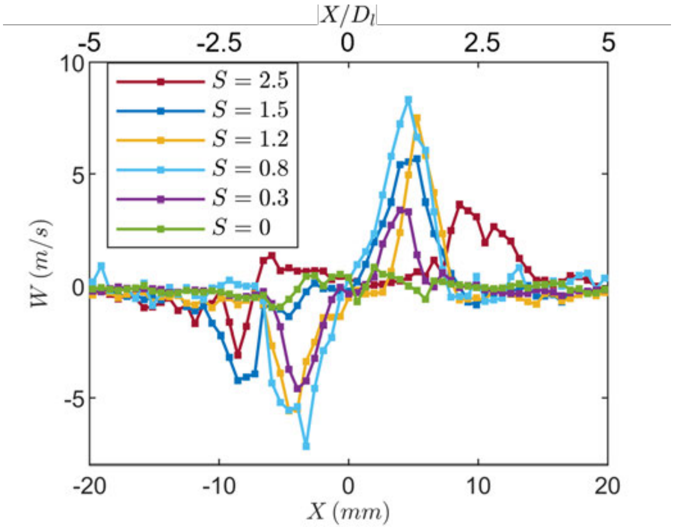

Figure 4.12: W vs X for various swirl numbers at $y = 0.6D_l$. $We_A = 40$ for $S \neq 0$; $We_A = 25$ for $S = 0$.

increase in S leads to further expansion of the annular swirling air flows, as mentioned above. When S remains constant, the locations of the shear layers do not change significantly as We_A is varied. This can be explained by the fact that S determines the extent of expansion of the annular swirling air flows, as mentioned above.

4.4 Spatial and Temporal Features of Large-scale Instabilities

The effect of aerodynamic forces and the strength of the air swirl on spatial and temporal features of the large-scale instabilities is investigated here. POD was performed on the high-speed shadowgrams for all the flow cases, to find the dominant large-scale instability modes of the liquid jets. Fig. 4.14 shows the topologies of the different types of the large-scale instabilities depicted by various POD modes for the flow cases with different swirl numbers and the same We_A. For each subplot, the values are normalized by their respective maxima. As shown in Fig. 4.14, the dominant breakup modes for all the flow cases are flapping modes, which are depicted by the first POD mode. This mode is characterised by the flapping tail end of the liquid jet. The wavy breakup modes, which are characterised by the bending/twisting of the liquid jet before it experiences breakup, appear as the secondary breakup mode for $S = 0.3$ and $S = 0.8$. The explosive breakup modes, which are characterised by the hollow-cone spray structure, appear as the secondary breakup mode for $S = 0$ and $S = 1.2$.

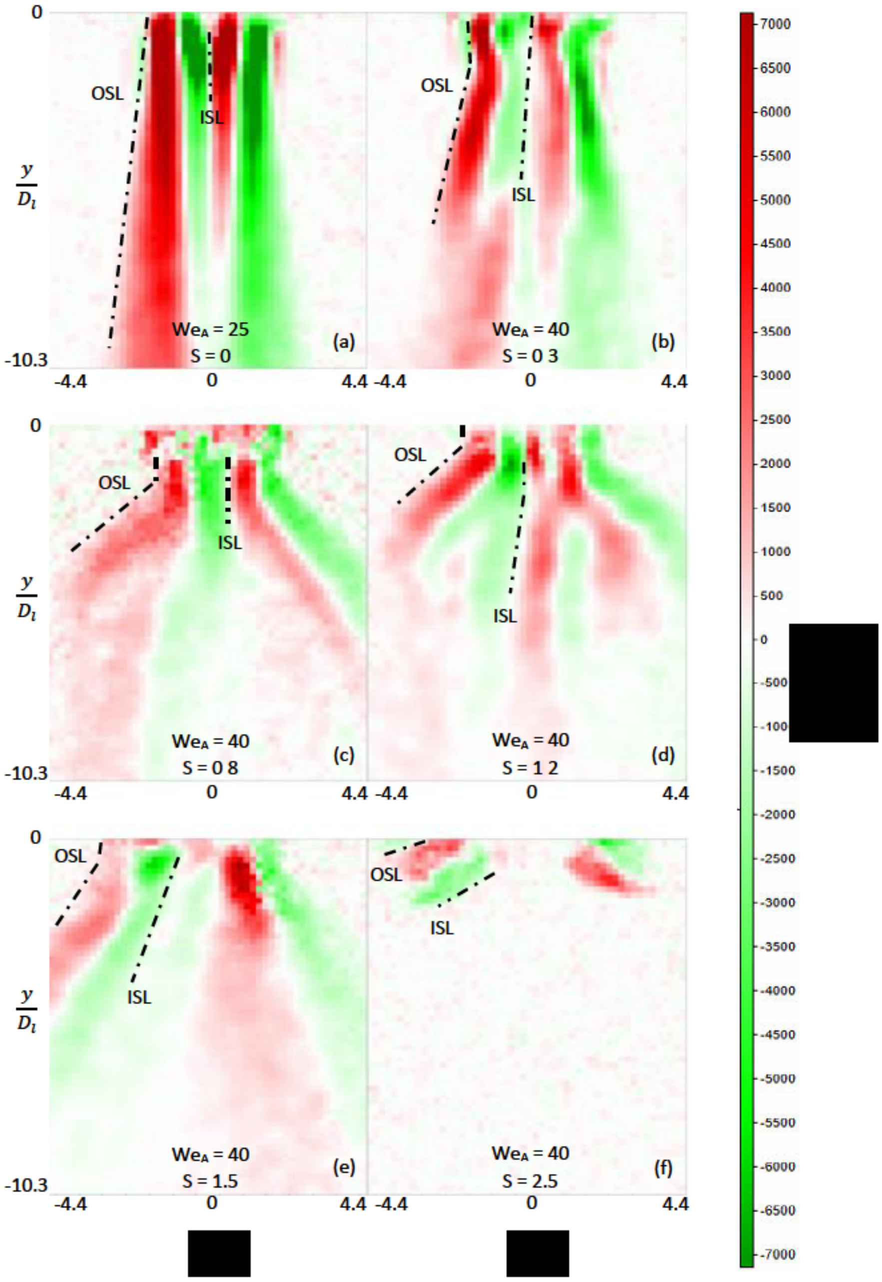

[redacted]

[redacted]

[redacted]

Figure 4.13: Vorticity maps for various swirl numbers. OSL: outer shear layer; ISL: inner shear layer. Note that these vorticity maps were extracted from the same frames as Fig. 4.9.

Generally, the singular value distribution of a principal component is used to evaluate how important that principal component is among all the principal components. The singular value distribution (ε_i) of a principal component is given by:

$$\varepsilon_i = \frac{\lambda_i}{\sum_{j=1}^{j=r} \lambda_j}, i \geq 1, \tag{4.1}$$

where λ_i is the singular value for that principal component, and r is total number of non-zero singular values and the rank of $\boldsymbol{K}$ in Eq. 3.10. Fig. 4.15 shows the singular value distributions for the flapping modes as a function of We_A (or, alternatively, M). Note that all the flapping modes in Fig. 4.15 are depicted by the first POD mode, and $\varepsilon_{\text{flap}}$ is the median of the multiple samplings for each flow case. It can be seen that $\varepsilon_{\text{flap}}$ decreases as We_A grows, which implies that further increases in We_A may change the topology of the first POD mode.

Figs. 4.16 and 4.17 illustrate the large-scale instability regime maps characterised by the swirl number and aerodynamic Weber number (or, alternatively, M). For each flow case, a data point for a certain operating condition is considered on the boundary if only one sampling of the POD data shows clear instability. If there is no evidence for clear instability, it will be assumed to have no clear mode. If there are more than one sampling with evidence for instability, the instability will be plotted. Fig. 4.16 indicates that the flapping instabilities dominate across all the flow cases. Apart from the flapping instability, Kumar and Sahu (2019) observed an explosive breakup mode when they investigated the breakup of a central turbulent water jet by a co-annular air jet with and without swirl. They found that the dominant breakup mode changes from the flapping mode to the explosive breakup mode when the momentum ratio is high (~26). In the present study, however, for some flow cases with momentum ratios in the range of $\sim 15-660$, the explosive breakup modes appear as a secondary breakup mode rather than a dominant breakup mode (see Fig. 4.17). This can be explained on the basis of the low kinetic energy that the central laminar liquid jet contains, as discussed in Sec. 4.1. Kumar and Sahu (2019) also observed the wavy breakup mode, and they found that wavy breakup mode appears as the secondary breakup mode when the momentum ratio falls within the range of $\sim 1-5$. They also found that further increases in M make the secondary breakup mode change from wavy breakup mode to explosive breakup mode, and the explosive breakup mode subsequently changes to flapping mode when the momentum ratio is high (~26). Fig. 4.17 illustrates that the wavy, explosive and flapping breakup modes appear as the secondary breakup mode over a wide range of operating conditions in this study. The wavy and explosive breakup modes happen when We_A is low (≤ 110). The flapping breakup modes appear for $S = 0.8$ with high We_A in the range of $\sim 282-440$, and for $S = 0$ with We_A of the order of 324.

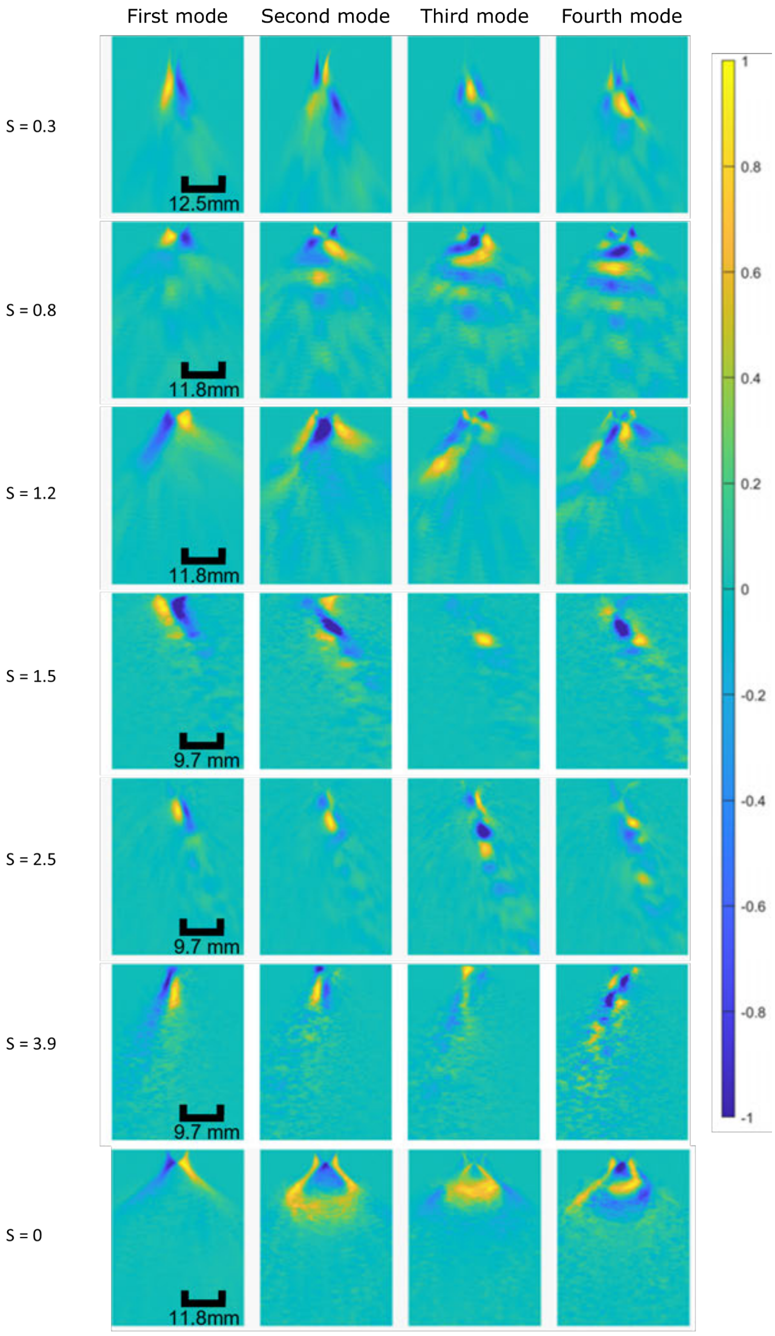

Figure 4.14: First four POD modes for swirling flow cases with different swirl numbers and $We_A = 40$, and for non-swirling flow case with $We_A = 25$. The scale bars are shown for all the operating conditions. Note that under the same operating condition, the images showing the associated POD modes have the same scale.

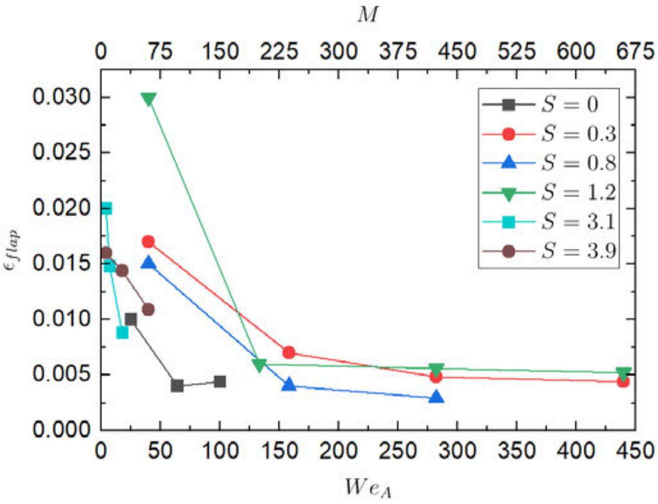

Figure 4.15: Singular value distributions for the flapping modes depicted by the first principal component.

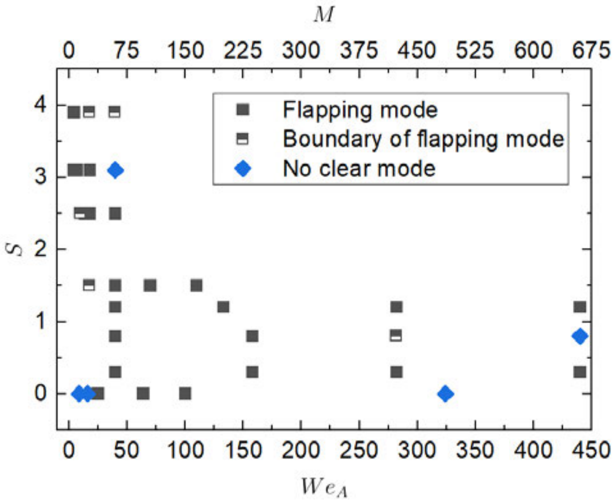

Figure 4.16: Dominant breakup mode depicted by the first principal component.

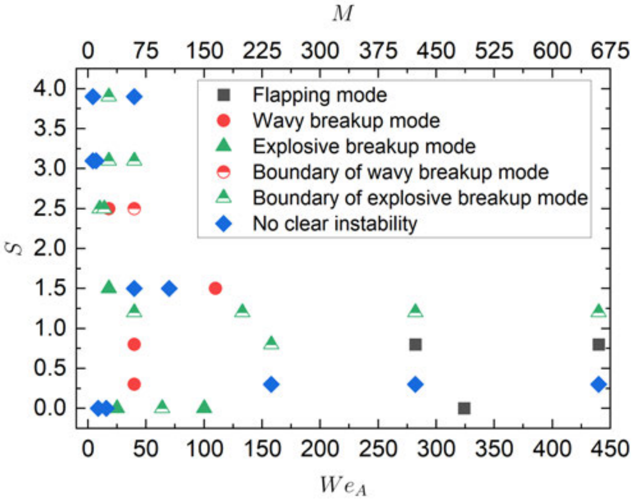

Figure 4.17: Secondary breakup modes depicted by the second principal component.

How the aerodynamic forces and the strength of the air swirl influence the frequency of the flapping instability is investigated next. Performing a fast Fourier transform (FFT) on the first column of the matrix $\boldsymbol{V}$ obtained from SVD yields the frequency of the first POD mode (Eq. 3.10). Fig. 4.18 illustrates the relationships between the frequencies of the flapping instabilities and aerodynamic Weber numbers/swirl numbers. Note that each data point in Fig. 4.18 represents the flapping instability, which is depicted by the first principal component. For the non-swirling and low swirling flow cases $(0 \leq S \leq 0.8)$, the frequency of the flapping instability increases as We_A grows, which indicates that the growth of the aerodynamic forces destabilizes the liquid jet more significantly without the presence of the central reversal air flows. For flow cases with S in the range of $\sim 0.3-0.8$, an increase in S results in the growth of f_{flap}, which indicates that the growth of the strength of the air swirl enhances the flapping instability when there are no central reversal air flows. This effect is stronger especially for the flow cases with medium aerodynamic Weber numbers $(158 \leq We_A \leq 282)$. Note that the data for the high swirling flow cases $(1.5 \leq S \leq 3.9)$ are included in the grey zone. As mentioned in Sec. 4.3, the central reversal flows happen when S falls within the range of $\sim 1.2-3.9$. For the high swirling flow cases with We_A's in the range of $\sim 4-133$, f_{flap} remains steadily below 37 Hz. The frequencies of the flapping instabilities for the high swirling flow cases are smaller than those for the low swirling flow cases, which indicates that the central reversal flows inhibit the flapping instability. For the high swirling flow cases, an increase in S reduces the frequency of the flapping instability. The reason behind this is that for the high swirling flow cases, after the annular swirling air flows leave the nozzle exit, the extent of the radial expansion is larger than for the low swirling flow cases. An increase of S causes further radial expansion of the annular swirling air flows, leading to weaker interaction between the central water jet and the annular swirling air jet, inhibiting the flapping instability.

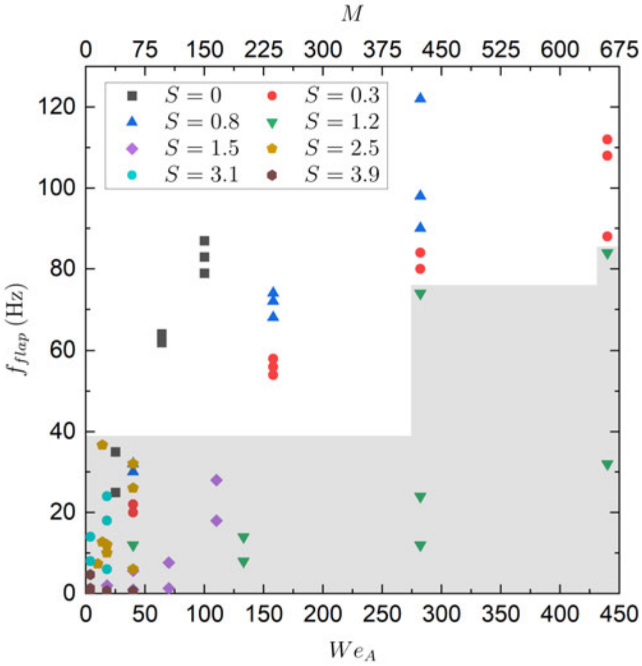

Figure 4.18: f_{flap} vs We_A for various swirl numbers. The data for the high swirling flow cases ($1.5 \leq S \leq 3.9$) are included in the grey zone.

4.5 Spatial and Temporal Frequencies of Shear Instabilities

In order to investigate how the aerodynamic forces and air swirl influence the shear instabilities on the air-water interfaces, the left-hand-side air-water interface positions were captured at many different moments in time, and a two-dimensional FFT was performed on the data to obtain the temporal (f_t) and spatial (f_x) frequencies of the shear instabilities. These temporal and spatial frequencies were detected in the cases 3, 6, 10, 14 and 30 (see Fig. 4.19 and Fig. 4.20). This was as expected because the long wave structures were observed in the high-speed shadowgrams for these five flow cases. There are no clear temporal and spatial frequencies for the rest of the flow cases. For the non-swirling flow cases with $We_A \leq 16$, long wave structures are observed, but there are no clear temporal and spatial frequencies for these flow cases. This can be explained by the fact that the wave structures in the high-speed shadowgrams for those non-swirling flow cases have much lower amplitude than the wave structures observed in the cases 3, 6, 10, 14 and 30. However, for the case 3 ($S = 0$ and $We_A = 25$), the flapping instability starts to appear, which increases the amplitudes of the long wave structures to some extent (see Fig. 4.16). This might account for the temporal and spatial frequencies that were observed in the case 3. Further increases in We_A with $S = 0$ decrease the breakup lengths, which shortens the wave structures. This results in the absence of clear temporal and spatial frequencies for the cases 4 and 5. For the low swirling flow cases ($0 < S \leq 0.8$), $|f_t|$ increases as S goes up, which indicates that an increase in the strength of the air swirl increases the temporal frequency of the shear instability. However, the temporal

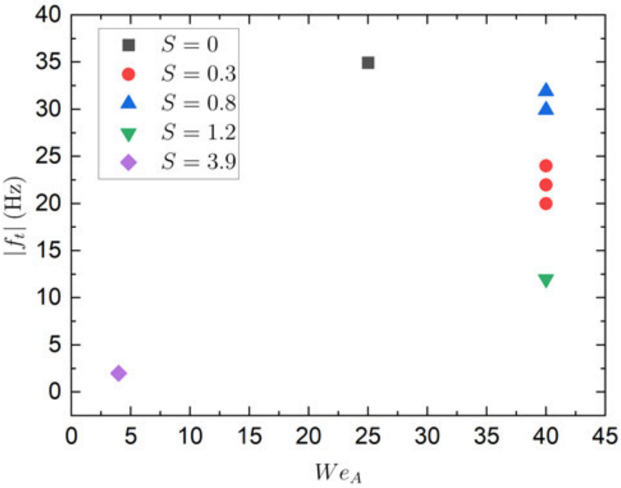

Figure 4.19: Temporal frequency $|f_t|$ vs We_A for the cases 3, 6, 10, 14 and 30.

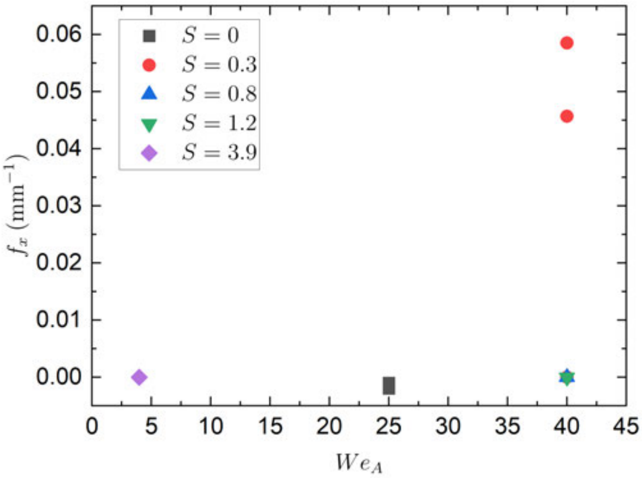

Figure 4.20: Spatial frequency f_x vs We_A for the cases 3, 6, 10, 14 and 30.

frequency of the instability reduces significantly when S increases to 1.2. The reason behind this is that the reversal flows starts to appear when $S \geq 1.2$, as mentioned in Sec. 4.3, and the reversal flows tend to stabilize the air-water interfaces. A further increase in S from 1.2 to 3.9 makes $|f_t|$ drop to 2 Hz. The spatial frequencies remain low ($\leq 0.06\ \mathrm{mm}^{-1}$) for the cases 3, 6, 10, 14 and 30.

Chapter 5

Turn-off Behaviour and Droplet Size and Velocity Distributions

In this chapter, spray morphology and droplet size and velocity distributions are reported and analyzed.

5.1 Droplet Size and Velocity Distributions

The breakup of coaxial air-water jets involves the interaction between the gas and liquid phases. Hence, the annular air flow fields can influence droplet size and velocity distributions. The annular air flow fields and vorticity maps, which were obtained via SPIV, are presented in Sec.4.3 (see Fig. 4.9 and Fig. 4.13). Significantly more detail, including turbulence statistics, can be found at the online database Liang et al. (2022a). As mentioned in Sec.4.3, a central reversal air flow occurs when $S \geq 1.2$ (see Fig. 4.9). In this project, it was found that recirculating air flows and vortices affect the droplet velocity distributions (this is discussed in more detail in the rest of this subsection). As mentioned in Sec.4.3, it was reported that radial expansion of the annular swirling air jets was observed near the nozzle exit, and it becomes larger as S goes up. When S remains constant, the extent of the radial expansion of the annular swirling air flows does not change as We_A is varied. Note that SPIV measurements were done for the annular air flows with medium We_A (≤ 440). We did not do SPIV for part of the flow cases with $440 < We_A \leq 1426$ in this paper, owing to a particle density problem, although there is no dependence of the radial expansion on We_A. When We_A increases, the topologies of the air flow fields do not change, except for the magnitudes of the velocity vectors. The value of S determines the extent of the radial expansion of the annular swirling air flows. Note that we discuss the annular air flows with specific We_A, despite the fact that the liquid was not flowing when we did SPIV measurements. By this we mean to designate the air flows used to create a specific We_A. Since, when flowing, the liquid jet flow rate was not changed, it is the air flow rate that sets We_A.

Droplet size and velocity distributions were measured for the flows in Table 3.4 in the present study.

Fig. 5.1 shows the radial distributions of the median droplet diameters (D) for various swirl numbers at two downstream positions of $5D_l$ and $10D_l$. Note that the median droplet diameter is presented here instead of the Sauter mean diameter (D_{32}).

As mentioned in Sec. 3.5, for each operating condition, 5000 droplet samples were collected at each measurement position. At a certain measurement position, if the diameter of a droplet is more than 1.5 times the interquartile range, away from the 25^{th} or 75^{th} percentiles of the droplet size data, they will be considered "outliers". For each droplet size dataset, the ratio of the number of "outliers" to the overall number of samples falls within the range of $\sim 0.9\% - 8.3\%$. Although those ratios are fairly low, it was found that at specific symmetrical measurement positions, if there is a very large "outlier" existing at either of those measurement positions, it will cause a significant difference in the value of D_{32} there. D_{32} tends towards the tail of positively skewed droplet distributions because the numerator of D_{32} contains the sum of the droplet diameters to the power of three. In effect, large droplets have a greater weight in the calculation of D_{32}. D_{32} can vary widely if there are significant outliers, when compared to the more robust median statistic. The median is insensitive to outliers while still including them in the calculation. Therefore, the median droplet diameter is presented here.

For each operating condition, the radial distribution of droplet diameters is symmetric with respect to the central axis of the nozzle exit. The droplet diameter distributions for all the operating conditions can be found in Liang et al. (2022b), and the raw PDI data are included. For $S = 0$, droplets were detected from $r = -2.5D_l$ to $r = 2.5D_l$ at the downstream position of $5D_l$. As S increases to 0.3, the radial range within which the droplets distribute themselves expands to $[-5D_l, 5D_l]$ at that downstream position (see Fig. 5.1a and Fig. 5.1b). With further increase in S, droplets start to appear at the radial positions of $r = \pm 7.5D_l$, as expected (see Fig. 5.1a and Fig. 5.1b). This can be explained by the fact that as S increases, the droplets start to spread along the radial direction due to the radial expansion of the annular swirling air flows, as shown in Fig. 4.9. Note that with the addition of air swirl, the radial ranges within which the droplets distribute themselves expand to $[-7.5D_l, 7.5D_l]$ at $y = 10D_l$ (see Fig. 5.1c and Fig. 5.1d).

D reduces somewhat as We_A increases, as expected, since the magnitudes of the aerodynamic forces acting on the liquid jets and the droplets increase. For $S = 0$ at $r = \pm 2.5D_l$, D increases somewhat further downstream (see Fig. 5.1). This can be caused by the collisions between droplets, which consequently leads to droplet coalescence. Droplet coalescence was also observed by Lasheras et al. (1998) when they used high-speed shadowgraphy and PDI to investigate a coaxial non-swirling air-water jet. They found that secondary breakup and coalescence of the droplets in the far field of the spray jet mainly depend on the total kinetic energy flux (mainly contained in the air jet) per unit total mass of the spray jet. Their total kinetic energy per unit time per unit total mass of air and water ranges from $23\ \mathrm{kJ/(kg \cdot s)}$ to $1.9 \times 10^6\ \mathrm{kJ/(kg \cdot s)}$, and in this work, it ranges from $9.5 \times 10^3\ \mathrm{kJ/(kg \cdot s)}$ to $1.4 \times 10^4\ \mathrm{kJ/(kg \cdot s)}$ which is a subset of their kinetic energy range. Hardalupas and Whitelaw (1998) investigated the breakup of a turbulent water jet by a co-annular air stream with S in the range of $\sim 0-7.9$. They used PDI to measure the diameters, velocities and liquid fluxes of the droplets over a wide range of aerodynamic Weber numbers, $We_A(230-630)$. Hardalupas and Whitelaw (1998) found that the droplet size is related with the local Weber number (We_D) rather than We_A. The local Weber number (We_D) is based on the droplet diameter and the relative velocity between the gas and liquid phases (Hardalupas & Whitelaw, 1998). Note that in this work, the local Weber number cannot be calculated since SPIV was performed on the annular air flow fields in the absence of the central water jet.

Dunand et al. (2005) ejected a turbulent water jet into a coaxial air jet with S and M in the ranges of $\sim 0-0.6$ and $\sim 3-13.3$, respectively. They found that when S goes beyond S_{cr}, small droplets are located in the hollow-cone region caused by the recirculating air flows, while large droplets appear on the jet periphery. They also found that the droplet size distributions with $S < S_{cr}$ are opposite to the ones with $S > S_{cr}$. However, in this work, D tends to be unrelated to S (see Fig. 5.1 and Fig. 5.2). This is because the spray morphologies for the breakup of the central laminar and turbulent liquid jets are different. Hollow-cone spray structures were not observed in this work due to the low kinetic energy contained in the central laminar liquid jet (this is discussed in more detail in Sec. 5.2). As mentioned in earlier, Hardalupas and Whitelaw (1998) investigated the breakup of a central turbulent water jet by a co-annular air jet with S in the range of $\sim 0-7.9$. They utilised PDI to measure the diameters, velocities and liquid fluxes of the droplets over a small range of aerodynamic Weber numbers, $We_A(230-630)$. They found that for $S=0$ with We_A in the range of $494-598$, the median droplet diameters at $Y=26D_l$ ranged from 148 μm to 159 μm. Those median droplet diameters are much larger than the median droplet diameters generated by the coaxial non-swirling jet in this work (< 20 μm) (see Figs. 5.1a and 5.1b). This implies that turbulence in the liquid generates bigger drops. This point can be explained by the fact that droplet sizes partly depend on spray morphologies which are different for the breakup of the central laminar and turbulent liquid jets. As one of the breakup mechanisms, turbulence in the liquid influences spray morphologies in a way that changes the jet velocity profile and makes a difference to the shear instability. The sizes of the droplets, which are peeled off from the liquid jet surface due to shear instability, are therefore influenced by the turbulence in the liquid. Lasheras et al. (1998) measured D_{32} at $r=0$ at the axial range of $[10D_l,\ 133D_l]$ when they investigated a non-swirling air-water jet with Re_l ranging from 494 to 2086, and with We_A of the order of 1267. They found that D_{32} increases with Re_l at all measurement positions, which also indicates that turbulence in the liquid tends to generate bigger drops. Similarly, Eroglu et al. (1991) ejected a water jet into coflowing air without swirl. They measured the radial distributions of D_{32} at $y=10D_l$ for Re_l ranging from 1453 to 2519, and for We_A of the order of 277. They found that D_{32} increases as Re_l increases, which is consistent with what Lasheras et al. (1998) found. An increase in the momentum of the central water jet results in a longer breakup length, which leads to a bigger SMD (Eroglu & Chigier, 1991). Note

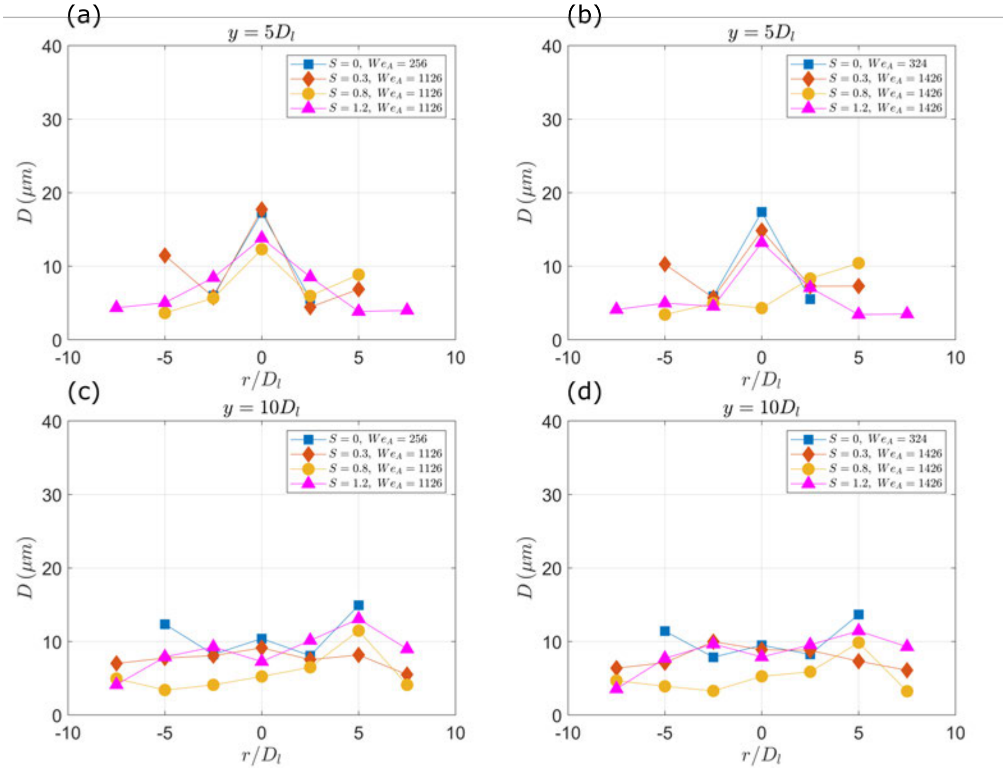

Figure 5.1: Distributions of median droplet diameters (D) for $S = 0 - 1.2$ at $y = 5D_l$ and $y = 10D_l$. (a) Distributions of D for cases 1, 3, 5 and 7 at $y = 5D_l$. (b) Distributions of D for cases 2, 4, 6 and 8 at $y = 5D_l$. (c) Distributions of D for cases 1, 3, 5 and 7 at $y = 10D_l$. (d) Distributions of D for cases 2, 4, 6 and 8 at $y = 10D_l$.

that although the radial distributions of D for $S = 2.5$ are a bit asymmetrical (see Fig. 5.2), the statistical distributions of the droplet diameters (D_{drop}) for that are symmetrical (see Fig 5.3). The asymmetry falls within the measurement uncertainty, and, thus, should be ignored. When a spray performance is evaluated, statistical distributions of D_{drop} should be considered first. The statistical distributions of D_{drop} for all the operating conditions are symmetrical with respect to the central axis of the nozzle exit. Those data can be found in the database (Liang et al., 2022b).

Fig. 5.4 shows the relationship between the swirl numbers and the axial velocities of the droplets at the downstream position of $5D_l$. The coordinate system is shown in Fig. 3.1. The statistical distributions of the axial velocities of the droplets are shown using box plots (see Fig. 5.4). Note that the central line of each box indicates the median. The top and bottom edges of each box represent 25th and 75th percentiles, respectively. Whiskers extend to the most extreme points. If sample values are more than 1.5 times the interquartile range away from the bottom or top edges of the boxes, they will be considered "outliers" and will be plotted using circular symbols. It was found that when $S \geq 0.8$, some of the droplets ($< 25\%$) located at the central axis of the nozzle start to move upward. This can be explained on the basis of

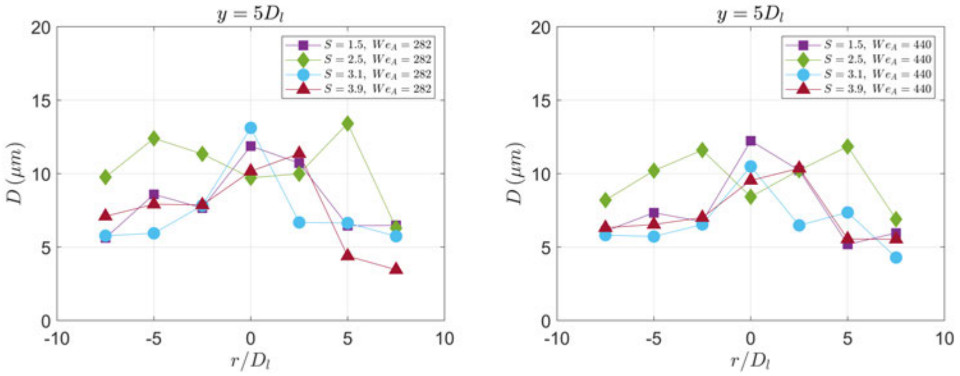

Figure 5.2: Distributions of median droplet diameters (D) for $S = 1.5 - 3.9$ at $y = 5D_l$.

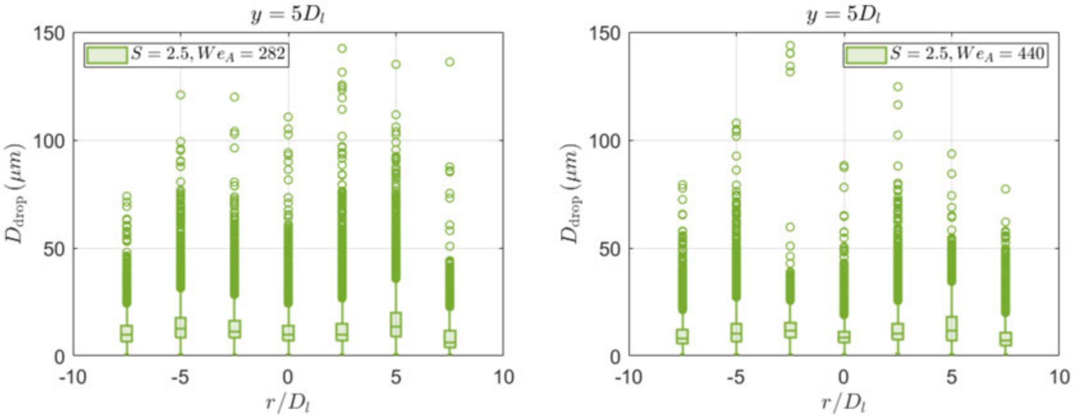

Figure 5.3: Statistical distributions of droplet diameters for $S = 2.5$ at $y = 5D_l$. Note that the central line of each box indicates the median. The top and bottom edges of each box represent 25th and 75th percentiles, respectively. Whiskers in the plot extend to the most extreme points. If sample values are more than 1.5 times the interquartile range away from the bottom or top edges of the boxes, they will be considered as “outliers” and will be plotted using circular symbols. For each box plot shown in this figure, the ratio of the number of outliers to the overall number of samples falls within the range of $\sim 2.1\% - 8.3\%$. Note that D_{drop} with magnitudes smaller than $150\ \mu m$ was plotted since there are few "outliers" with magnitudes larger than $150\ \mu m$.

recirculating air flows, as shown in Fig. 4.9 and discussed by Liang et al. (2022a). For $S = 0.3$ and $S = 0.8$, the differences between the medians of the axial velocities at $r = \pm 2.5$ are of the order of 53%. It can be found that for $S = 0.3$ and $S = 0.8$, 75% of the statistical distributions at $r = \pm 2.5D_l$ overlap with each other (see Fig. 5.4). Note that recirculating air flows occur for $S = 0.3$ and $S = 0.8$ which are indicated by the positive axial velocities of droplets (see Fig. 5.4). Although 75% of the statistical distributions at $r = \pm 2.5D_l$ overlap with each other, recirculating air flows and vortices (as indicated in Fig. 4.13) can cause variation in the median of the axial velocities. When S increases from 0.3 to 0.8, the radial location where the droplets with higher velocities were detected changes from $r = 2.5D_l$ to $r = -2.5D_l$. This can be explained on the basis of the recirculating air flows which are indicated by upward motion of droplets for $S = 0.3$ and $S = 0.8$ (see Fig. 5.4). Note that Figs. 4.9 and 4.13 are the average 3D vector fields and vorticity maps, respectively. The average results were presented since the frequency of the dual-pulse Nd: YAG laser was low (10 Hz). However, when we observed instantaneous air flow fields using a high-speed laser, we observed vortices and central recirculating air flows which were unsteady. The intensities and streamlines of recirculating air flows and vortices vary with time. When S increases from 0.3 to 0.8, switching of the high velocity point from $r = 2.5D_l$ to $r = -2.5D_l$ can be explained on the basis of the unsteadiness of recirculating air flows and vortices. It was found that when $S \geq 0.3$, upward motion of droplets located at the central axis of the nozzle was observed at the downstream position of $10D_l$. For each measurement position, the axial velocity of the droplet increases as We_A increases, as expected. This can be explained by the fact that when shear forces increase, liquid lumps pinch off from the liquid core with higher velocities. Momentum transfer between the liquid lumps and surrounding high-speed air occurs Lasheras et al. (1998). This causes the acceleration of liquid lumps, together with breakup and coalescence of drops (Lasheras et al. (1998)). The breakup of those liquid lumps can lead to droplets with high velocities.

Fig. 5.5 shows the relationship between the swirl numbers and the radial velocities of the droplets at the downstream position of $5D_l$. It was found that for S in the range of $\sim 0 - 0.8$, most of the droplets ($\geq 75\%$) located at $r = \pm 2.5D_l$ are blown outward away from the central axis of the nozzle at the downstream position of $5D_l$. However, when S increases to 1.5, 75% of the droplets located at $r = 2.5D_l$ are blown inward to the central axis of the jet. As S increases to 2.5, 50% of the droplets located at $r = \pm 2.5D_l$ move inward (see Fig. 5.5). This can be explained by the fact that when high swirl ($S \geq 1.2$) is added into the annular air jet, a strong central recirculating air flow occurs (see Fig. 4.9). As a result, the reversal air flows change the statistical distributions of the radial velocities of the droplets.

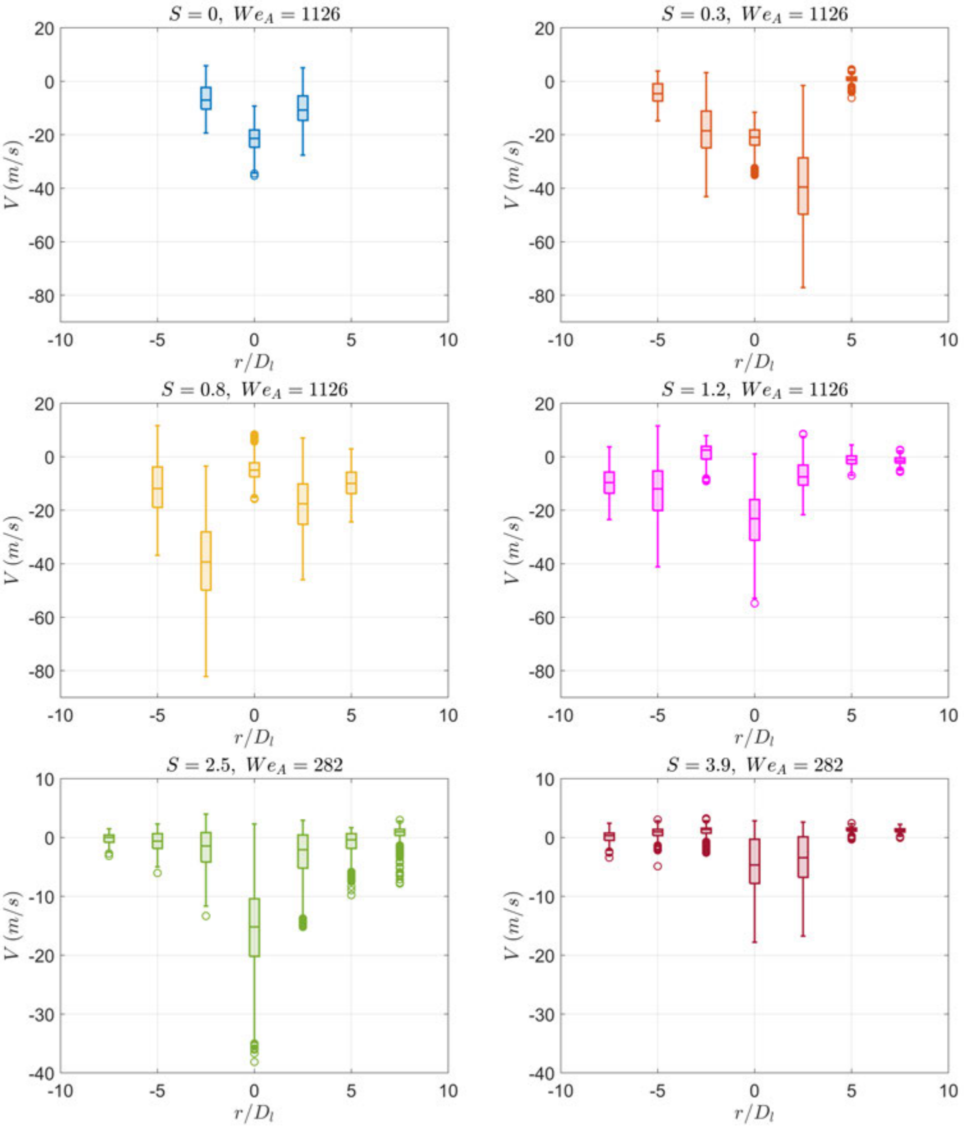

Figure 5.4: Axial velocity distributions of droplets for $S = 0 - 3.9$ at $y = 5D_l$.

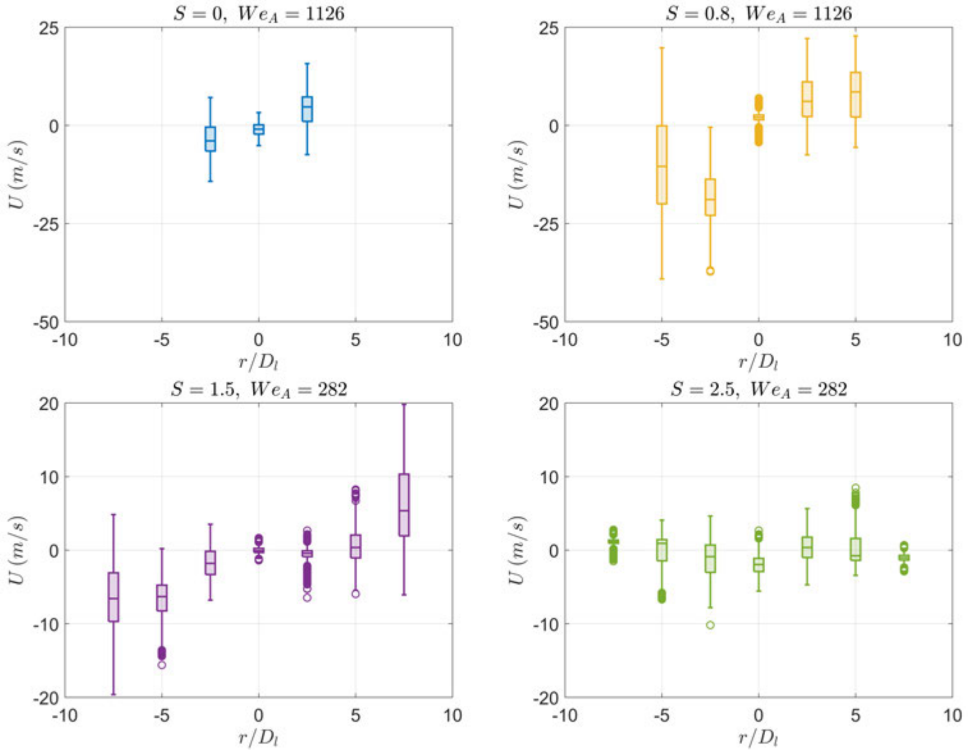

Figure 5.5: Radial velocity distributions of droplets for $S = 0,\ 0.8,\ 2.5$ and 3.9 at $y = 5D_l$.

5.2 Turn-off behaviour

The high-speed shadowgrams indicate that when S increases to 2.5, recirculating air flows start to penetrate to the water tube, which momentarily stops portions of the central laminar water jets from exiting, called the turn-off behaviour here. Those central recirculating air flows were observed in the SPIV measurement4.9f). Fig. 5.6b illustrates the turn-off behaviour for flow case 47 ($S = 3.9,\ We_A = 282$). Note that Figs. 5.6a and 5.6b were produced by applying background subtraction to the high-speed shadowgrams. In order to study the turn-off behaviour qualitatively and quantitatively, spatial POD was performed on the high-speed images for all the swirling flow cases mentioned in Table 3.4. The spatial POD can be determined using singular value decomposition (SVD)Liang et al. (2022a); Taira et al. (2017). How spatial POD was applied to the jet shadowgrams is presented in Sec. 3.6.

It was found that the turn-off behaviours appear as the first modes for cases 44 and 47 (see Fig. 5.7 and Fig. 4.14). This is consistent with what we observed using high-speed shadowgraphy. Note that for each figure, the values are normalized by their respective maxima. The positive and negative magnitudes reveal the spatial patterns which occur at different moments. Figs. 5.7 and 4.14 show that for each first POD mode, there is a central region with large positive values (> 0.5), which accounts for the turn-on condition, while there are small regions with small negative values (< -0.5) near the nozzle exit, which accounts for the turn-off condition. Note that the turn-off condition is caused by recirculating air flows which stop portions of the central laminar water jets from exiting, rather than stopping all of the water jets (see Fig. 5.6). This is why there are small blue regions near the nozzle exit in the first POD mode, which represents a few of the water jets exiting from the water tube when the turn-off behaviour occurs. In Figs. 5.7 and 4.14, the interpretation on the topology of each POD mode is consistent with what was observed using high-speed shadowgraphy. The first POD mode was used to reconstruct the shadowgrams, and it was found that the turn-on and turn-off conditions occur in the reconstructed images. This confirms that the first POD mode accounts for the turn-on and turn-off conditions. The reconstructed images using the first four POD modes, and the high-speed videos for all the flow cases can be found in the online database Liang et al. (2022b). Note that ε_1' is much larger than ε_1, which implies that the turn-off behaviour (as revealed by the first POD mode) becomes more dominant when S increases from 2.5 to 3.9 (see Fig. 5.7 and Fig. 4.14).

In order to study the turn-off behaviour quantitatively, a fast Fourier transform was performed on the first column of matrix $\boldsymbol{V}$ to yield the frequency of the turn-off behaviour which is revealed by the first POD mode (see Eq. 3.11). A broad spread of frequencies of almost equal amplitude was observed in the frequency spectra of the first POD modes for those two flow cases. This means that the timing of turn-off initiation is random for cases 44 and 47. However, it was found from the high-speed shadowgraphy measurements that for case 44, each turn-off event exists for around 7.5×10^{-4} s, while for case 47, it exists for a period of time between 3.33 ms and 6.67 ms. This is as expected, since as S increases, a wide range of recirculating air flows occur (see fig. 4.9), and as a result they stop portions of the central laminar water jets from exiting for a longer time. Note that the durations of each turn-off event are consistently the times given here. This observation is in contrast to the timing of turn-off initiation, which tends to be random. The liquid mass flow controller could potentially have an effect on the turn-off behaviours because it is designed to maintain flow, but if it does we expect the effect to be small. The duration of each turn-off event is much shorter than the update time of the liquid mass flow controller (50 ms). The controller would not respond fast enough to over-power the turn-off events. If anything, the turn-off behaviours may have a small effect on the average liquid flow rate. The high-speed videos for all the flow cases mentioned in Table 3.3 can be found in Liang et al. (2022b).

Turn-off behaviour has not been reported by other researchers mentioned in Chapter 1, since their central liquid jets were turbulent. They observed hollow-cone spray structures instead, which was not observed in this work. An equilibrium among the static pressure, the kinetic energy of the liquid jet and gas flow, and the ambient pressure should be achieved to sustain the hollow-cone spray structure (Hopfinger & Lasheras, 1996; Liang et al., 2022a). However, in the present study, the kinetic energy inside the central laminar water jet is not high enough to fulfil that requirement, and as a result for the high swirling flow cases ($S \geq 2.5$), the upward air flows with high momentum tend to momentarily stop portions of the central laminar water jets from exiting instead.

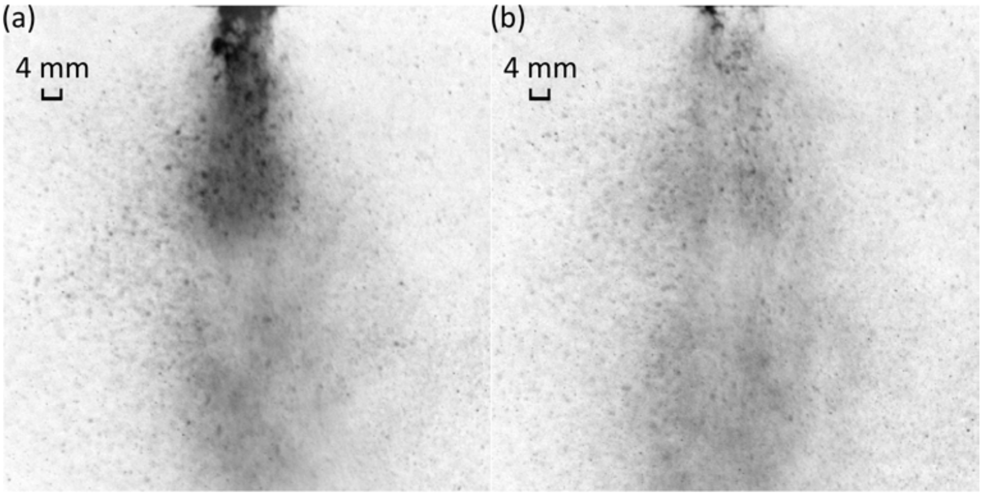

Figure 5.6: Shadowgrams that reveals the turn-off behaviour ($S = 3.9,\ We_A = 282$). (a) Turn-on condition. (b) Turn-off condition.

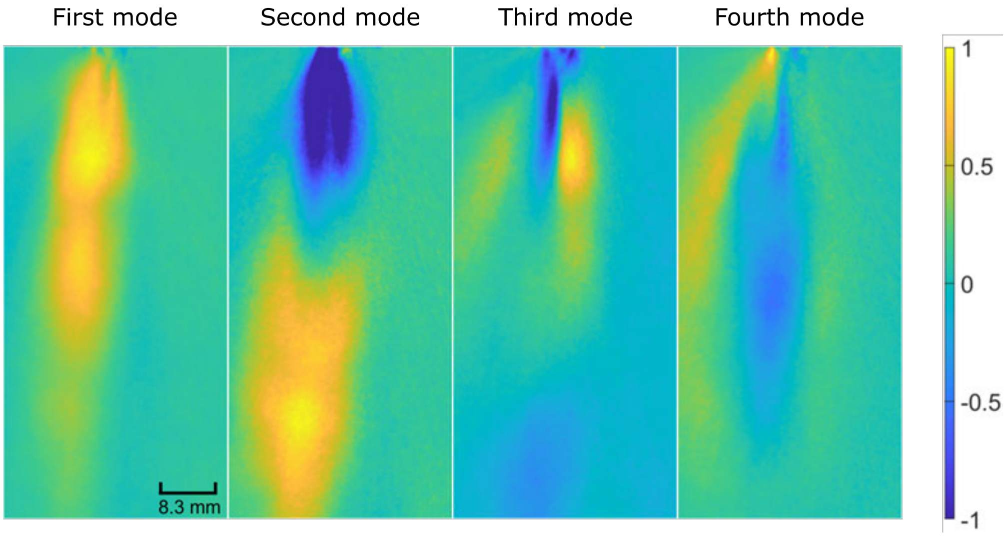

Figure 5.7: First four POD modes for case 44 ($S = 2.5,\ We_A = 440$). The singular value distributions of the first (ε_1), second (ε_2) and third (ε_3) modes are 0.0063, 0.0047, 0.0031 and 0.0026, respectively. Note that the images showing those POD modes have the same scale.

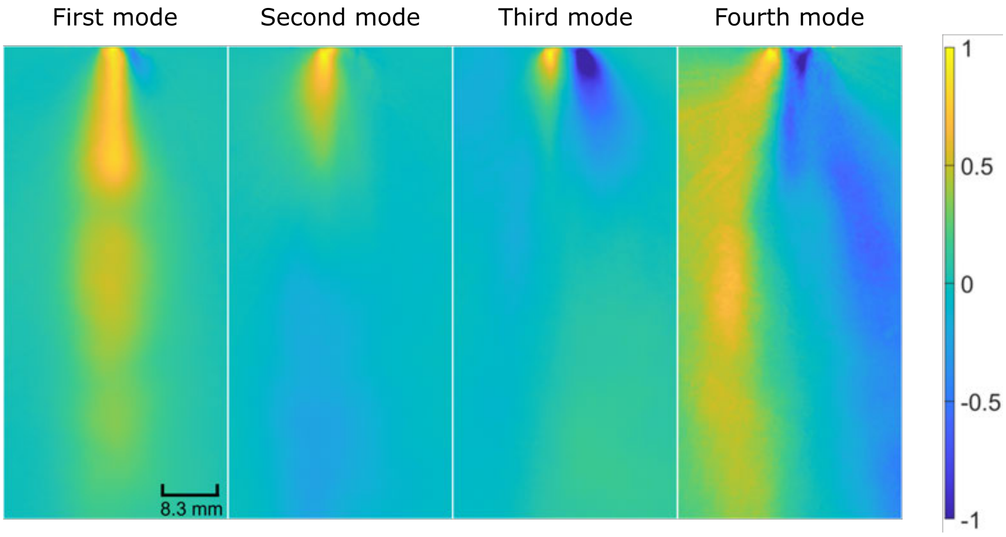

Figure 5.8: First four POD modes for case 47 ($S = 3.9,\ We_A = 282$). The singular value distributions of the first (ε_1'), second (ε_2') and third (ε_3') modes are 0.0166, 0.009, 0.0082 and 0.0065, respectively. Note that the images showing those POD modes have the same scale.

Chapter 6

Conclusions

The goal of the present work is to develop a comprehensive database for spray formation caused by shear forces, in part by removing turbulence from the liquid jet. In order to investigate how the strength of the air swirl influences the spray formation, air swirl is introduced into the annular air flows using four-vane swirlers with S in the range of $0.3 - 3.9$. High-speed shadowgraphic visualization was performed over a wide range of breakup regimes. For the flow cases shown in Table 3.3, data post-processing was applied to the high-speed shadowgrams to measure the breakup lengths and first droplet locations. 2D FFT and POD were performed on the high-speed shadowgrams to obtain 2D spectra and detect the large-scale instabilities, respectively. In order to investigate how the strength of the air swirl influences the air flow field, SPIV measurements were performed on the annular air jets with S in the range of $0 - 2.5$. For the flow cases shown in Table 3.4, PDI was utilised to measure the droplet size and velocity distributions. A turn-off behaviour was observed for the high swirling flow cases ($S \geq$2.5). POD was performed on the shadowgrams to study the underlying mechanisms behind the turn-off behaviour. All the data obtained from this project were stored in the online databases(Liang et al., 2022a, 2022b). The following statements are concluded from the measurements.

1. Four breakup regimes were observed over a wide range of operating conditions. They are first-wind induced, second-wind induced, bag breakup and fiber-type atomization regimes. Air swirl promotes the morphological development of the jets, especially for the high swirling flow cases with $1.2 \leq S \leq 2.5$.

2. Both the normalized breakup length and first droplet location are normally distributed (Liang et al., 2022a). A quadratic relationship between the medians of the normalized breakup lengths and first droplet locations was found (Liang et al., 2022a).

3. Radial expansion of the annular swirling air jets was observed near the nozzle exit. The extent of the radial expansion of the swirling air flows becomes larger as S goes up. Consequently, an increase in S leads to the shift of the shear layers towards the positions which are right below the outer edges of the co-flow tube. A central reversal air flow was observed when $S \geq 1.2$.

4. POD was performed on the high-speed shadowgrams for all the flow cases to find the dominant large-scale instability modes of the liquid jets. It was found that flapping instabilities dominate across most of the flow cases, as revealed by the first POD mode. Wavy and explosive breakup appear as the secondary breakup modes when We_A is low (≤ 110). In the absence of the reversal air flows, an increase in the aerodynamic forces destabilizes the liquid jet more significantly. For the low swirling flow cases ($0 < S \leq 0.8$), increasing the strength of the air swirl enhances flapping instabilities. The reversal flow inhibits the flapping instability, and an increase in S reduces the frequency of the flapping instability when $S \geq 1.2$.

5. Air-water interface positions were captured at many different moments in time, and a two-dimensional FFT was performed on the data to obtain the temporal and spatial frequencies of the shear instabilities. The temporal and spatial frequencies of the shear instabilities were detected in the flow cases which have long wave structures. In the absence of the central reversal air flows, increasing the strength of the air swirl increases the temporal frequency of the shear instability. A significant reduction of the temporal frequency of the shear instability was observed when $S \geq 1.2$, which implies that the central reversal air flows tend to stabilize the air-water interfaces. The spatial frequencies remain low ($\leq 0.06\ \mathrm{mm}^{-1}$) across all the flow cases which show the long wave structures.

6. Few droplets were observed in the high-speed shadowgrams over the operating conditions shown in Table 3.3 (the high speed videos for those flow cases can be found in the database Liang et al. (2022a)). Those drop sizes are big when compared with the drops produced by the flows defined in Table 3.4. Many smaller droplets were produced when the liquid jet entered the fiber-type breakup regime.

7. For the flow cases shown in Table 3.4, As S increases, the atomization of a central laminar water jet is improved in a way that the droplets are blown outward from the central axis of the nozzle, which is consistent with what Hardalupas and Whitelaw (1998) found when they investigated the breakup of a turbulent jet by a coaxial swirling air stream. However, in the present study, for the coaxial jets within bag breakup regimes with $Re_l = 438$ and S in the range of $\sim 0 - 0.3$, D was found to be not related to S. For the coaxial jets within fiber-type atomizaton regime or on the boundary of fiber-type atomization regime with $Re_l = 438$ and S in the range of $\sim 0.8 - 3.9$, D was found to be not related to S. For $S \geq 0.3$, upward motion of droplets located at the central axis of the nozzle was observed, which was caused by recirculating air flows.

8. For the flow cases shown in Table 3.4, When S increases to 2.5, recirculating air flows start to penetrate to the water tube, which momentarily stops portions of the central laminar water jets from exiting. This is called the turn-off behaviour.The timing of turn-off initiation is random. However, the durations of each turn-off event are consistently the times given in Sec. 5.1. This observation is contrast to the timing of turn-off initiation.

As mentioned above, this work aims to investigate shear-based spray formation. Comparisons between the breakup of laminar and turbulent jets haven been made in Chapters 4 and 5 . The following statements are concluded from those comparisons.

9. Four typical breakup regimes were observed for shear-based spray formation. The types of these breakup regimes are consistent with what Lasheras and Hopfinger (2000) observed when they investigated the breakup of a central turbulent or laminar water jet by a coaxial non-swirling air jet.

10. As mentioned in Chapter 1, Hopfinger and Lasheras (1996), Dunand et al. (2005) and Kumar and Sahu (2019) investigated the breakup of a central turbulent jet by a coaxial air jet with and without swirl. They observed hollow-cone sprays, which are formed by strong reversal air flows, when S goes beyond S_{cr} or when high M is achieved. However, in the present study, the hollow-cone spray structure does not appear in the flow cases where S goes beyond S_{cr} or where high M is achieved. This can be explained on the basis of the low kinetic energy that the central laminar liquid jet contains, as discussed in Sec. 4.1.

11. Kumar and Sahu (2019) observed an explosive breakup mode when they investigated the breakup of a central turbulent jet by a coaxial swirling air jet. They found that the dominant breakup mode changes from the flapping mode to the explosive breakup mode when the momentum ratio is high ($\sim$26). In the present study, however, for some flow cases with momentum ratios in the range of $\sim 15-660$, the explosive breakup modes appear as a secondary breakup mode rather than a dominant breakup mode (see Fig. 4.17). This can be explained on the basis of the low kinetic energy that the central laminar liquid jet contains, as discussed in Sec. 4.1. This is also consistent with the fact that hollow-cone spray structure does not appear in this work, as mentioned in point 10.

12. turbulence in the liquid tends to generate bigger drops. The breakup length of a liquid jet in a coaxial gas jet is proportional to the axial velocity of the liquid jet at the nozzle exit (Villermaux, 1998). An increase in the momentum of the central water jet results in a longer breakup length, which leads to a bigger SMD (Eroglu & Chigier, 1991).

13. Turn-off behaviour has not been reported by other researchers mentioned in Chapter 1, since their central liquid jets were turbulent. They observed hollow-cone spray structures instead, which was not observed in this work. An equilibrium among the static pressure, the kinetic energy of the liquid jet and gas flow, and the ambient pressure should be achieved to sustain the hollow-cone spray structure (Hopfinger & Lasheras, 1996; Liang et al., 2022a). However, in the present study, the kinetic energy inside the central laminar water jet is not high enough to fulfil that requirement, and as a result for the high swirling flow cases ($S \geq 2.5$), the upward air flows with high momentum tend to momentarily stop portions of the central laminar water jets from exiting instead.

6.1 Data Availability Statement

Two databases were set up to store the data that supports the findings of this work.

The first database is openly available in Edinburgh DataShare at https://doi.org/10.7488/ds/3459 (Liang et al., 2022a). It contains the data for the flow cases listed in Table 3.3. Those data include the drawings of the air swirlers, non-dimensional breakup lengths, first droplet locations, vector fields of the annular air flows, vorticity maps, POD modes, frequencies of the flapping instabilities, and 2D spectra. The full citation of the first database is shown below.

- Database 1: Liang, Y., Johansen, L. C., & Linne, M. (2022a). Breakup of a laminar liquid jet by coaxial non-swirling and swirling air streams. University of Edinburgh. (dataset. https://doi.org/10.7488/ds/3459)

The second database is openly available in Edinburgh DataShare at https://doi.org/10.7488/ds/3478 (Liang et al., 2022b). It contains the data for the flow cases listed in Table 3.4. Those data include the POD results and the droplet size and velocity distributions. The full citation of the second database is shown below.

- Liang, Y., Johansen, L. C., & Linne, M. (2022b). Characteristics of sprays produced by coaxial non-swirling and swirling air-water jets with high aerodynamic Weber numbers. University of Edinburgh. (dataset. https://doi.org/10.7488/ds/3478)

6.2 Future Work

In this project, there is an experimental limit to the maximum of We_A that can be reached, as stated in Sec. 3.2. The breakup of a central laminar water jet by a coaxial swirling air jet with $1.5 \leq S \leq 3.9$ and $We_A > 440$, and with $0 < S \leq 1.2$ and $We_A > 1426$, remain unknown and should be explored in the future. It was found that an increase in We_A or S improves atomization. Investigation on these operating conditions with high We_A or S will give a profound insight into how to improve atomization for the associated industrial applications.

Lasheras and Hopfinger (2000) pointed out that at large We_A (greater than 316), the breakup of a coaxial non-swirling air jet occurs in the forms of fibers, which produces finer droplets. This is called fiber-type atomizaion. In general, fiber-type atomization creates a dense droplet cloud near the nozzle exit. It is hard to measure the sizes of the droplets near the nozzle exit ($y < 5D_l$) using PDI, since those droplets are within a dense droplet cloud. It is also difficult to image the gas-liquid interfaces and liquid cores within a dense droplet cloud. Linne (2013) stated that ballistic imaging could be used to interrogate that region.

The limitation of PDI is that it is a point-wise technique and can only be utilized to investigate small and spherical drops (Bachalo, 2000). For a high-speed spray, the gas-liquid interfaces and the surfaces of primary drops are elongated. Hence, it is hard to measure the velocity fields at gas-liquid interfaces and primary droplets. Techniques such as planar laser drop sizing or digital in-line holography could be applied to extract volumetric size and velocity information (Berrocal et al., 2023).

An air-water jet was investigated in this project, as stated in Sec. 3.2. In order to investigate how the surface tension influence the breakup of a coaxial jet, the properties of the central liquid jet should be changed.

Appendix A

Drawings of Nozzle

This appendix shows the drawings of the nozzle. Both the assembled view and the single view for each component can be found in this appendix. Some of the drawings of the basic components were cited from Langeslag and Linne (2016) since they designed part of the basic structures for the nozzle studied in this project. The liquid tube, flow bench connector, air swirlers and perforated plate were designed and manufactured in this project. The units of the dimensions in each drawing are millimeter.

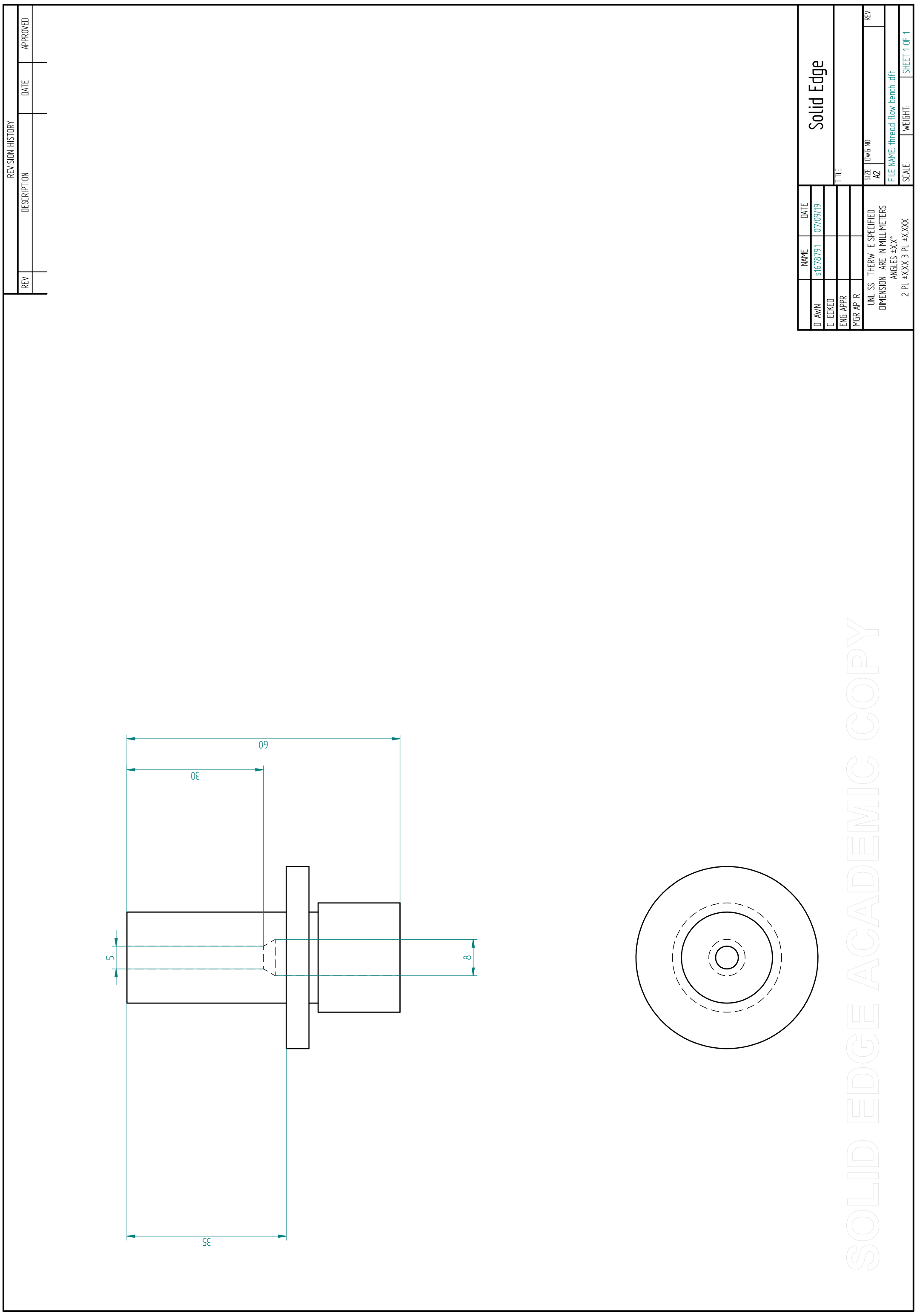

Figure A.1: Flow bench connector.

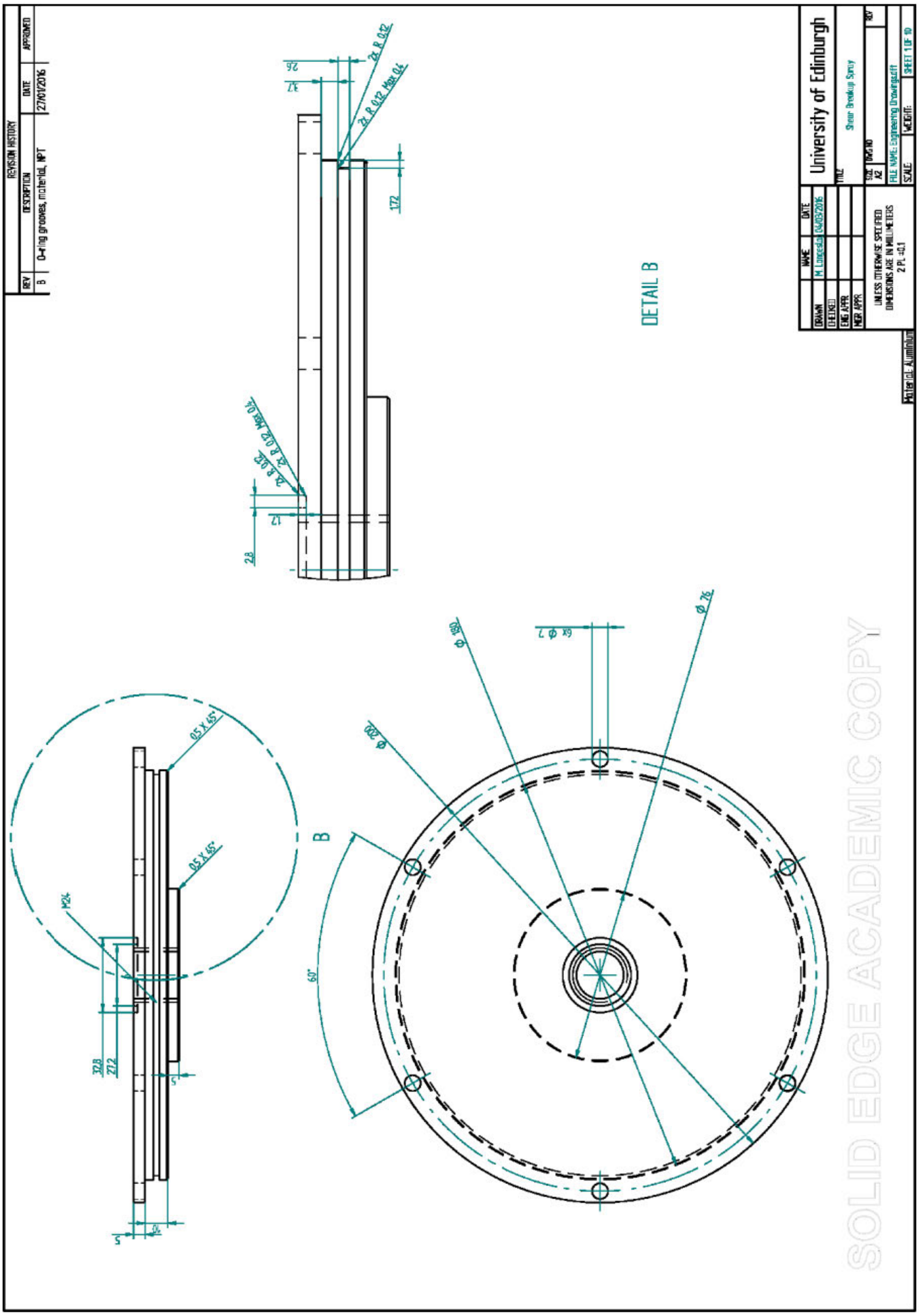

Figure A.2: Gas Drum lid (Langeslag & Linne, 2016).

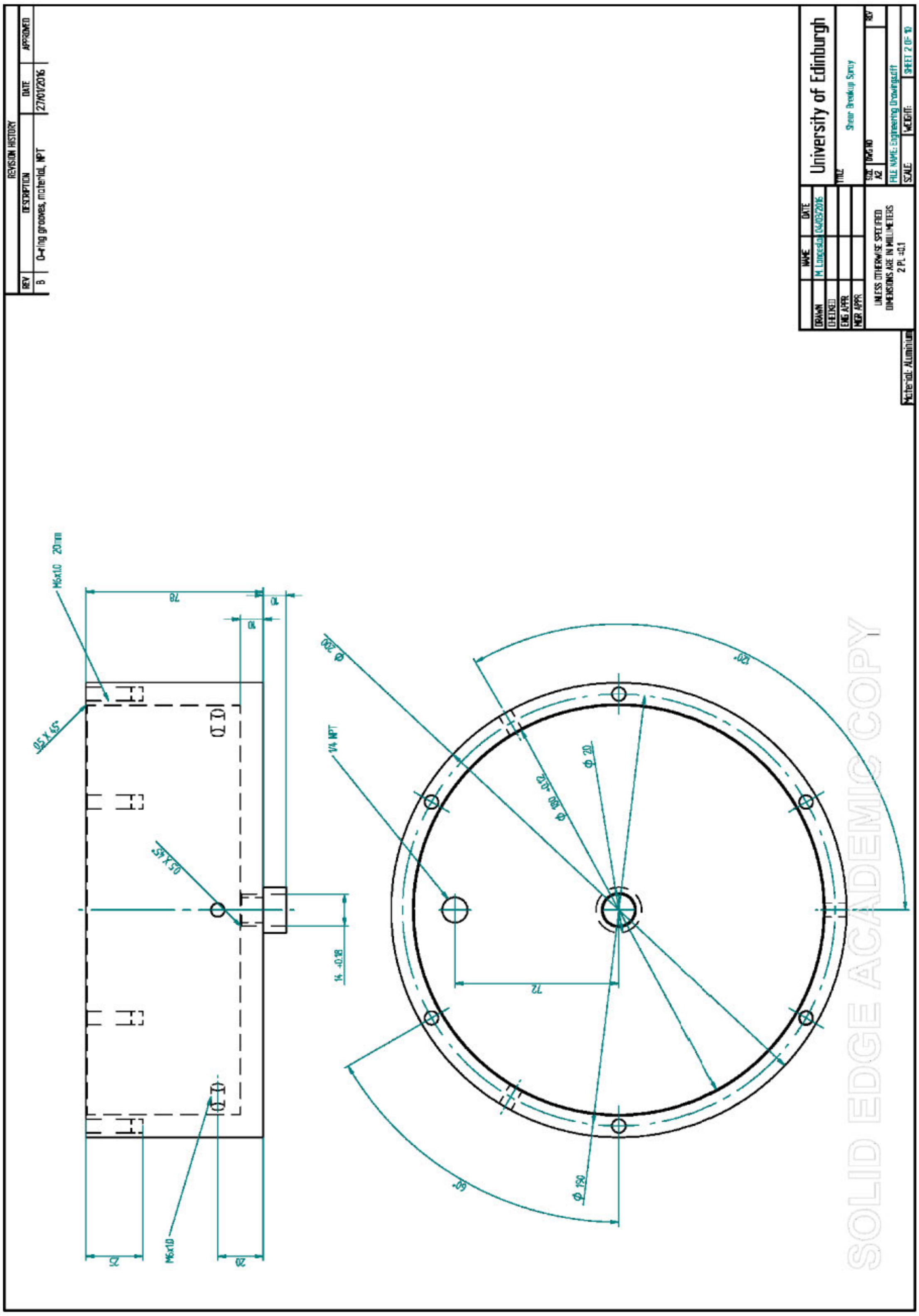

Figure A.3: Gas drum (Langeslag & Linne, 2016).

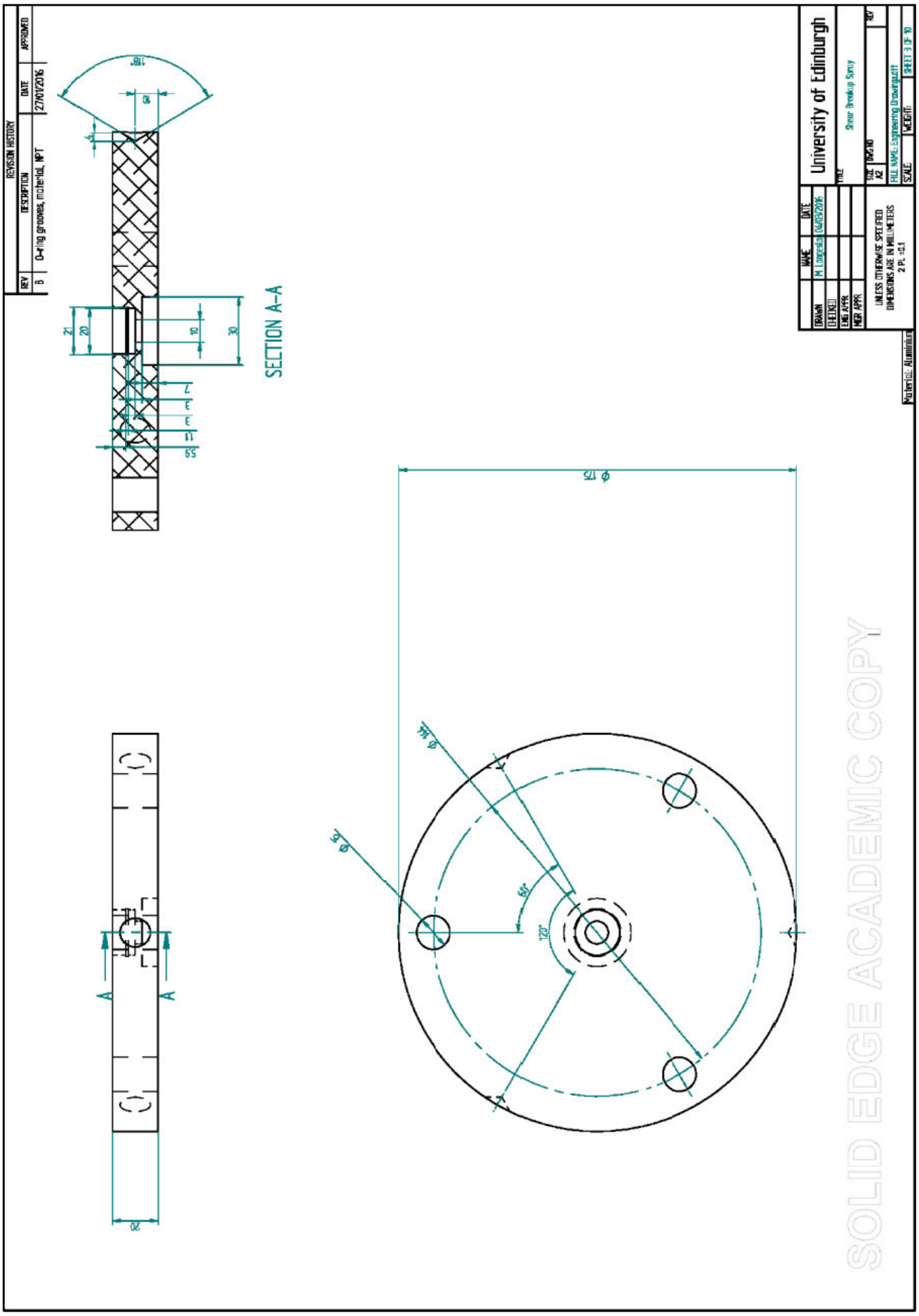

Figure A.4: Adjustment plate (Langeslag & Linne, 2016).

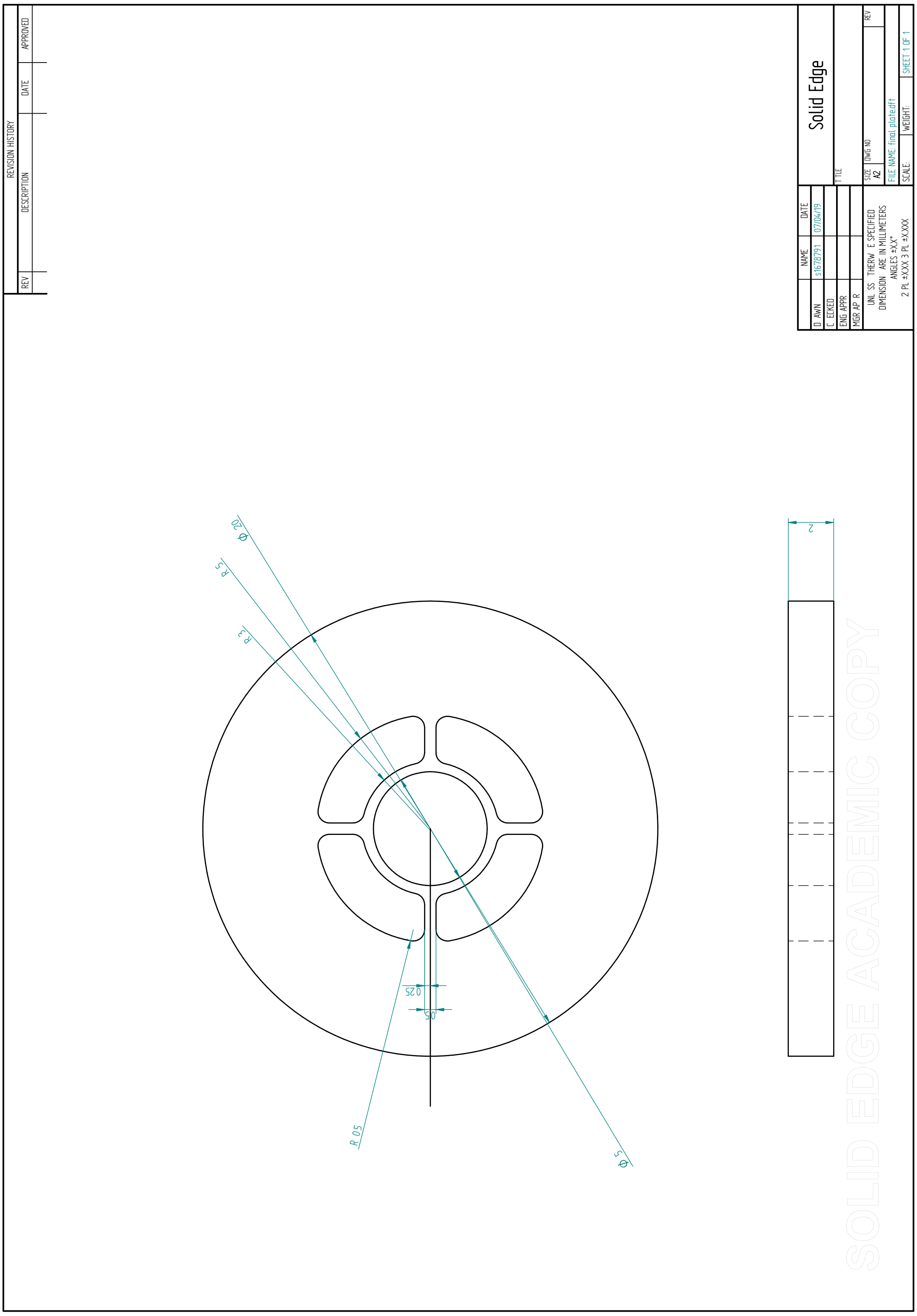

Figure A.5: Perforated plate.

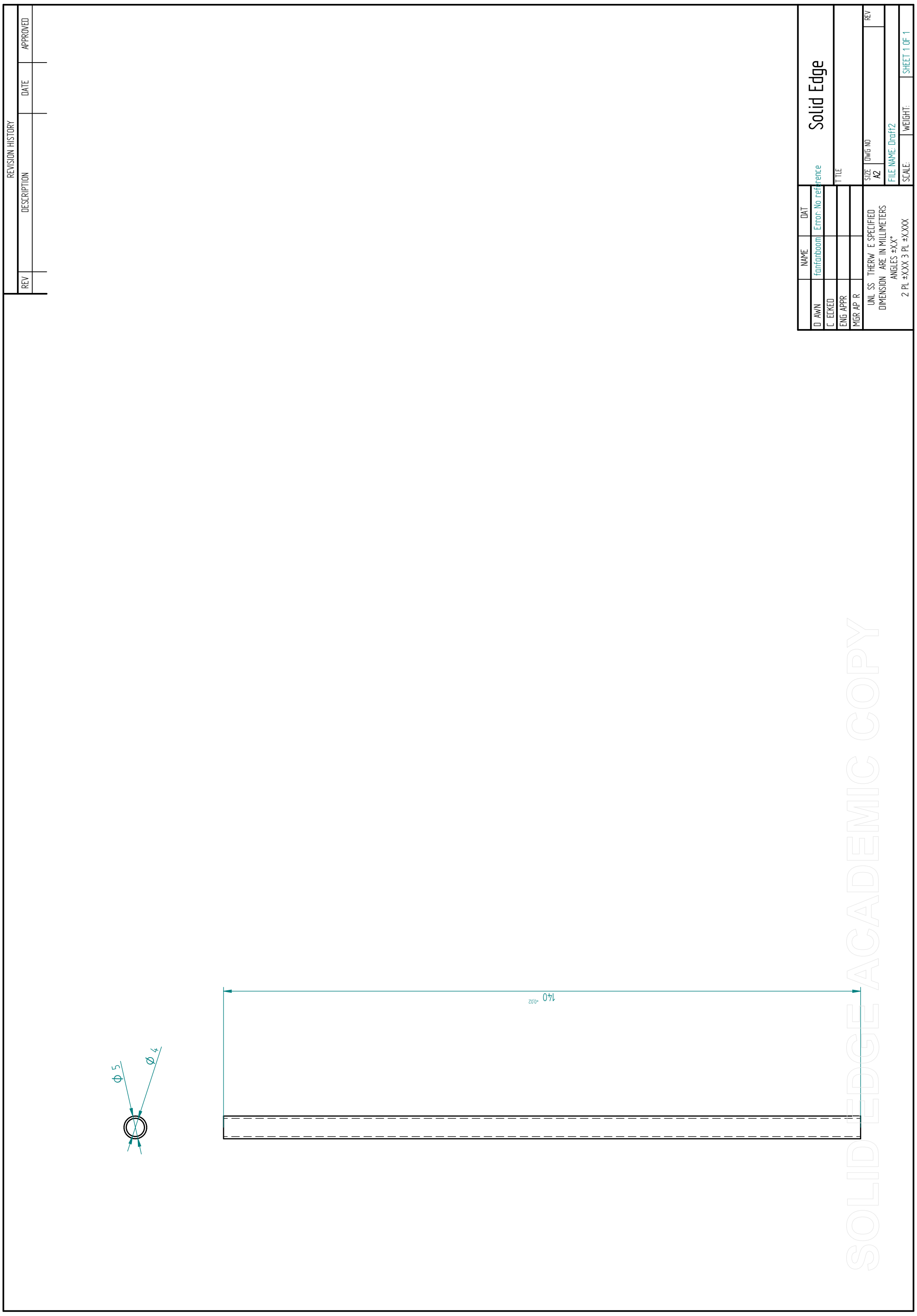

Figure A.6: Liquid tube.

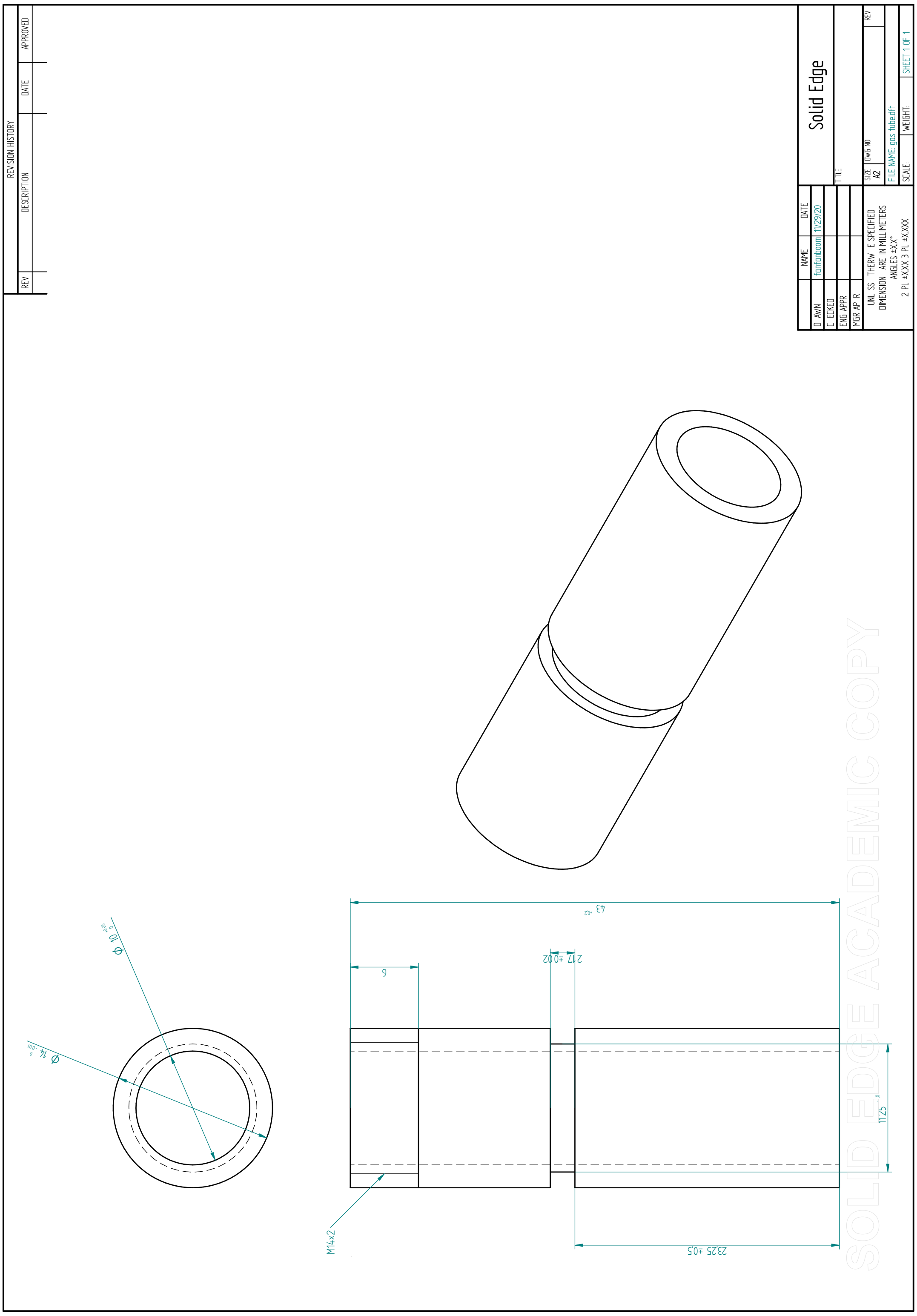

Figure A.7: Gas tube (Langeslag & Linne, 2016).

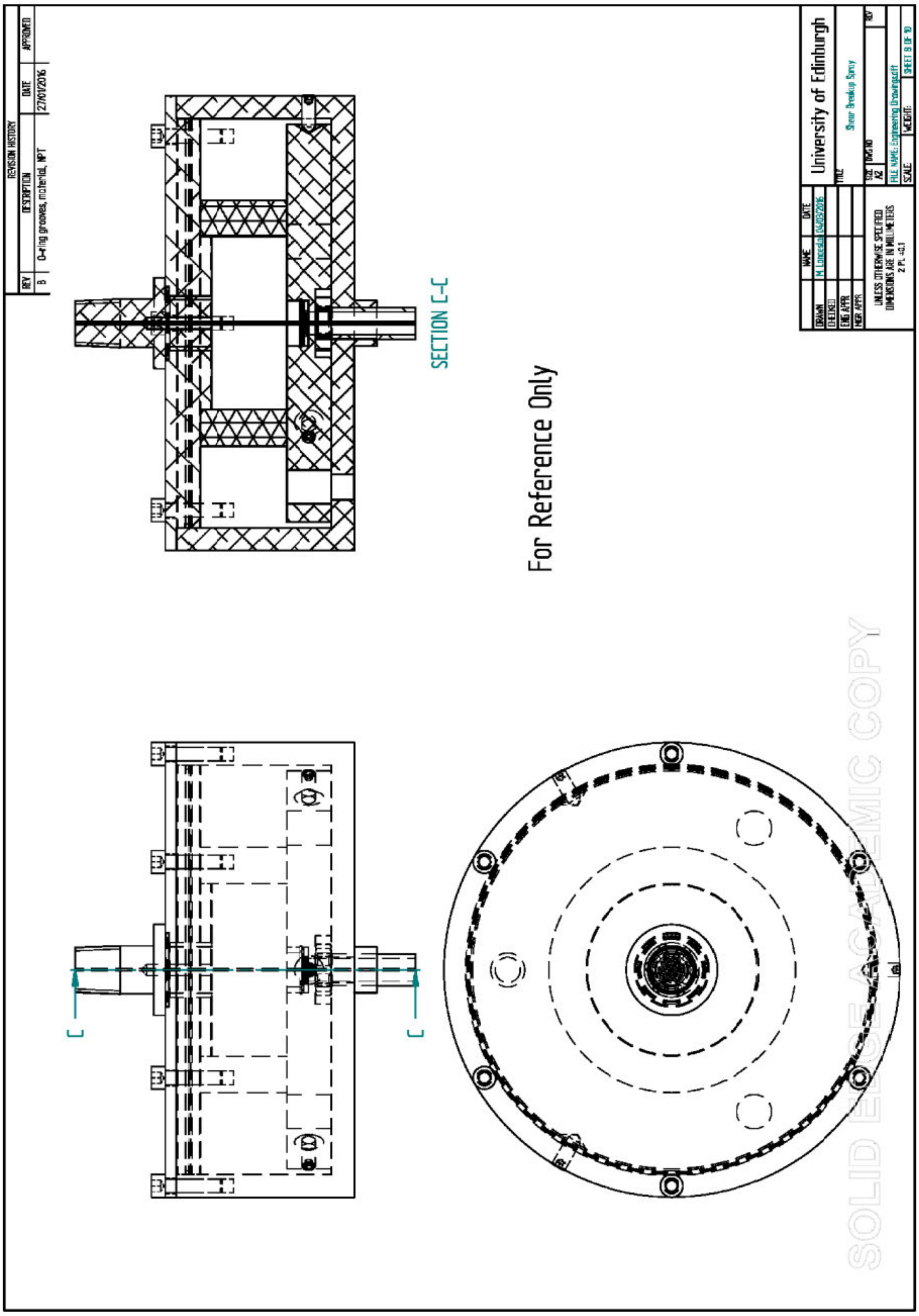

Figure A.8: Assembled view (Langeslag & Linne, 2016).

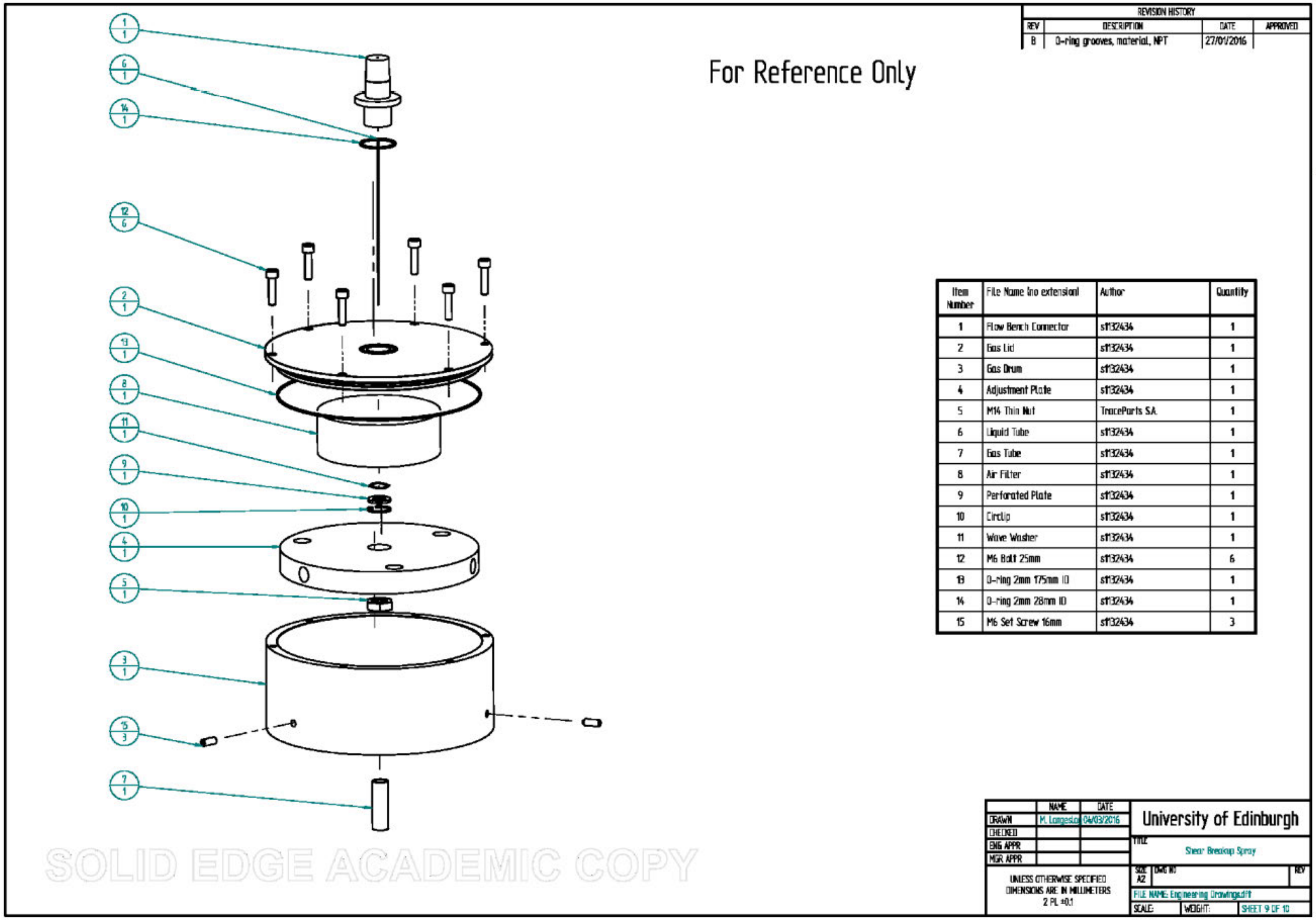

Item Number	File Name (no extension)	Author	Quantity
1	Flow Bench Connector	s1132434	1
2	Gas Lid	s1132434	1
3	Gas Drum	s1132434	1
4	Adjustment Plate	s1132434	1
5	M14 Thin Nut	TraceParts S.A.	1
6	Liquid Tube	s1132434	1
7	Gas Tube	s1132434	1
8	Air Filter	s1132434	1
9	Perforated Plate	s1132434	1
10	Circlip	s1132434	1
11	Wave Washer	s1132434	1
12	M6 Bolt 25mm	s1132434	6
13	O-ring 2mm 175mm ID	s1132434	1
14	O-ring 2mm 28mm ID	s1132434	1
15	M6 Set Screw 16mm	s1132434	3

Figure A.9: Exploded view (Langeslag & Linne, 2016).

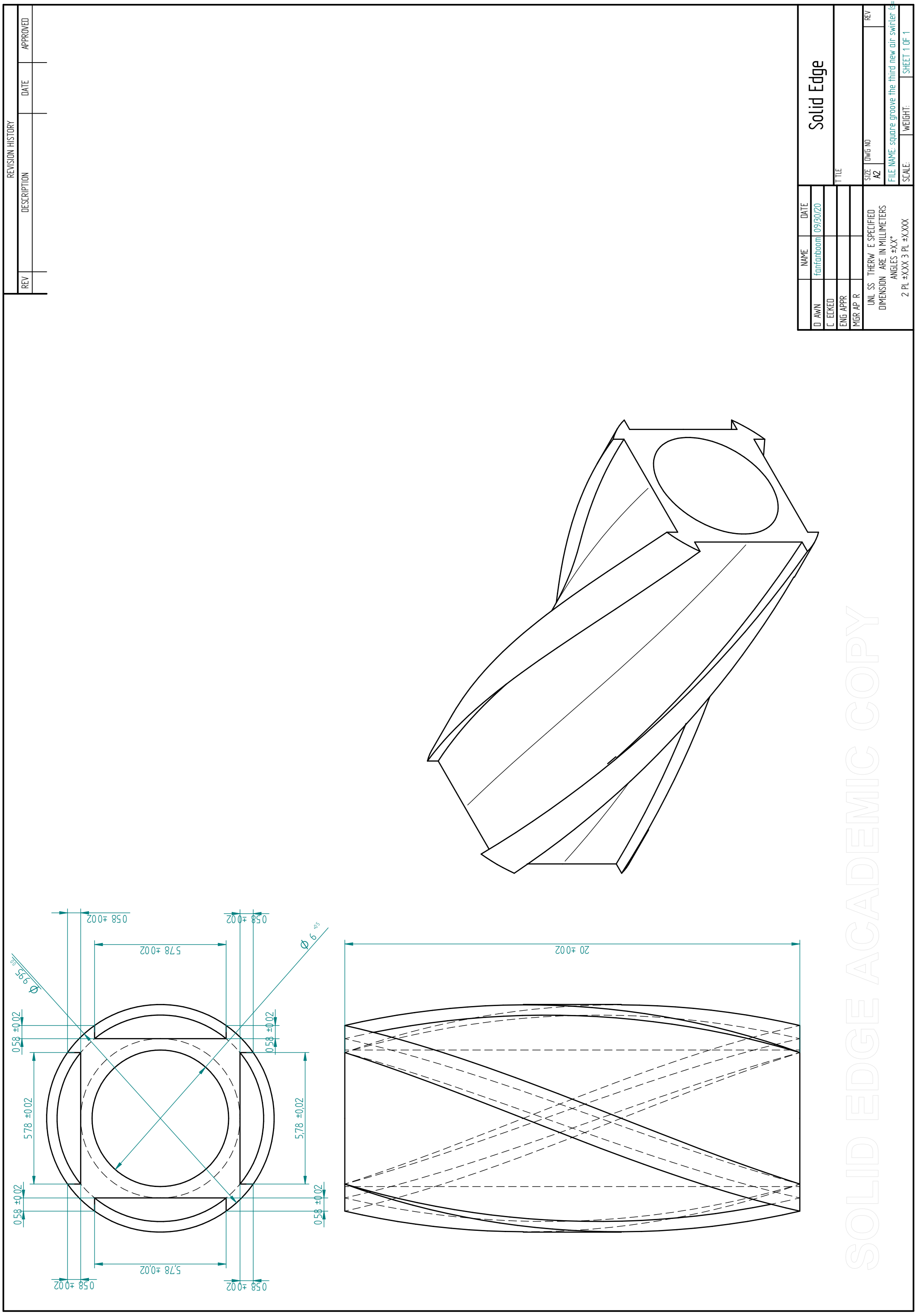

Figure A.10: Air swirler ($S = 0.3$).

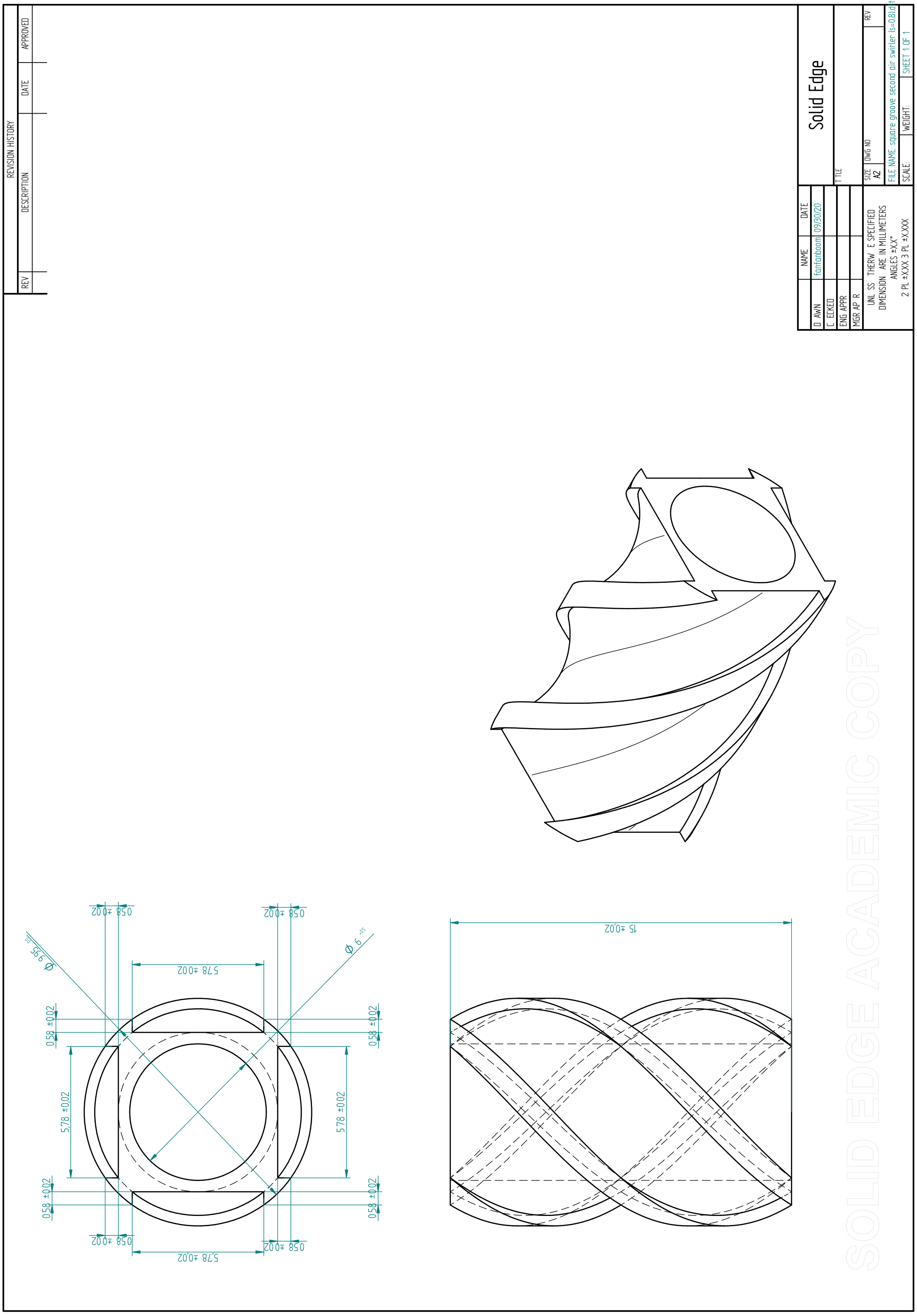

Figure A.11: Air swirler ($S = 0.8$).

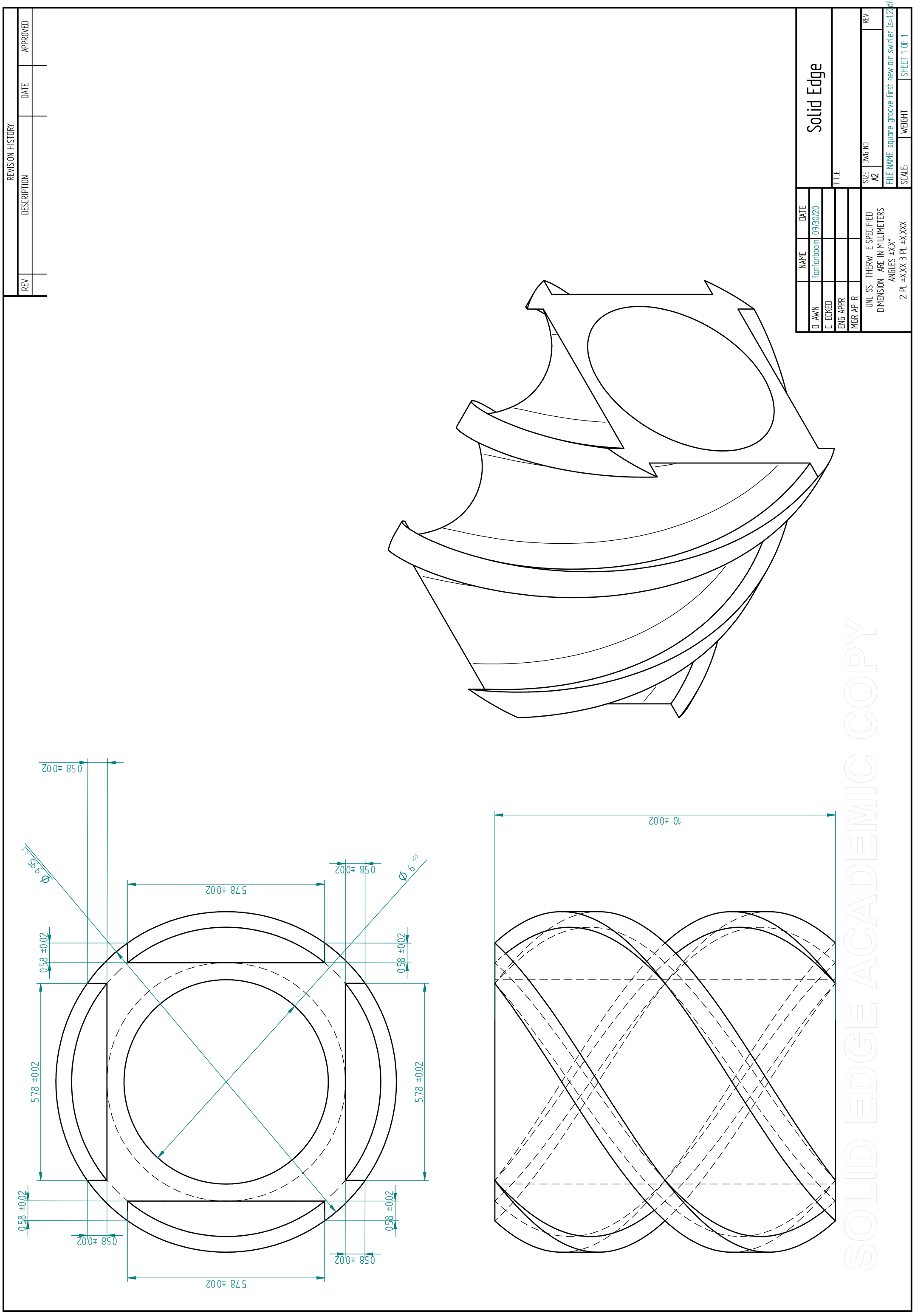

Figure A.12: Air swirler ($S = 1.2$).

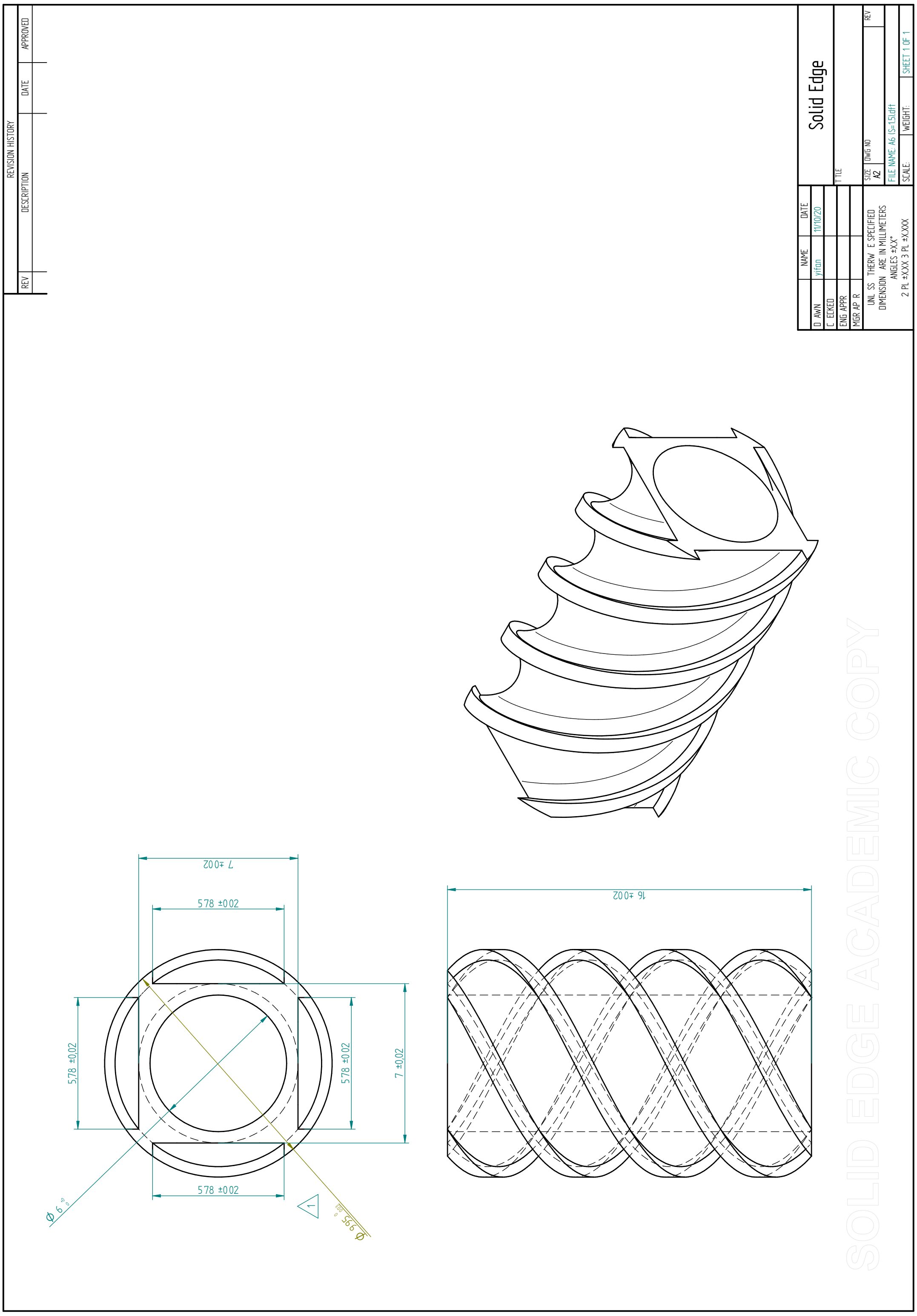

Figure A.13: Air swirler ($S = 1.5$).

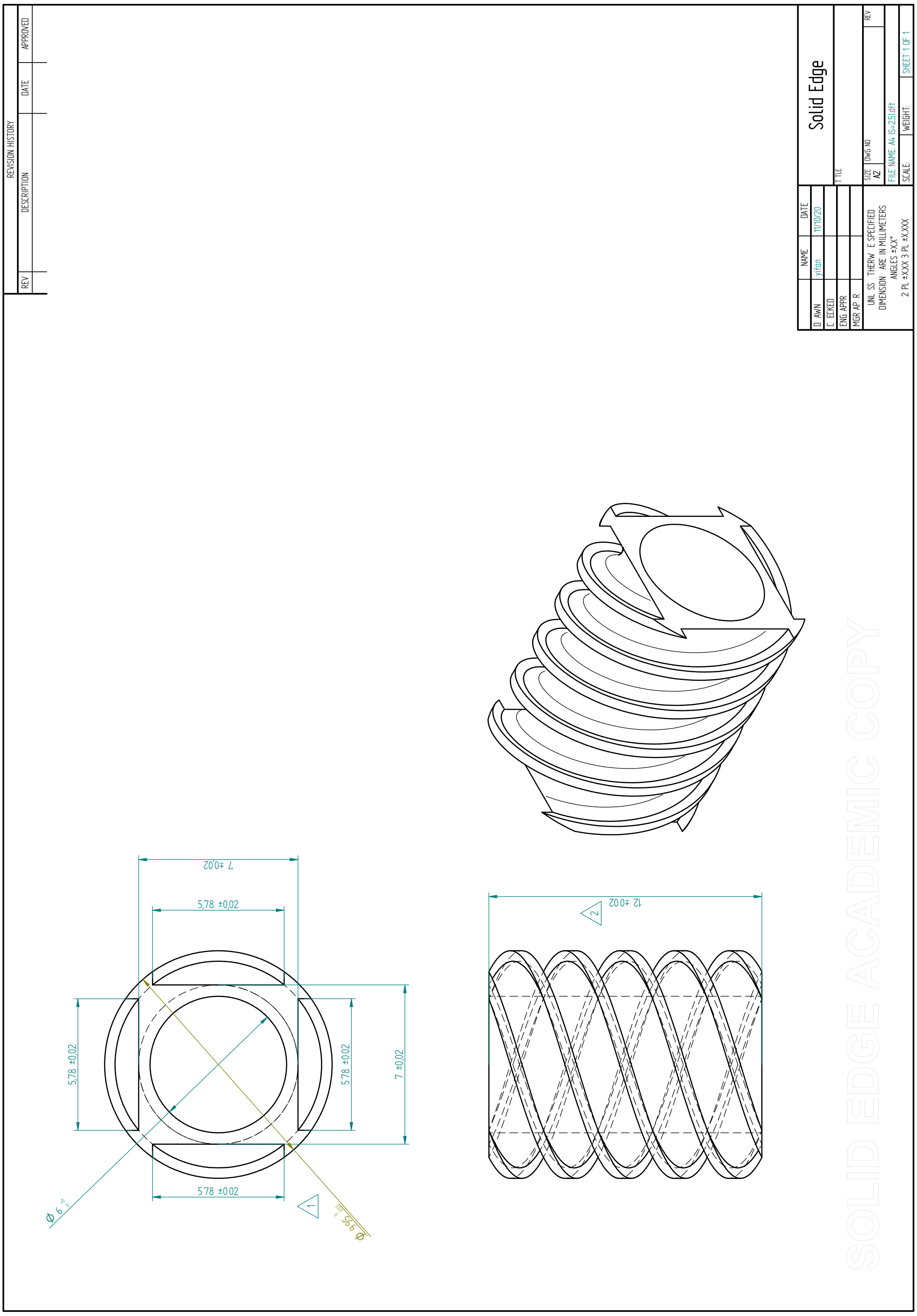

Figure A.14: Air swirler ($S = 2.5$).

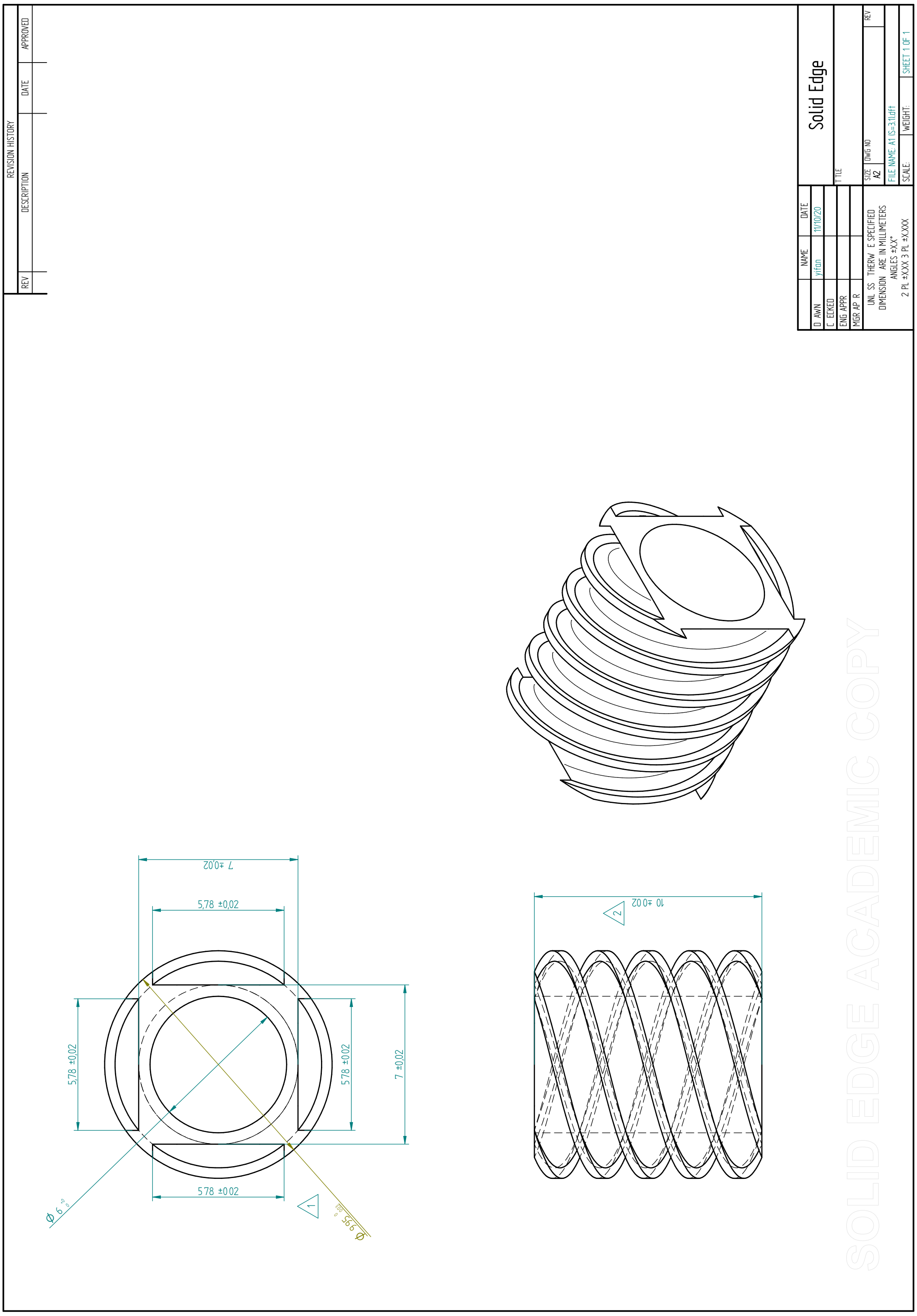

Figure A.15: Air swirler ($S = 3.1$).

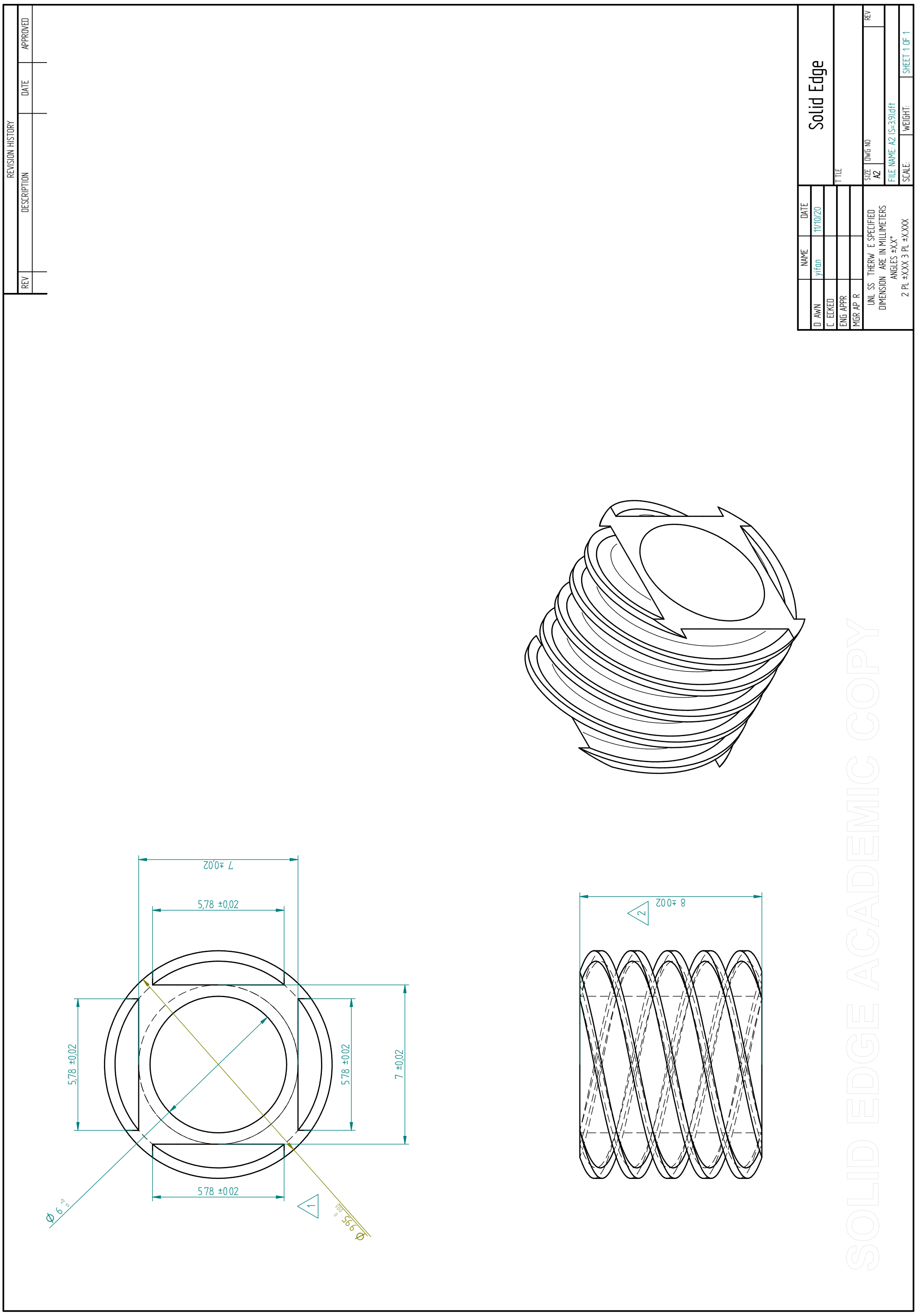

Figure A.16: Air swirler ($S = 3.9$).

Appendix B

MATLAB Code

As mentioned in Sec. 3.3, MATLAB was used for the data post-processing in this project. The algorithms of the MATLAB codes were explained in Sec. 3.6.1 and Sec. 3.6.2. In addition, MATLAB was used for the data plotting and scientific calculation in this project. All the MATLAB codes used in this work are shown in this appendix. What the codes are used for and how to use them are stated at the beginning of the m files.

B.1 threshlevel.m

```
% this code is used to detect the first droplet location and
    breakup length
% for one image

% The premises (i.e. keypoint) of this code:
% you should specify a row number larger than the smallest
   row number of the water jet region


%Variables list

%breakuplength: breakuplength (unit:mm)
%location1: the location of the first drop
%location2: the location of the largest region
%stats: regionprops(new_matrix,'filledimage');
%stats123: regionprops(new_matrix,'PixelList');
%stats456: regionprops(new_matrix,'Image');
%lowest_row: the specified row number

% clc
% clear all
% close all
```

```

cd 'D:\onedrive\OneDrive - University of Edinburgh\New data\s=3.9 (3)\air=2'
img_dir='D:\onedrive\OneDrive - University of Edinburgh\New data\s=3.9 (3)\air=2\';


% read one image to get image to determine crop region and the bottom edge
% of the gas tube
img_no = "0405";
img = imread(img_dir + "h" + img_no + ".tif");
figure(10)
imshow(img, [])
axis equal

magnification=0.12; % the magnification of the image (unit: mm/pixel)
resolution_x=800;% the horizontal resolution of the image (unit:pixel)
lowest_row=6;% the specified row number which should be larger than the smallest row number of the water jet region (in the cropped image)
crop_indx = [[291, 845]; [1, resolution_x]];% image region to crop to

file='background.tif';
a=imread(file);% read the background
a_crop = a(crop_indx(1,1):crop_indx(1,2), crop_indx(2,1):crop_indx(2,2));% background image to crop to
aa=int16(a_crop);

img_crop = img(crop_indx(1,1):crop_indx(1,2), crop_indx(2,1):crop_indx(2,2));% the original image to crop to
bb=int16(img_crop);
cc=aa-bb;% the matrix you want to threshold

cc=cc+int16(255);%?

```

```
[p,q]=size(cc);% p is the number of the rows of cc matrix; q
    is the number of the columns of cc matrix
level=725;%the threshold level????
new_matrix=logical(zeros(p,q));

%thresholding
for i=1:1:p
    for j=1:1:q
        if cc(i,j)>=level
           new_matrix(i,j)=logical(1); % if value is above
              level, it will be regarded as white
        end
    end
end

%the four rows code below will show you the image after
   background
%subtraction has been done

figure(4);
imagesc(cc)
colormap(gray(256))
axis equal
title('the rescaled image after background subtraction')

%plot the original photo and binarized image
figure(1)
imshow(img_crop,[])
title('the croppped photo')
figure(2)
imshow(new_matrix)
title('the binarized image')

%detect the first droplet
stats=regionprops(new_matrix,'filledimage');
stats123=regionprops(new_matrix,'PixelList');
stats456=regionprops(new_matrix,'Image');

kk=size(stats123);
```

```
kkk=kk(1);
compare=53100; % the reference value used to detect the first droplet location
compare1=5;
location2=0;
location1=[];
% mini_groups=zeros(kkk,2);
% mini_groups_size=zeros(kkk,1);

%detecting the water jet region
for i=1:1:kkk

      BB=stats123(i).PixelList;
      minimum=min(BB,[],1);
      mini_column=minimum(2);
      mini_row=minimum(1);
      c=size(BB);
      size_region=c(1)*c(2);

        if mini_column<=lowest_row % this means that the smallest row number for
                                   % potential water jet region should be larger than
                                   % the row number you specified at the
                                   % beginning
        if size_region>compare1
        compare1=size_region;
        location2=i;%the location of the largest region
        end

        end


end

%detecing the location of bag breakup and costic holes
```

```
largest=stats(location2).FilledImage; % the largest connective region in the graph
largest_size=size(largest);
for i=1:1:largest_size(2) %detecting the start point of the largest connective area in the local graph (used to calculating coordinate conversion)
    if largest(1,i)==1
        start_y=i;
        break
    end
end

ko=stats123(location2).PixelList;
ko_mini=min(ko,[],1);
ko_mini_column=ko_mini(2); %ko_mini_column is the x-coordinate of the start point of the largest connective area in the original graph
ko_compare=resolution_x;
ko_size=size(ko);
for i=1:1:ko_size(1) %detecting the y-coordinate of the start point of the largest connective area in the original graph (used to calculating coordinate conversion)

    if ko(i,2)==ko_mini(2)
        if ko(i,1)<ko_compare
        start_y_original=ko(i,1);
        ko_compare=start_y_original;
        end
    end
end
diff=stats(location2).FilledImage-stats456(location2).Image;
ccc=size(diff);
bag_x=[];
bag_y=[];
cs=1;% the number of the bag matrix elements at current stage should be (cs-1)

for i=1:1:ccc(1)
```

```
    for j=1:1:ccc(2)
        if diff(i,j)~=0 %this i and j are not the same as the coordinate used in the original graph
           bag_x(cs)=i+(ko_mini_column-1); % coordinate conversion
           bag_y(cs)=j+(start_y_original-start_y);% coordinate conversion
           cs=cs+1;
        end
    end
end


%detecting the first drop
for i=1:1:kkk

    BB=stats123(i).PixelList;
    minimum=min(BB,[],1);
    mini_column=minimum(2);
    mini_row=minimum(1);
    c=size(BB);
    size_region=c(1)*c(2);
    candy=[];
    candy_co=1;% the number of the candidates at current stage should be (candy_co-1)
    over=0;

    if mini_column>ko_mini_column && mini_column<compare && c(1)>=3 %c(1)>1 means the size of the droplet should be larger
        for pppp=1:1:c(1)                             % than 1. mini_column>ko_mini_column means that the  first droplet location should be below the gas tube
            if BB(pppp,2)==mini_column
               candy(candy_co)=BB(pppp,1);
               candy_co=candy_co+1;
            end
        end
```

```
        for ppp=1:1:(cs-1) % detect if the droplet is located inside the bag. If yes, ignore this droplet and find the next possible droplet
            if bag_x(ppp)==mini_column

               for qqqq=1:1:(candy_co-1)
               if bag_y(ppp)==candy(qqqq)
                  over=1;
                  break
               end
               end
            end

            if over>0
               break
            end

        end

    if over==0
        compare=mini_column;
        location1(1)=i;% the location of the first drop
    end

    end
end

%double check whether there is paralled first drop?
% AA=stats123(location1).PixelList;
% minimum=min(AA,[],1);
% drop_mini_column=minimum(2);
% i_num1=1:1:(location2-1);
% i_num2=(location2+1):1:kkk;
% i_num=[i_num1 i_num2];
% num=2;
%
% for i=i_num
%     BB=stats123(i).PixelList;
%     minimum=min(BB,[],1);
```

```
%     mini_column=minimum(2);
%     mini_row=minimum(1);
%
%     if i~=location1
%        if mini_column ==drop_mini_column
%           location1(num)=i;% the location of the first drop
%           num=num+1;
%        end
%
%     end
% end

breaklength=size(stats456(location2).Image);
breaklength=magnification*breaklength(1);%unit:mm
                                             % -1 means that remove the bottom surface of the water tube
                                             % when calculation the breakup length

figure(3)
imshow(stats(location2).FilledImage)
title('the largest connective region')
stats123(location1).PixelList
```

B.2 manyphotos.m

```
% this code is used to detect the first droplet location and breakup length
% for a group of images
clc
clear
close all
```

```matlab

cd 'D:\OneDrive - University of Edinburgh\3.30.2021 final data\T=0.5s\s=1.2 (3)\air=10'

n=3001;% number of photos (including background)
thresh_range=750:50:950; % the range of the thresholding level
magnification=0.14; % the magnification of the image (unit: mm/pixel)
resolution_x=832;% the horizontal resolution of the image (unit:pixel)
lowest_row=37;% the specified row number which should be larger than the smallest row number of the water jet region (in the cropped image)
crop_indx = [[1, 512]; [1, resolution_x]];% image region to crop to

I=cell(1,n);
a=imread('background.tif');% read the background
a_crop=a(crop_indx(1,1):crop_indx(1,2), crop_indx(2,1):crop_indx(2,2));% background image to crop to
I{1}=int16(a_crop);% we put background at the first element
[~,num_column]=size(thresh_range);
breaklength=zeros(n-1,num_column);%  preallocate array to store the breakup length as columns
firstdrop=zeros(n-1,num_column);% preallocate array to store the first droplet location as columns

% read several images
for i=0:1:(n-1)
    if i<10
    imageName=strcat('h','000',num2str(i),'.tif');
    elseif i>=10&&i<100
    imageName=strcat('h','00',num2str(i),'.tif');
    elseif i>=100&&i<1000
    imageName=strcat('h','0',num2str(i),'.tif');
    else
    imageName=strcat('h',num2str(i),'.tif');
    end
```

```

    img=imread(imageName);
    img_crop = img(crop_indx(1,1):crop_indx(1,2), crop_indx(2,1):crop_indx(2,2));% background image to crop to
    I{i+2}=int16(img_crop);
end

%do the background subtraction for each images
for i=2:1:n
    I{i}=I{1}+(-1).*I{i};
end

% rescaling (note: this rescaling is to plus 255 for each pixels values)
for qqq=2:1:n
cc=I{qqq};
cc=cc+int16(255);
I{qqq}=cc;


end

% thresholding each image
[p,q]=size(I{1}); % get the identical image size


for k=2:1:n % the biggest loop
    ii=1;
for level=thresh_range % thresholding the image under different thresholding level
    cc=I{k};
    ccc=false(p,q);
    for i=1:1:p
        for j=1:1:q
            if cc(i,j)>=level
            ccc(i,j)=true;
            end
        end
    end
```

```

%detecting the first droplet
new_matrix1=ccc;
stats=regionprops(new_matrix1,'filledimage');
stats123=regionprops(new_matrix1,'PixelList');
stats456=regionprops(new_matrix1,'Image');

[kkk,~]=size(stats123);
compare=53100; % the reference value used to detect the first droplet location
compare1=10;
location2=0;
location1=[];


%detect the water jet region
for i=1:1:kkk

    BB=stats123(i).PixelList;
    minimum=min(BB,[],1);
    mini_column=minimum(2);
    mini_row=minimum(1);
    c=size(BB);
    size_region=c(1)*c(2);

    if mini_column<=lowest_row % this means that the smallest row number for
                                   % potential water jet region should be larger than
                                   % the row number you specified at the
                                   % beginning

    if size_region>compare1
    compare1=size_region;
    location2=i;%the location of the largest region
    end

```

```
    end

end

%detecing the location of bag breakup and costic holes
largest=stats(location2).FilledImage;
largest_size=size(largest);
for i=1:1:largest_size(2) %detecting the start point of the largest connective area in the local graph (used to calculating coordinate conversion)
    if largest(1,i)==1
        start_y=i;
        break
    end
end

ko=stats123(location2).PixelList;
ko_mini=min(ko,[],1);
ko_mini_column=ko_mini(2); %ko_mini_column is the x-coordinate of the start point of the gas tube in the original graph
ko_compare=resolution_x;
ko_size=size(ko);
for i=1:1:ko_size(1) %detecting the y-coordinate of the start point of the air tube in the original graph (used to calculating coordinate conversion)

    if ko(i,2)==ko_mini(2)
        if ko(i,1)<ko_compare
        start_y_original=ko(i,1);
        ko_compare=start_y_original;
        end
    end
end
diff=stats(location2).FilledImage-stats456(location2).Image;
ccc=size(diff);
bag_x=[];
bag_y=[];
```

```
cs=1;% the number of the bag matrix elements at current stage should be (cs-1)

for i=1:1:ccc(1)
    for j=1:1:ccc(2)
        if diff(i,j)~=0 %this i and j are not the same as the coordinate used in the original graph
           bag_x(cs)=i+(ko_mini_column-1); % coordinate conversion
           bag_y(cs)=j+(start_y_original-start_y);% coordinate conversion
           cs=cs+1;
        end
    end
end


%detecting the first drop
for i=1:1:kkk

    BB=stats123(i).PixelList;
    minimum=min(BB,[],1);
    mini_column=minimum(2);
    mini_row=minimum(1);
    c=size(BB);
    size_region=c(1)*c(2);
    candy=[];
    candy_co=1;% the number of the candidates at current stage should be (candy_co-1)
    over=0;

    if mini_column>ko_mini_column && mini_column<compare && c(1)>=3 %c(1)>1 means the size of the droplet should be larger
        for pppp=1:1:c(1)                              % than 1. mini_column>ko_mini_column means that the first droplet location should be below the gas tube
            if BB(pppp,2)==mini_column
```

```
               candy(candy_co)=BB(pppp,1);
               candy_co=candy_co+1;
            end
        end
        for ppp=1:1:(cs-1)
            if bag_x(ppp)==mini_column

               for qqqq=1:1:(candy_co-1)
               if bag_y(ppp)==candy(qqqq)
                  over=1;
                  break
               end
               end
            end

            if over>0
               break
            end

        end

    if over==0
        compare=mini_column;
        location1(1)=i;% the location of the first drop
    end

    end
end

%double check whether there is paralled first drop? can this part be
%deleted in the future? are we interested in the number of the paralled
%first drop? ask Mark.
% AA=stats123(location1).PixelList;
% minimum=min(AA,[],1);
% drop_mini_column=minimum(2);
% i_num1=1:1:(location2-1);
% i_num2=(location2+1):1:kkk;
```

```
% i_num=[i_num1 i_num2];
% num=2;
%
% for i=i_num
%     BB=stats123(i).PixelList;
%     minimum=min(BB,[],1);
%     mini_column=minimum(2);
%     mini_row=minimum(1);
%
%     if i~=location1
%        if mini_column ==drop_mini_column
%           location1(num)=i;% the location of the first drop
%           num=num+1;
%        end
%
%     end
% end

breaklength_size=size(stats456(location2).Image);
breaklength(k-1,ii)=magnification*breaklength_size(1);%unit: mm


kkkk=stats123(location1).PixelList; % calculate the smallest vertical coordinater for the first droplet
mini=min(kkkk,[],1);
column=mini(2);
firstdrop(k-1,ii)=column; % record it in the 'firstdrop' matrix.k-1 is the (k-1)th image.ii is the (ii)th threshold value.

ii=ii+1;
end

end

nn=5;
```

```matlab
%calculate the mean value and the standard deviation of the breakup lengths for one flow case
breaklength_c=mean(breaklength(:,nn))% the mean value of the breakup lengths for one flow case under a specified level(mm)
cigma=std(breaklength(:,nn))% the standard deviation of the breakup lengths for one flow case

nn=5;
mm=23;
%calculate the mean value and the standard deviation of the firstdrop locations for one flow case
firstdrop_c=mean((firstdrop(:,nn)-mm)*0.14)% the mean value of the firstdrop locations for one flow case under a specified level(mm)
delta=std((firstdrop(:,nn)-mm)*0.14)% the standard deviation of the first drople locations for one flow case

% detect the linear region in order to determine the universal thresholding
% level
[~,column]=size(breaklength);
thresh=650:50:950;
% thresh=450:25:850;

for i=1:1:column
figure(3)
hold on
plot(thresh(i),breaklength(3000,i),'bo')
hold off
end

A=(firstdrop-23)*0.14;
[~,column]=size(A);
thresh=650:50:950;
for i=1:1:column
figure(3)
hold on
plot(thresh(i),firstdrop(950,i),'ro')
```

```
hold off
end

figure(3)
hold on
xlabel('thresholding level')
ylabel('first droplet location (unit: pixel)')
```

B.3 L_single_img.m

```
% this code is only used to detect the breakup length
% for one image

% The premises (i.e. keypoint) of this code:
% you should specify a row number larger than the smallest
   row number of the water jet region in the cropped image


%Variables list

%breakuplength: breakuplength (unit:mm)
%location1: the location of the first drop
%location2: the location of the largest region
%stats: regionprops(new_matrix,'filledimage');
%stats123: regionprops(new_matrix,'PixelList');
%stats456: regionprops(new_matrix,'Image');
%lowest_row: the specified row number

% clc
% clear all
% close all

img_dir='D:\OneDrive - University of Edinburgh\3.30.2021
   final data\T=1.0s\s=0.0 (1)\air=4\';
cd (img_dir)

% read one image to get image to determine crop region and
   the bottom edge
% of the gas tube
```

```
img_no = "0000";
img = imread(img_dir + "h" + img_no + ".tif");
figure(10)
imshow(img, [])
axis equal

%%
magnification = 0.14; % the magnification of the image (unit:mm/pixel)
resolution_x = 704;% the horizontal resolution of the image (unit:pixel)
lowest_row = 6;% the specified row number which should be larger than the smallest row number of the water jet region (in the cropped image)
crop_indx = [[27, 512]; [1, resolution_x]];% image region to crop to

file='background.tif';
a=imread(file);% read the background
figure(10);
imagesc(a)
a_crop = a(crop_indx(1,1):crop_indx(1,2), crop_indx(2,1):crop_indx(2,2));% background image to crop to
aa=int16(a_crop);

img_crop = img(crop_indx(1,1):crop_indx(1,2), crop_indx(2,1):crop_indx(2,2));% the original image to crop to
bb=int16(img_crop);
cc=aa-bb;% the matrix you want to threshold

cc=cc+int16(255);%?

[p,q]=size(cc);% p is the number of the rows of cc matrix; q is the number of the columns of cc matrix
level=850;%the threshold level????
new_matrix=logical(zeros(p,q));

%thresholding
for i=1:1:p
```

```
    for j=1:1:q
        if cc(i,j)>=level
           new_matrix(i,j)=logical(1); % if value is above
              level, it will be regarded as white
        end
    end
end

%the four rows code below will show you the image after
   background
%subtraction has been done

figure(4);
imagesc(cc)
colormap(gray(256))
axis equal
title('the rescaled image after background subtraction')

%plot the original photo and binarized image
figure(1)
imshow(img_crop,[])
title('the croppped photo')
figure(2)
imshow(new_matrix)
title('the binarized image')


stats=regionprops(new_matrix,'filledimage');
stats123=regionprops(new_matrix,'PixelList');
stats456=regionprops(new_matrix,'Image');

%detecting the water jet region
kk=size(stats123);
kkk=kk(1);
compare1=5;
location2=0;
location1=[];

for i=1:1:kkk
```

```

      BB=stats123(i).PixelList;
      minimum=min(BB,[],1);
      mini_column=minimum(2);
      mini_row=minimum(1);
      c=size(BB);
      size_region=c(1)*c(2);

        if mini_column<=lowest_row % this means that the smallest row number for
                                   % potential water jet region should be larger than
                                   % the row number you specified at the
                                   % beginning
        if size_region>compare1
        compare1=size_region;
        location2=i;%the location of the largest region
        end

        end


end

breaklength=size(stats456(location2).Image);
breaklength=magnification*breaklength(1);%unit:mm
                                             % -1 means that remove the bottom surface of the water tube
                                             % when calculation the breakup length

```

```
figure(3)
imshow(stats(location2).FilledImage)
title('the largest connective region')
stats123(location1).PixelList
```

B.4 L_many_imgs.m

```
% this code is used to detect the breakup length for a group of images

% The premises (i.e. keypoint) of this code:
% you should specify a row number larger than the smallest row number of the water jet region in the cropped image

clc
clear
close all

img_dir='D:\OneDrive - University of Edinburgh\New data\s=3.9 (3)\air=3'; % image folder path
res_dir='D:\OneDrive - University of Edinburgh\L\data1\s=3.9 (3)\air=3'; % result folder path
cd (img_dir)

water_dia=4;% unit:mm
thresh_range=800:50:850; % the range of the thresholding level
magnification=0.12; % the magnification of the image (unit:mm/pixel)
resolution_x=800;% the horizontal resolution of the image (unit:pixel)

n=1501;% number of photos (including background)
start_row=291;% the row number u want to start to crop
lowest_row=6;% the specified row number which should be larger than the smallest row number of the water jet region (in the croppped image)
crop_indx = [[start_row, 845]; [1, resolution_x]];% image region to crop to
```

```matlab

I=cell(1,n);
a=imread('background.tif');% read the background
a_crop=a(crop_indx(1,1):crop_indx(1,2), crop_indx(2,1):
   crop_indx(2,2));% background image to crop to
I{1}=int16(a_crop);% we put background at the first element
[~,num_column]=size(thresh_range);
breaklength=zeros(n-1,num_column);%  preallocate array to
   store the breakup length as columns
firstdrop=zeros(n-1,num_column);% preallocate array to store
    the first droplet location as columns

% read several images
for i=0:1:(n-1)
    if i<10
    imageName=strcat('h','000',num2str(i),'.tif');
    elseif i>=10&&i<100
    imageName=strcat('h','00',num2str(i),'.tif');
    elseif i>=100&&i<1000
    imageName=strcat('h','0',num2str(i),'.tif');
    else
    imageName=strcat('h',num2str(i),'.tif');
    end

    img=imread(imageName);
    img_crop = img(crop_indx(1,1):crop_indx(1,2), crop_indx
       (2,1):crop_indx(2,2));% background image to crop to
    I{i+2}=int16(img_crop);
end

%do the background subtraction for each images
for i=2:1:n
    I{i}=I{1}+(-1).*I{i};
end

% rescaling (note: this rescaling is to plus 255 for each
   pixels values)
for qqq=2:1:n
cc=I{qqq};
```

```
cc=cc+int16(255);
I{qqq}=cc;


end

% thresholding each image
[p,q]=size(I{1}); % get the identical image size


for k=2:1:n % the biggest loop
    ii=1;
for level=thresh_range % thresholding the image under
   different thresholding level
    cc=I{k};
    ccc=false(p,q);
    for i=1:1:p
        for j=1:1:q
            if cc(i,j)>=level
            ccc(i,j)=true;
            end
        end
    end

%detecting the first droplet
new_matrix1=ccc;
stats=regionprops(new_matrix1,'filledimage');
stats123=regionprops(new_matrix1,'PixelList');
stats456=regionprops(new_matrix1,'Image');

[kkk,~]=size(stats123);

compare1=10;
location2=0;
location1=[];


%detect the water jet region
for i=1:1:kkk
```

```

    BB=stats123(i).PixelList;
    minimum=min(BB,[],1);
    mini_column=minimum(2);
    mini_row=minimum(1);
    c=size(BB);
    size_region=c(1)*c(2);

    if mini_column<=lowest_row % this means that the smallest row number for
                                   % potential water jet region should be larger than
                                   % the row number you specified at the
                                   % beginning

    if size_region>compare1
    compare1=size_region;
    location2=i;%the location of the largest region
    end

    end

end

breaklength_size=size(stats456(location2).Image);
breaklength(k-1,ii)=magnification*breaklength_size(1)/water_dia;% non-dimensional breakuplength

ii=ii+1;
end

end

cd (res_dir)
save('L divided by D','breaklength')
```

B.5 Swirl_num2.m

```
% this code is used to calculte the acutal swirl number (data from the specific downstream position)
clc
clear all

Swirl_num = 0.3; % theoretical swirl number
Downstream = 54.0262; % the downstream location (Y = 54.0262 mm : y = 0.27D_l) (Y = 53.3675mm : y = 0.43D_l) (Y = 52.7089mm : y = 0.6D_l) (Nozzle exit (X = -3.534mm, Y= 55.096mm))

Folder_path = sprintf('C:/Users/fanfanboom/OneDrive/Desktop/SPIV/Avg/s=%.1f',Swirl_num);
cd (Folder_path)
Filename = sprintf('s=%.1f_air=3.csv',Swirl_num);
V = readmatrix(Filename); % velocity matrix
V_z = []; % w velocity matrix
V_y = []; % v velocity matrix
shift = 3.534; % unit: mm
Delta_r = 0.6587; % Grid length (unit: mm)
R_outer = 14; % Gas tube outer radius (unit: mm)
[numRows,numCols] = size(V);
ii=1;

for i=1:numRows
    if ii > 1
        if V(i,2) ~= Downstream % i.e. y=0.4D_l
           break
        end
    end

    if V(i,2) == Downstream
       V_z (ii,2) = V(i,5); % w velocity
       V_z (ii,1) = V(i,1); % X coordinate
       V_y (ii,2) = V(i,4); % v velocity
       V_y (ii,1) = V(i,1); % X coordinate
       ii = ii + 1;
    end
```

```
end

%calculate the S
V_z(:,1) = V_z(:,1)+shift; % spatial correction
V_y(:,1) = V_y(:,1)+shift;
[numRows1,numCols1] = size(V_z);
%%
for j=1:numRows1
    if V_z(j,1)>=0
        break
    end
end
a1 = 0;
b1 = 0;
a2 = 0;
b2 = 0;

for i=j:numRows1
    a = abs(V_y(i,2))*abs(V_z(i,2))*V_z(i,1)^2*Delta_r;
%   b = R_outer*(V_y(i,2)^2 - 1/2*V_z(i,2)^2)*abs(V_z(i,1))*Delta_r;
    b = R_outer*V_y(i,2)^2*abs(V_y(i,1))*Delta_r;

    a1 = a1 + a;
    b1 = b1 + b;

end
S_right = a1/b1 % Swirl number

for i=1:(j-1)
    a3 = abs(V_y(i,2))*abs(V_z(i,2))*V_z(i,1)^2*Delta_r;
%   b = R_outer*(V_y(i,2)^2 - 1/2*V_z(i,2)^2)*abs(V_z(i,1))*Delta_r;
    b3 = R_outer*V_y(i,2)^2*abs(V_y(i,1))*Delta_r;

    a2 = a2 + a3;
    b2 = b2 + b3;

end
```

```
S_left = a2/b2 % Swirl number
S_aver = (S_left+S_right)/2 % Average swirl number
```

B.6 clean_img.m

```
%This code is used to produce clean shadowgrams which are used in the paper
clc
close all
clear all

% img_dir='D:\onedrive\OneDrive - University of Edinburgh\3.30.2021 final data\T=1.0s\s=0.0 (1)\air=3\';
% img_dir='D:\onedrive\OneDrive - University of Edinburgh\3.30.2021 final data\T=0.5s\s=1.2 (3)\air=3.0\';
% img_dir='D:\onedrive\OneDrive - University of Edinburgh\3.30.2021 final data\T=0.5s\s=0.8 (1)\air=6\';
img_dir = 'X:\Videos with high M\S=2.5\air=10\';
% img_dir = 'X:\Videos with high M\S=3.9\air=8\';

res_dir = 'D:\onedrive\OneDrive - University of Edinburgh\Desktop\clean imgs';
cd (img_dir)

% read one image to get image to determine crop region and the bottom edge
% of the gas tube
img_no = 3992;
%The image number for various cases
%0361(s=0(1) air=3)
%-488(s=1.2(3) air=3)
%-281 (s=0.8(1) air=6)
%03992(s=2.5 air=10)
%20 (s=3.9 air=8)
%41 (s=3.9 air=8)

img_name = sprintf("h%05d.tif", img_no);
img = imread(img_dir + img_name);
figure(1)
```

```
imshow(img, [])
axis equal

%%
% crop_indx = [[28, 391]; [167,531]];% image region to crop
    to (S=0)
% crop_indx = [[28, 391]; [173,537]];% image region to crop
    to (S=1.2)
% crop_indx = [[24, 387]; [173,539]];% image region to crop
    to (S=0.8)
% crop_indx = [[298, 661]; [234, 598]]; % image region to
    crop to (S=2.5)
crop_indx = [[298, 661]; [234, 598]]; % image region to crop
     to (S=3.9)

file='background.tif';
a=imread(file);% read the background
a_crop = a(crop_indx(1,1):crop_indx(1,2), crop_indx(2,1):
    crop_indx(2,2));% background image to crop to
aa=int16(a_crop);
img_crop = img(crop_indx(1,1):crop_indx(1,2), crop_indx(2,1)
    :crop_indx(2,2));% the original image to crop to
bb=int16(img_crop);
cc=bb-aa;% the matrix you want to threshold
cd (res_dir)
%% Rescale the image for S=2.5
figure(2)
histogram(cc) % Histogram of the image matrix
figure(3)
imshow(cc,[min(min(cc)),-23])
ax = gca;
exportgraphics(ax,'Turn-on.tif','Resolution',600)
figure(4)
imshow(cc,[])
%% Rescale the images for S=0, 0.8 and 1.2
% cc=cc-min(min(cc));
% cc=cc/max(max(cc));
% figure(2)
% imshow(cc,[])
```

```
% ax = gca;
% exportgraphics(ax,'Turn-off.tif','Resolution',600)
```

B.7 D32_part1.m

```
% D32 for X=5D
clc;
close all
clear all

x = 5; % x coordinate
air = 8; % air mass flow rate (kg/h)
% swirl = [0.0 0.3 0.8 1.2]; % swirl number matrix (0-1.2)
swirl = [1.5 2.5 3.1 3.9]; % swirl number matrix (1.5-3.9)
res_dir = 'D:\onedrive\OneDrive - University of Edinburgh\
    final data plots\PDI results\New results\D32\'; % result
    folder path
kk = 5; % color matrix index (if 0<=S<=1.2, kk=1 else kk=5)
% New_dataset_path1 = 'D:/OneDrive - University of Edinburgh
    /New dataset/X=%dD/S=%.1f/R=%.1fD'; % used for Lenovo pc
% New_dataset_path2 = 'D:/OneDrive - University of Edinburgh
    /New dataset/X=%dD/S=%.1f/R=%dD'; % used for lenovo pc
% Old_dataset_path1 = 'D:/OneDrive - University of Edinburgh
    /Dataset/X=%dD/S=%.1f/R=%.1fD'; % used for Lenovo pc
% Old_dataset_path2 = 'D:/OneDrive - University of Edinburgh
    /Dataset/X=%dD/S=%.1f/R=%dD'; % used for lenovo pc

New_dataset_path1 = 'D:/onedrive/OneDrive - University of
    Edinburgh/New dataset/X=%dD/S=%.1f/R=%.1fD'; % used for
    alienware pc
New_dataset_path2 = 'D:/onedrive/OneDrive - University of
    Edinburgh/New dataset/X=%dD/S=%.1f/R=%dD'; % used for
    alienware pc
Old_dataset_path1 = 'D:/onedrive/OneDrive - University of
    Edinburgh/Dataset/X=%dD/S=%.1f/R=%.1fD'; % used for
    alienware pc
Old_dataset_path2 = 'D:/onedrive/OneDrive - University of
    Edinburgh/Dataset/X=%dD/S=%.1f/R=%dD'; % used for
    alienware pc
```

```

color = zeros(1,3,8); % preallocate color matrix for
    plotting
color(:,:,1) = [0 0.4470 0.7410];%(s=0)
color(:,:,2) = [0.8500 0.3250 0.0980];%(s=0.3)
color(:,:,3) = [0.9290 0.6940 0.1250];%(s=0.8)
color(:,:,4) = [1 0 1];%(s=1.2)
color(:,:,5) = [0.4940 0.1840 0.5560];%(s=1.5)
color(:,:,6) = [0.4660 0.6740 0.1880];%(s=2.5)
color(:,:,7) = [0.3010 0.7450 0.9330];%(s=3.1)
color(:,:,8) = [0.6350 0.0780 0.1840];%(s=3.9)


for j = swirl % swirl number
    if j==0.0
        r = [-2.5 0 2.5]; % r coordinate matrix
    elseif j==0.3 || j==0.8
        r = [-5 -2.5 0 2.5 5];
    else
        r = [-7.5 -5 -2.5 0 2.5 5 7.5];
    end

    [~,col] = size(r);
    D = NaN(1,col); % preallocate matrix to store D32
    jj = 1;

    for i = r % r coordinate
        newFolder = '';
        % load the new dataset
        if j == 0.0
            if i == 2.5 || i == -2.5
                newFolder = sprintf(New_dataset_path1,x,j,i);
            end
        end

        if j == 0.3
            if i == 2.5 || i == 5 || i == -2.5 || i == -5
                if i==0 || i==5 || i==-5
```

```
                   newFolder = sprintf(New_dataset_path2,x,j,i);
               else
                   newFolder = sprintf(New_dataset_path1,x,j,i);
               end
            end
        end

        if j == 0.8
            if i == 0 && air == 18
               newFolder = sprintf(New_dataset_path2,x,j,i);
            end
            if i == -2.5 || i == -5
               if i==0 || i==5 || i==-5
                   newFolder = sprintf(New_dataset_path2,x,j,i);
               else
                   newFolder = sprintf(New_dataset_path1,x,j,i);
               end
            end
            if i == 2.5 && air == 16
               newFolder = sprintf(New_dataset_path1,x,j,i);
            end
        end

        if j == 1.2
            if i == -2.5 || i == -5 || i == 5 || i == -7.5 || i == 7.5
               if i==0 || i==5 || i==-5
                   newFolder = sprintf(New_dataset_path2,x,j,i);
               else
                   newFolder = sprintf(New_dataset_path1,x,j,i);
               end
            end
        end
```

```

        if j == 1.5
            if i == -5 || i == -7.5
               if i==0 || i==5 || i==-5
                   newFolder = sprintf(New_dataset_path2,x,j,i);
               else
                   newFolder = sprintf(New_dataset_path1,x,j,i);
               end
            end
        end

        if j == 2.5
            if i == -2.5 && air == 10
               newFolder = sprintf(New_dataset_path1,x,j,i);
            end
            if i == 7.5 && air == 8
               newFolder = sprintf(New_dataset_path1,x,j,i);
            end
        end

        if j == 3.1
            if i == 7.5 && air == 10
               newFolder = sprintf(New_dataset_path1,x,j,i);
            end
        end

        if j == 3.9
            if air == 8
                if i == 5
                   newFolder = sprintf(New_dataset_path2,x,j,i);
                elseif i == 7.5
                   newFolder = sprintf(New_dataset_path1,x,j,i);
                end
            end
        end
```

```

        if newFolder == "" % load the old dataset if the new
            dataset does not have the corresponding data for
            the flow cases
            if i==0 || i==5 || i==-5
                newFolder = sprintf(Old_dataset_path2,x,j,i);
            else
                newFolder = sprintf(Old_dataset_path1,x,j,i);
            end
        end

        cd(newFolder);
        filename = sprintf('air=%d D32 PVC.csv',air);
        D(1,jj) = xlsread(filename,'B1:B1'); % D32 (um)
        jj = jj+1;
    end

    hold on
    fig = figure(1);
    plot(r,D,'s-','color',color(:,:,kk),'MarkerSize',10,'
       MarkerEdgeColor',color(:,:,kk),'MarkerFaceColor',
       color(:,:,kk))
    box on
    grid on
    ax = gca;
    ax.FontSize = 15; % set the font size for the tick
       labels
    xlabel('$r/D_1$','Interpreter','latex','FontSize',16.5)
    xlim([-10,10])
    ylabel('$D_{32}\,(\mu m)$','Interpreter','latex','
       FontSize',16.5)
    ylim([0,80])
    title(sprintf('$y=%dD_1$',x),'Interpreter','latex','
       FontSize',16.5)
    hold off
    kk = kk+1;
end

% plot the legends
```

```
if j == 1.2
    if air == 16
    legend('$S=0,\ We_A=256$','$S=0.3,\ We_A=1126$','$S=0.8,\ We_A=1126$','$S=1.2,\ We_A=1126$','Interpreter','latex','Location','northeast','FontSize',10)
    elseif air ==18
    legend('$S=0,\ We_A=324$','$S=0.3,\ We_A=1426$','$S=0.8,\ We_A=1426$','$S=1.2,\ We_A=1426$','Interpreter','latex','Location','northeast','FontSize',10)
    end
elseif j == 3.9
    if air == 8
    legend('$S=1.5,\ We_A=282$','$S=2.5,\ We_A=282$','$S=3.1,\ We_A=282$','$S=3.9,\ We_A=282$','Interpreter','latex','FontSize',10)
    elseif air == 10
    legend('$S=1.5,\ We_A=440$','$S=2.5,\ We_A=440$','$S=3.1,\ We_A=440$','$S=3.9,\ We_A=440$','Interpreter','latex','FontSize',10)
    end
end

cd(res_dir)
saveas(fig,sprintf('S=%.1f-%.1f_air=%d_Y=%dD.fig',swirl(1),swirl(4),air,x)) % save image
```

B.8 D32_part2.m

```
% D32 for X=10D
clc;
clear all
close all

x = 10; % x coordinate
air = 18; % air mass flow rate (kg/h)
swirl = [0.0 0.3 0.8 1.2]; % swirl number matrix (0-1.2)
% swirl = [1.5 2.5 3.1 3.9]; % swirl number matrix (1.5-3.9)
res_dir = 'D:\OneDrive - University of Edinburgh\final data plots\PDI results\New results\D32\'; % result folder path
```

```
kk = 1; % color matrix index (if 0<=S<=1.2, kk=1 else kk=5)
New_dataset_path1 = 'D:/OneDrive - University of Edinburgh/New dataset/X=%dD/S=%.1f/R=%.1fD'; % used for Lenovo pc
New_dataset_path2 = 'D:/OneDrive - University of Edinburgh/New dataset/X=%dD/S=%.1f/R=%dD'; % used for lenovo pc
Old_dataset_path1 = 'D:/OneDrive - University of Edinburgh/Dataset/X=%dD/S=%.1f/R=%.1fD'; % used for Lenovo pc
Old_dataset_path2 = 'D:/OneDrive - University of Edinburgh/Dataset/X=%dD/S=%.1f/R=%dD'; % used for lenovo pc

% New_dataset_path1 = 'D:/onedrive/OneDrive - University of Edinburgh/New dataset/X=%dD/S=%.1f/R=%.1fD'; % used for alienware pc
% New_dataset_path2 = 'D:/onedrive/OneDrive - University of Edinburgh/New dataset/X=%dD/S=%.1f/R=%dD'; % used for alienware pc
% Old_dataset_path1 = 'D:/onedrive/OneDrive - University of Edinburgh/Dataset/X=%dD/S=%.1f/R=%.1fD'; % used for alienware pc
% Old_dataset_path2 = 'D:/onedrive/OneDrive - University of Edinburgh/Dataset/X=%dD/S=%.1f/R=%dD'; % used for alienware pc

color = zeros(1,3,8); % preallocate color matrix for plotting
color(:,:,1) = [0 0.4470 0.7410];%(s=0)
color(:,:,2) = [0.8500 0.3250 0.0980];%(s=0.3)
color(:,:,3) = [0.9290 0.6940 0.1250];%(s=0.8)
color(:,:,4) = [1 0 1];%(s=1.2)
color(:,:,5) = [0.4940 0.1840 0.5560];%(s=1.5)
color(:,:,6) = [0.4660 0.6740 0.1880];%(s=2.5)
color(:,:,7) = [0.3010 0.7450 0.9330];%(s=3.1)
color(:,:,8) = [0.6350 0.0780 0.1840];%(s=3.9)

for j = swirl % swirl number
    if j==0.0
        r = [-5 -2.5 0 2.5 5]; % r coordinate matrix
    elseif j==3.9 && air==10
        r = [-7.5 -5 -2.5 0 2.5 5];
```

```
    else
       r = [-7.5 -5 -2.5 0 2.5 5 7.5];
    end

    [~,col] = size(r);
    D = NaN(1,col); % preallocate matrix to store D32
    jj = 1;

    for i = r % r coordinate
        newFolder = '';
        % load the new dataset
        if j == 0.0
            if i == -2.5
               newFolder = sprintf(New_dataset_path1,x,j,i);
            end
        end

        if j == 1.2
            if i == -2.5 && air == 18
               newFolder = sprintf(New_dataset_path1,x,j,i);
            end
            if i == -5 || i == -7.5
               if i==0 || i==5 || i==-5
                   newFolder = sprintf(New_dataset_path2,x,j,i);
               else
                   newFolder = sprintf(New_dataset_path1,x,j,i);
               end
            end
        end

        if j ==0.8
            if i == -2.5 || i == 5 || i == 7.5
               if i==0 || i==5 || i==-5
                   newFolder = sprintf(New_dataset_path2,x,j,i);
               else
```

```
                   newFolder = sprintf(New_dataset_path1,x,j,i);
               end
            end

            if i == -5
               newFolder = sprintf(New_dataset_path2,x,j,i);
            end

            if i == -7.5
                newFolder = sprintf(New_dataset_path1,x,j,i);
            end
        end

        if j == 0.3
            if i == 0 || i == 2.5 || i == -2.5
               if i==0 || i==5 || i==-5
                   newFolder = sprintf(New_dataset_path2,x,j,i);
               else
                   newFolder = sprintf(New_dataset_path1,x,j,i);
               end
            end
        end

        if newFolder == "" % load the old dataset if the new dataset does not have the corresponding data for the flow cases
            if i==0 || i==5 || i==-5
               newFolder = sprintf(Old_dataset_path2,x,j,i);
            else
               newFolder = sprintf(Old_dataset_path1,x,j,i);
            end
        end

           cd(newFolder);
           filename = sprintf('air=%d D32 PVC.csv',air);
```

```
            D(1,jj) = xlsread(filename,'B1:B1'); % D32 (um)
            jj = jj+1;
    end

    hold on
    fig = figure(1);
    plot(r,D,'s-','color',color(:,:,kk),'MarkerSize',10,'MarkerEdgeColor',color(:,:,kk),'MarkerFaceColor',color(:,:,kk))
    box on
    grid on
    ax = gca;
    ax.FontSize = 15; % set the font size for the tick labels
    xlabel('$r/D_l$','Interpreter','latex','FontSize',16.5)
    xlim([-10,10])
    ylabel('$D_{32}\,(\mu m)$','Interpreter','latex','FontSize',16.5)
    title(sprintf('$y=%dD_l$',x),'Interpreter','latex','FontSize',16.5)
    hold off
    kk = kk+1;
end

% plot the legends
if j == 1.2
    if air == 16
    legend('$S=0,\ We_A=256$','$S=0.3,\ We_A=1126$','$S=0.8,\ We_A=1126$','$S=1.2,\ We_A=1126$','Interpreter','latex','Location','northeast','FontSize',10)
    elseif air ==18
    legend('$S=0,\ We_A=324$','$S=0.3,\ We_A=1426$','$S=0.8,\ We_A=1426$','$S=1.2,\ We_A=1426$','Interpreter','latex','Location','northeast','FontSize',10)
    end
elseif j == 3.9
    if air == 8
```

```
    legend('$S=1.5,\ We_A=282$','$S=2.5,\ We_A=282$','$S=3.1,\ We_A=282$','$S=3.9,\ We_A=282$','Interpreter','latex','FontSize',10)
    elseif air == 10
    legend('$S=1.5,\ We_A=440$','$S=2.5,\ We_A=440$','$S=3.1,\ We_A=440$','$S=3.9,\ We_A=440$','Interpreter','latex','FontSize',10)
    end
end

cd(res_dir)
saveas(fig,sprintf('S=%.1f-%.1f_air=%d_Y=%dD.fig',swirl(1),swirl(4),air,x)) % save image
```

B.9 Dia_distribution_part1.m

```
% droplet diameter distributions for X=5D
clc;
clear all
close all

x = 5; % x coordinate
air = 8; % air mass flow rate (kg/h)
% swirl = [0.0 0.3 0.8 1.2]; % swirl number matrix (0-1.2)
swirl = [1.5 2.5 3.1 3.9]; % swirl number matrix (1.5-3.9)
res_dir = 'D:\onedrive\OneDrive - University of Edinburgh\final data plots\PDI results\New results\Diameter distribution\'; % result folder path
kk = 5; % color matrix index (if 0<=S<=1.2, kk=1 else kk=5)
% New_dataset_path1 = 'D:/OneDrive - University of Edinburgh/New dataset/X=%dD/S=%.1f/R=%.1fD'; % used for Lenovo pc
% New_dataset_path2 = 'D:/OneDrive - University of Edinburgh/New dataset/X=%dD/S=%.1f/R=%dD'; % used for lenovo pc
% Old_dataset_path1 = 'D:/OneDrive - University of Edinburgh/Dataset/X=%dD/S=%.1f/R=%.1fD'; % used for Lenovo pc
% Old_dataset_path2 = 'D:/OneDrive - University of Edinburgh/Dataset/X=%dD/S=%.1f/R=%dD'; % used for lenovo pc

```

```
New_dataset_path1 = 'D:/onedrive/OneDrive - University of Edinburgh/New dataset/X=%dD/S=%.1f/R=%.1fD'; % used for alienware pc
New_dataset_path2 = 'D:/onedrive/OneDrive - University of Edinburgh/New dataset/X=%dD/S=%.1f/R=%dD'; % used for alienware pc
Old_dataset_path1 = 'D:/onedrive/OneDrive - University of Edinburgh/Dataset/X=%dD/S=%.1f/R=%.1fD'; % used for alienware pc
Old_dataset_path2 = 'D:/onedrive/OneDrive - University of Edinburgh/Dataset/X=%dD/S=%.1f/R=%dD'; % used for alienware pc

color = zeros(1,3,8); % preallocate color matrix for plotting
color(:,:,1) = [0 0.4470 0.7410];%(s=0)
color(:,:,2) = [0.8500 0.3250 0.0980];%(s=0.3)
color(:,:,3) = [0.9290 0.6940 0.1250];%(s=0.8)
color(:,:,4) = [1 0 1];%(s=1.2)
color(:,:,5) = [0.4940 0.1840 0.5560];%(s=1.5)
color(:,:,6) = [0.4660 0.6740 0.1880];%(s=2.5)
color(:,:,7) = [0.3010 0.7450 0.9330];%(s=3.1)
color(:,:,8) = [0.6350 0.0780 0.1840];%(s=3.9)

for j = swirl % swirl number
    if j==0.0
       r = [-2.5 0 2.5]; % r coordinate matrix
    elseif j==0.3 || j==0.8
       r = [-5 -2.5 0 2.5 5];
    else
       r = [-7.5 -5 -2.5 0 2.5 5 7.5];
    end

     for i = r % r coordinate
        newFolder = '';
        % load the new dataset
        if j == 0.0
            if i == 2.5 || i == -2.5
               newFolder = sprintf(New_dataset_path1,x,j,i);
```

```
            end
        end

        if j == 0.3
            if i == 2.5 || i == 5 || i == -2.5 || i == -5
               if i==0 || i==5 || i==-5
                   newFolder = sprintf(New_dataset_path2,x,j,i);
               else
                   newFolder = sprintf(New_dataset_path1,x,j,i);
               end
            end
        end

        if j == 0.8
            if i == 0 && air == 18
               newFolder = sprintf(New_dataset_path2,x,j,i);
            end
            if i == -2.5 || i == -5
               if i==0 || i==5 || i==-5
                   newFolder = sprintf(New_dataset_path2,x,j,i);
               else
                   newFolder = sprintf(New_dataset_path1,x,j,i);
               end
            end
            if i == 2.5 && air == 16
               newFolder = sprintf(New_dataset_path1,x,j,i);
            end
        end

        if j == 1.2
            if i == -2.5 || i == -5 || i == 5 || i == -7.5 || i == 7.5
               if i==0 || i==5 || i==-5
                   newFolder = sprintf(New_dataset_path2,x,j,i);
```

```
               else
                   newFolder = sprintf(New_dataset_path1,x,j,i);
               end
            end
        end

        if j == 1.5
            if i == -5 || i == -7.5
               if i==0 || i==5 || i==-5
                   newFolder = sprintf(New_dataset_path2,x,j,i);
               else
                   newFolder = sprintf(New_dataset_path1,x,j,i);
               end
            end
        end

        if j == 2.5
            if i == -2.5 && air == 10
               newFolder = sprintf(New_dataset_path1,x,j,i);
            end
            if i == 7.5 && air == 8
               newFolder = sprintf(New_dataset_path1,x,j,i);
            end
        end

        if j == 3.1
            if i == 7.5 && air == 10
               newFolder = sprintf(New_dataset_path1,x,j,i);
            end
        end

        if j == 3.9
            if air == 8
                if i == 5
                   newFolder = sprintf(New_dataset_path2,x,j,i);
```

```matlab
                elseif i == 7.5
                   newFolder = sprintf(New_dataset_path1,x,j,i);
                end
            end
        end

        if newFolder == "" % load the old dataset if the new dataset does not have the corresponding data for the flow cases
            if i==0 || i==5 || i==-5
               newFolder = sprintf(Old_dataset_path2,x,j,i);
            else
               newFolder = sprintf(Old_dataset_path1,x,j,i);
            end
        end

           cd(newFolder);
           filename = sprintf('air=%d Dia vs time.csv',air);
           D = xlsread(filename,'B:B'); % Diameters (um)
           [n,~]=size(D);% get the number of rows of data
           g1 = repmat(i,n,1); % label each row
           fig = figure(kk);
           hold on
           bbb = boxchart(g1,D,'LineWidth',1.5); % box plot
           bbb.BoxWidth = 0.5; % box width
           bbb.WhiskerLineColor = color(:,:,kk);
           bbb.BoxFaceColor = color(:,:,kk);
           bbb.MarkerColor = color(:,:,kk);
           grid on
           xlabel('$r/D_1$','Interpreter','latex')
           ylabel('$D\,(\mu m)$','Interpreter','latex')
           title(sprintf('Y=%dD air=%dkg/h S=%.1f',x,air,j))
           hold off

     end

    hold on %insert legend
```

```
    if j==0.0
        legend('$S=0$','Interpreter','latex')
    elseif j==0.3
        legend('$S=0.3$','Interpreter','latex')
    elseif j==0.8
        legend('$S=0.8$','Interpreter','latex')
    elseif j==1.2
        legend('$S=1.2$','Interpreter','latex')
    elseif j==1.5
        legend('$S=1.5$','Interpreter','latex')
    elseif j==2.5
        legend('$S=2.5$','Interpreter','latex')
    elseif j==3.1
        legend('$S=3.1$','Interpreter','latex')
    else
        legend('$S=3.9$','Interpreter','latex')
    end
    hold off

    cd(res_dir);
    saveas(fig,sprintf('S=%.1f_air=%d_X=%dD.fig',j,air,x)) % save the image
    kk = kk+1;
end
```

B.10 Dia_distribution_part2.m

```
% droplet diameter distributions for X=10D
clc;
clear all
close all

x = 10; % x coordinate
air = 18; % air mass flow rate (kg/h)
swirl = [0.0 0.3 0.8 1.2]; % swirl number matrix (0-1.2)
% swirl = [1.5 2.5 3.1 3.9]; % swirl number matrix (1.5-3.9)
res_dir = 'D:\OneDrive - University of Edinburgh\final data plots\PDI results\New results\Diameter distribution\'; % result folder path
```

```
kk = 1; % color matrix index (if 0<=S<=1.2, kk=1 else kk=5)
New_dataset_path1 = 'D:/OneDrive - University of Edinburgh/New dataset/X=%dD/S=%.1f/R=%.1fD'; % used for Lenovo pc
New_dataset_path2 = 'D:/OneDrive - University of Edinburgh/New dataset/X=%dD/S=%.1f/R=%dD'; % used for lenovo pc
Old_dataset_path1 = 'D:/OneDrive - University of Edinburgh/Dataset/X=%dD/S=%.1f/R=%.1fD'; % used for Lenovo pc
Old_dataset_path2 = 'D:/OneDrive - University of Edinburgh/Dataset/X=%dD/S=%.1f/R=%dD'; % used for lenovo pc

% New_dataset_path1 = 'D:/onedrive/OneDrive - University of Edinburgh/New dataset/X=%dD/S=%.1f/R=%.1fD'; % used for alienware pc
% New_dataset_path2 = 'D:/onedrive/OneDrive - University of Edinburgh/New dataset/X=%dD/S=%.1f/R=%dD'; % used for alienware pc
% Old_dataset_path1 = 'D:/onedrive/OneDrive - University of Edinburgh/Dataset/X=%dD/S=%.1f/R=%.1fD'; % used for alienware pc
% Old_dataset_path2 = 'D:/onedrive/OneDrive - University of Edinburgh/Dataset/X=%dD/S=%.1f/R=%dD'; % used for alienware pc

color = zeros(1,3,8); % preallocate color matrix for plotting
color(:,:,1) = [0 0.4470 0.7410];%(s=0)
color(:,:,2) = [0.8500 0.3250 0.0980];%(s=0.3)
color(:,:,3) = [0.9290 0.6940 0.1250];%(s=0.8)
color(:,:,4) = [1 0 1];%(s=1.2)
color(:,:,5) = [0.4940 0.1840 0.5560];%(s=1.5)
color(:,:,6) = [0.4660 0.6740 0.1880];%(s=2.5)
color(:,:,7) = [0.3010 0.7450 0.9330];%(s=3.1)
color(:,:,8) = [0.6350 0.0780 0.1840];%(s=3.9)

for j = swirl % swirl number
    if j==0.0
        r = [-5 -2.5 0 2.5 5]; % r coordinate matrix
    elseif j==3.9 && air==10
        r = [-7.5 -5 -2.5 0 2.5 5];
```

```
    else
       r = [-7.5 -5 -2.5 0 2.5 5 7.5];
    end

    for i = r % r coordinate
        newFolder = '';
        % load the new dataset
        if j == 0.0
            if i == -2.5
               newFolder = sprintf(New_dataset_path1,x,j,i);
            end
        end

        if j == 1.2
            if i == -2.5 && air == 18
               newFolder = sprintf(New_dataset_path1,x,j,i);
            end
            if i == -5 || i == -7.5
               if i==0 || i==5 || i==-5
                   newFolder = sprintf(New_dataset_path2,x,j
                      ,i);
               else
                   newFolder = sprintf(New_dataset_path1,x,j
                      ,i);
               end
            end
        end

         if j ==0.8
            if i == -2.5 || i == 5 || i == 7.5
               if i==0 || i==5 || i==-5
                   newFolder = sprintf(New_dataset_path2,x,j
                      ,i);
               else
                   newFolder = sprintf(New_dataset_path1,x,j
                      ,i);
               end
            end

```

```
            if i == -5
               newFolder = sprintf(New_dataset_path2,x,j,i);
            end

            if i == -7.5
                newFolder = sprintf(New_dataset_path1,x,j,i);
            end
        end

        if j == 0.3
            if i == 0 || i == 2.5 || i == -2.5
               if i==0 || i==5 || i==-5
                   newFolder = sprintf(New_dataset_path2,x,j,i);
               else
                   newFolder = sprintf(New_dataset_path1,x,j,i);
               end
            end
        end

        if  newFolder == "" % load the old dataset if the new dataset does not have the corresponding data for the flow cases
            if i==0 || i==5 || i==-5
               newFolder = sprintf(Old_dataset_path2,x,j,i);
            else
               newFolder = sprintf(Old_dataset_path1,x,j,i);
            end
        end

           cd(newFolder);
           filename = sprintf('air=%d Dia vs time.csv',air);
           D = xlsread(filename,'B:B'); % Velocity data
           [n,~]=size(D);% get the number of the rows of data
           g1 = repmat(i,n,1); % label each row
           fig = figure(kk);
```

```
           hold on
           bbb = boxchart(g1,D,'LineWidth',1.5); % box plot
           bbb.BoxWidth = 0.5; % box width
           bbb.WhiskerLineColor = color(:,:,kk);
           bbb.BoxFaceColor = color(:,:,kk);
           bbb.MarkerColor = color(:,:,kk);
           grid on
           xlabel('$r/D_1$','Interpreter','latex')
           ylabel('$D\,(\mu m)$','Interpreter','latex')
           title(sprintf('Y=%dD air=%dkg/h S=%.1f',x,air,j))
           hold off
    end

    hold on %insert legend
    if j==0.0
       legend('$S=0$','Interpreter','latex')
    elseif j==0.3
       legend('$S=0.3$','Interpreter','latex')
    elseif j==0.8
       legend('$S=0.8$','Interpreter','latex')
    elseif j==1.2
       legend('$S=1.2$','Interpreter','latex')
    elseif j==1.5
       legend('$S=1.5$','Interpreter','latex')
    elseif j==2.5
       legend('$S=2.5$','Interpreter','latex')
    elseif j==3.1
       legend('$S=3.1$','Interpreter','latex')
    else
       legend('$S=3.9$','Interpreter','latex')
    end
    hold off

    cd(res_dir);
    saveas(fig,sprintf('S=%.1f_air=%d_Y=%dD.fig',j,air,x)) % save the image
    kk = kk+1;
end
```

B.11 v_distribution_part1.m

```
% Droplet velocity distributions for X=5D (U or V component)
clc;
clear all
close all

x = 5; % x coordinate
air = 8; % air mass flow rate (kg/h)
% swirl = [0.0 0.3 0.8 1.2]; % swirl number matrix (0-1.2)
swirl = [1.5 2.5 3.1 3.9]; % swirl number matrix (1.5-3.9)
res_dir = 'D:\onedrive\OneDrive - University of Edinburgh\
    final data plots\PDI results\New results\w distribution\
    used for paper\'; % result folder path
kk = 5; % color matrix index (if 0<=S<=1.2, kk=1 else kk=5)
% New_dataset_path1 = 'D:/OneDrive - University of Edinburgh
    /New dataset/X=%dD/S=%.1f/R=%.1fD'; % used for Lenovo pc
% New_dataset_path2 = 'D:/OneDrive - University of Edinburgh
    /New dataset/X=%dD/S=%.1f/R=%dD'; % used for lenovo pc
% Old_dataset_path1 = 'D:/OneDrive - University of Edinburgh
    /Dataset/X=%dD/S=%.1f/R=%.1fD'; % used for Lenovo pc
% Old_dataset_path2 = 'D:/OneDrive - University of Edinburgh
    /Dataset/X=%dD/S=%.1f/R=%dD'; % used for lenovo pc

New_dataset_path1 = 'D:/onedrive/OneDrive - University of
    Edinburgh/New dataset/X=%dD/S=%.1f/R=%.1fD'; % used for
    alienware pc
New_dataset_path2 = 'D:/onedrive/OneDrive - University of
    Edinburgh/New dataset/X=%dD/S=%.1f/R=%dD'; % used for
    alienware pc
Old_dataset_path1 = 'D:/onedrive/OneDrive - University of
    Edinburgh/Dataset/X=%dD/S=%.1f/R=%.1fD'; % used for
    alienware pc
Old_dataset_path2 = 'D:/onedrive/OneDrive - University of
    Edinburgh/Dataset/X=%dD/S=%.1f/R=%dD'; % used for
    alienware pc

color = zeros(1,3,8); % preallocate color matrix for
    plotting
color(:,:,1) = [0 0.4470 0.7410];%(s=0)
```

```
color(:,:,2) = [0.8500 0.3250 0.0980];%(s=0.3)
color(:,:,3) = [0.9290 0.6940 0.1250];%(s=0.8)
color(:,:,4) = [1 0 1];%(s=1.2)
color(:,:,5) = [0.4940 0.1840 0.5560];%(s=1.5)
color(:,:,6) = [0.4660 0.6740 0.1880];%(s=2.5)
color(:,:,7) = [0.3010 0.7450 0.9330];%(s=3.1)
color(:,:,8) = [0.6350 0.0780 0.1840];%(s=3.9)

for j = swirl % swirl number
    if j==0.0
       r = [-2.5 0 2.5]; % r coordinate matrix
    elseif j==0.3 || j==0.8
       r = [-5 -2.5 0 2.5 5];
    else
       r = [-7.5 -5 -2.5 0 2.5 5 7.5];
    end

    for i = r % r coordinate
        newFolder = '';
        % load the new dataset
        if j == 0.0
            if i == 2.5 || i == -2.5
               newFolder = sprintf(New_dataset_path1,x,j,i);
            end
        end

        if j == 0.3
            if i == 2.5 || i == 5 || i == -2.5 || i == -5
               if i==0 || i==5 || i==-5
                   newFolder = sprintf(New_dataset_path2,x,j
                       ,i);
               else
                   newFolder = sprintf(New_dataset_path1,x,j
                       ,i);
               end
            end
        end

        if j == 0.8
```

```
            if i == 0 && air == 18
               newFolder = sprintf(New_dataset_path2,x,j,i);
            end
            if i == -2.5 || i == -5
               if i==0 || i==5 || i==-5
                   newFolder = sprintf(New_dataset_path2,x,j,i);
               else
                   newFolder = sprintf(New_dataset_path1,x,j,i);
               end
            end
            if i == 2.5 && air == 16
               newFolder = sprintf(New_dataset_path1,x,j,i);
            end
        end

        if j == 1.2
            if i == -2.5 || i == -5 || i == 5 || i == -7.5 || i == 7.5
               if i==0 || i==5 || i==-5
                   newFolder = sprintf(New_dataset_path2,x,j,i);
               else
                   newFolder = sprintf(New_dataset_path1,x,j,i);
               end
            end
        end

        if j == 1.5
            if i == -5 || i == -7.5
               if i==0 || i==5 || i==-5
                   newFolder = sprintf(New_dataset_path2,x,j,i);
               else
                   newFolder = sprintf(New_dataset_path1,x,j,i);
               end
```

```
            end
        end

        if j == 2.5
            if i == -2.5 && air == 10
               newFolder = sprintf(New_dataset_path1,x,j,i);
            end
            if i == 7.5 && air == 8
               newFolder = sprintf(New_dataset_path1,x,j,i);
            end
        end

        if j == 3.1
            if i == 7.5 && air == 10
               newFolder = sprintf(New_dataset_path1,x,j,i);
            end
        end

        if j == 3.9
            if air == 8
                if i == 5
                   newFolder = sprintf(New_dataset_path2,x,j
                      ,i);
                elseif i == 7.5
                   newFolder = sprintf(New_dataset_path1,x,j
                      ,i);
                end
            end
        end

        if newFolder == "" % load the old dataset if the new
            dataset does not have the corresponding data for
            the flow cases
            if i==0 || i==5 || i==-5
               newFolder = sprintf(Old_dataset_path2,x,j,i);
            else
               newFolder = sprintf(Old_dataset_path1,x,j,i);
            end
        end
```

```

           cd(newFolder);
           filename = sprintf('air=%d w vs t.csv',air);
           D = xlsread(filename,'B:B'); % Velocity data
           [n,~]=size(D);% get the number of the rows of data
           g1 = repmat(i,n,1); % label each row
           fig = figure(kk);
           hold on
           bbb = boxchart(g1,D,'LineWidth',1.5); % box plot
           bbb.BoxWidth = 0.5; % box width
           bbb.WhiskerLineColor = color(:,:,kk);
           bbb.BoxFaceColor = color(:,:,kk);
           bbb.MarkerColor = color(:,:,kk);
           box on
           grid on
           ax = gca;
           ax.FontSize = 15; % set the font size for the tick labels
           xlabel('$r/D_1$','Interpreter','latex','FontSize',16.5)
           xlim([-10,10])
           ylabel('$U\,(m/s)$','Interpreter','latex','FontSize',16.5)
           hold off
    end

    hold on %insert title
    if j==0.0
       if air==16
       title('$S=0,\ We_A=1126$','Interpreter','latex','FontSize',16.5)
       elseif air==18
       title('$S=0,\ We_A=1426$','Interpreter','latex','FontSize',16.5)
       end
    elseif j==0.3
       if air==16
```

```
       title('$S=0.3,\ We_A=1126$','Interpreter','latex','FontSize',16.5)
       elseif air==18
       title('$S=0.3,\ We_A=1426$','Interpreter','latex','FontSize',16.5)
       end
    elseif j==0.8
       if air==16
       title('$S=0.8,\ We_A=1126$','Interpreter','latex','FontSize',16.5)
       elseif air==18
       title('$S=0.8,\ We_A=1426$','Interpreter','latex','FontSize',16.5)
       end
    elseif j==1.2
       if air==16
       title('$S=1.2,\ We_A=1126$','Interpreter','latex','FontSize',16.5)
       elseif air==18
       title('$S=1.2,\ We_A=1426$','Interpreter','latex','FontSize',16.5)
       end
    elseif j==1.5
       if air==8
       title('$S=1.5,\ We_A=282$','Interpreter','latex','FontSize',16.5)
       elseif air==10
       title('$S=1.5,\ We_A=440$','Interpreter','latex','FontSize',16.5)
       end
    elseif j==2.5
       if air==8
       title('$S=2.5,\ We_A=282$','Interpreter','latex','FontSize',16.5)
       elseif air==10
       title('$S=2.5,\ We_A=440$','Interpreter','latex','FontSize',16.5)
       end
    elseif j==3.1
```

```
        if air==8
        title('$S=3.1,\ We_A=282$','Interpreter','latex','FontSize',16.5)
        elseif air==10
        title('$S=3.1,\ We_A=440$','Interpreter','latex','FontSize',16.5)
        end
    else
        if air==8
        title('$S=3.9,\ We_A=282$','Interpreter','latex','FontSize',16.5)
        elseif air==10
        title('$S=3.9,\ We_A=440$','Interpreter','latex','FontSize',16.5)
        end
    end
    hold off

    cd(res_dir);
    saveas(fig,sprintf('S=%.1f_air=%d_Y=%dD.fig',j,air,x)) % save the image
    kk = kk+1;
end
```

B.12 v_distribution_part2.m

```
% Droplet velocity distributions for X=10D (U or V component)
clc;
clear all
close all

x = 10; % x coordinate
air = 18; % air mass flow rate (kg/h)
swirl = [0.0 0.3 0.8 1.2]; % swirl number matrix (0-1.2)
% swirl = [1.5 2.5 3.1 3.9]; % swirl number matrix (1.5-3.9)
res_dir = 'D:\OneDrive - University of Edinburgh\final data plots\PDI results\New results\v distribution\'; % result folder path
```

```
kk = 1; % color matrix index (if 0<=S<=1.2, kk=1 else kk=5)
New_dataset_path1 = 'D:/OneDrive - University of Edinburgh/New dataset/X=%dD/S=%.1f/R=%.1fD'; % used for Lenovo pc
New_dataset_path2 = 'D:/OneDrive - University of Edinburgh/New dataset/X=%dD/S=%.1f/R=%dD'; % used for lenovo pc
Old_dataset_path1 = 'D:/OneDrive - University of Edinburgh/Dataset/X=%dD/S=%.1f/R=%.1fD'; % used for Lenovo pc
Old_dataset_path2 = 'D:/OneDrive - University of Edinburgh/Dataset/X=%dD/S=%.1f/R=%dD'; % used for lenovo pc

% New_dataset_path1 = 'D:/onedrive/OneDrive - University of Edinburgh/New dataset/X=%dD/S=%.1f/R=%.1fD'; % used for alienware pc
% New_dataset_path2 = 'D:/onedrive/OneDrive - University of Edinburgh/New dataset/X=%dD/S=%.1f/R=%dD'; % used for alienware pc
% Old_dataset_path1 = 'D:/onedrive/OneDrive - University of Edinburgh/Dataset/X=%dD/S=%.1f/R=%.1fD'; % used for alienware pc
% Old_dataset_path2 = 'D:/onedrive/OneDrive - University of Edinburgh/Dataset/X=%dD/S=%.1f/R=%dD'; % used for alienware pc

color = zeros(1,3,8); % preallocate color matrix for plotting
color(:,:,1) = [0 0.4470 0.7410];%(s=0)
color(:,:,2) = [0.8500 0.3250 0.0980];%(s=0.3)
color(:,:,3) = [0.9290 0.6940 0.1250];%(s=0.8)
color(:,:,4) = [1 0 1];%(s=1.2)
color(:,:,5) = [0.4940 0.1840 0.5560];%(s=1.5)
color(:,:,6) = [0.4660 0.6740 0.1880];%(s=2.5)
color(:,:,7) = [0.3010 0.7450 0.9330];%(s=3.1)
color(:,:,8) = [0.6350 0.0780 0.1840];%(s=3.9)

for j = swirl % swirl number
    if j==0.0
        r = [-5 -2.5 0 2.5 5]; % r coordinate matrix
    elseif j==3.9 && air==10
        r = [-7.5 -5 -2.5 0 2.5 5];
```

```
    else
       r = [-7.5 -5 -2.5 0 2.5 5 7.5];
    end

    for i = r % r coordinate
        newFolder = '';
        % load the new dataset
        if j == 0.0
            if i == -2.5
               newFolder = sprintf(New_dataset_path1,x,j,i);
            end
        end

        if j == 1.2
            if i == -2.5 && air == 18
               newFolder = sprintf(New_dataset_path1,x,j,i);
            end
            if i == -5 || i == -7.5
               if i==0 || i==5 || i==-5
                   newFolder = sprintf(New_dataset_path2,x,j,i);
               else
                   newFolder = sprintf(New_dataset_path1,x,j,i);
               end
            end
        end

        if j ==0.8
            if i == -2.5 || i == 5 || i == 7.5
               if i==0 || i==5 || i==-5
                   newFolder = sprintf(New_dataset_path2,x,j,i);
               else
                   newFolder = sprintf(New_dataset_path1,x,j,i);
               end
            end

```

```
            if i == -5
               newFolder = sprintf(New_dataset_path2,x,j,i);
            end

            if i == -7.5
                newFolder = sprintf(New_dataset_path1,x,j,i);
            end
        end

        if j == 0.3
            if i == 0 || i == 2.5 || i == -2.5
               if i==0 || i==5 || i==-5
                   newFolder = sprintf(New_dataset_path2,x,j,i);
               else
                   newFolder = sprintf(New_dataset_path1,x,j,i);
               end
            end
        end

        if  newFolder == "" % load the old dataset if the new dataset does not have the corresponding data for the flow cases
            if i==0 || i==5 || i==-5
               newFolder = sprintf(Old_dataset_path2,x,j,i);
            else
               newFolder = sprintf(Old_dataset_path1,x,j,i);
            end
        end

           cd(newFolder);
           filename = sprintf('air=%d v vs t.csv',air);
           D = xlsread(filename,'B:B'); % Velocity data
           [n,~]=size(D);% get the number of the rows of data
           g1 = repmat(i,n,1); % label each row
           fig = figure(kk);
```

```
           hold on
           bbb = boxchart(g1,D,'LineWidth',1.5); % box plot
           bbb.BoxWidth = 0.5; % box width
           bbb.WhiskerLineColor = color(:,:,kk);
           bbb.BoxFaceColor = color(:,:,kk);
           bbb.MarkerColor = color(:,:,kk);
           grid on
           xlabel('$r/D_1$','Interpreter','latex')
           ylabel('$V\,(m/s)$','Interpreter','latex')
           title(sprintf('Y=%dD air=%dkg/h S=%.1f',x,air,j))
           hold off
    end

    hold on %insert legend
    if j==0.0
       legend('$S=0$','Interpreter','latex')
    elseif j==0.3
       legend('$S=0.3$','Interpreter','latex')
    elseif j==0.8
       legend('$S=0.8$','Interpreter','latex')
    elseif j==1.2
       legend('$S=1.2$','Interpreter','latex')
    elseif j==1.5
       legend('$S=1.5$','Interpreter','latex')
    elseif j==2.5
       legend('$S=2.5$','Interpreter','latex')
    elseif j==3.1
       legend('$S=3.1$','Interpreter','latex')
    else
       legend('$S=3.9$','Interpreter','latex')
    end
    hold off

    cd(res_dir);
    saveas(fig,sprintf('S=%.1f_air=%d_Y=%dD.fig',j,air,x)) % save the image
    kk = kk+1;
end
```

B.13 Histogram.m

```matlab
%% Histogram
close all
j = 0.0; % swirl number
x = 10; %X = xD
i = [-5 5]; %r = iD

air = [16 18]; % air mass flow rate (kg/h)
k = 1; % loop index

for ii = i %r = iD
    for jj = air % air mass flow rate (kg/h)

if ii==0 || ii==5 || ii==-5
newFolder = sprintf('D:/onedrive/OneDrive - University of Edinburgh/Dataset/X=%dD/S=%.1f/R=%dD',x,j,ii);
else
newFolder = sprintf('D:/onedrive/OneDrive - University of Edinburgh/Dataset/X=%dD/S=%.1f/R=%.1fD',x,j,ii);
end

cd(newFolder);
filename = sprintf('air=%d w vs t.csv',jj);
D = xlsread(filename,'B:B'); % Diameter data data
figure(k)
histogram(D,300)
if ii==0 || ii==5 || ii==-5
    title(sprintf('S=%.1f R=%dD air=%d X=%dD',j,ii,jj,x))
else
    title(sprintf('S=%.1f R=%.1fD air=%d X=%dD',j,ii,jj,x))
end
k = k + 1;
    end
end
```

B.14 FFt_2D.m

```
% this code is used to detect the 2D spectrum (for left handside wave)

% The premises (i.e. keypoint) of this code:
% 1. the corresponding global Y coordinates of the upper-left point of the
% largest connective region should be uniform for all images
% 2. the photo should have long wave structure to ensure that the largest
% connective region is the water jet ranther than the big droplet.
% Moreover, Long wave structure guarantees that the 2D spetrum will makes sense.

% tip: check the value of the variable 'premise' after you run this code.
% Then you will know whether u can apply this code to your images correctly

%%
clc
clear all
close all

img_dir='D:\OneDrive - University of Edinburgh\3.30.2021 final data\T=1.0s\s=0.0 (2)\air=4\';
cd(img_dir)
% res_dir='D:\OneDrive - University of Edinburgh\final data plots\2D FFT results\s=0.3 air=3 (2)\'; % result folder

%specify the following parameters before you run this code
magnification = 0.14; % the magnification of the image (unit:mm/pixel)
n = 1130 + 1;% number of photos (including background)
level = 725;% the thresholding level
sampling_rate = 600;% sampling rate or sampling frequency (unit:fps or Hz)
```

```
liquid_dia = 4;%the inner diameter of the liquid tube (unit: mm)
resolution_x = 704;% the horizontal resolution of the image (unit:pixel)
resolution_y = 512;% the vertical resolution of the image (unit:pixel)
value2=liquid_dia/2/magnification;  % reference value (unit: pixel) used to check the premise (i.e. The distance betweeen the most upstream
                                    % points of the edge data should be less than this referennce value)

y_start = 32; %vertical region to crop to [y_start,y_end]
y_end = 223;
x_start= 277; %horizontal region to crop to [x_start,x_end]
x_end = 445;

% read one image to get image to determine crop region and magnification
img_no = "0218";
img = imread(img_dir + "h" + img_no + ".tif");
figure(6)
imshow(img, [])
axis equal

%%
% image region to crop to
crop_indx = [[y_start, y_end]; [x_start, x_end]];
% cropped image dimensions
img_crop_dim = [crop_indx(1,2) - crop_indx(1,1) + 1, crop_indx(2,2) - crop_indx(2,1) + 1];

n_actual=n-1; %number of photos after excluding background
time_interval= 1/sampling_rate; % time interval between each frame (unit:second)
```

```
time=0:time_interval:(n_actual-1)*time_interval; %moment matrix (note: the corresponding moment for each matrix can be found in moment matrix) )

I=cell(1,n);
img=imread('background.tif');
img_crop = img(crop_indx(1,1):crop_indx(1,2), crop_indx(2,1):crop_indx(2,2));
I{1}=int16(img_crop);% we put background at the first element

% read several images
for i=0:1:(n_actual-1)

imageName = sprintf("h%04d.tif",i-529);
img=imread(imageName);
img_crop = img(crop_indx(1,1):crop_indx(1,2), crop_indx(2,1):crop_indx(2,2));
I{i+2} = int16(img_crop);
end

%do the background subtraction for each images
for i=2:1:n
    I{i}=I{1}+(-1).*I{i};
end

% B-type rescaling (note: this rescaling is like plus 255 for each pixels values)
for qqq=2:1:n
cc=I{qqq};
cc=cc+int16(255);
I{qqq}=cc;


end

% thresholding each image

new_matrix=cell(1,n);
```

```
ii=1;

for i=1:1:n
[p,q]=size(I{i});
new_matrix{i}=logical(zeros(p,q));
end

for k=1:1:n
    cc=I{k};
    ccc=new_matrix{k}; % stores images after thresholding
    for i=1:1:p
        for j=1:1:q
            if cc(i,j)>=level
            ccc(i,j)=logical(1);
            end
        end
    end
    new_matrix{k}=ccc;
end

% calculate the limit of the spatial matrix (x)

for k=2:1:n

new_matrix1=new_matrix{k};

stats123=regionprops(new_matrix1,'PixelList');
stats456=regionprops(new_matrix1,'Image');

kk=size(stats123);
kkk=kk(1);

compare1=10; % reference value

%detect the largest region
for i=1:1:kkk
    BB=stats123(i).PixelList;
    c=size(BB);
    size_region=c(1)*c(2);
```

```

    if size_region>compare1
    compare1=size_region;
    location2=i;%the location of the largest region
    end



end
    breaklength_size=size(stats456(location2).Image);
    Largest_location(k)=location2;
    breaklength_pixels(k-1)=breaklength_size(1); % the breakup length (unit: pixel)
end

spatial_limit=min(breaklength_pixels,[],2);

% Based on the spatial limit, detect the edge for all images
for k=2:1:n

    % calculate the coordinate transformation at first
    new_matrix1=new_matrix{k};
    stats123=regionprops(new_matrix1,'PixelList');
    stats456=regionprops(new_matrix1,'Image');

    op=stats456(Largest_location(k)).Image; % the local image of the largest region
    stats999=regionprops(op,'PixelList'); % the local coordinates for the largest region
    opop=stats999(1).PixelList; % change the struct to matrix
    BB=stats123(Largest_location(k)).PixelList; % the global coordinates for the largest region

    row_distance=BB(1,2)-opop(1,2);
    column_distance=BB(1,1)-opop(1,1);

    global_row_num_for_local_first_row(k-1)=1+row_distance; %the global Y coordinate for the most upstream point
```

```
    % prepare for checking the premise of this code

    %detect the edge for one image based on the spatial limit
    for kk=1:1:spatial_limit % the spatial limit is used here
       for kkk=1:1:resolution_x
       if op(kk,kkk)==1
          column_coordinate_local(kk)=kkk;
          break
       end
       end
    end

    column_coordinate_global{k}=column_coordinate_local+column_distance; % global X coordinate of the edge (unit: pixel)
    column_coordinate_global_mag{k}=column_coordinate_global{k}*magnification;% global X coordinate of the edge (unit: mm)

end

```

```
% check the premise of this code
count_check=0;
count_check1=0;

for k=2:1:n % check whether the most upstream point of each water jet corresponds to the same global Y coordinate
    if global_row_num_for_local_first_row(k-1)-global_row_num_for_local_first_row(1)~=0
        premise1=sprintf("fail. you cannot use this code because the global Y coordinate for the most upstream point of the edge for h%04d is different to other images.",k-2);
        count_check1=1;
        break
    end
end

check=column_coordinate_global{2};
compare_check=check(1); % the global X coordinate for the upper-left point of the water jet region for the first image

if count_check1==1
    premise1
else  % check whether all edge data starts from the upper-left point rather than the upper-right point
    for k=2:1:n                                  %because the edge data can start from the upper-right point due to bad background where the water is left near the water tube
    check=column_coordinate_global{k};
    value1=abs(check(1)-compare_check); % the distance between the global X coordinates of the upper-left points of the water jet regions (unit: pixel)

    if  value1 >= value2
       premise=sprintf("fail. you cannot use this code because the detected edge in h%04d start from the upper-right point.",k-2);
```

```
       count_check=1;
       break
    end

    end
    if count_check~=1
    premise='congratulation! you can use this code'
    else
       premise
    end
end



% spacial sampling
dx = magnification; % x sample spacing (mm/pixel)
xe = (spatial_limit-1)*magnification; % final x coord
x = 0.0:dx:xe; % x sample coords
nx = length(x); % no. of x samples (i.e spatial_limit)

% time sampling
dt = time_interval; % t sample period (s)
te = (n_actual-1)*dt; % final t time (coord)
t = 0.0:dt:te; % t sample coords
nt = length(t); % no. of t samples (i.e n_actual)


%convert the cell(column_coordinate_global_mag) to matrix form (M)
M=zeros(nt,nx);
for i=2:1:n
    M1=column_coordinate_global_mag{i};
    for ii=1:1:nx
        M(i-1,ii)=M1(1,ii);
    end
end

% subtract the M matrix with its mean value
mean_value=mean(mean(M));
```

```
M=M-mean_value;

% coordinates and data
[X,T] = meshgrid(x,t); % coord matrices

% data sampling frequencies for plot
ft = fftshift(fftfreq(nt, dt)); % time sampling frequencies
fx = fftshift(fftfreq(nx, dx)); % space sampling frequencies

%data fft
Y0f = fftshift(fft2(M)); % fft
Y0fa = abs(Y0f); % fft absolute value
Y0fam = max(max(Y0fa)); % max value for colormap scaling

Y0fa=log(1+Y0fa);
Y0fam=max(max(Y0fa));
% Y0fam=12;

%frequency axes for fft plot
Y0fRI = imref2d(size(Y0f));
Y0fRI.XWorldLimits = fx([1, end]);
Y0fRI.YWorldLimits = ft([1, end]);

%plot fft in 2D
fig4=figure(4);
imshow(Y0fa, Y0fRI, 'DisplayRange', [0, Y0fam])
colormap('default')
colorbar
xlabel('f_x(1/mm)','fontsize',10)
ylabel('f_t(Hz)','fontsize',10)
ax = gca;
ax.YAxis.Exponent = 0; % turn off y axis tick exponent format
daspect auto % turn off equal aspect ratio (for resizing plot)
title('FFT of the wave', 'Interpreter', 'latex','fontsize',20)
set(gca,'Fontsize',20)
% saveas(fig4,strcat(res_dir,'Spectrum (2D view)'))
```

```

% exportgraphics(gcf,'wave_3.pdf','ContentType','vector')

% %plot fft in 3D
% [Fx,Ft]=meshgrid(fx,ft);
% fig5=figure(5);
% surf(Fx,Ft,Y0fa)
% xlabel('f_x(1/mm)','fontsize',30)
% ylabel('f_t(Hz)','fontsize',30)
% zlabel('Amplitude','fontsize',30)
% set(gca,'Fontsize',30)
% colorbar
% % saveas(fig5,strcat(res_dir,'Spectrum (3D view)'))

% imagesc(Y0fa)

function f = fftfreq(n, d)
    if mod(n, 2.0) % n odd length
        f0 = (0:1.0:((n-1)/2))/(n*d);
        f1 = ((-(n-1)/2):1.0:-1.0)/(n*d);
        f = [f0, f1];
    else % n even length
        f0 = (0:1.0:(n/2-1))/(n*d);
        f1 = ((-n/2):1.0:-1.0)/(n*d);
        f = [f0, f1];
    end
end
```

B.15 filenames.m

```
%% change the names for several groups of files
clc
clear all

x = 10; % x coordinate
swirl = ["0p0" "0p3" "0p8" "1p2" "1p5" "2p5" "3p1" "3p9"];

```

```matlab
Dataset_path1 = 'D:/onedrive/OneDrive - University of Edinburgh/Desktop/PDI Dataset/X=%dD/S=%s/R=%sD'; % used for alienware pc
Dataset_path2 = 'D:/onedrive/OneDrive - University of Edinburgh/Desktop/PDI Dataset/X=%dD/S=%s'; % used for alienware pc

for j = swirl % swirl number
%     if j=="0p0" % for x=5
%        r = ["-2p5" "0" "2p5"]; % r coordinate matrix
%     elseif j=="0p3" || j=="0p8"
%        r = ["-5" "-2p5" "0" "2p5" "5"];
%     else
%        r = ["-7p5" "-5" "-2p5" "0" "2p5" "5" "7p5"];
%     end

      if j=="0p0" % for x=10
         r = ["-5" "-2p5" "0" "2p5" "5"]; % r coordinate matrix
      else
         r = ["-7p5" "-5" "-2p5" "0" "2p5" "5" "7p5"];
      end

    for i = r
       newFolder = sprintf(Dataset_path1,x,j,i);

       if j == "0p0" || j == "0p3" || j == "0p8" || j == "1p2"
       cd(newFolder);
       movefile("air=18_D32.csv", "air_18_D32.csv") % change filenames
       movefile("air=18_Dia.csv", "air_18_Dia.csv")
       movefile("air=18_v.csv", "air_18_v.csv")
       movefile("air=18_w.csv", "air_18_w.csv")
       movefile("air=16_D32.csv", "air_16_D32.csv")
       movefile("air=16_Dia.csv", "air_16_Dia.csv")
       movefile("air=16_v.csv", "air_16_v.csv")
       movefile("air=16_w.csv", "air_16_w.csv")
       elseif x==10 && j=="3p9" && i=="7p5"
```

```
      cd(newFolder);
      movefile("air=8_D32.csv", "air_8_D32.csv") % change filenames
      movefile("air=8_Dia.csv", "air_8_Dia.csv")
      movefile("air=8_v.csv", "air_8_v.csv")
      movefile("air=8_w.csv", "air_8_w.csv")
      else
      cd(newFolder);
      movefile("air=8_D32.csv", "air_8_D32.csv") % change filenames
      movefile("air=8_Dia.csv", "air_8_Dia.csv")
      movefile("air=8_v.csv", "air_8_v.csv")
      movefile("air=8_w.csv", "air_8_w.csv")
      movefile("air=10_D32.csv", "air_10_D32.csv")
      movefile("air=10_Dia.csv", "air_10_Dia.csv")
      movefile("air=10_v.csv", "air_10_v.csv")
      movefile("air=10_w.csv", "air_10_w.csv")
      end
   end

   Folder = sprintf(Dataset_path2,x,j);
   cd(Folder);

   if x==5
      if j=="0p0"
         movefile("R=0D","R_0D") % change foldernames
         movefile("R=2p5D", "R_2p5D")
         movefile("R=-2p5D", "R_-2p5D")
      elseif j=="0p3" || j=="0p8"
         movefile("R=0D","R_0D") % change foldernames
         movefile("R=2p5D", "R_2p5D")
         movefile("R=-2p5D", "R_-2p5D")
         movefile("R=5D","R_5D")
         movefile("R=-5D","R_-5D")
      else
         movefile("R=0D","R_0D") % change foldernames
         movefile("R=2p5D", "R_2p5D")
         movefile("R=-2p5D", "R_-2p5D")
         movefile("R=5D","R_5D")
```

```
          movefile("R=-5D","R_-5D")
          movefile("R=7p5D", "R_7p5D")
          movefile("R=-7p5D", "R_-7p5D")
       end
    elseif x==10
        if j=="0p0"
           movefile("R=0D","R_0D") % change foldernames
           movefile("R=2p5D", "R_2p5D")
           movefile("R=-2p5D", "R_-2p5D")
           movefile("R=5D","R_5D")
           movefile("R=-5D","R_-5D")
        else
           movefile("R=0D","R_0D") % change foldernames
           movefile("R=2p5D", "R_2p5D")
           movefile("R=-2p5D", "R_-2p5D")
           movefile("R=5D","R_5D")
           movefile("R=-5D","R_-5D")
           movefile("R=7p5D", "R_7p5D")
           movefile("R=-7p5D", "R_-7p5D")
        end
    end
end
```

B.16 draft_plot2.m

```
%plot the data manually
water_dia=4;
breakuplength_mean_matrix=[11.53 11.8 11.7802 11.1870 11.56 12.1806]/water_dia;
cigma_matrix=[2.96 2.74 3.363 3.58 3 3.035]/water_dia;

firstdrop_mean_matrix=[6.8271 7.8093 7.5252 6.7568 6.7 7.6337]/water_dia;
delta_matrix=[3.9 3.2 3.4 3.1 3.2 3.6]/water_dia; %a mtarix of standard deviation of the ratio of the mean values of first droplet locations to water tube diameter for non-swirling cases

T=[0.25/2 0.25 0.5 1 2 3];
```

```

%calculate the uncertainty of the data on the mean values of the breakup lengths
yneg=cigma_matrix;% the lower lengths of the vertical error bars
ypos=cigma_matrix;% the upper lengths of the vertical error bars

%specify the uncertainty of the data on the mean values of the first
%droplet locations
yneg_drop=delta_matrix;% the lower lengths of the vertical error bars
ypos_drop=delta_matrix;% the upper lengths of the vertical error bars

%plot the mean values of the breakup lengths vs aerodynamic Weber number
figure(1)
hold on
errorbar(T,breakuplength_mean_matrix,yneg,ypos,'-s','LineWidth',2,'MarkerSize',10,'MarkerEdgeColor','red','MarkerFaceColor','red','color',[0 0.447 0.741])
xlabel('recoding time duration(s)','FontSize',20)
ylabel('L/D_l','FontSize',20)
title('air=3kg/h,s=2.5,2000fps','FontSize',20)
xlim([0 3])
ylim([0 4])
set(gca,'Fontsize',20)
hold off

%plot the mean values of the first droplet locations vs aerodynamic Weber number
figure(2)
hold on
errorbar(T,firstdrop_mean_matrix,yneg_drop,ypos_drop,'-s','LineWidth',2,'MarkerSize',10,'MarkerEdgeColor','red','MarkerFaceColor','red','color',[0 0.447 0.741])
xlabel('recoding time duration(s)')
```

```
ylabel('X_d/D_l')
title('air=3kg/h,s=2.5,2000fps','FontSize',20)
xlim([0 3])
ylim([0 3])
set(gca,'Fontsize',20)
hold off

%scatter plot
No_img=249;
t=T(1)+zeros(No_img,1);
figure(3)
hold on
scatter(t,breaklength(:,5)/water_dia)
hold off

figure(4)
hold on
scatter(t,(firstdrop(:,5)-4)*0.15/water_dia)
hold off

figure(3)
hold on
xlabel('recording time duration(s)','FontSize',20)
ylabel('L/D_l','FontSize',20)
title('air=3kg/h,s=2.5,2000fps','FontSize',20)
hold off

figure(4)
hold on
xlabel('recording time duration(s)','FontSize',20)
ylabel('X_d/D_l','FontSize',20)
title('air=3kg/h,s=2.5,2000fps','FontSize',20)
hold off

%%box plot

%load the breakup length data
% breakuplength1=breaklength(:,5)/water_dia;
```

```
cd 'D:\OneDrive - University of Edinburgh\3.30.2021 final
    data\T=1s\s=0\air=5\data'
load 'L 750 50 950.mat'
breakuplength2=breaklength(:,3)/water_dia;
cd 'D:\OneDrive - University of Edinburgh\3.30.2021 final
    data\T=1s\s=0\air=5\data'
load 'L 750 50 950.mat'
breakuplength3=breaklength(:,3)/water_dia;
% cd 'D:\OneDrive - University of Edinburgh\3.30.2021 final
    data\T=2s\s=3.9\air=1\data'
% load 'L 750 50 950.mat'
% breakuplength4=breaklength(:,3)/water_dia;

breakuplength=[breakuplength2;breakuplength3];

t1=0.5+zeros(700,1);
t2=1+zeros(700,1);
t3=2+zeros(1000,1);
t=[t1;t2;t3];

figure(5)
boxplot(breakuplength,t)
xlabel('recording time duration(s)','FontSize',20)
ylabel('L/D_l','FontSize',20)
title('air=1kg/h, s=3.9','FontSize',20)

%box plot
breakuplength1=breaklength(:,1)/water_dia;
breakuplength2=breaklength(:,2)/water_dia;
breakuplength3=breaklength(:,3)/water_dia;
breakuplength4=breaklength(:,4)/water_dia;
breakuplength5=breaklength(:,5)/water_dia;
breakuplength6=breaklength(:,6)/water_dia;
breakuplength7=breaklength(:,7)/water_dia;

breakuplength=[breakuplength1;breakuplength2;breakuplength3;
    breakuplength4;breakuplength5;breakuplength6;
    breakuplength7];

```

```
mm=2999;
t1=650+zeros(mm,1);
t2=700+zeros(mm,1);
t3=750+zeros(mm,1);
t4=800+zeros(mm,1);
t5=850+zeros(mm,1);
t6=900+zeros(mm,1);
t7=950+zeros(mm,1);
t=[t1;t2;t3;t4;t5;t6;t7];

figure(5)
boxplot(breakuplength,t)
xlabel('thresholding level','FontSize',20)
ylabel('L/D_l','FontSize',20)
title('air=10kg/h, s=0.3, 6000fps,','FontSize',20)



%load the first drop data
cd 'C:\Users\s1678791\OneDrive - University of Edinburgh
   \3.30.2021 final data\T=0.5s\s=0.8\air=10\data'
load 'firstdrop 3 pixels.mat'
nn=23;
mm=0.14;

firstdrop1=(firstdrop(:,3)-nn)*mm/water_dia;
load 'firstdrop 4 pixels.mat'
firstdrop2=(firstdrop(:,3)-nn)*mm/water_dia;
load 'firstdrop 5 pixels.mat'
firstdrop3=(firstdrop(:,3)-nn)*mm/water_dia;
firstdroplet=[firstdrop1;firstdrop2;firstdrop3];

zz=3000;
size_drop1=3+zeros(zz,1);
size_drop2=4+zeros(zz,1);
size_drop3=5+zeros(zz,1);
size_drop=[size_drop1;size_drop2;size_drop3];

figure(6)
```

```
boxplot(firstdroplet,size_drop)
xlabel('minimum droplet size(unit:pixel)','FontSize',20)
ylabel('X_d/D_l','FontSize',20)
title('air=10kg/h, s=0.8, 6000fps, thresholding level=850,
   recording time duration=0.5s','FontSize',20)

figure(7)
scatter(size_drop,firstdroplet)
xlabel('minimum droplet size(unit:pixel)','FontSize',20)
ylabel('X_d/D_l','FontSize',20)
title('air=3kg/h, s=2.5, 2000fps, thresholding level=850,
   recording time duration=3s','FontSize',20)

%load the first drop data
nn=23;
mm=0.14;

firstdrop_1=(firstdrop(:,1)-nn)*mm/water_dia;
firstdrop_2=(firstdrop(:,2)-nn)*mm/water_dia;
firstdrop_3=(firstdrop(:,3)-nn)*mm/water_dia;
firstdrop_4=(firstdrop(:,4)-nn)*mm/water_dia;
firstdrop_5=(firstdrop(:,5)-nn)*mm/water_dia;
% firstdrop_6=(firstdrop(:,6)-nn)*mm/water_dia;
% firstdrop_7=(firstdrop(:,7)-nn)*mm/water_dia;
firstdrop_data=[firstdrop_1;firstdrop_2;firstdrop_3;
   firstdrop_4;firstdrop_5];

zz=3000;
% tt_1=650+zeros(zz,1);
% tt_2=700+zeros(zz,1);
tt_3=750+zeros(zz,1);
tt_4=800+zeros(zz,1);
tt_5=850+zeros(zz,1);
tt_6=900+zeros(zz,1);
tt_7=950+zeros(zz,1);
tt=[tt_3;tt_4;tt_5;tt_6;tt_7];

figure(8)
boxplot(firstdrop_data,tt)
```

```
xlabel('thresholding level','FontSize',20)
ylabel('X_d/D_l','FontSize',20)
title('air=10kg/h,s=0.8,6000fps','FontSize',20)

%box plot
nn=30;
mm=0.14;

cd 'D:\OneDrive - University of Edinburgh\3.30.2021 final
    data\T=0.5s\s=3.9\air=1\data'
load 'X 3 pixels.mat'
firstdrop_1=(firstdrop(:,3)-nn)*mm/water_dia;
cd 'D:\OneDrive - University of Edinburgh\3.30.2021 final
    data\T=1s\s=3.9\air=1\data'
load 'X 3 pixels.mat'
firstdrop_2=(firstdrop(:,3)-nn)*mm/water_dia;
cd 'D:\OneDrive - University of Edinburgh\3.30.2021 final
    data\T=2s\s=3.9\air=1\data'
load 'X 3 pixels.mat'
firstdrop_3=(firstdrop(:,3)-nn)*mm/water_dia;

firstdrop_data=[firstdrop_1;firstdrop_2;firstdrop_3];

tt_2=0.5+zeros(250,1);
tt_3=1+zeros(500,1);
tt_4=2+zeros(1000,1);
tt=[tt_2;tt_3;tt_4];

figure(9)
boxplot(firstdrop_data,tt)
xlabel('recording time duration(s)','FontSize',20)
ylabel('X_d/D_l','FontSize',20)
title('air=1kg/h, s=3.9','FontSize',20)

%comparison of multiple samplings

cd 'D:\OneDrive - University of Edinburgh\3.30.2021 final
    data\T=0.5s\s=1.2 (1)\air=10.0\data'
load 'L 750 50 950.mat'
```

```
L_first=breaklength(:,3)/water_dia;

cd 'D:\OneDrive - University of Edinburgh\3.30.2021 final data\T=0.5s\s=1.2 (2)\air=10.0\data'
load 'L 750 50 950.mat'
L_second=breaklength(:,3)/water_dia;

cd 'D:\OneDrive - University of Edinburgh\3.30.2021 final data\T=0.5s\s=1.2 (3)\air=10.0\data'
load 'L 750 50 950.mat'
L_third=breaklength(:,3)/water_dia;

L_sampling=[L_first;L_second;L_third];

[a,~]=size(L_first);
g1 = repmat({'First'},a,1);
g2 = repmat({'Second'},a,1);
g3 = repmat({'Third'},a,1);
g = [g1;g2;g3];

figure(10)
boxplot(L_sampling,g)
ylabel('L/D_l','FontSize',20)
title('air=10kg/h, s=1.2','FontSize',20)

% box plot
% cd 'D:\OneDrive - University of Edinburgh\3.30.2021 final data\T=0.5s\s=1.5\air=5\data'
% load 'X 3 pixels.mat'
% X_fourth=(firstdrop(:,3)-72)*0.14/water_dia;

cd 'D:\OneDrive - University of Edinburgh\3.30.2021 final data\T=0.5s\s=3.9 (3)\air=3\data'
load 'X 3 pixels.mat'
X_third=(firstdrop(:,3)-28)*0.14/water_dia;

cd 'D:\OneDrive - University of Edinburgh\3.30.2021 final data\T=0.5s\s=3.9 (2)\air=3\data'
load 'X 3 pixels.mat'
```

```
X_second=(firstdrop(:,3)-28)*0.14/water_dia;

cd 'D:\OneDrive - University of Edinburgh\3.30.2021 final
    data\T=0.5s\s=3.9\air=3\data'
load 'X 3 pixels.mat'
X_first=(firstdrop(:,3)-29)*0.14/water_dia;

X_sampling=[X_first;X_second;X_third];

[a,~]=size(X_first);
g1 = repmat({'First'},a,1);
g2 = repmat({'Second'},a,1);
g3 = repmat({'Third'},a,1);
% g4 = repmat({'Fourth'},700,1);
g = [g1;g2;g3];

figure(11)
boxplot(X_sampling,g)
ylabel('X/D_l','FontSize',20)
title('air=3kg/h, s=3.9, minimum droplet size=3 pixels','
    FontSize',20)

for i=1:1:2999
    for j=1:1:7
        if isnan(firstdrop(i,j))
            wrong=1
            break
        end
        if firstdrop(i,j)==0
            wrong=1
            break
        end
    end
end
```

B.17 draft_plot3.m

```
% this code is used to create the final data plot for first droplet
% location with We as the X axis
clear
water_dia=4;% water tube diameter (mm)

for ii=[0.0 0.3 0.8] % swirl number matrix
    zz=1;
    data=[];
    g2=[];
    if ii==0.0
        jj = 1.0; % recording time duration (s)
        air_vel = [4 5 8 10];% air velocities matrix
        nn=[27 71 27 27;26 71 26 26;27 71 27 27;0 71 0 0];% the matrix containing the y coordinates for the water tube (s=0)
    elseif ii==0.3
        jj = 0.5;
        air_vel = [3 6 8 10];
        nn=[3 23 23 23;23 23 23 23;24 24 24 24];% the matrix containing the y coordinates for the water tube (s=0.3)
    else
        jj = 0.5;
        air_vel = [3 6 8 10];
        nn=[21 21 21 21;23 23 23 23;25 25 25 25];% the matrix containing the y coordinates for the water tube (s=0.8)
    end
for i=air_vel

    if ii==0.0 && i==5 %if s=0 and air=5?
        sample=[1 2 3 4]; % times matrix
    else
        sample=[1 2 3];% times matrix
    end

    kk=1;
```

```
    for j=sample

       if ii==0.3 && j==1 && i==3
           mag=0.15; % magnification (mm/pixel)
       elseif ii==2.5 && j==1 && i==3
           mag=0.15;
       else
           mag=0.14; % magnification (mm/pixel)
       end

       if ii==0.3 && i==10 %if s=0.3 and air=10?
       newFolder = sprintf('D:/OneDrive - University of Edinburgh/3.30.2021 final data/T=0.25s/s=0.3 (%d)/air=%d/data',j,i);
       cd(newFolder);
       elseif ii==2.5 || ii==3.1 || ii==1.2 %if s=2.5 or s=3.1 or s=1.2?
       newFolder = sprintf('D:/OneDrive - University of Edinburgh/3.30.2021 final data/T=%.1fs/s=%.1f (%d)/air=%.1f/data',jj,ii,j,i);
       cd(newFolder);
       else newFolder = sprintf('D:/OneDrive - University of Edinburgh/3.30.2021 final data/T=%.1fs/s=%.1f (%d)/air=%d/data',jj,ii,j,i);
       cd(newFolder);

       end

    load 'X 3 pixels.mat'

    X_data=(firstdrop(:,3)-nn(kk,zz))*mag/water_dia;

    [n,~]=size(X_data);% get the number of the rows of data

    if ii==0.0
       We = i^2; %calculate the aero We
    else
       We = round(4.4*i^2);
    end
```

```

    g1 = repmat(We,n,1); % label each row

    g2=[g2;g1];% the matrix which contains label

    data=[data;X_data];% stack the data in one column

    breaklength=[];

    kk=kk+1;
    end
    zz=zz+1;
end
    if ii==0.0 %subplot for S=0
    hold on
    fig = figure(1);
    t1 = tiledlayout(1,3,'TileSpacing','compact','Padding','normal');
    ax31 = nexttile;
    boxplot(data,g2,'OutlierSize',4);
    ylim([0 18])
    grid on
    title('$S=0$','Interpreter','latex','FontSize',10)
    ylabel('$X_d/D_1$','Interpreter','latex','FontSize',10)
    hold off
    elseif ii==0.3 %subplot for S=0.3
    hold on
    ax32 = nexttile;
    boxplot(data,g2,'OutlierSize',4);
    ylim([0 18])
    grid on
    title('$S=0.3$','Interpreter','latex','FontSize',10)
    xlabel('$We_A$','Interpreter','latex','FontSize',10)
    hold off
    elseif ii==0.8 %subplot for S=0.8
    hold on
    ax33 = nexttile;
    boxplot(data,g2,'OutlierSize',4);
    ylim([0 18])
```

```
    grid on
    title('$S=0.8$','Interpreter','latex','FontSize',10)
    hold off
    end
end
%%
% hold on
% subplot(1,3,1)
% bbb=boxchart(g2,data,'LineWidth',1.5);
% bbb.BoxWidth = 1;
% bbb.WhiskerLineColor=color;
% bbb.BoxFaceColor=color;
% bbb.MarkerColor=color;
% xlim([5 110])
% ylim([0 18])
% grid on
% lgd = legend('$S=0$','Interpreter','latex');
% lgd.FontSize = 20; % legend font size
% xlabel('$We_A$','Interpreter','latex','FontSize',20)
% ylabel('$X_d/D_l$','Interpreter','latex','FontSize',20)
% hold off
```

B.18 draft_plot5.m

```
% this code is used to create the final data plot for break-up length
% for S in the range of 0-1.2 with We as the X axis
clc
clear
water_dia=4;% water tube diameter
% color=[0 0.4470 0.7410];%(s=0)
% color=[0.8500 0.3250 0.0980];%(s=0.3)
% color=[0.9290 0.6940 0.1250];%(s=0.8)
% color=[1 0 1];%(s=1.2)
% color=[0.4940 0.1840 0.5560];%(s=1.5)
% color=[0.4660 0.6740 0.1880];%(s=2.5)
% color=[0.3010 0.7450 0.9330];%(s=3.1)
% color=[0.6350 0.0780 0.1840];%(s=3.9)

```

```
for ii=[0.0 0.3 0.8 1.2] % swirl number matrix
    data=[];
    g2=[];
    if ii==0.0
        jj = 1.0; % recording time duration (s)
        air_vel = [3 4 5 8 10]; % air velocities matrix
    elseif ii==0.3 || ii==0.8
        jj = 0.5;
        air_vel = [3 6 8 10];
    else
        jj = 0.5;
        air_vel = [3.0 5.5 8.0 10.0];
    end

    for i=air_vel

    if ii==0.0 && i==5 %if s=0 and air=5?
        sample=[1 2 3 4]; % times matrix
    elseif ii==1.5
        sample=[1 2 3 4]; % times matrix
    else
        sample=[1 2 3];% times matrix
    end

       for j=sample

       if ii==0.3 && i==10 %if s=0.3 and air=10?
       newFolder = sprintf('D:/OneDrive - University of Edinburgh/3.30.2021 final data/T=0.25s/s=0.3 (%d)/air=%d/data',j,i);
       cd(newFolder);
       elseif ii==1.2 %if s=1.2
       newFolder = sprintf('D:/OneDrive - University of Edinburgh/3.30.2021 final data/T=%.1fs/s=%.1f (%d)/air=%.1f/data',jj,ii,j,i);
       cd(newFolder);
       elseif ii==2.5 || ii==3.1 %if s=2.5 or s=3.1?
       newFolder = sprintf('D:/OneDrive - University of Edinburgh/New data/s=%.1f (%d)/air=%.1f',ii,j,i);
```

```
      cd(newFolder);
      elseif ii==1.5 || ii==3.9 %if s=1.5 or s=3.9?
      newFolder = sprintf('D:/OneDrive - University of Edinburgh/New data/s=%.1f (%d)/air=%d',ii,j,i);
      cd(newFolder);
      else
         newFolder = sprintf('D:/OneDrive - University of Edinburgh/3.30.2021 final data/T=%.1fs/s=%.1f (%d)/air=%d/data',jj,ii,j,i);
      cd(newFolder);

      end

      if ii==0.0 || ii==0.3 || ii==0.8 || ii==1.2
         load 'L 750 50 950.mat'
         if j==3 && i==10 && ii==0.0 %if this is the third sampling for s=0 and air=10 (only be applied for break-up length data)
            L_data=breaklength;
         else
            L_data=breaklength(:,3)/water_dia;
         end
      else
         load 'L divided by D.mat'
         L_data=breaklength(:,2);
      end

   [n,~]=size(L_data);% get the number of the rows of data

   if ii==0.0
      We = i^2; %calculate the aero We
   else
      We = round(4.4*i^2);
   end

   g1 = repmat(We,n,1); % label each row

   g2=[g2;g1];% the matrix which contains label

```

```
    data=[data;L_data];% stack the data in one column

    breaklength=[];

        end
    end

    if ii==0.0 % subplot for S=0
        hold on
        fig = figure(1);
        t1 = tiledlayout(1,4,'TileSpacing','compact','Padding','normal');
        ax31 = nexttile;
        boxplot(data,g2,'OutlierSize',4);
        ylim([0 18])
        grid on
        title('$S=0$','Interpreter','latex','FontSize',10)
        ylabel('$L_d/D_l$','Interpreter','latex','FontSize',10)
        hold off
    elseif ii==0.3 %subplot for S=0.3
        hold on
        ax32 = nexttile;
        boxplot(data,g2,'OutlierSize',4);
        ylim([0 18])
        grid on
        title('$S=0.3$','Interpreter','latex','FontSize',10)
        xlabel('$We_A$','Interpreter','latex','FontSize',10)
        hold off
    elseif ii==0.8 %subplot for S=0.8
        hold on
        ax33 = nexttile;
        boxplot(data,g2,'OutlierSize',4);
        ylim([0 18])
        grid on
        title('$S=0.8$','Interpreter','latex','FontSize',10)
        hold off
    elseif ii==1.2 %subplot for S=1.2
        hold on
```

```
        ax34 = nexttile;
        boxplot(data,g2,'OutlierSize',4);
        ylim([0 18])
        grid on
        title('$S=1.2$','Interpreter','latex','FontSize',10)
        hold off
    end
end
%%
% hold on
% % subplot(1,4,1)
% bbb=boxchart(g2,data,'LineWidth',1.5);
% bbb.BoxWidth = 1;
% bbb.WhiskerLineColor = color;
% bbb.BoxFaceColor = color;
% bbb.MarkerColor = color;
% xlim([0 270])
% ylim([0 17])
% grid on
% legend('s=1.2')
% xlabel('$We_A$','Interpreter','latex','FontSize',20)
% ylabel('$L_d/D_l$','Interpreter','latex','FontSize',20)
% title('break-up length vs aerodynamic Weber number','
    FontSize',20)
% hold off
```

B.19 draft_plot6.m

```
%comparison of multiple samplings for breakup length only
clear all

water_dia=4;

cd 'D:\OneDrive - University of Edinburgh\3.30.2021 final
    data\T=0.5s\s=1.2 (1)\air=10.0\data'
load 'L 750 50 950.mat'
L_first=breaklength(:,3)/water_dia;

```

```
cd 'D:\OneDrive - University of Edinburgh\3.30.2021 final data\T=0.5s\s=1.2 (2)\air=10.0\data'
load 'L 750 50 950.mat'
L_second=breaklength(:,3)/water_dia;

cd 'D:\OneDrive - University of Edinburgh\3.30.2021 final data\T=0.5s\s=1.2 (3)\air=10.0\data'
load 'L 750 50 950.mat'
L_third=breaklength(:,3)/water_dia;

% cd 'D:\OneDrive - University of Edinburgh\3.30.2021 final data\T=1.0s\s=0.0 (4)\air=5\data'
% load 'L 750 50 950.mat'
% L_fourth=breaklength(:,3)/water_dia;

L_sampling=[L_first;L_second;L_third];
% L_sampling=[L_first;L_second;L_third;L_fourth];

[a,~]=size(L_second);
g1 = repmat({'First'},a,1);
g2 = repmat({'Second'},a,1);
g3 = repmat({'Third'},a,1);
% g4 = repmat({'Fourth'},a,1);
g = [g1;g2;g3];
% g = [g1;g2;g3;g4];

fig1=figure(1);
boxplot(L_sampling,g)
ylabel('L/D_l','FontSize',20)
title('air=3kg/h, s=0','FontSize',20)

%%
newFolder = 'C:\Users\fanfanboom\OneDrive\Desktop\L\s=1.2 (1)\air=10';
cd(newFolder);
save('L divided by D.mat','L_first')

newFolder = 'C:\Users\fanfanboom\OneDrive\Desktop\L\s=1.2 (2)\air=10';
```

```
cd(newFolder);
save('L divided by D.mat','L_second')

newFolder = 'C:\Users\fanfanboom\OneDrive\Desktop\L\s=1.2
    (3)\air=10';
cd(newFolder);
save('L divided by D.mat','L_third')

% newFolder = 'C:\Users\fanfanboom\OneDrive\Desktop\L\s=0.0
    (4)\air=5';
% cd(newFolder);
% save('L divided by D.mat','L_fourth')
```

B.20 draft_plot7.m

```
% this code is used to plot PIV data

cd 'D:\OneDrive - University of Edinburgh\Journal papers\PIV
    data used to plot\Plot_HorLine\Z velocity'

x0S = readmatrix('0S0001.csv');
x0_3S = readmatrix('0.3S0001.csv');
x0_8S = readmatrix('0.8S0001.csv');
x1_2S = readmatrix('1.2S0001.csv');
x1_5S = readmatrix('1.5S0001.csv');
x2_5S = readmatrix('2.5S0001.csv');

shift = 3.534; %unit: mm
figure(3)
hold on
plot(x2_5S(:,1)+shift,x2_5S(:,2),'-s','MarkerFaceColor'
    ,[0.6350 0.0780 0.1840],'color',[0.6350 0.0780 0.1840])

plot(x1_5S(:,1)+shift,x1_5S(:,2),'s-','MarkerFaceColor',[0
    0.4470 0.7410],'color',[0 0.4470 0.7410])

plot(x1_2S(:,1)+shift,x1_2S(:,2),'s-','MarkerFaceColor'
    ,[0.9290 0.6940 0.1250],'color',[0.9290 0.6940 0.1250])

```

```
plot(x0_8S(:,1)+shift,x0_8S(:,2),'s-','MarkerFaceColor'
    ,[0.3010 0.7450 0.9330],'color',[0.3010 0.7450 0.9330])

plot(x0_3S(:,1)+shift,x0_3S(:,2),'s-','MarkerFaceColor'
    ,[0.4940 0.1840 0.5560],'color',[0.4940 0.1840 0.5560])

plot(x0S(:,1)+shift,x0S(:,2),'s-','MarkerFaceColor',[0.4660
    0.6740 0.1880],'color',[0.4660 0.6740 0.1880])

legend ('$S=2.5$','$S=1.5$','$S=1.2$','$S=0.8$','$S=0.3$','$
    S=0$','Interpreter','latex')
hold off
```

B.21 draft_plot9.m

```
% this code is used to create the final data plot for new
    break-up length
% for S = 1.5-3.9 with We as the X axis
clear
water_dia=4;% water tube diameter(mm)

for ii=[1.5 2.5 3.1 3.9] % swirl number matrix
    data=[];
    g2=[];
if ii==1.5
    air_vel = [2 3 4 5]; % air velocities matrix
elseif ii==2.5
    air_vel = [1.5 1.8 2 3];
elseif ii==3.1
    air_vel = [1.0 1.3 2 3];
else
    air_vel = [1 2 3];
end

for i=air_vel

    if ii==1.5 %if s=1.5?
        sample=[1 2 3 4]; % times matrix
    else
```

```
        sample=[1 2 3];% times matrix
    end

    for j=sample

       if ii==2.5 || ii==3.1 %if s=2.5 or s=3.1?
       newFolder = sprintf('D:/OneDrive - University of Edinburgh/L/data1/s=%.1f (%d)/air=%.1f',ii,j,i);
       cd(newFolder);
       elseif ii==1.5 || ii==3.9 %if s=1.5 or s=3.9?
       newFolder = sprintf('D:/OneDrive - University of Edinburgh/L/data1/s=%.1f (%d)/air=%d',ii,j,i);
       cd(newFolder);
       end

          load 'L divided by D.mat'
          L_data=breaklength(:,2);

    [n,~]=size(L_data);% get the number of the rows of data

    if ii==0.0
       We = i^2; %calculate the aero We
    else
       We = round(4.4*i^2);
    end

    g1 = repmat(We,n,1); % label each row

    g2=[g2;g1];% the matrix which contains label

    data=[data;L_data];% stack the data in one column

    breaklength=[];

    end

end

    if ii==1.5 % subplot for S=1.5
```

```
        hold on
        fig = figure(1);
        t1 = tiledlayout(1,4,'TileSpacing','compact','Padding','normal');
        ax31 = nexttile;
        boxplot(data,g2,'OutlierSize',4);
        ylim([0 18])
        grid on
        title('$S=1.5$','Interpreter','latex','FontSize',10)
        ylabel('$L_d/D_l$','Interpreter','latex','FontSize',10)
        hold off
    elseif ii==2.5 %subplot for S=2.5
        hold on
        ax32 = nexttile;
        boxplot(data,g2,'OutlierSize',4);
        ylim([0 18])
        grid on
        title('$S=2.5$','Interpreter','latex','FontSize',10)
        xlabel('$We_A$','Interpreter','latex','FontSize',10)
        hold off
    elseif ii==3.1 %subplot for S=3.1
        hold on
        ax33 = nexttile;
        boxplot(data,g2,'OutlierSize',4);
        ylim([0 18])
        grid on
        title('$S=3.1$','Interpreter','latex','FontSize',10)
        hold off
    elseif ii==3.9 %subplot for S=3.9
        hold on
        ax34 = nexttile;
        boxplot(data,g2,'OutlierSize',4);
        ylim([0 18])
        grid on
        title('$S=3.9$','Interpreter','latex','FontSize',10)
        hold off
    end

```

```
end
%%
% hold on
% % subplot(1,4,1)
% bbb=boxchart(g2,data,'LineWidth',1.5);
% bbb.BoxWidth = 1;
% bbb.WhiskerLineColor = color;
% bbb.BoxFaceColor = color;
% bbb.MarkerColor = color;
% xlim([0 270])
% ylim([0 17])
% grid on
% legend('s=3.9')
% xlabel('$We_A$','Interpreter','latex','FontSize',20)
% ylabel('$L_d/D_l$','Interpreter','latex','FontSize',20)
% title('break-up length vs aerodynamic Weber number','
   FontSize',20)
% hold off
```

B.22 pca_ori.m

```
% POD on shadowgrams
%% read one image to get image to determine crop region
close all
clear all
clc
swirl = 2.5; % swirl number
air = 10; % air mass flow rate (kg/h)
frame_rate = 4000; %frame rate of your data (fps)
rec_time = 1; %recording time duration (s)
y_start = 297; %vertical region to crop to [y_start,y_end] (
   length = 576 pixel)
y_end = 873;
x_start = 279; %horizontal region to crop to [x_start,x_end]
    (width = 136*2 pixel)
x_end = 551;

mov_frame_rate = 5; % the desired frame rate of your movie (
   fps)
```

```
mov_quality = 100; % the desired quality of the movie

img_dir = sprintf('X:/Videos with high M/S=%.1f/air=%d/',swirl,air);% image folder
% res_dir = sprintf('Y:/Videos with high M/POD results/S=%.1f/air=%d/',swirl,air);% result folder
% res_dir = 'D:\OneDrive - University of Edinburgh\Journal papers\POD data repository\s=3.1 (3)\air=3\'; % result folder
img_no = "00001";
img = imread(img_dir + "h" + img_no + ".tif");
figure(1)
imshow(img, [])
axis equal
%% image region to crop to
crop_indx = [[y_start, y_end]; [x_start, x_end]];
% cropped image dimensions
img_crop_dim = [crop_indx(1,2) - crop_indx(1,1) + 1, crop_indx(2,2) - crop_indx(2,1) + 1];

% preallocate array to store images as columns
no_img = frame_rate*rec_time; % no of images to read
img_list = zeros(img_crop_dim(1), img_crop_dim(2), no_img);
dt = 1/frame_rate; % t sample period (s)
% read images and store as columns

for i=1:no_img
    img_name = sprintf("h%05d.tif", i);
    img = imread(img_dir + img_name);
    img_crop = img(crop_indx(1,1):crop_indx(1,2), crop_indx(2,1):crop_indx(2,2));
    img_list(:, :, i) = img_crop;
end

% Singular value decomposition of centered images
img_col_len = img_crop_dim(1)*img_crop_dim(2); % length of a cropped image rearranged as a vector
img_list_col = reshape(img_list, img_col_len, no_img); % array of images as column vectors
```

```
img_list_m = mean(img_list_col, 2); % row means
img_list_c = img_list_col - img_list_m; % center rows of image column array for PCA
[U,S,V] = svd(img_list_c, "econ"); % SVD on centered image column array (PCA)

% Semilog plot of singular values
fig2 = figure(2);
stem(diag(S),'MarkerSize',10,'MarkerEdgeColor','red','MarkerFaceColor','red') % look for large singular values to determine if there dominant modes
set(gca,'Fontsize',20)
xlim([1,no_img])
%title("Singular values")
xlabel("The No. of the modes",'Fontsize',20)
ylabel("The singular values",'Fontsize',20)
grid

% Principle component images and frequencies of principal components
imgP1 = reshape(U(:,1), img_crop_dim(1), img_crop_dim(2)); % 1st principal component
imgP2 = reshape(U(:,2), img_crop_dim(1), img_crop_dim(2)); % 2nd principal component
imgP3 = reshape(U(:,3), img_crop_dim(1), img_crop_dim(2)); % 3rd principal component
imgP4 = reshape(U(:,4), img_crop_dim(1), img_crop_dim(2)); % 4th principal component
fig3 = figure(3);
t3 = tiledlayout(2,4,'TileSpacing','compact','Padding','normal');
ax31 = nexttile;
imshow(imgP1'/(max(max(imgP1))), 'Colormap', parula, 'DisplayRange', [-1,1]); %normalize imgP1
title("1st mode")
ax32 = nexttile;
imshow(imgP2'/(max(max(imgP2))), 'Colormap', parula, 'DisplayRange', [-1,1]);
title("2nd mode")
```

```
ax33 = nexttile;
imshow(imgP3'/(max(max(imgP3))), 'Colormap', parula, '
    DisplayRange', [-1,1]);
title("3rd mode")
ax34 = nexttile;
imshow(imgP4'/(max(max(imgP4))), 'Colormap', parula, '
    DisplayRange', [-1,1]);
title("4th mode")
ax35 = nexttile;
fx = fftfreq(no_img, dt); % frequency axis for fft plot (
    values are fraction of total recording duration)
F1 = fft(V(:, 1)); % frequency of 1st principal component
stem(fx(:,1:no_img/2), abs(F1(1:no_img/2,:)))
set(gca,'Fontsize',20)
xlim([0,max(fx)])
grid
xlabel("Frequency (Hz)",'Fontsize',15)
% ylabel("|P1(f)|",'Fontsize',15)
ylabel("Magnitude",'Fontsize',15)
ax36 = nexttile;
F2 = fft(V(:, 2)); % frequency of 2nd principal component
stem(fx(:,1:no_img/2), abs(F2(1:no_img/2,:)))
set(gca,'Fontsize',20)
xlim([0,max(fx)])
grid
xlabel("Frequency (Hz)",'Fontsize',15)
ax37 = nexttile;
F3 = fft(V(:, 3)); % frequency of 3rd principal component
stem(fx(:,1:no_img/2), abs(F3(1:no_img/2,:)))
set(gca,'Fontsize',20)
xlim([0,max(fx)])
grid
xlabel("Frequency (Hz)",'Fontsize',15)
ax38 = nexttile;
F4 = fft(V(:, 4)); % frequency of 4th principal component
stem(fx(:,1:no_img/2), abs(F4(1:no_img/2,:)))
set(gca,'Fontsize',20)
xlim([0,max(fx)])
grid
```

```
xlabel("Frequency (Hz)",'Fontsize',15)

saveas(fig2,strcat(res_dir,'sig')) % save fig2 in a specific folder with a name called 'sig'
saveas(fig3,strcat(res_dir,'modes')) % save fig3 in a specific folder with a name called 'modes'
%% make a video to show the reconstructed images
% Compare reconstructed image using 4 first principal components with original (movie version)
img_list_col_r = U(:,1:4)*S(1:4,1:4)*V(:,1:4)' + img_list_m; % Reconstuct images with first 4 principal components
% img_list_col_r = U(:,1)*S(1,1)*V(:,1)' + img_list_m; % Reconstuct images with the first principal components
img_list_r = reshape(img_list_col_r, img_crop_dim(1), img_crop_dim(2), no_img); % Reshape reconstructed array to original array shape

% make a video to compare the reconstruted image with original
pause(2.0) % casual pause
close all
writerObj = VideoWriter(strcat(res_dir,'rec_first_pc.mp4'),'MPEG-4'); % save the video in a specfic folder with a name called rec.mp4
writerObj.FrameRate = mov_frame_rate; % frame_rate of the movie (fps)
writerObj.Quality= mov_quality; % quality of the movie
F(no_img) = struct('cdata',[],'colormap',[]); % Preallocate an array F to store the movie frames.
open(writerObj);

max_img_list_r = max(max(max(img_list_r(:,:,:))));
fig4 = figure('units','normalized','outerposition',[0 0 1 1]);
tiledlayout(1,2)
ax41 = nexttile;
im1 = imshow(img_list(:,:,1)/max_img_list_r, 'Colormap', parula, 'DisplayRange', [0,1]);
title(ax41, "Original")
```

```
ax42 = nexttile;
im2 = imshow(img_list_r(:,:,1)/max_img_list_r, 'Colormap',
   parula, 'DisplayRange', [0,1]);
title(ax42, "PC reconstruct")

for i=2:no_img/2
    im1 = imshow(img_list(:,:,i)/max_img_list_r, 'Colormap',
       parula, 'DisplayRange', [0,1], 'Parent', ax41);
    im2 = imshow(img_list_r(:,:,i)/max_img_list_r, 'Colormap'
       , parula, 'DisplayRange', [0,1], 'Parent', ax42);
    title(ax41, "Original")
    title(ax42, "PC reconstruct")

    F(i)=getframe(gcf);
    writeVideo(writerObj, F(i))
end
close(writerObj);

% % Compare reconstructed image using 4 first principal
    components with original (animation version)
% img_list_col_r = U(:,1:4)*S(1:4,1:4)*V(:,1:4)' +
    img_list_m; % Reconstuct images with first 4 principal
    components
% img_list_r = reshape(img_list_col_r, img_crop_dim(1),
    img_crop_dim(2), no_img); % Reshape reconstructed array
    to original array shape
%
% fig4 = figure('Position', [0 0 400 802]);
% tiledlayout(1,2)
% ax41 = nexttile;
% im1 = imshow(img_list(:,:,1), 'Colormap', parula, '
    DisplayRange', []);
% title(ax41, "Original")
% ax42 = nexttile;
% im2 = imshow(img_list_r(:,:,1), 'Colormap', parula, '
    DisplayRange', []);
% title(ax42, "PC reconstruct")
% % uncomment export graphics to produce an image for each
    time step (for making a movie file with ffmpeg)
```

```
% %exportgraphics(fig4, sprintf("%02d.png", 1));
% for i=2:no_img
%     im1 = imshow(img_list(:,:,i), 'Colormap', parula, '
   DisplayRange', [], 'Parent', ax41);
%     im2 = imshow(img_list_r(:,:,i), 'Colormap', parula, '
   DisplayRange', [], 'Parent', ax42);
%     title(ax41, "Original")
%     title(ax42, "PC reconstruct")
%     pause(0.1)
%     %exportgraphics(fig4, sprintf("%02d.png", i));
% end

function f = fftfreq(n, d)
    if mod(n, 2.0) % n odd length
        f0 = (0:1.0:((n-1)/2))/(n*d);
        f1 = ((-(n-1)/2):1.0:-1.0)/(n*d);
        f = [f0, f1];
    else % n even length
        f0 = (0:1.0:(n/2-1))/(n*d);
        f1 = ((-n/2):1.0:-1.0)/(n*d);
        f = [f0, f1];
    end
end
```

Bibliography

2D PDI user manual [Computer software manual]. (2022). (available at https://www.artium.com)

Adrian, R. J. (1991). Particle-imaging techniques for experimental fluid mechanics. *Annu. Rev. Fluid Mech*, *23*, 261–304.

Albrecht, H. E., Borys, M., Damaschke, N., & Tropea, C. (2003). *Laser doppler and phase doppler measurement techniques*. Springer.

Aliseda, A., Hopfinger, E. J., Lasheras, J. C., Kremer, D. M., Berchielli, A., & Connollyr, E. K. (2008). Atomization of viscous and non-newtonian liquids by a coaxial, high-speed gas jet. experiments and droplet size modelling. *International Journal of Multiphase Flow*, *34*, 161-175.

Arienti, M., & Soteriou, M. C. (2009). Time-resolved proper orthogonal decomposition of liquid jet dynamics. *Phys. Fluids*, *21*, 112104.

Arunachalam, S., Khairnar, S., & Desale, B. (2013). The fast fourier transform algorithm and its application in digital image processing. *Mathematical theory and modeling*, *3*, 267-273.

Atkins, M. D. (2016). *Application of thermo-fluidic measurement techniques: An introduction*. Elsevier.

Bachalo, W. (2000). Spray diagnostics for the twenty-first century. *Atomization and Sprays*, *10*, 439-474.

Benjamin, T. B. (1967). Some developments in the theroy of vortex breakdown. *J. Fluid Mech*, *28*, 65–84.

Berrocal, E., Paciaroni, M., Mazumdar, Y., Andersson, M., Falgout, Z., & Linne, M. (2023). Optical spray imaging diagnostics. In A. Steinberg & S. Roy (Eds.), *Optical combustion diagnostics for propulsion and power systems: Theory and application.* American Institute of Aeronautics and Astronautics.

Billant, P., Chomaz, J. M., & Huerre, P. (1998). Experimental study of vortex breakdown in swirling jets. *J. Fluid Mech*, *376*, 183-219.

Born, M. (1933). *Optik*. Springer.

Born, M., & Wolf, E. (1999). *Principles of optics*. Cambridge University Press.

Bozonnet, C., Matas, J.-P., Balarac, G., & Desjardins, O. (2022). Stability of an air–water mixing layer: focus on the confinement effect. *Journal of Fluid Mechanics*, *933*, A14. doi: 10.1017/jfm.2021.1069

Brunton, S. L., & Kutz, J. N. (2019). *Data-driven science and engineering: Machine learning, dynamical systems, and control.* Cambridge University Press.

Charalampous, G., & Hardalupas, Y. (2014). Application of proper orthogonal decomposition to the morphological analysis of confined co-axial jets of immiscible liquids with comparable densities. *Phys. Fluids*, *26*, 113301.

Collection of solved problems in physics. (2018, June). Retrieved from `https://physicstasks.eu/1966/interference-of-two-plane-waves-propagating-in-different-directions` (Online)

Dumouchel, C. (2008). On the experimental investigation on primary atomization of liquid streams. *Exp Fluids*, *45*, 371-422.

Dunand, A., Carreau, J. L., & Roger, F. (2005). Liquid jet breakup and atomization by annular swirling gas jet. *Atomization and Sprays*, *15*, 223–247.

Eisenklam, P., & Hooper, P. (1958). The flow characteristics of laminar and turbulent jets of liquid. *Ministry of Supply D.G.G.W. Report/EMR/58/10*.

Engelbert, C., Hardalupas, Y., & Whitelaw, J. H. (1995). Breakup phenomena in coaxial airblast atomizers. *Proc. R. Soc*, *451*, 189–229.

Eroglu, H., & Chigier, N. (1991). Initial drop size and velocity distributions for airblast coaxial atomizers. *Journal of Fluids Engineering*, *113*, 453–459.

Eroglu, H., Chigier, N., & Farago, Z. (1991). Coaxial atomizer liquid intact lengths. *Physics of Fluids A: Fluid Dynamics*, *3*, 303—308.

Farago, Z., & Chigier, N. (1992). Morphological classification of disintegration of round liquid jets in a coaxial air stream. *Atomization Sprays*, *2*, 137-153.

Flowmaster [Computer software manual]. (2020). (available at https://www.lavision.de/en/downloads/manuals/systems.php)

Giannadakis, A., Perrakis, K., & Panidis, T. (2008). A swirling jet under the influence of a coxial flow. *Experimental Thermal and Fluid Science*, *32*, 1548–1563.

Hardalupas, Y., & Whitelaw, J. H. (1998). Coaxial airblast atomizers with swirling air stream. *Recent advances in spray combustion: measurements and model simulation (American Institute of Aeronautics and Astronautics)*, *2*, 201–232.

Hecht, E. (2018). *Optik*. De Gruyter. Retrieved 2022-05-05, from `https://doi.org/10.1515/9783110526653`.

Heywood, J. B. (2018). *Internal combustion engine fundamentals*. McGraw-Hill.

Hopfinger, E. J. (1998). Liquid jet instability and atomization in a coaxial gas stream. In U. Frisch (Ed.), *Advances in turbulence vii* (pp. 69–78). Dordrecht: Springer Netherlands.

Hopfinger, E. J., & Lasheras, J. C. (1996). Explosive breakup of a liquid jet by a swirling coaxial gas jet. *Physics of Fluids*, *8*, 1696–1698.

Ibrahim, A. A., & Jog, M. A. (2006). Nonlinear breakup of a coaxial liquid jet in a swirling gas stream. *Physics of Fluids*, *18*, 114101.

Ibrahim, E. A., & Marshall, S. O. (2000). Instability of a liquid jet of parabolic velocity profile. *Chemical Engineering Journal*, *76*, 17–21.

Ivanic, T., Foucault, E., & Pecheux, J. (2003). Dynamics of swirling jet flows. *Experiments in Fluids*, *35*, 317–324.

Joseph, D. D., Beavers, G. S., & Funada, T. (2002). Rayleigh–taylor instability of viscoelastic drops at high weber numbers. *J. Fluid Mech*, *453*, 109-132.

Keane, R. D., & Adrian, R. J. (1992). Theory of cross-correlation analysis of PIV images. *Appl. Sci. Res*, *49*, 191–215.

Kumar, A., & Sahu, S. (2018a). Liquid jet breakup unsteadiness in a coaxial air-blast atomizer. *International Journal of Spray and Combustion Dynamics*, *10*, 211–230.

Kumar, A., & Sahu, S. (2018b). Optical visualization and measurement of liquid jet core in a coaxial atomizer with annular swirling air. *J. Flow Visualization Image Process*, *25*, 229–244.

Kumar, A., & Sahu, S. (2019). Large scale instabilities in coaxial air-water jets with annular air swirl. *Physics of Fluids*, *31*, 124103.

Langeslag, M., & Linne, M. (2016). *The design, construction and testing of a shear-breakup spray* (Unpublished master's thesis). University of Edinburgh.

Lasheras, J. C., & Hopfinger, E. J. (2000). Liquid jet instability and atomization in a coaxial gas stream. *Annual Review of Fluid Mechanics*, *32*, 275–308.

Lasheras, J. C., Villermaux, E., & Hopfinger, E. J. (1998). Break-up and atomization of a round water jet by a high-speed annular air jet. *J. Fluid Mech*, *357*, 351–379.

Lefebvre, A. H., & McDonell, V. (2017). *Atomization and sprays (2nd edition)*. CRC Press.

Leroux, B., Delabroy, O., & Lacas, F. (2007). Experimental study of coaxial atomizers scaling. Part I: dense core zone. *Atomization and Sprays*, *17*, 381—407.

Lian, Z. W., & Lin, S. P. (1990). Breakup of a liquid jet in a swirling gas. *Physics of Fluids*, *2*, 2134–2139.

Liang, Y., Johansen, L. C., & Linne, M. (2022a). Breakup of a laminar liquid jet by coaxial non-swirling and swirling air streams. *University of Edinburgh*. (dataset. https://doi.org/10.7488/ds/3459)

Liang, Y., Johansen, L. C., & Linne, M. (2022b). Characteristics of sprays produced by coaxial non-swirling and swirling air-water jets with high aerodynamic Weber numbers. *University of Edinburgh*. (dataset. https://doi.org/10.7488/ds/3478)

Liao, Y., Jeng, S. M., Jog, M. A., & Benjamin, M. A. (2000). The effect of air swirl profile on the instability of a viscous liquid jet. *J. Fluid. Mech*, *424*, 1-20.

Lin, S. P. (1996). Regimes of jet break up and break up mechanisms (mathematical aspects). *Recent advacnes in spray combustion: spray atomization and droplet burning phenomena*, *166*, 109-136.

Lin, S. P., Hudman, M., & Chen, J. N. (1999). Absolute and convective instability of a liquid jet. In *Proceedings of the fourth microgravity fluid physics and transport phenomena conference.* Springer Netherlands.

Linne, M. (2013). Imaging in the optically dense regions of a spray: A review of developing techniques. *Progress in Energy and Combustion Science*, *39*(5), 403-440. Retrieved from `https://www.sciencedirect.com/science/article/pii/S0360128513000282` doi: https://doi.org/10.1016/j.pecs.2013.06.001

Machicoane, N., Bothell, J. K., Li, D., Morgan, T. B., Heindel, T. J., Kastengren, A. L., & Aliseda, A. (2019). Synchrotron radiography characterization of the liquid core dynamics in a canonical two-fluid coaxial atomizer. *International Journal of Multiphase Flow*, *115*, 1-8.

Machicoane, N., Ricard, G., Osuna-Orozco, R., Huck, P. D., & Aliseda, A. (2020). Influence of steady and oscillating swirl on the near-field spray characteristics in a two-fluid coaxial atomizer. *International Journal of Multiphase Flow*, *129*, 103318.

Maddahian, R., Farhanieh, B., & Firoozabadi, B. (2011). Turbulent flow in converging nozzles, part one: boundary layer solution. *Appl. Math. Mech*, *32*, 645–662.

Maddahian, R., Kebriaee, A., Farhanieh, B., & Firoozabadi, B. (2011). Analytical investigation of boundary layer growth and swirl intensity decay rate in a pipe. *Appl. Math. Mech*, *81*, 489–501.

Marklund, M., & Engstrom, F. (2010). Water spray characterization of a coaxial air-assisted swirling atomizer at sonic conditions. *Atomization Sprays*, *20*, 955–963.

Matas, J.-P., Delon, A., & Cartellier, A. (2018). Shear instability of an axisymmetric air–water coaxial jet. *J. Fluid Mech*, *843*, 575-600.

Matas, J.-P., Marty, S., & Cartellier, A. (2011). Experimental and analytical study of the shear instability of a gas-liquid mixing layer. *Physics of Fluids*, *23*, 094112.

Otto, T., Rossi, M., & Boeck, T. (2013). Viscous instability of a sheared liquid-gas interface: Dependence on fluid properties and basic velocity profile. *Physics of Fluids*, *25*, 032103.

Prasad, A. K. (2000). Stereoscopic particle image velocimetry. *Experiment in Fluids*, *29*, 103-116.

Prasad, A. K., Adrain, R. J., Landreth, C. C., & Offutt, P. W. (1992). Effect of resolution on the speed and accuracy of particle image velocimetry interrogation. *Exp. Fluids*, *13*, 105–116.

Raffel, M., Willert, E. C., Wereley, T. S., & Kompenhans, J. (2018). *Particle image velocimetry: A practical guide*. Springer.

Rajamanickam, K., & Saptarshi, B. (2017a). Insights into the dynamics of spray-swirl interactions. *J. Fluid Mech*, *810*, 82–126.

Rajamanickam, K., & Saptarshi, B. (2017b). On the dynamics of vortex–droplet interactions, dispersion and breakup in a coaxial swirling flow. *J. Fluid Mech*, *827*, 572–613.

Rajamanickam, K., & Saptarshi, B. (2018). Insights into the dynamics of conical breakdown modes in coaxial swirling flow field. *J. Fluid Mech*, *853*, 72–110.

Ranz, W. E. (1956). *On sprays and spraying*. College of Engineering and Architecture.

Raynal, L. (1997). Instabilite et entrainement a l'interface d'une couche de melange liquide-gaz. *Ph.D thesis*.

Reitz, R. D. (1978). Atomization and other breakup regimes of a liquid jet. *Ph.D thesis*.

Reitz, R. D., & Bracco, F. V. (1986). Mechanisms of breakup of round liquid jets. *The Encyclopedia of Fluid Mechanics*, *3*, 223–249.

Samimy, M., & Lele, S. K. (1991). Motion of particles with inertia in a compressible free shear layer. *Phys. Fluids*, *3*, 1915-1923.

Santhosh, R., Miglant, A., & Basu, S. (2014). Transition in vortex breakdown modes in a coaxial isothermal unconfined swirling jet. *Phys. Fluids*, *26*, 043601.

Schlichting, H., & Gersten, K. (2017). *Boundary layer theory*. Springer.

Settles, G. (2001). *Schlieren and shadowgraph techniques*. Berlin: Springer.

Soloff, S. M., Adrian, R. J., & Liu, Z.-C. (1997). Distortion compensation for generalized stereoscopic particle image velocimetry. *Meas Sci Technol*, *8*, 1441-1454.

Strang, G. (2016). *Introduction to linear algebra* (5th ed.). Wellesley-Cambridge Press.

Strang, G. (2019). *Linear algebra and learning from data*. Wellesley-Cambridge press.

Taira, K., Brunton, S. L., Dawson, S. T. M., Rowley, C. W., Colonius, T., McKeon, B. J., ... Ukeiley, L. S. (2017). Modal analysis of fluid flows: an overview. *American Institute of Aeronautics and Astronautics*, *55*, 4013–4041.

Umemura, A. (2014). Model for the initiation of atomization in a high-speed laminar liquid jet. *J. Fluid Mech*, *757*, 665-700.

Varga, C. M., Lasheras, J. C., & Hopfinger, E. J. (2003). Initial breakup of a small-diameter liquid jet by a high-speed gas stream. *J. Fluid Mech*, *497*, 405-434.

Vihinen, I., Honohan, A. M., & Lin, S. P. (1997). Image of absolute instability in a liquid jet. *Physics of Fluids*, *9*, 3117-3119.

Villermaux, E. (1998). Mixing and spray formation in coaxial jets. *Journal of Propulsion and Power*, *14*, 807-817.

Westerweel, J. (1997). Fundamentals of digital particle image velocimetry. *Meas. Sci. Technol*, *8*, 1379–1392.

Westerweel, J. (2000). Theoretical analysis of the measurement precision in particle image velocimetry. *Exp. Fluids*, *29*, S003–S012.

White, F. M. (2005). *Viscous fluid flow* (3rd ed.). McGraw-Hill.

White, F. M. (2016). *Fluid mechanics*. McGraw-Hill.

Willert, C. E. (2006). Assessment of camera models for use in planar velocimetry calibration. *Experiment in Fluids*, *41*, 135-143.

Yang, L., Gao., Y., Li, J., & Fu, Q. (2020). Theoretical atomization model of a coaxial gas-liquid jet. *Physics of Fluids*, *32*, 124108.

Zhao, H., Liu, H. F., Tian, X. S., Xu, J. L., Li, W. F., & Lin, K. F. (2014). Influence of atomizer exit area ratio on the breakup morphology of coaxial air and round water jets. *AIChE Journal*, *60*, 2335—2345.